University of Pavia

Faculty of Engineering

Department of Civil Engineering and Architecture

PhD in Design, modelling and simulation in engineering

Cycle XXXVI

PhD Thesis

Lagrangian numerical modelling of wave-structure interaction

Modellazione numerica Lagrangiana di interazione onda-struttura

A.A. 2023/2024

Candidate:
Nicoló Salis

Supervisor:
Prof. Sauro Manenti

Alla mia famiglia, in particolare Gigi, Graziella e Maura che hanno creduto in me e continuano a farlo, nonostante tutto.

A Ilde che mi è stata acanto nei momenti più difficili, riaccendendo la speranza e regalandomi un sorriso.

Al professor Sauro Manenti, che mi ha accompagnato in questi anni di formazione e crescita professionale, instaurando un rapporto di reciproca stima e fiducia.

Al professor Alessandro Reali, che fin dal primo giorno ha creduto nelle mie potenzialità.

Al professor Luo Min, per la cui collaborazione è stata preziosa in questi anni.

Ai professori Alessandro Franci, Sergio Idelsohn, Eugenio Oñate per l'ospitalità dimostrata durante i mesi trascorsi al CIMNE.

Al professor Xiangiu Hu, per avermi coinvolto nel suo team di ricerca al TUM di Monaco di Baviera.

Lagrangian numerical modelling of waves-structure interaction

Salis Nicoló

Abstract

Offshore structure design requires a reliable definition of the wave loads. With climate change, extreme wave events pose significant concerns in coastal and ocean engineering. Moreover, these events are expected to increase in frequency and severity. Waves have the potential to inflict extensive damage on offshore and coastal structures, leading to human and economic losses. The research community has underlined the importance of understanding wave action on an offshore structure. This study aims to analyse wave generation, propagation and structure interaction using Lagrangian particle methods. Multiple models will be utilised and developed to simulate various scenarios: from the generation regular waves in a channel to the modelling of nonlinear wave interacting with floating structures.

Sommario

I carichi generati dalle onde sulle strutture offshore necessitano di una corretta definizione. I cambiamenti climatici aumentano la probabilità di eventi estremi, questi rappresentano una grave preoccupazione per tutte quelle strutture inserite nel contesto marittimo, dalle navi ai parchi eolici. Onde di grande dimensioni possono causare gravi danni oltre che alle strutture, anche al personale tecnico. Inoltre possono essere cause di gravi perdite economiche. Questo lavoro propone di analizzare la generazione, propagazione e interazione di onde con strutture utilizzando metodi numerici Lagrangiani particellari. Diversi modelli sono stati studiati e sviluppati applicandoli a una grande varietà di casi studio: dalla generazione di onde regolari in canale alla modellazione dell'interazione di onde non lineari con strutture flottanti.

Contents

1

Introduction

The marine environment is highly complex and demanding, introducing many challenges in the field of offshore engineering. The population of marine structures has significantly increased and is expected to continue growing. Marine structures encompass a wide array of constructions found in the sea, ranging from large vessels to offshore wind farms and oil rigs. Concurrently, the marine environment is rapidly evolving, with sea conditions deteriorating due to climate change. This includes rising mean sea levels, increased mean wave heights, and more frequent extreme wave events. Consequently, existing marine structures require thorough assessment to ensure the safety of both the structure and its operators. Moreover, newly designed structures necessitate accurate definition of wave loads.

Wave loads are typically assessed using empirical methods, often overlooking the loads generated by extreme waves. Achieving a precise definition of wave load requires scaled experimental models. However, such experimental campaigns are costly and require a minimum scale to avoid inaccuracies. Additionally, any changes to the experimental setup can be prohibitively expensive and may necessitate a complete redesign. Numerical simulations can complement laboratory experiments and, once validated, can guide the design of offshore structures and experimental campaigns.

In this study, we explore the potential of modelling wave loads using Lagrangian particle methods. Various models are developed and validated across a range of scenarios. Lagrangian particle methods hold significant appeal due to their ability to accurately reproduce large domain deformations and fragmentation (e.g., wave breaking), as well as strong velocity and pressure gradients (e.g., wave-structure impact).

The work starts with a discussion on the role of mathematical models in engineering. The governing equations of fluid dynamics (Navier-Stokes equations) are introduced, with analytical solutions achievable only for relatively simple cases. To obtain the solution for engineering problems of practical interest, these equations must be discretized and solved using approximate numerical techniques. The approaches utilised in this study are presented and analysed.

The first approach discussed is Smoothed Particle Hydrodynamics (SPH), a Lagrangian particle-based method relying on the kernel approximation of field functions. A comprehensive overview of the method is provided, covering both fundamental principles and advanced features. The second approach, the Particle Finite Element Method (PFEM), also a Lagrangian particle-based method, combines the advantages of particle methods with the positive features of using computational grids. A remeshing technique based on Delaunay triangulation is introduced to model large domain deformations. Additionally, the Simulating WAves Nearshore (SWAN) model, which solves the spectral balance equation for the action density spectrum, is presented for hindcasting and forecasting sea waves in coastal contexts.

Then, the work illustrates the fundamental aspects of free surface waves, beginning with a bibliographic overview. The small wave theory (Airy) and analytical solutions of boundary value problems are discussed, followed by topics such as dispersion equations and dynamic pressure in regular waves. The generation of waves in a channel is explored, including the presentation of transfer functions for different wavemaker types, with a focus on piston type wavemakers. The study delves into non-linear waves, particularly solitary waves, and introduces the focusing wave theory before discussing short-term wave analysis of random sea states, including the definition of directional wave spectra.

Subsequently, these models are applied for the analysis of problems of practical interests, from the definition of wind-generated wave conditions, to the wave propagation toward the shore and the impact with rigid structures. The first study focuses on wave hindcasting in a portion of the Mediterranean Sea using the SWAN model, generating waves from wind forecast data and modelling main physical processes of wave generation and transformation. Validation against field measurements from a wave measurement station is performed across a large sea area utilizing digital terrain models. Then, modeling regular wave generation in a two-dimensional channel using the SPHERA v9.0.0 is carried out. Non negligible wave height and velocity dissipation prompted the introduction of a renormalisation technique on the kernel derivative. Results are detailed in a conference paper titled: “SPH Simulation of Water Waves and Impact with a Rigid Offshore Structure in a 2D Flume". Subsequent investigation involves non-linear wave impact with a fixed box-shaped structure, highlighting the advantages of modeling both water and air. The development of a new strategy for modeling multi-phase flows with high density ratio is addressed, focusing on water-air simulations and using as primary computational variable the mass rather rather than density. The paper titled: “Wave generation and wave-structure impact modeling with WCSPH" features the simulation of multi-phase dam breaks and the validation of the single-phase formulation, albeit with noted numerical aberrations i.e. tensile instability and particle clusters.

The PFEM model demonstrates promising applications, addressing regular, non-linear, and solitary waves. This research runs parallel to the development of the SPH model, culminating in a comprehensive comparison between the two Lagrangian methods. Results are compared and validated against experimental data, providing a detailed comparison across various scenarios. This comparison is detailed in the publication titled: “Lagrangian particle-based simulation of waves: a comparison of SPH and PFEM approaches".

The research, thus far, has primarily focused on wave impacts with fixed structures. However, floating structures are of great concern in the marine environment. The study shifts focus to a floating structure moored with cables to the seabed, necessitating a 3D simulation to account for tridimensional effects. An SPH model (SPHinXsys) is coupled with a multi-body model (Simbody) to simulate fluid impact, structure displacement (based on hydrodynamic forces) and cable tension. Validation of the model accurately reproduces structure movement and impact pressures, as reported in the paper titled: “3D SPH analysis of focused waves interacting with a floating structure".

The development of the multiphase model, derived from SPHERA v9.0.0 (RSE SpA), allows overcoming those issues identified in the initial formulation. This involves the introduction of new numerical schemes, notably a particle shifting technique, aimed at preventing non-physical movement of the free surface. The introduction of an adaptive method, relying on a newly introduced particle identification method based on the determinant of the particle concentration matrix, ensures accurate simulation of multiphase flows with high density ratios. Early results demonstrate promising applications, with ongoing improvements discussed.

The objective of this work is to develop, apply and validate Lagrangian particle methods illustrated in this thesis, to the modeling of wave generation, propagation and wave-structure interaction. The main scientific contributions of this work are:

- Development of the kernel gradient normalization (KGN) with the introduction of a threshold value for the application of KGN in the momentum balance equation for reduction of numerical dissipation in slow dynamic flows maintaining numerical stability during rapidly varying flows, such as wave-structure impacts.
- Development of a novel formulation of weakly compressible smoothed particle hydrodynamics (SPH) for handling fluids with high density ratio. Furthermore, computationally efficient diffusive terms are introduced in the continuity equation instead of pressure smoothing.
- A particle shifting technique based on Fick’s law is developed, featuring a novel free surface identification procedure to prevent non-physical movement of the free surface. This technique also includes interface treatment using Riemann solvers.
- For the first time, a comparison between the SPH method and the PFEM method for modeling waves and wave-structure impacts is presented, highlighting advantages and drawbacks of each method.

- For the first time, development of an SPH model coupled with a multi-body dynamic model, for the simulation of a freak wave impact and interaction with a complex three-dimensional floating structure moored with tendons, analyzing both kinematic and dynamic aspects.

All the author's contributions to the codes development, as illustrated in this thesis, are traced on GitHub.

2

Introduction to mathematical modelling

Role of Numerical Methods

In the pre-computer era, solving complex problems relied on two main methods. The first was the traditional theoretical approach, which often required approximations and assumptions. However, these theoretical solutions frequently failed to fully capture physical phenomena, leading to the necessity for experimental campaigns to be conducted. These campaigns resulted in the development of empirical formulas. However, the empirical descriptions derived from such campaigns were limited in validity to the specific cases investigated. Conducting experiments was costly due to the high precision required, time-consuming due to the large amount of data needed, and often subject to scale effects that couldn't be disregarded. Achieving a minimum scale reduction to obtain reliable data was not always feasible.

In contrast, numerical methods emerged as a cheaper alternative to experimental campaigns, offering greater versatility by enabling rapid and cost-effective adjustments to setups. They have the potential to model a wide range of physical phenomena and eliminate many of the assumptions inherent in analytical descriptions.

However, employing numerical methods requires model calibration and validation. They are typically considered as complementary tools to experimental models, rather than standalone instruments of investigation [1, 2].

2.1 Grid Based and Mesh-less Methods

A mathematical model might interpret a real physical problem. The model is a collection of governing equations (ordinary or partial differential equations PDE) with need of initial or/and boundary conditions. If analytical description cannot be obtained, the computational domain and the governing equations must be discretized and solved in approximate way using numerical techniques.

2.1.1 Grid Based Methods

Continuum mechanics analysis can be conducted using two alternative approaches: Lagrangian and Eulerian. These two approaches are mathematically related.

In the Lagrangian framework the time rate of change of physical quantities is evaluated in a frame of reference moving with the material continuum adopting the total time derivative $\frac{D}{Dt}$ (also known as the material derivative), which can be expressed through the linear combination of the local derivative $\frac{\partial}{\partial t}$ and the convective derivative $u_i \frac{\partial}{\partial x_i}$, describing the Eulerian framework. In Equation (2.1), $\mathfrak{F}$ represents a generic field function, and the Einstein convention is applied on the right-hand side, where a repeated index implies summation over that index.

$$\frac{D\mathfrak{F}}{Dt} = \frac{\partial \mathfrak{F}}{\partial t} + u_i \frac{\partial \mathfrak{F}}{\partial x_i} \tag{2.1}$$

Lagrangian Approach describes the physical properties of a material particle within a reference frame moving with the particle itself. Computationally, the grid attached to the continuum follows its deformation without any mass flux between adjacent cells. This material continuum deformation implies relative motion between mesh nodes, which can result in distortion of mesh cells, potentially causing numerical issues [2].

Here is a list of features for the Lagrangian approach:

- ✓ Lack of convective term in the governing equation.
- ✓ Easy tracking of field variables over time.
- ✓ Mesh adapts to irregular and complex geometries, describing free or moving boundaries and material interfaces.
- ✓ Grid points only needed inside the continuum.
- ✗ Large deformation of the continuum and high mesh distortion can disrupt numerical accuracy.
- ✗ Adaptive mesh rezoning is used to control mesh distortion, introducing high computational effort.

Eulerian Approach describes any physical property of a material continuum within a space-fixed frame of reference. Computationally, a fixed grid is generated in both space and time, with no deformation occurring and mass flux between adjacent cells. Large deformation in the object does not affect the grid, thus avoiding numerical problems. Eulerian methods are commonly used in Computational Fluid Dynamics (CFD) simulations where flow of continuum dominates [3, 2].

Here are the characteristics of the Eulerian approach:

- ✗ Convective transport must be estimated, influencing the time stepping.
- ✗ Tracking the time history of field variables at a fixed material point is complex.
- ✗ Cumbersome numerical mapping is required to model complex geometries, making accurate location of free or moving boundaries and material interfaces difficult.
- ✗ Computational grids must anticipate where the fluid can move, resulting in large grids.
- ✓ Continuum deformation does not induce mesh distortion nor affect the numerical solution.
- ✓ Adaptive mesh behaviour is not necessary.

These two approaches can be combined arbitrarily to obtain Lagrangian-Eulerian formulations, offering computational advantages. However, description of these methods falls beyond the scope of this brief introduction to the basics of numerical modelling.

2.1.2 Mesh-free Methods

In mesh-free methods, the continuum is discretised using a set of arbitrarily distributed nodes that have no physical connection between them. Each node represents a material continuum. Considering the scale of the problem, each node represents an arbitrary volume that is large enough to neglect the effects of microscopic disorder yet small enough to disregard macroscopic heterogeneity. This enables to describe the physical properties by means of continuous functions of space and time.

2.1.3 Comparison Between Methods

The methods provide distinct approaches, with each being better suited to specific applications.

Key advantages of mesh-free methods include:

- ✓ Ability to handle large deformations of the continuum.
- ✓ Direct acquisition of particle tracking and physical quantities from the governing equations.
- ✓ Straightforward tracking of free and moving surfaces.

2.2 Derivation of the Navier-Stokes Equations

The governing equations for a Newtonian fluid are the Navier-Stokes equations. When applied in real engineering applications, some assumptions are made to simplify their formulation. Figure 2.1 illustrates the schematics of a control volume and the fluxes involved in the problem. From this scheme, two equations are derived: the mass balance equation, also known as the continuity equation, and the momentum balance equation, also known as the motion equation.

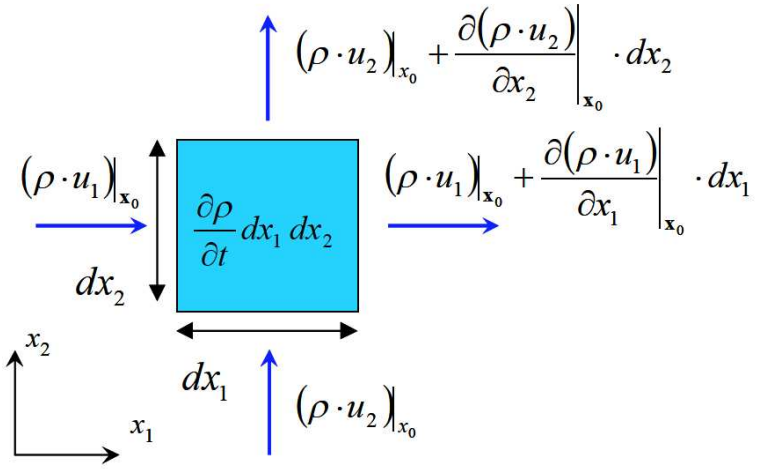

Figure 2.1: Two-dimensional infinitesimal control volume element and its mass fluxes.

Mass Balance Equation This equation is derived from the principle of mass conservation. It states that the time rate of mass change within an infinitesimal control volume must balance the net mass flux through its boundaries. Considering a control volume with constant boundaries as depicted in Fig. 2.1, the mass balance equation asserts that the difference between inward and outward fluxes of specific mass through the volume W must equal the time rate of density.

$$\begin{array}{l} \frac{\partial \rho}{\partial t} + \frac{\partial \rho u_j}{\partial x_j} = 0 \quad \text{or} \\ \frac{\partial \rho}{\partial t} + u_j \frac{\partial \rho}{\partial x_j} + \rho \frac{\partial u_j}{\partial x_j} = 0 \end{array} \tag{2.2}$$

Equation (2.2) is written according to the Eulerian approach. Applying relation (2.1) yields the Lagrangian formulation.

$$\frac{D\rho}{Dt} + \rho \frac{\partial u_j}{\partial x_j} = 0 \quad \text{or} \quad \frac{D\rho}{Dt} = -\rho \nabla \cdot \mathbf{u} \tag{2.3}$$

Momentum Balance Equation Newton's second law states that within an inertial frame of reference, the vector sum of forces $\mathbf{F}$ on a material point equals the mass m times its acceleration $\mathbf{a}$: $\mathbf{F} = m\mathbf{a}$. Applying this law to a material fluid particle of volume dW, the overall external force $\mathbf{F}$, such as surface forces and volume forces, acting on the particle must equal the material derivative of the linear momentum, defined as the product of mass $m = \rho dW$ times velocity $\mathbf{u}$.

$$\frac{D(\mathbf{u}\rho dW)}{Dt} = \mathbf{F} \tag{2.4}$$

The external force $\mathbf{F}$ include body forces, pressure forces, and viscous forces. The time rate of change of the linear momentum equals the resultant force acting on it. Using Gauss's theorem, the equation of motion, represented in Eulerian form, is derived:

$$\frac{\partial u_i}{\partial t} + u_j \frac{\partial u_i}{\partial x_j} = -\frac{1}{\rho} \frac{\partial (p + \rho g x_3)}{\partial x_i} + \frac{1}{\rho} \frac{\partial \tau_{ij}}{\partial x_j} \quad \text{for } i = 1, 2, 3 \tag{2.5}$$

The second term on the right-hand side of (2.5) is the viscous stress acting on on the surface of the particle. The balance on surface stresses is depicted in Fig. 2.2, considering a three-dimensional control volume.

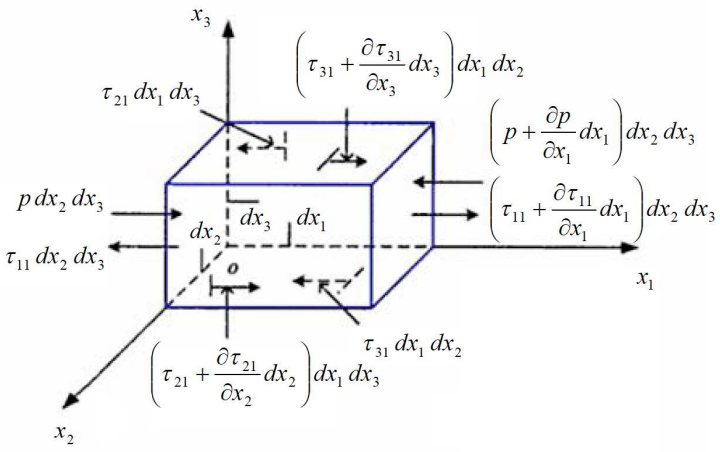

Figure 2.2: Stress components on the surface of a cubic infinitesimal element for translational equilibrium in x_1 direction.

In a Newtonian Fluid, the rheological behaviour linearly relates the viscous stress tensor τ_{ij} to the components of the strain rate tensor ε_{ij}, the proportional factor μ being the dynamic viscosity.

$$\tau_{ij} = \mu\left[\frac{\partial u_i}{\partial x_j} + \frac{\partial u_j}{\partial x_i} - \frac{2}{3}\frac{\partial u_k}{\partial x_k}\delta_{ij}\right] \tag{2.6}$$

The right-hand side shows the deviatoric part of the strain rate tensor. When (2.6) is substituted into (2.2), the momentum balance for Newtonian fluid is obtained.

$$\begin{aligned}&\tfrac{\partial u_i}{\partial t} + u_j\tfrac{\partial u_i}{\partial x_j} = -\tfrac{1}{\rho}\tfrac{\partial(p+\rho g x_3)}{\partial x_i} + \tfrac{\mu}{\rho}\left[\tfrac{\partial}{\partial x_j}\tfrac{\partial u_i}{\partial x_j} + \tfrac{1}{3}\tfrac{\partial}{\partial x_j}\tfrac{\partial u_j}{\partial x_i}\right] \quad \text{for } i=1,2,3\\ &\text{or}\\ &\tfrac{D\mathbf{u}}{Dt} = -\tfrac{1}{\rho}\nabla(p+\rho g x_3) + \tfrac{\mu}{\rho}\left[\nabla^2\mathbf{u} + \tfrac{1}{3}\nabla(\nabla\cdot\mathbf{u})\right]\end{aligned} \tag{2.7}$$

The ratio μ/ρ represents the kinematic viscosity, typically denoted by ν.

2.3 The Smoothed Particle Hydrodynamics Method

Smoothed Particle Hydrodynamics (SPH) is a mesh-free Lagrangian method used to describe field functions through integral representation and particle approximation. Initially developed for studying astrophysical problems [4, 5], SPH has since been extended to model various continuum problems, including free surface flows [6] and impact and penetration into solids [7].

2.3.1 Basics of SPH Method

Figure 2.3 illustrates the continuum discretised according to the SPH particle approximation, consisting of a set of particles arbitrarily distributed in space.

A field variable $\varrho(\mathbf{r})$, such as mass or velocity, is defined in the spatial domain Ω. The spatial position of each particle, represented by the position vector $\mathbf{r}$, influences the variable. Equation (2.8) defines the integral representation of a field function.

$$\varrho(\mathbf{r}) = \int_\Omega \delta(\mathbf{r}-\mathbf{r}')\varrho(\mathbf{r}')\,d\Omega_{\mathbf{r}'} \tag{2.8}$$

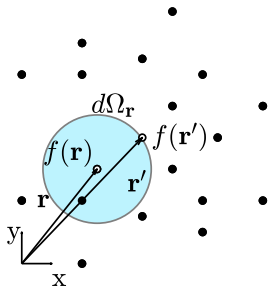

Figure 2.3: Discretization and distribution of a field variable within the domain.

In Figure 2.3, $d\Omega_{\mathbf{r}'}$ represents the elementary volume surrounding the computational particle identified by the position vector $\mathbf{r}'$, and $\delta(\mathbf{r}-\mathbf{r}')$ is the Dirac delta function.

$$\delta(\mathbf{r}'-\mathbf{r}) = \begin{cases} 0, & \text{if } \mathbf{r}' < \mathbf{r} - \frac{\varepsilon}{2} \\ \frac{1}{\varepsilon}, & \text{if } \mathbf{r} - \frac{\varepsilon}{2} < \mathbf{r}' < \mathbf{r} + \frac{\varepsilon}{2} \\ 0, & \text{if } \mathbf{r}' > \mathbf{r} + \frac{\varepsilon}{2} \end{cases} \tag{2.9}$$

The Dirac delta function lacks some mathematical features such as continuity and differentiability. To address this, various mathematical formulations known as kernel functions Φ have been proposed. Kernels depend on the relative distance between particles $r = |\mathbf{r}-\mathbf{r}'|$ and are defined over a compact support $\Psi(\kappa h)$. The compact support extension is proportional through the constant κ to the smoothing length. The choice of the smoothing function is crucial for the accuracy of the method and depends on the problem being investigated [8]. Here, we introduce two widespread kernel functions: the Gaussian kernel (2.10) and the cubic spline kernel (2.11).

$$\Phi(r,h) = \frac{1}{(\pi h^2)^{\frac{n}{2}}} \exp^{-\frac{r^2}{h^2}} \tag{2.10}$$

The Gaussian kernel (2.10) is continuous and differentiable to any orders. It approaches rapidly to zero, it is not compactly supported but for numerical computation purposes can be treated as it is. The radius of the support may increase significantly for high-order derivatives to assure the compact requirement.

$$\Phi(r,h) = \begin{cases} \frac{C_n}{h_n}\left(1 - \frac{3}{2}\tilde{r}^2 + \frac{3}{4}\tilde{r}^3\right), & 0 \le \tilde{r} \le 1 \\ \frac{C_n}{h_n}\left(\frac{1}{4}(2-\tilde{r})^3\right), & 1 \le \tilde{r} \le 2 \\ 0, & \text{otherwise} \end{cases} \tag{2.11}$$

Where $\tilde{r} = r/h$ is the non-dimensional radius and C_n is the normalisation factor assuming different values depending on the problem dimension n.

$$C_n = \begin{cases} \frac{2}{3} & n = 1 \\ \frac{10}{7\pi} & n = 2 \\ \frac{1}{\pi} & n = 3 \end{cases}$$

The cubic spline kernel (2.11) has a narrow support while resembling the Gaussian. The second derivative is linear, therefore less smooth and can lead to numerical issues while dealing with high particle disorder.

Once introduced the kernel function, equation (2.8) becomes (2.12) which is the integral or kernel approximation of a field variable.

$$\langle \varrho(\mathbf{r}) \rangle = \int_{\Omega} \Phi(r,h)\varrho(\mathbf{r}')\, d\Omega_{\mathbf{r}'} \tag{2.12}$$

Properties of Kernel All kernel functions used in fluid dynamics share common features.

The partition of unity principle dictates that within the compact support, the integral of the kernel function must be unity:

$$\int_{\Omega} \Phi(|\mathbf{r}-\mathbf{r}'|, h)\, d\Omega_{\mathbf{r}'} = 1 \tag{2.13}$$

This condition ensures normalization.

As the smoothing length tends to zero, the kernel function approaches the Dirac delta function:

$$\lim_{h\to 0} \Phi(\mathbf{r}-\mathbf{r}', h) = \delta(\mathbf{r}-\mathbf{r}') \tag{2.14}$$

The kernel function, as defined in equation (2.15), is zero when the distance between particles exceeds a certain threshold:

$$\Phi(\mathbf{r}-\mathbf{r}', h) = 0 \quad \text{if} \quad |\mathbf{r}-\mathbf{r}'| \geq \kappa\chi \tag{2.15}$$

The kernel function is a central function of $r = |\mathbf{r}-\mathbf{r}'|$, which ensures that the gradient between two particles is independent of the computational particle:

$$\nabla_{\mathbf{r}}\Phi(\mathbf{r}-\mathbf{r}', h) = \frac{\partial\Phi}{\partial r}\frac{(\mathbf{r}-\mathbf{r}')}{|\mathbf{r}-\mathbf{r}'|} = -\nabla_{\mathbf{r}'}\Phi(\mathbf{r}'-\mathbf{r}, h) \tag{2.16}$$

The subscript on the gradient symbol indicates the computational particle where the gradient is evaluated.

Kernel Approximation of a Function Derivative Equation (2.12) demonstrates how to compute the gradient of a field function by substituting the function with its gradient:

$$\langle \nabla_{\mathbf{r}} \cdot \varrho(\mathbf{r})\rangle = \int_{\Omega} [\nabla_{\mathbf{r}} \cdot \varrho(\mathbf{r}')]\Phi(r, h)\, d\Omega_{\mathbf{r}'} \tag{2.17}$$

Considering the identity (2.18):

$$[\nabla \cdot \varrho]\Phi = \nabla \cdot [\varrho\Phi] - \varrho \cdot [\nabla\Phi] \tag{2.18}$$

Substituting into (2.16) and applying the divergence theorem:

$$\begin{aligned}\langle \nabla \cdot \varrho(\mathbf{r})\rangle = &\int_{\partial\Omega} \varrho(\mathbf{r}')\Phi(r, h) \cdot \mathbf{n}\, dS \\ &- \int_{\Omega} \varrho(\mathbf{r}') \cdot [\nabla_{\mathbf{r}'}\Phi(r, h)]\, d\Omega_{\mathbf{r}'}\end{aligned} \tag{2.19}$$

The first integral on the right-hand side is evaluated on the boundary $\partial\Omega$. If the compact support of the kernel Φ lies entirely within the domain Ω (as depicted in Fig. 2.4), the integral must be zero according to (2.15). Hence, using (2.16):

$$\langle \nabla \cdot \varrho(\mathbf{r})\rangle = \int_{\Psi(\kappa h)} \varrho(\mathbf{r}') \cdot [\nabla\Phi(r, h)]\, d\Omega_{\mathbf{r}'} \tag{2.20}$$

Here, the differential operator acts on the smoothing function Φ rather than on the field variable ϱ.

Particle Approximation of a Function and its Derivative The *particle approximation* (2.21) allows us to obtain the integral kernel approximation in discrete form for a material point (i-th) within the discretised continuum.

$$\langle \varrho(\mathbf{r}_i)\rangle \cong \sum_{j=1}^{N} \varrho(\mathbf{r}_j)\frac{m_j}{\rho_j}\Phi(r_{ij}, h) \tag{2.21}$$

In (2.21), the index j refers to the j-th neighbouring particle, each of which is within the compact support of the kernel centered on particle i. The j-th particle has a volume of $\Delta W_j = m_j/\rho_j$ within the influence domain of particle i (Ω_I). The distance between particles is denoted by $r_{ij} = |\mathbf{r}_i - \mathbf{r}_j|$.

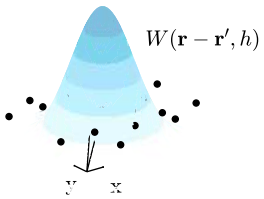

Figure 2.4: Representation of a kernel (smoothing) function.

The particle approximation states that a generic function ϱ for the i-th material point is estimated as the weighted sum of values assumed by ϱ at neighbouring particles j, within the compact support, the smoothing function being the weight. Particles closer to the i-th particle exert more influence on ϱ.

Similarly, the derivative is evaluated as:

$$\langle \nabla \cdot \varrho(\mathbf{r}_i) \rangle = \sum_{j=1}^{N} \frac{m_j}{\rho_j} \varrho(\mathbf{r}_j) \cdot \nabla \Phi(r_{ij}, h) \tag{2.22}$$

From equations (2.21) and (2.22), the distinct feature of SPH as a mesh-free method is evident. The particle approximation enables the estimation of ϱ without the need for a topological link or connection between material points.

The following properties of the particle approximation are useful developing the balance equations:

$$\begin{aligned} &\langle \varrho_1 + \varrho_2 \rangle = \langle \varrho_1 \rangle + \langle \varrho_2 \rangle \\ &\langle b\varrho_1 \rangle = b\langle \varrho_1 \rangle \\ &\langle \varrho_1 \varrho_2 \rangle = \langle \varrho_1 \rangle \langle \varrho_2 \rangle \end{aligned} \tag{2.23}$$

Here, b is a real constant. The first and second equations in (2.23) state that the kernel approximation $\langle\rangle$ is a linear operator.

Further identities can be derived:

$$\begin{aligned} &\rho \nabla \cdot \varrho = \nabla \cdot (\rho \varrho) - \varrho \cdot \nabla \rho \\ &\tfrac{\nabla \cdot \varrho}{\rho} = \tfrac{\varrho}{\rho^q} \cdot \nabla (\tfrac{1}{\rho^{1-q}}) + \tfrac{1}{\rho^{2-q}} \nabla \cdot (\tfrac{\varrho}{\rho^{q-1}}) \end{aligned} \tag{2.24}$$

These alternative mathematical formulations of the derivative of the generic ϱ function can be obtained by applying the particle approximation on each side of equation (2.24), and remembering the linear properties in equations (2.23). From equation (2.22), it follows:

$$\begin{aligned} &\rho_i \langle \nabla \cdot \varrho(\mathbf{r}_i) \rangle = \textstyle\sum_{j=1}^{N} m_j [\varrho(\mathbf{r}_j) - \varrho(\mathbf{r}_i)] \cdot \nabla \Phi(r_{ij}, h) \\ &\tfrac{1}{\rho_i} \langle \nabla \cdot \varrho(\mathbf{r}_i) \rangle = \textstyle\sum_{j=1}^{N} m_j [\tfrac{\varrho(\mathbf{r}_j)}{\rho_j^q} \tfrac{1}{\rho_i^{2-q}} - \tfrac{\varrho(\mathbf{r}_i)}{\rho_i^q} \tfrac{1}{\rho_j^{2-q}}] \cdot \nabla \Phi(r_{ij}, h) \end{aligned} \tag{2.25}$$

SPH Discretization of Governing Equations The SPH discrete form of the balance equations is obtained by applying the integral representation of a function. The mass balance equation (2.3) in Lagrangian form for mediated quantities is:

$$\left\langle \frac{D\rho}{Dt} \right\rangle_i = -\sum_{j=1}^{N} m_j (\mathbf{u}_j - \mathbf{u}_i) \cdot \nabla \Phi_{ij} \tag{2.26}$$

Here, $\Phi_{ij} = \Phi(r_{ij}, h)$ and the relative velocity between particles $(\mathbf{u}_j - \mathbf{u}_i) = \mathbf{u}_{ij}$. The SPH approximation is obtained for an inviscid fluid, i.e., $\mu = 0$, taking into account the second equation in (2.25) with $q = 2$:

$$\left\langle \frac{D\mathbf{u}}{Dt} \right\rangle_i = -\sum_{j=1}^{N} m_j \Big(\frac{p_i}{\rho_i^2} + \frac{p_j}{\rho_j^2} \Big) \nabla \Phi_{ij} + \mathbf{g} \tag{2.27}$$

By deriving (2.27) from (2.7), the kernel approximation of $\langle \rho g z \rangle_i$ is substituted by the gravity acceleration vector $\mathbf{g}$.

Weakly Compressible Fluid The weakly compressible fluid hypothesis is valid as long as the local variations from the reference value of density ρ_i remain small enough (on the order of one per cent) [8]. This hypothesis allows for the decoupling of the governing equations and the adoption of a larger time step in the numerical solution. The Courant-Friedrichs-Lewy condition for explicit integration must be satisfied: $\Delta t(c_s + u)/h \leq C_{CFL} \in [0 \div 1]$. For a single-phase physical system, the adopted state equation is:

$$\frac{p}{p_i} = K\left(\frac{\rho}{\rho_i}\right)^{\gamma} - 1 \tag{2.28}$$

The weakly compressible hypothesis implies that the Mach number must be small enough. According to [6], the following condition must be satisfied, where u is the characteristic velocity modulus of the problem and c_s is the artificial sound velocity of the fluid:

$$Ma = \frac{u}{c_s} \cong 0.1 \tag{2.29}$$

The characteristic flow velocity u is given by Torricelli's velocity $\sqrt{2gz}$ for some surface problems, where g is the modulus of the gravitational acceleration and z is a representative reference height.

2.3.2 Advanced Numerical Aspects

In this section, is provided a brief overview of some advanced numerical aspects. For detailed aspects one is referred to the related publications.

Artificial Viscosity Artificial viscosity is used to obtain numerical stability. It is an additive term to the momentum balance equation (2.27), enabling the simulation of shock wavefronts and impact problems. This approach is based on the Von Neumann-Richtmyer artificial viscosity, which converts kinetic energy into heat during sudden compression of the continuum. Monaghan (1989) proposes the following formulation, which also prevents particle penetration:

$$\Phi_{ij} = \begin{cases} \frac{-\alpha_M 0.5(c_{si}+c_{sj})\varkappa_{ij} + \beta_M \varkappa_{ij}^2}{0.5(\rho_i - \rho_j)} & \text{if} \quad \mathbf{u}_{ij} \cdot \mathbf{r}_{ij} < 0 \\ 0 & \text{if} \quad \mathbf{u}_{ij} \cdot \mathbf{r}_{ij} > 0 \end{cases} \tag{2.30}$$

Here, c_{si} and c_{sj} are the artificial sound velocities of the i-th and j-th particles; α_M and β_M are coefficients (typically $\beta_M = 0$); and $\varkappa_{ij}$ is defined as:

$$\varkappa_{ij} = \frac{h\mathbf{u}_{ij} \cdot \mathbf{r}_{ij}}{x_{ij}^2 + (0.1h)^2} \tag{2.31}$$

It's important to note that in (2.31), the dependency on the viscous stress is introduced due to the term $\mathbf{x}_{ij}$, which corresponds to to the inter particle spacing length scale [8].

Tensile Instability Large volume deformations in SPH are straightforward, but some numerical issues can affect the results. As particles are going to be subjected to traction stress, tensile instability causes the exponential growth of particle velocities for small perturbations. This problem has been carefully investigated, and references such as Dyka & Ingel (1995), Morris (1996), Monaghan (2000), and Colagrossi (2004) offer detailed discussions [8].

Correction of Kernel In free-surface flows, particles near the free-moving boundary are characterised by kernel truncation due to the lack of neighbouring particles (see Fig. 2.5). As the validity of Eq. (2.13) decreases, a correction to the smoothing function is required:

$$\tilde{\Phi}_{ij} = \Phi_{ij} A_{ij} \left(1 + B_{ij} |\mathbf{r}_i - \mathbf{r}_j|\right) \tag{2.32}$$

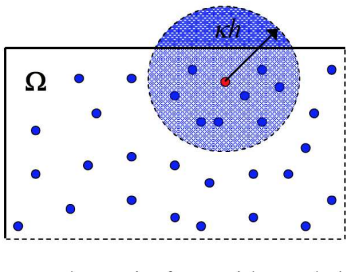

Figure 2.5: Particle near the boundary and kernel truncation.

Here, the constants A_{ij} and B_{ij} can be evaluated by imposing a correctly interpolated velocity:

$$\mathbf{u}_i = \sum_{j=1}^{N} \mathbf{u}_j \tilde{\Phi}_{ij} \Delta W_j \tag{2.33}$$

By considering a Taylor series expansion (first-order truncation) around the i-th point of the velocity field:

$$\mathbf{u}_j = \mathbf{u}_i + \frac{d\mathbf{u}_i}{dx_{ij}} x_{ij} + \cdots \tag{2.34}$$

A second-order approximation is valid with the substitution of (2.34) into (2.33). The velocity field is evaluated only in relation to the i-th material point:

$$\mathbf{u}_i = \mathbf{u}_i \sum_{j=1}^{N} \tilde{\Phi}_{ij} \Delta W_j + \frac{d\mathbf{u}_i}{dx_{ij}} \sum_{j=1}^{N} x_{ij} \tilde{\Phi}_{ij} \Delta W_j \tag{2.35}$$

This identity implies:

$$\begin{array}{l} \sum_{j=1}^{N} \tilde{\Phi}_{ij} \Delta W_j = 1 \\ \sum_{j=1}^{N} x_{ij} \tilde{\Phi}_{ij} \Delta W_j = 0 \end{array} \tag{2.36}$$

Shepard (1968) proposes an interpolation technique where the corrected form is assumed to be constant. From equations (2.36) and (2.32), one may derive:

$$\begin{array}{l} A_{ij}^{-1} = \sum_{j=1}^{N} \Phi_{ij} \Delta W_j \\ \tilde{\Phi}_{ij} = \frac{\Phi_{ij}}{\sum_{j=1}^{N} \Phi_{ij} \Delta W_j} \end{array} \tag{2.37}$$

Other types of smoothing function correction, such as using the kernel's gradient, have been proposed, e.g., Bonet & Lok (1999) [9]. During computation with increased particle disorder, the smoothing approximation could be inaccurate. Falappi (2006) [10] investigated the influence of particle disorder on the interpolation of a quadratic field function. The error between the analytic solution and the interpolated one (both functions and derivatives) is higher near the boundary of the computational domain. This problem can be mitigated with the adoption of Eq. (2.37) [8].

Neighbouring Particle Search Identifying which particles surround the computational particle is crucial for accurately estimating field functions. Neighbouring particles of a computational particle are those that fall within the interaction domain defined by the smoothing length ($\kappa\chi$). Since particles lack a topological connection, the set of neighbouring particles changes over time. Therefore, the computational particle requires continuous searching to identify its neighbours. The cell-linked list algorithm, proposed by Liu & Liu (2007), is widely adopted to maintain a constant smoothing length.

Figure 2.6 illustrates a mesh over the computational domain. All particles are assigned to their respective cells through a linked list. The search for neighbouring particles of the i-th particle is restricted to the mesh cells near the one in which the i-th particle is located. In a squared mesh with a side length equal to the kernel radius, only nine cells (in 2D) are investigated for neighbouring search [8].

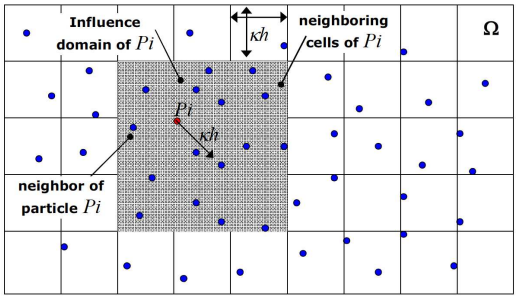

Figure 2.6: Linked List Algorithm.

Boundary Conditions In astrophysics, no boundary conditions exist, but in fluid mechanics, boundary conditions are essential, especially regarding the interaction of the fluid with solids, which is the focus of many fluid mechanics studies. Several approaches are employed:

- **Boundary Forces**: This technique, stemming from studies on intermolecular repulsive forces, was proposed by Lennard-Jones, further developed by Monaghan & Koss (2000).
- **Ghost Particles**: Introduced by Libersky et al. (1993), this method involves simulating the boundary by creating particles that mirror those in the domain within a thin layer extending beyond the boundary. Pressure and velocity are properly assigned.
- **Semi-Analytic Integral**: Boundary contribution to each term of the balance equations is computed by solving an integral which is extended to the portion of the interaction domain of a computational particle beyond the boundary, as proposed by Di Monaco et al. (2007). Pressure and velocity are assigned, and the boundary is assumed to be continuous.

2.4 Basics of the Particle Finite Element Method

The Particle Finite Element Method (PFEM), briefly PFEM, is the second Lagrangian particle method utilised during my PhD. Since its inception in the early works [11, 12], PFEM has been employed to study complex fluid dynamics problems, particularly those involving continuous interface changes and fluid-structure interaction with free surfaces, where intricate contact problems arise.

The fundamental concept of PFEM is to amalgamate the advantages of particle methods and finite element methods. A computational mesh is generated over an array of particles, facilitating the finite element solution of the Lagrangian governing equations. To accommodate large deformations of the domain, this method relies on a fast and efficient remeshing technique [13].

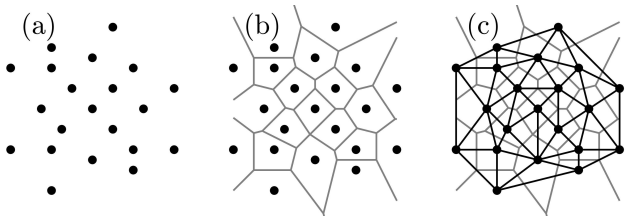

Figure 2.7: Delaunay triangulation process. a) array of nodes, b) Voronoi diagram, c) Delaunay triangulation [13].

In PFEM, particle positions (and consequently the mesh) are continuously updated in a Lagrangian fashion according to the solution of the governing equations. To ensure good discretisation quality for problems involving large deformations, the mesh is continuously rebuilt. This is achieved by erasing all elements of the previous (distorted) mesh while retaining the nodes. The new mesh is then constructed over this distribution of nodes using the Delaunay triangulation, as illustrated in Figure 2.7 [14]. The Alpha-Shape method (Figure 2.8) is employed to remove mesh elements that exceed a critical radius. The main steps of the PFEM remeshing procedure are summarized below:

1. At each remeshing step:
2. Erase the elements of the previous mesh while retaining the nodes.
3. Create a Delaunay triangulation.
4. Perform an Alpha-Shape check to reconstruct the boundaries.

The Delaunay triangulation ensures good element quality for a given cloud of nodes, while the Alpha-Shape method enables the recovery of the physical contours of the computational domain with high accuracy. The outcome is a high-quality mesh ready for use in the finite element method (FEM) solution of subsequent computational steps. Further details about the PFEM remeshing procedure and its implications on the PFEM solution can be found in [15].

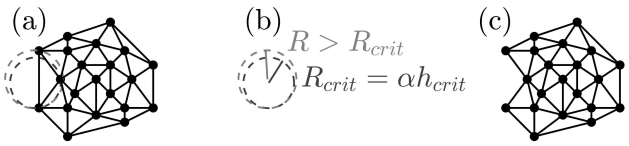

Figure 2.8: Alpha-shape method [13].

Figure 2.9 depicts the PFEM remeshing steps, including the array of nodes, Delaunay triangulation, and Alpha-Shape method. The image showcases the impact of a water jet on a wall, demonstrating rapid and significant domain deformation.

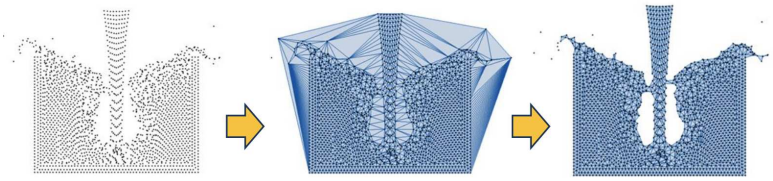

Figure 2.9: PFEM remeshing. Left: array of nodes, middle: Delaunay triangulation, right: Alpha-shape method [13].

While this remeshing technique offers several advantages, such as the ability to model flows with high domain deformation while maintaining good mesh quality, it also presents some disadvantages. These include the potential for inducing artificial changes in topology and the significant concern of mass conservation loss. Additionally, it incurs additional computational costs and results in the loss of elemental information stored at Gauss points because FEM structures must be constantly rebuilt [13].

2.4.1 Finite Element Method Discretisation

The PFEM formulation used is the velocity-pressure solver for Newtonian fluids as presented in [16]. Linear interpolation is employed for both velocity and pressure unknowns. Finite Calculus (FIC) stabilisation [16] is utilised to mitigate spurious oscillations resulting from the non-fulfillment of the inf-sup condition [17]. The governing equations of a Newtonian fluid are discretised according to the standard Galerkin Finite Element Method (FEM). Considering a computational domain divided into N_e finite elements with n nodes, linear triangles ($n = 3$) are considered for 2D problems. Linear shape functions N_i^e of the element e are defined for both velocity and pressure at each node i [18, 19, 20]. Following the variational equation approach in [16], the mass balance and momentum balance equations for a Newtonian fluid can be expressed in matrix form as:

$$\boldsymbol{M}_i\dot{\bar{\boldsymbol{u}}} + \boldsymbol{K}\bar{\boldsymbol{u}} + \boldsymbol{Q}\bar{\boldsymbol{p}} = \boldsymbol{f} \tag{2.38}$$

$$\boldsymbol{M}_1\dot{\bar{\boldsymbol{p}}} + \boldsymbol{M}_2\ddot{\bar{\boldsymbol{p}}} + \boldsymbol{Q}^T\bar{\boldsymbol{u}} + (\boldsymbol{L} + \boldsymbol{M}_j)\bar{\boldsymbol{p}} = \boldsymbol{f}_p \tag{2.39}$$

Here, $\boldsymbol{M}_i$ is the mass matrix, $\boldsymbol{K}$ is the viscous matrix, $\mathbf{Q}$ is the gradient matrix, $\boldsymbol{f}$ represents external forces, $\boldsymbol{M}_1$ is the bulk matrix, and $\boldsymbol{S}_\tau$ encompasses all terms arising from the FIC stabilisation procedure. The vectors $\bar{\boldsymbol{u}}$

and $\bar{\boldsymbol{p}}$ contain nodal velocities and pressures, respectively. The notation $\dot{\bar{\boldsymbol{a}}}$ denotes the first material derivative of vector $\bar{\boldsymbol{a}}$. The tensors of Eqs. (2.38) and (2.39) are defined as follows:

$$\boldsymbol{M}^e_{0ij} = \int_{\Omega^e} \rho N^e_i N_j \boldsymbol{I} d\Omega$$

$$\boldsymbol{K}^e_{ij} = \int_{\Omega^e} \boldsymbol{B}^{eT}_i \boldsymbol{D} \boldsymbol{B}^{eT}_j d\Omega$$

$$\boldsymbol{Q}^e_{ij} = \int_{\Omega^e} \boldsymbol{B}^{eT}_i \boldsymbol{m} N^e_j d\Omega$$

$$M^e_{1ij} = \int_{\Omega^e} \tfrac{1}{k} N^e_i N^e_j d\Omega$$

$$M^e_{2ij} = \int_{\Omega^e} \tfrac{\tau}{c^2} N^e_i N^e_j d\Omega$$

$$M^e_{bij} = \int_{\Omega^e} \tfrac{2\tau}{h_n} N^e_i N^e_j d\Gamma$$

$$L^e_{ij} = \int_{\Omega^e} \tau (\nabla^T N^e_i) \nabla N^e_j d\Omega$$

$$f^e_i = \int_{\Omega^e} N^e_i \boldsymbol{b} d\Omega + \int_{\Gamma_t} N^e_i \mathbf{t} d\Omega$$

$$f^e_{pi} = \int_{\Gamma^t} \tau N^e_i [\rho \dot{u}_n - \tfrac{2}{h_n}(2\mu\epsilon_n - t_n)] d\Gamma - \int_{\Omega^e} \tau \nabla^T N^e_i \boldsymbol{b} d\Omega$$

The integrals are defined over the element domain Ω^e or at the boundary Γ^t. The sub-index n refers to the normal component, and the mesh size is denoted as h. The stabilisation parameter τ arising from the FIC procedure is defined as:

$$\tau = \left(\frac{8\mu}{h^2} + \frac{2\rho}{\delta} \right)^{-1} \tag{2.40}$$

where h and δ represent characteristic space and time lengths, respectively. The tensors introduced in the mass balance and momentum balance equations are listed below:

- $\boldsymbol{D} = \mu \begin{pmatrix} 4/3 & -2/3 & 0 \\ -2/3 & 4/3 & 0 \\ 0 & 0 & 2 \end{pmatrix}$
- $\boldsymbol{B}^e_i = \begin{pmatrix} \frac{\partial N_i}{\partial x} & 0 \\ 0 & \frac{\partial N_i}{\partial y} \\ \frac{\partial N_i}{\partial y} & \frac{\partial N_i}{\partial x} \end{pmatrix}$
- $\boldsymbol{N}^e_i = N^e_i \boldsymbol{I}$
- $\nabla = \left(\frac{\partial}{\partial x}, \frac{\partial}{\partial y} \right)^T$
- $m = [1, 1, 0]^T$

For the full mathematical development of the discretised equations, the reader is referred to [16].

2.4.2 PFEM Solution Scheme

At each time step $[{}^n t; {}^{n+1} t]$ of duration Δt, the linear momentum and mass balance equations are iteratively solved for the nodal velocities and pressures. The main steps of this implicit PFEM scheme are summarised below:

1. At each nonlinear iteration i:
2. Compute the nodal velocities $\bar{\boldsymbol{u}}^{i+1}$
3. Update the nodal coordinates: ${}^{n+1}\bar{\boldsymbol{x}}^{i+1}$
4. Compute the nodal pressures $\bar{\boldsymbol{p}}^{i+1}$
5. Check for convergence: $\frac{\|\bar{\boldsymbol{u}}^{i+1} - \bar{\boldsymbol{u}}^i\|}{\|{}^n\bar{\boldsymbol{u}}\|} \leq e_u$, $\frac{\|\bar{\boldsymbol{p}}^{i+1} - \bar{\boldsymbol{p}}^i\|}{\|{}^n\bar{\boldsymbol{p}}\|} \leq e_p$, where e_u and e_p represent prescribed error norms for velocities and pressures.
6. If condition 4 is not fulfilled, return to step 1 with $i \leftarrow i + 1$.

2.5 SWAN Model

The SWAN model, introduced by Booij et al. [21], allows computing the propagation ov waves near shore by solving the wave action balance equation with sources and sinks. The spectral action balance equation in Cartesian coordinates, as defined by Hasselmann et al. [22], is expressed as:

$$\frac{\partial}{\partial t}(N) + \frac{\partial}{\partial x}(c_x N) + \frac{\partial}{\partial y}(c_y N) + \frac{\partial}{\partial \theta}(c_\theta N) + \frac{\partial}{\partial \sigma}(c_\sigma N) = \frac{S_{\text{in/out}}}{\sigma} \tag{2.41}$$

When hydrodynamic currents are taken into account, the energy spectrum S may vary while the wave action density spectrum N remains constant [23]. Here, N represents the ratio of energy S to the relative frequency σ, which is the frequency evaluated in a frame of reference moving with the current. The terms contributing to the local time rate of change of N include propagation in geographical space, refraction, and frequency shifting induced by bottom variations and current. The right-hand side of Equation 2.41 encompasses the source/sink term incorporating effects of generation, dissipation, and wave-wave nonlinear interactions.

2.5.1 Coordinates

SWAN operates in either a Cartesian coordinate system or a spherical coordinate system, corresponding to a flat plane or a spherical portion of the Earth. In the input and output of SWAN, the direction of wind and waves can be defined according to either:

- Cartesian convention: the direction to which the vector points, measured counterclockwise from the positive x-axis (in degrees), or
- Nautical convention: the direction from which the wind or waves come, measured clockwise from geographic North.

Figure 2.10: Coordinate system.

2.5.2 Grids

Spatial grids in SWAN can be structured or unstructured. Structured grids may be rectilinear (uniform or rectangular) or curvilinear, always consisting of quadrilaterals with four grid cells meeting at each internal grid point. Unstructured grids, on the other hand, may have an arbitrary number of cells meeting at each internal point, usually between 4 and 10. In SWAN, only triangular meshes can be used for unstructured grids.

Spatial grids defined by the user include:

- A computational spatial grid for SWAN computations.
- Spatial input grid(s) for bottom, current field, water level, bottom friction, and wind, if spatially variable.
- Spatial output grid(s) for desired SWAN output.

For inputs like wind and bottom friction, uniform values are used if they are constant over the area of interest.

Spatial Grids

The spatial resolution for input grids should be chosen to appropriately resolve spatial details relevant for analysis, such as bathymetry, currents, bottom friction, and wind. Often, characteristic spatial scales of wind waves propagating from deep to shallow waters vary significantly, necessitating local mesh refinement near the coast. This can be achieved traditionally through nesting, computing waves first on a coarse grid for a larger region and then on a finer grid for a smaller region.

Computational Spectral Grid

The computational spectral grid is defined by the user, specifying a minimum and maximum frequency and a logarithmic frequency resolution (e.g., $\Delta f = 0.1f$). The lowest frequency value must be somewhat smaller than 0.7 times the lowest peak frequency expected, while the highest frequency value should be at least 2.5 to 3 times the highest peak frequency expected. In directional space, the default range is $360°$, but a limited directional range can be specified for computational efficiency.

2.5.3 Boundary Condition

In SWAN, land absorbs all incoming wave energy, while water boundaries where no wave conditions are imposed are assumed to allow waves to freely enter or leave the area. These boundaries should be sufficiently far from the area of interest to minimize computational errors.

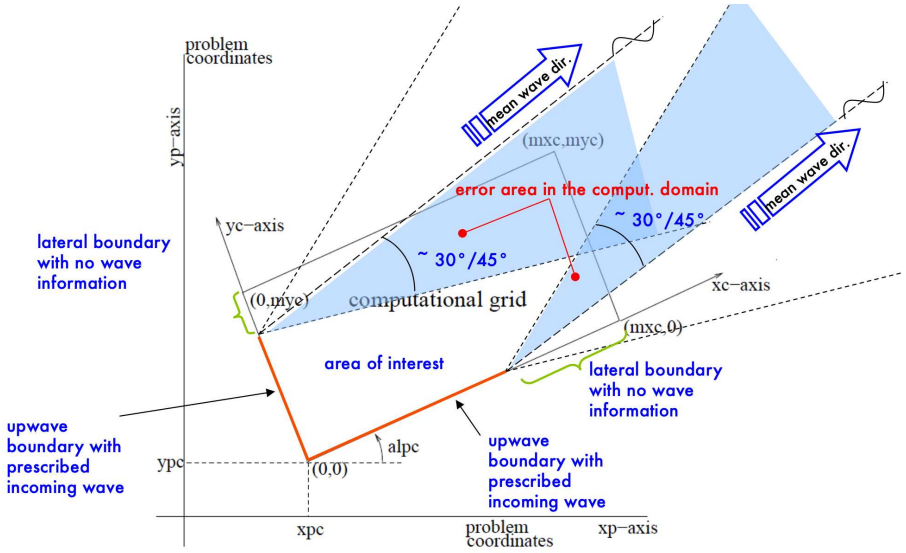

Figure 2.11: SWAN boundary condition [3].

2.5.4 Physical Processes

SWAN incorporates various physical processes that influence wave energy, including generation, dissipation, and energy shift. These processes include:

- Wind input (I, II, and III generation modes)
- Whitecapping (steepness-induced wave-breaking)
- Depth-induced wave breaking in shallow water
- Bottom friction
- Dissipation due to vegetation, mud, or turbulence

- Obstacle transmission
- Nonlinear wave-wave interactions (quadruplets and triads)
- Wave-induced set-up

To assess the relevance of a specific physical process, SWAN computations can be performed both with and without the process, using standard values chosen within SWAN.

3

Introduction to free surface waves

3.1 Basics of Linear Free Surface Wave Problems

Airy wave theory, also known as linear wave theory, mathematically describes small free surface waves. A wave is represented by a harmonic function (3.1) [24].

$$\eta(x,t) = a\cos(kx - \omega t) \tag{3.1}$$

Here, a is the wave amplitude, $k = \frac{2\pi}{L}$ is the wavenumber related to the inverse of the wave length to the wavelength L, ω is the angular frequency, $c = \frac{\omega}{k} = \frac{L}{T}$ is the phase velocity, and $H = 2a$ is the wave height.

3.1.1 Boundary Value Problem

Analytical solution of small free surface waves can be obtained by solving the boundary value problem. This means determining the solution to the set of partial differential equations that satisfies the conditions at the bounbdary of the computational domain. To complete the system of equations, particular conditions must be imposed at the boundaries.

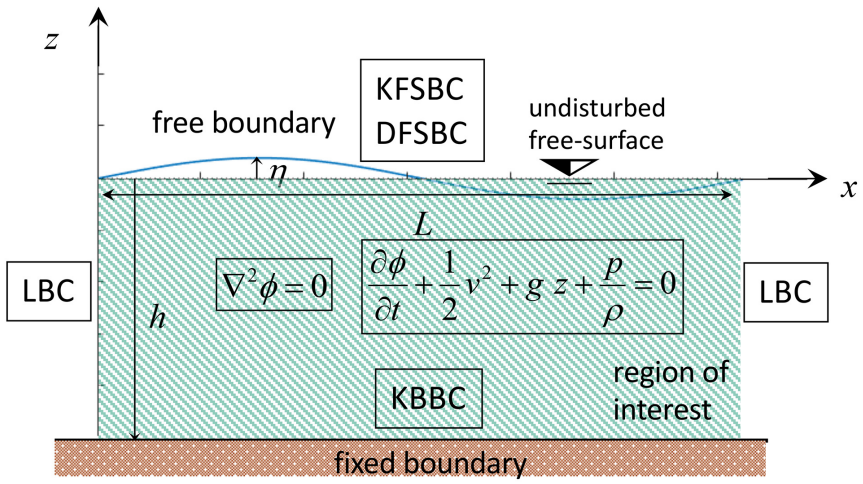

Figure 3.1: Boundary value problem scheme [3].

The assumptions of the problem include an incompressible and inviscid fluid (negligible viscous effects), barotropic flow, state equation is independent from temperature, conservative body forces, and irrotational flow at theinitial time. These assumptions, combined with Kelvin's theorem, imply that the velocity field remains irrotational. Hence, the velocity field can be described by its potential $\phi(x,z,t)$.

$$\mathbf{u} = \nabla\phi(x, z, t) \tag{3.2}$$

where ϕ must satisfy the Laplace equation:

$$\nabla^2\phi = 0 \tag{3.3}$$

The assumption of conservative body forces allows expressing the body force field as the gradient of the gravitational scalar potential $\varphi(x, z, t) = -gz$. Thus, the generalized formulation of Bernoulli equation for unsteady flow is:

$$\frac{\partial\phi}{\partial t} + \frac{1}{2}\left[\left(\frac{\partial\phi}{\partial x}\right)^2 + \left(\frac{\partial\phi}{\partial y}\right)^2 + \left(\frac{\partial\phi}{\partial z}\right)^2\right] + gz + \frac{p}{\rho} = 0 \tag{3.4}$$

To find the solution, the conditions on the boundaries are required. Assuming the bottom is impermeable, the normal component of the velocity must be zero, resulting in the first kinematic condition (KBBC).

$$\frac{\partial\phi}{\partial x}\frac{\partial h}{\partial x} + \frac{\partial\phi}{\partial y}\frac{\partial h}{\partial y} + \frac{\partial\phi}{\partial z} = 0 \qquad \text{at} \qquad z = -h \tag{3.5}$$

The kinematic free-surface boundary condition (KFSBC).

$$\frac{\partial\phi}{\partial x}\frac{\partial\eta}{\partial x} + \frac{\partial\phi}{\partial y}\frac{\partial\eta}{\partial y} + \frac{\partial\eta}{\partial t} = \frac{\partial\phi}{\partial z} \qquad \text{at} \qquad z = \eta(x, t) \tag{3.6}$$

The surface elevation $\eta(x, t)$ is unknown a priori, and Bernoulli's equation for unsteady potential flow is introduced as dynamic free surface boundary condition (DFSBC). The pressure above the free surface is considered constant and equal to zero.

$$\frac{\partial\phi}{\partial t} + \frac{1}{2}\left[\left(\frac{\partial\phi}{\partial x}\right)^2 + \left(\frac{\partial\phi}{\partial y}\right)^2 + \left(\frac{\partial\phi}{\partial z}\right)^2\right] + gz = 0 \qquad \text{at} \qquad z = \eta(x, t) \tag{3.7}$$

Additional conditions on the lateral boundaries may vary to suit the peculiarities of the problem. For the considered problem, where a free surface cylindrical wave propagates along the x-direction, no motion occurs in the y-direction. The velocity field potential depends only on time and the coordinates x and z. The free surface profile is a function only of time and the coordinate x. For waves that are periodic in time and space, the conditions are expressed as periodic conditions (LBCs).

$$\begin{aligned} \phi(x, z, t) &= \phi(x + L, z, t) \\ \phi(x, z, t) &= \phi(x, z, t + T) \end{aligned} \tag{3.8}$$

3.1.2 Solution of the Linearized Boundary Value Problem (LBVP)

The problem is linearised from a BVP representing cylindrical periodic water waves of small amplitude. If H is the wave height, linear waves are characterised by:

$$\frac{H}{L} \ll 1, \quad \frac{H}{h} \ll 1, \quad u, w, \eta \ll 1 \tag{3.9}$$

This assumption allows eliminating non-linear terms in the system of partial differential equations defined above, and the solution can be found at the undisturbed free surface. The general solution of the Laplace equation is:

$$\phi = \frac{gH}{2\omega}\frac{\cosh(k(h + z))}{\cosh(kh)}\sin(kx - \omega t) \tag{3.10}$$

The solution for the free surface elevation is:

$$\eta = \frac{H}{2}\cos(kx - \omega t) \tag{3.11}$$

Equation (3.11) represents the free surface progressive wave propagating in the x-direction with the celerity given by

$$c = \frac{\omega}{k} = \frac{L}{T} \tag{3.12}$$

3.1.3 Dispersion Equation

Solutions of ϕ and η for the the LBVP are substituted into the linear kinematic free surface boundary condition (LKFSBC):

$$\frac{\partial \eta}{\partial t} - \frac{\partial \phi}{\partial z} = 0 \qquad \text{at} \qquad z = 0 \tag{3.13}$$

This substitution yields the dispersion equation:

$$\omega^2 = gk \tanh(kh) \tag{3.14}$$

Equation 3.14 relates the wave characteristics k and omega for a given water depth h. By substituting the celerity (3.12) into the dispersion equation (3.14), we obtain:

$$c^2 = \frac{g}{k} \tanh(kh) \tag{3.15}$$

Differentiating by k (3.15) and applying the definition of wave celerity allows us to differentiate by k (3.14):

$$\begin{aligned} \frac{dc}{dk} &= -\frac{1}{2}\frac{c}{k}(1-G) \\ \frac{d\omega}{dk} \equiv \frac{d(ck)}{dk} &= c + \frac{dc}{dk}k \end{aligned} \tag{3.16}$$

Combining the two equations in (3.16), we obtain (3.17). From the definition of wave celerity, c can be derived by ω, resulting in (3.18).

$$\frac{d\omega}{dk} = c\left(\frac{1+G}{2}\right) \tag{3.17}$$

$$\frac{dc}{d\omega} \equiv \frac{d(\omega/k)}{\omega} = \frac{1}{k} - \frac{\omega}{k^2}\frac{dk}{d\omega} = -\frac{c}{\omega}\frac{1-G}{1+G} \tag{3.18}$$

In the previous equations, the quantity G has been introduced:

$$G = \frac{2kh}{\sinh(2kh)} \tag{3.19}$$

If $x = kh$, G assumes values between zero and one, respectively $G = 1$ as $x \to 0$ and $G = 0$ as $x \to \infty$. Therefore:

$$\frac{dc}{d\omega} \leq 0 \tag{3.20}$$

In Fig. 3.2, $x = kh$; from (3.20), it follows that for $0 < x < \frac{\pi}{10}$, or equivalently $\frac{h}{L} < \frac{1}{20}$, wave celerity is independent of the wave frequency. In this case, the waves are considered in shallow water, and $c = \sqrt{gh}$. When $x > \pi$, or equivalently $\frac{h}{L} > \frac{1}{2}$, this is the case of deep water, where $\tanh(x)$ can be approximated with 1, giving the expression of celerity $c_i = \frac{g}{2\pi}T$. When $\frac{\pi}{10} < x < \pi$, or equivalently $\frac{1}{20} < \frac{h}{L} < \frac{1}{2}$, waves are found to be in intermediate water, and thus the dispersion equation must be solved in the general form.

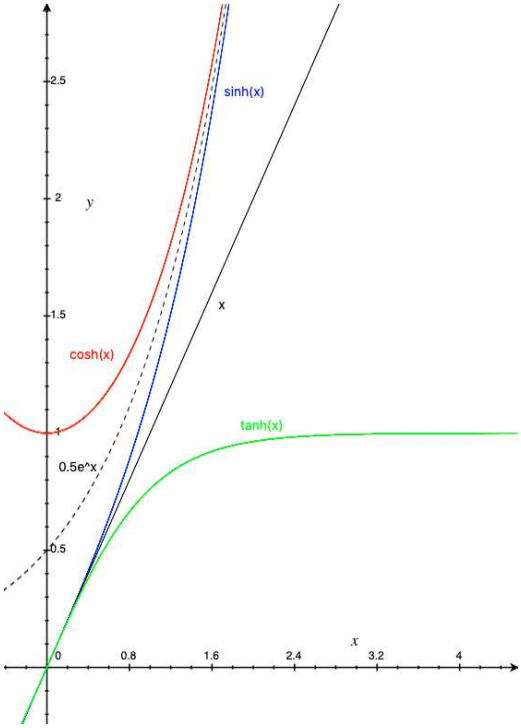

Figure 3.2: Hyperbolic Functions [3].

3.1.4 Dynamic Pressure

The pressure beneath the free surface of linear waves deviates from hydrostatic distribution and can be analysed using the linearised Bernoulli equation:

$$\frac{\partial \phi}{\partial t} + gz + \frac{p}{\rho} = 0 \tag{3.21}$$

The excess pressure, therefore, is:

$$\delta p \equiv \rho g z + p = -\rho \frac{\partial \phi}{\partial t} \tag{3.22}$$

By substituting the definition of velocity potential (3.10) into (3.22), the dynamic pressure becomes:

$$\delta p = \rho g z \eta_{(x,t)} K_{p(z)} \tag{3.23}$$

This dynamic pressure is dependent on the free surface elevation η and the pressure response factor $K_{p(z)}$. For a given water depth h:

$$K_{p(z)} = \frac{\cosh[k(h+z)]}{\cosh(kh)} \leq 1 \tag{3.24}$$

Observing the behaviour of $\cosh(x)$ in Fig. 3.2: $K_{p(z)} = 1$ if $z = 0$ and $K_{p(z)} = \frac{1}{\cosh(kh)}$ if $z = -h$. The pressure field is composed of hydrostatic pressure $\rho g h$ and dynamic pressure δp, so it can be expressed as:

$$p = \rho g(\eta_{(x,t)} K_{p(z)} - z) \tag{3.25}$$

3.1.5 Velocity Profiles

The velocity components on the vertical profile are obtained by the partial derivatives of the velocity potential:

$$u(x,z,t) = \frac{\partial \phi}{\partial x} = \frac{ag}{\omega} k \frac{\cosh(k(h+z))}{\cosh(kh)} \cos(kx_p - \omega t) \tag{3.26}$$

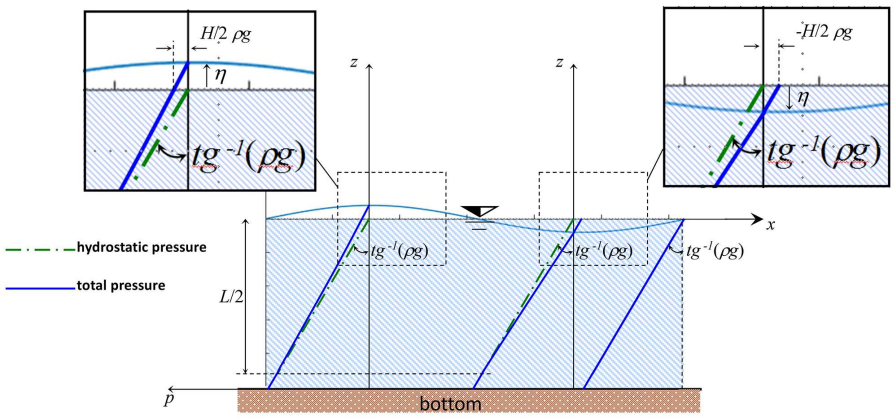

Figure 3.3: Pressure field [3].

$$w(x,z,t) = \frac{\partial \phi}{\partial z} = \frac{ag}{\omega} k \frac{\sinh(k(h+z))}{\cosh(kh)} \sin(kx_p - \omega t) \tag{3.27}$$

Each particle follows a closed trajectory around a mean position (x_i, y_i). Integrating the velocity components over time at the mean particle position, the following particle trajectories are distinguished in Fig. 3.4.

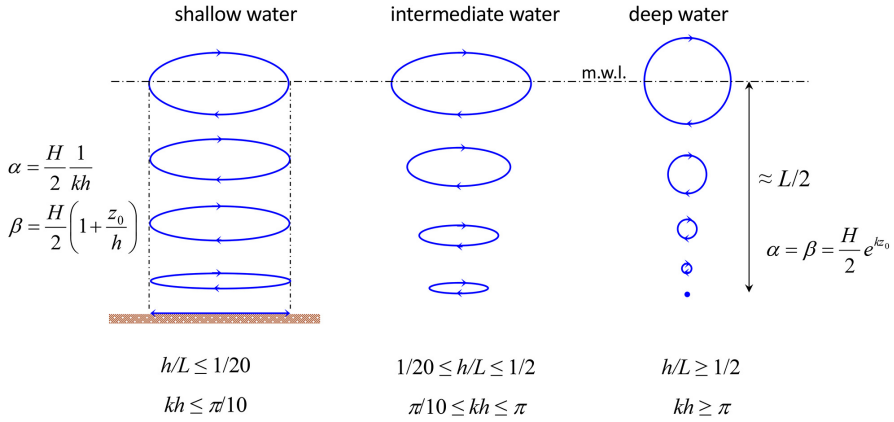

Figure 3.4: Particle paths under waves in different water depths [3].

Starting from one crest, the subsequent node (Node 1) is found at a distance of $\frac{T}{4}$, the following point is the trough, found at a distance of $\frac{T}{2}$, and the last point of interest is the subsequent node (Node 2), found at a distance of $\frac{3T}{4}$. The velocity profiles under the free water surface at these four situations are characterised by:

- Crest: Maximum positive velocity distribution along x and zero along z.
- Node 1: Maximum negative velocity distribution along z and zero along x.
- Trough: Maximum negative velocity distribution along x and zero along z.
- Node 2: Maximum positive velocity distribution along z and zero along x.

3.1.6 Wave Energy

Wave Specific Energy The total energy is the sum of kinetic E_k and potential energy E_p. The specific energy is the average of the two components over the wavelength L and the period T.

$$E = E_p + E_k$$
$$E = \frac{1}{LT}\left(\int_x^{x+L}\int_t^{t+T}\frac{\rho g}{2}(h+\eta)^2\,dx\,dt + \int_{-h}^{0}\int_x^{x+L}\int_t^{t+T}\frac{\rho}{2}(u^2+w^2)\,dx\,dz\,dt\right) \tag{3.28}$$
$$E = \frac{1}{8}\rho g H^2$$

Wave Energy Flux The flux is associated with the rate of energy transfer through a fixed vertical surface, extending from the bottom to the free surface and with a unitary width in the transversal direction.

$$E_f = \frac{1}{T}\int_{-h}^{0}\int_t^{t+T}\left[p + \frac{\rho}{2}(u^2+w^2)\right]u\,dt\,dz \tag{3.29}$$

Equation (3.29) represents the energy flux, which after some mathematical developments is found to be the product of wave energy E (3.28) and the group celerity c_g (the rate at which wave energy propagates).

$$E_f = Ec_g \tag{3.30}$$

The group celerity is related to phase celerity

$$c_g = \frac{c}{2}(1+G) = \begin{cases} c & if \quad kh \to 0 \\ \frac{c}{2} & if \quad kh \to \infty \end{cases} \tag{3.31}$$

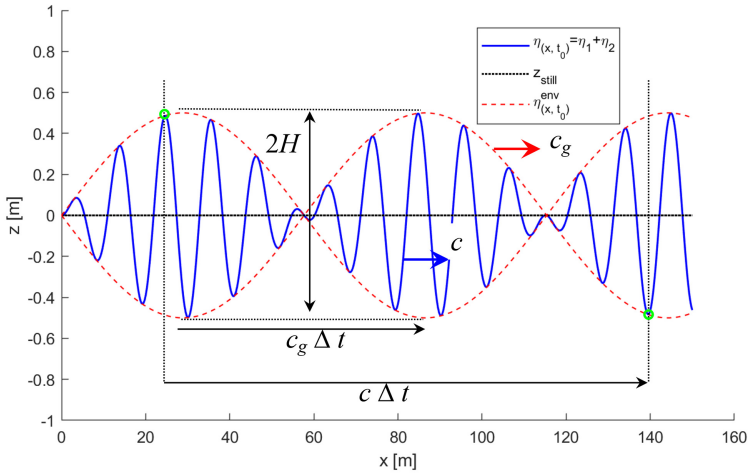

Figure 3.5: Wave groups [3].

3.2 Biésel Transfer Functions

In 1951, F. Biésel presented analytical solutions for the generation of regular waves in a flume [25]. The transfer function, given a specific wavemaker, links the displacement of the wavemaker to the wave amplitude law.

In Fig. 3.6, the following elements can be identified:

- $e(z,t)$: Displacement of the wave paddle along x
- $S(z)$: Stroke of the wave paddle
- $\eta(x,t)$: Surface elevation
- H: Wave height far from the wave maker

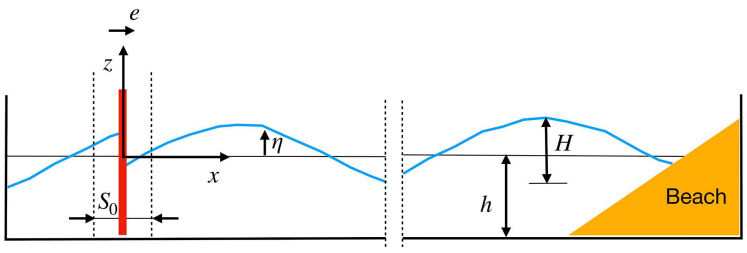

Figure 3.6: Piston-type wave maker.

- h: Water depth (assumed to be constant)

Assuming a piston-type wave paddle, is displaced with a sine law (3.32), where $\omega = 2\pi/T$.

$$e(z,t) = \frac{S(z)}{2}\sin(\omega t) \tag{3.32}$$

The solution is a linear combination of the decoupled solutions that satisfy the free surface boundary conditions. The velocity potential (3.33) and free surface are:

$$\begin{aligned}\phi(x,z,t) = &-\frac{\omega}{k}c_i\cosh(k(z+h))\sin(\omega t - kx)\\ &-\sum_{n=1}^{\infty} c_n\frac{\omega}{k_n}\cos(k_n(z+h))\exp^{-k_n x}\cos(\omega t)\end{aligned} \tag{3.33}$$

$$\begin{aligned}\eta(x,t) = &\, c_i\sinh(kh)\cos(\omega t - kx)\\ &+\sum_{n=1}^{\infty} c_n\sin(k_n h)\exp^{-k_n x}\sin(\omega t)\end{aligned} \tag{3.34}$$

The first term at the right-hand side of equations (3.33) and (3.34) represents the far-field solution (long distance from the wavemaker), and the second term represents the near-field solution. The near-field term, representing the standing waves, decreases with distance from the paddle. Within a distance of 1 or 2 wavelengths, the near-field term is smaller than 1% of the solution, and therefore, it can be neglected. Considering the wavemaker displacement law (3.32) [26].

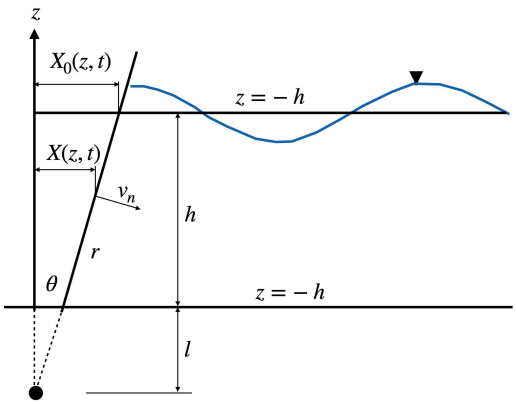

Figure 3.7: General wave maker.

Eq. (3.35) shows the coefficient c_i has a similar expression referring to the far-field solution.

$$c_i = \frac{2\omega}{gk}\frac{S_i}{\sinh(2kh)+2kh}\cdot\left[\sinh(kh)+\frac{1-\cosh(kh)}{k(h+l)}\right] \tag{3.35}$$

At the dispersion relation $\omega^2 = gk\tanh(kh)$ and considering the ratio between $H = 2c$ and S_i:

$$\frac{H}{S_i} = \frac{4\sinh(kh)}{\sinh(kh)+2kh} \cdot \left[\sinh(kh) + \frac{1-\cosh(kh)}{k(h+l)}\right] \tag{3.36}$$

For a piston-type wavemaker, as $l \to \infty$, the final Biésel transfer law is obtained.

$$\frac{H}{S_i} = \frac{4\sinh^2(kh)}{\sinh(kh)+2kh} \tag{3.37}$$

Given an appropriate distance from the paddle, the numerical solution must be very close to the analytic curve (3.37) for the problem [8].

3.3 Solitary Waves

Solitary waves, also known as waves of translation, were studied first by by John Scott Russell in 1834 [27]. These waves are characterised by the following properties:

- Stable waves
- Can travel large distances without flattening or steepening
- Speed is a function of the wave size, width, and the water depth
- Unlike normal waves, they will never merge; i.e., a small wave is overtaken by a large one
- If a wave is too big for the depth of water, it splits into two components: one big and one small

In a flume, these waves are generated by a single push of a piston-type wavemaker. The velocity of the wavemaker can be expressed by a time-dependent polynomial function:

$$u = at^4 + bt^3 + ct^2 + dt + e \tag{3.38}$$

where t is the time variable and a, b, c, d, and e are real constants.

3.4 Rogue Waves and Focused Wave Theory

Freak or rogue waves are among the most dangerous phenomena at sea. These waves are characterised by a wave height that exceeds the expected height according to the prevailing sea state [28]. Their formation is random and they appear arbitrarily in ocean areas with various depths [29]. Tridimensional wave focusing, among other factors, contributes to the formation of these waves [30]. Field measurements show enormous heights, such as the Draupner wave with a height of 18.49 m [31]. The focusing wave theory [32] is presented. In the defined frequency spectrum, characterised by a minimum frequency f_{min} (Hz) and maximum frequency f_{max} (Hz), N_w small amplitude linear waves are considered. Usually, their amplitude a_i is constant and through superposition, they produce a rogue wave at a specific focusing time t_f and spatial position y_f.

$$\eta(y,t) = \sum_{i=1}^{N_w} a_i \cos[k_i(y-y_f) - 2\pi f_i(t-t_f)] \tag{3.39}$$

According to the focusing wave theory, Eq. (3.39) describes the free surface evolution. The subscript i refers to the i-th linear wave component, k_i is the wave number (according to the linear dispersion equation). The linear transfer function for the piston-type wavemaker is employed (Eq. (3.37)) [25]. The boundary condition to the wavemaker is imposed prescribing the position δ, velocity u, and acceleration a.

$$\begin{cases} \delta = \sum_i^N \frac{1}{2} S_i \cos(-k_i y_f - \omega_i(t-t_f)) \\ u = \sum_i^N \frac{1}{2} S_i \omega_i \sin(-k_i y_f - \omega_i(t-t_f)) \\ a = \sum_i^N -\frac{1}{2} S_i \omega_i^2 \cos(-k_i y_f - \omega_i(t-t_f)) \end{cases} \tag{3.40}$$

Where $\omega_i = 2\pi f_i$ is the angular frequency of the i-th regular wave component.

3.5 Spectral Analysis

Some functions or signals, generically called γ, can be composed of an infinite sum of harmonics. If the Fourier series of γ exists, the Fourier transform is defined as [33]

$$\mathbb{F}(\gamma) = \mathbb{F}(k) = \hat{\gamma}(k) = \int_{-\infty}^{\infty} e^{-ikx}\gamma(x)dx \tag{3.41}$$

Where i is the unit imaginary number, k is the index of the Fourier series of γ. This transform allows visualizing the frequencies composing that signal. The spectrum amplitude $a = |\mathbb{F}(k)|$, i.e., the module of γ's Fourier transform, is equal to the amplitude of the single harmonics [33]. The Fast Fourier Transform (FFT) is an algorithm widely adopted to extract information from sampled signals. Given $\hat{\gamma}(x)$ as the sampled signal, the discrete Fourier transform is given in Eq. (3.42). The demonstration is omitted but can be found in [34].

$$\tilde{g}\left(\frac{n}{2lN}\right) = \sum_{k=0}^{N-1} \gamma(2lk)e^{\frac{-2\pi ink}{N}} \qquad n = 0, 1, 2, \ldots, N-1 \tag{3.42}$$

This expression relates the N time samples and N frequency samples by means of the continuous Fourier transform.

3.6 Short-Term Wave Analysis

When studying sea wave data, short-term analysis refers to waves that occur within one wave train or storm [35]. The real sea surface is random; therefore, a number of simplifications can be made on the field recordings. Waves may appear in a variety of heights and lengths. Therefore, statistical analysis is used. Defining z as the instantaneous water level referred to a datum and η as the difference between the instantaneous and mean water level, these are functions of time t and spatial position (x, y).

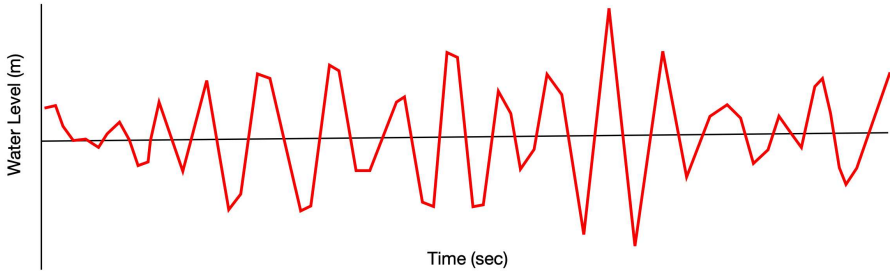

Figure 3.8: Water level record $z(t)$.

Figure 3.8 shows the water level record, i.e., one realisation of the process $z(t)$. A set of evaluations of one process is called an Ensemble. All values of z at $t = j\Delta t$ in the k realisations can be used to compute statistical parameters such as the mean $\bar{z}_j$ and standard deviation σ_j.

$$\bar{z}_j = \frac{1}{K}\sum_{k=1}^{K} z_{k,j} \quad \text{and} \quad \sigma_j = \sqrt{\frac{1}{K}\sum_{k=1}^{K}(z_{k,j} - \bar{z}_j)^2} \tag{3.43}$$

In the ensemble, higher-order moments, i.e., skewness and kurtosis, can be determined as well. The system can be called stationary if none of these statistical parameters varies in time; if only the mean and standard deviation are constant, the ensemble is considered weakly stationary. If the ensemble average is equal to the time average of each realisation, the process is called ergodic.

3.6.1 Wave Height Distribution

η is usually defined as the superposition of an infinite number of small waves. Each wave is generated by a small eddy at different locations and times. The sea surface is, therefore, defined as a sum of a large number of statistically independent processes, i.e., η is a random variable. The probability that η assumes a certain value can be found with a probability density function (PDF).

A random variable is described by a Gaussian or normal distribution. The probability of a certain wave height can be described by its mean and standard deviation.

$$p(\eta) = \frac{1}{\sigma\sqrt{2\pi}} e^{\frac{-\eta^2}{2\sigma^2}} \tag{3.44}$$

where the standard deviation σ is equal to the square root of the variance of η

$$\sigma^2 = \bar{\eta^2} = \frac{1}{N}\sum_{j=1}^{N} \eta_j^2 \tag{3.45}$$

If the waves occur within a narrow frequency band, the PDF of the maximum value is

$$p(\eta_{\text{max}}) = \frac{\eta_{\text{max}}}{\sigma^2} e^{\frac{-\eta^2}{2\sigma^2}} \tag{3.46}$$

If the wave height is $H = 2\eta_{\text{max}}$, the PDF for H becomes

$$p(H) = \frac{1}{4}\frac{H}{\sigma^2} e^{\frac{-H^2}{8\sigma^2}} \tag{3.47}$$

Equations (3.46) and (3.47) are known as the Rayleigh Distribution.

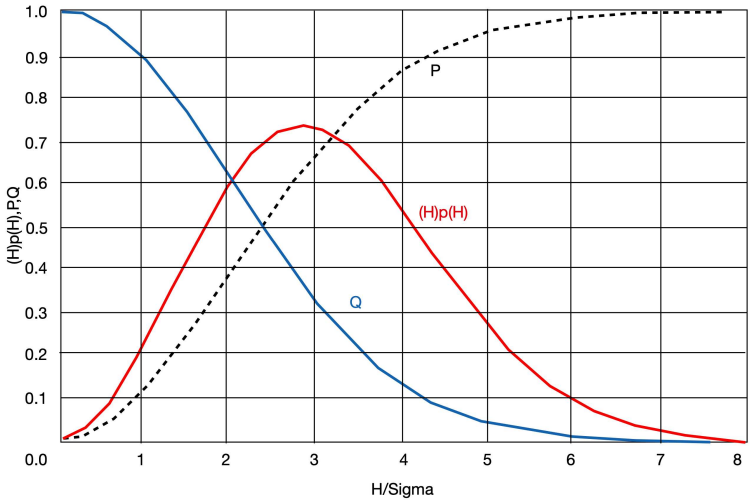

Figure 3.9: Rayleigh Distribution.

The cumulative distribution function (CDF) P of wave height is achieved with the integration of the probability density function. The probability that a wave with H' height exceeds a specified wave height H is given by Q

$$P(H' < H) = 1 - e^{\frac{-H^2}{8\sigma^2}} \quad \text{and} \quad Q(H' > H) = 1 - P(H' < H) = e^{\frac{-H^2}{8\sigma^2}} \tag{3.48}$$

The average of all waves higher than those with a given probability Q, in a storm, is determined as

$$\bar{H}_Q = \frac{\int_{H_Q}^{\infty} Hp(H)dH}{Q} \tag{3.49}$$

Of all the waves, with probability Q, the most important is defined as the average of the highest $\frac{1}{3}$ of the waves in a wave train, $\bar{H}_{1/3}$. This quantity is known as the Significant wave height H_s.

3.6.2 Frequency Analysis

In a random sea, the wave spectrum is composed of components with many frequencies. The wave spectrum can be characterised by its peak frequency, corresponding to the largest variance of energy. The peak spectral period is defined as

$$T_p = \frac{1}{f_p} \tag{3.50}$$

3.6.3 Directional Wave Spectra

The variable η has been considered until now only as a function of time at a single location. In real sea states,, η is also a directional function of x and y.

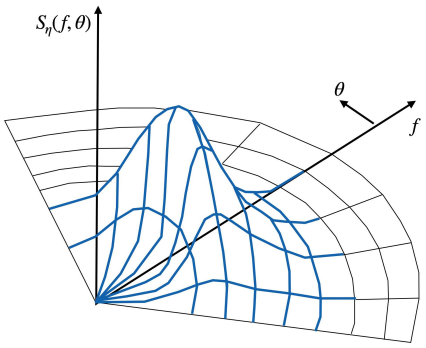

Figure 3.10: Directional wave spectrum.

Figure 3.10 shows a sketch of the directional wave spectrum as a function of frequency and direction. The simplest approach to describe the directional spectrum is:

$$S(f,\theta) = S(f)G(\theta) \tag{3.51}$$

where $S(f)$ is the frequency spectrum and $G(\theta)$ is called the directional spreading function which is tyipically assumed equal to cos^2.

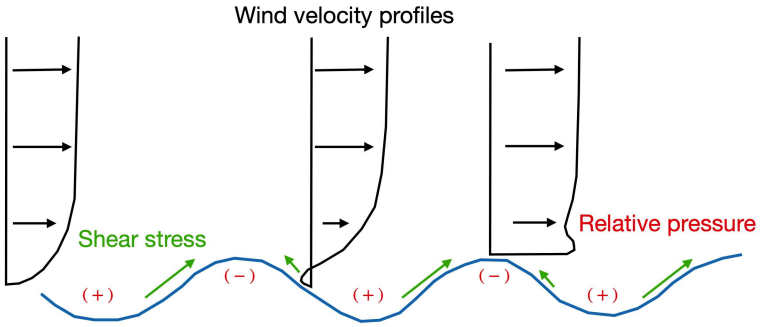

Figure 3.11: Wind energy transfer.

3.7 Wind Wave Generation

In the sea, when the wind blows, turbulent wind eddies periodically touch the water surface, forming small ripples. The maximum energy transfer between the wind and waves occurs when the wind velocity matches the wave velocity.

However, this alignment is generally not exact; the wind velocity is typically much higher than the wave velocity. Consequently, the waves form at an angle to the wind direction, causing the propagational velocity of waves to approach the wind velocity. Once the first small waves form, the wind continues to blow, transferring energy from the wind to the waves. Figure 3.11 illustrates the energy transfer mechanisms.

Sheltering causes the wind speed downwind of the wave to be smaller, or sometimes even the reverse of the wind velocity towards the upwind side. The resulting shear stress moves water toward the wave crest from both sides. The wind speed, due to the wave shape, increases over the crest and decreases at the trough, both phenomena described above contribute enhancing the wave height. According to Bernoulli's law, pressure is lower in the crest and higher in the trough.

Figure 3.12 depicts the process of wave generation. The majority of the wind energy is transferred to high-frequency waves. Small waves form on top of existing ones rather than increasing the height of existing ones. Subsequently, the energy is transferred from the higher-frequency waves to the lower-frequency ones via wave-wave interaction.

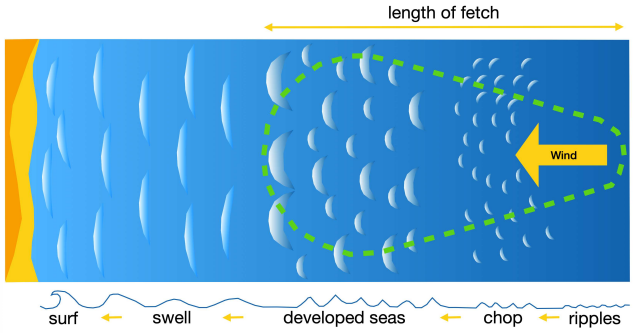

Figure 3.12: Wind wave generation.

3.7.1 Wind Velocity Profile

In the upper part of the atmosphere, at altitudes greater than 1 km, the winds are driven by the geostrophic balance between large-scale pressure gradients and the Coriolis force (Geostrophic region). Below 1 km altitude, frictional effects due to the presence of the Earth's surface affect the wind field (boundary layer). For the process of wave generation by wind, the lower part of the boundary layer is of main concern. It extends from above the free surface to about 100 m and is called the constant shear stress layer. In this layer, the wind speed and direction become dependent, on the elevation above the mean surface, surface roughness, and air-sea temperature gradients.

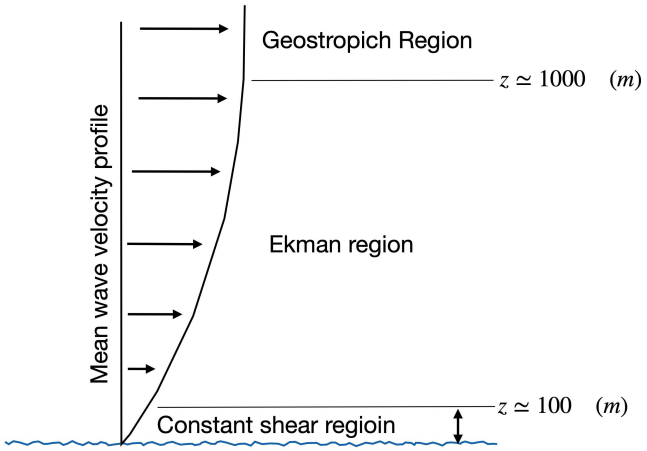

Figure 3.13: Wind velocity profile.

Assuming a logarithmic velocity profile of the wind in the constant shear layer, the wind speed U_z measured at any elevation z (less than 20 m) can be related to the wind speed U_{10} at 10 m elevation through a simplified law:

$$\frac{U_{10}}{U_z} = \left(\frac{10}{z}\right)^{\frac{1}{7}} \tag{3.52}$$

As the input of energy from the wind depends on the surface stress, parametric models use an adjusted wind speed (or wind stress factor) that accounts for the nonlinear relation between wind stress and wind speed:

$$U = 0.71 U_{10}^{1.23} \tag{3.53}$$

Usually, the measured wind speed is available as an hourly-average speed. If a duration greater than 1 hour is required as input for the parametric models, the hourly-average values may be averaged to achieve the desired duration. If these values differ significantly (say 3-5 m/s), the assumption of constant wind speed is not valid, and the prediction becomes dubious. Conventionally, the wind speed measured over the water is adopted in parametric models. If measurements of wind speed over land are available, they usually underestimate the speed over water (due to increased friction over land) and should be properly corrected.

3.7.2 Wave Hindcasting: The JONSWAP Method

Wave height, period, and direction are closely linked to wind conditions. By analysing measured wind records, it is possible to reconstruct the wave climate. This process is known as hindcasting. In the past, several methods have been developed to predict wave fields from wind data. These methods are called parametric methods because they use wind parameters to evaluate wave parameters (such as significant wave height H_S and peak period T_p) without developing a detailed description of the physics behind the generation process. The wind parameters involved are:

- Fetch F, the distance the wind blows over the water to generate waves.
- Duration t of the wind forcing.
- Wind speed U blowing over the sea.

The first empirical method, developed during World War II, aimed to predict wave conditions based on weather forecasts to assist in landing Allied troops [36] and [37]. This effort led to the development of the SMB method, as presented in [38]. Subsequently, the JONSWAP method, based on research conducted during the Joint North Sea Wave Project [22], extended to developing sea this early method in [39]. Figure 3.12 illustrates the wave generation process.

Determining fetch length for an open shore poses a challenge; however, for sufficiently large fetches, wave parameters are not highly sensitive to errors in fetch length. A fully developed sea occurs when fetch, duration, and depth are infinite. The energy content of the wave field is determined solely by wind speed, representing an equilibrium condition between wind transfer and dissipation through internal friction and turbulence. Adopting a simplified method for predicting waves in deep water is feasible only under the following conditions:

- The water body has a relatively simple geometry.
- Wave conditions are either fetch-limited, duration-limited, or fully developed.
- An adjusted wind speed U can be evaluated, representing a relatively constant average value over the fetch F.

Under fetch-limited conditions, the wind has blown consistently long enough for the wave height at the end of the fetch to reach equilibrium. In duration-limited conditions, wave heights are constrained by the length of time the wind has blown.

Assuming the non-dimensional fetch $F^* = gF/U^2$, the following relations are valid for determining non-dimensional wave height (H^*), non-dimensional wave period (T^*), and non-dimensional time (t^*).

$$\begin{aligned} H^* &= 1.6 \times 10^{-3}(F^*)^{\frac{1}{2}} \quad \text{with} \quad H^* = \frac{gH_{m0}}{U^2} \\ T^* &= 0.2868(F^*)^{\frac{1}{3}} \quad \text{with} \quad T^* = \frac{gT_p}{U} \\ t^* &= 68.6(F^*)^{\frac{2}{3}} \quad \text{with} \quad t^* = \frac{gt}{U} \end{aligned} \tag{3.54}$$

where H_{m0} is the spectrally based significant wave height and T_p is the peak period of the wave spectrum. In the case of a fully-developed sea, the following equations are assumed to evaluate the significant wave height and the peak period. Wind duration should be greater than that obtained from t^* in Eq. (3.55).

$$\begin{aligned} H^* &= \frac{gH_{m0}}{U^2} = 0.2433 \\ T^* &= \frac{gT_p}{U} = 8.134 \\ t^* &= \frac{gt}{U} = 7.17 \times 10^4 \end{aligned} \tag{3.55}$$

An interim method for forecasting waves generated by winds blowing over relatively shallow water (15–90 m) is provided in [39]. It accounts for bottom-induced dissipation by introducing the non-dimensional depth $d^* = \frac{gd}{U^2}$.

$$\begin{aligned} H* &= 0.283tanh\Big(0.530d*^{\frac{3}{4}}\Big)tanh\Big[\frac{0.00565F*^{\frac{1}{2}}}{tanh(0.530d*^{\frac{3}{4}})}\Big] \\ T* &= 7.54tanh\Big(0.833d*^{\frac{3}{8}}\Big)tanh\Big[\frac{0.0379F*^{\frac{1}{3}}}{tanh(0.833d*^{\frac{3}{8}})}\Big] \\ t* &= 537(T*)^{\frac{7}{3}} \end{aligned} \tag{3.56}$$

Figure 3.14 shows the block diagram to apply the JONSWAP method.

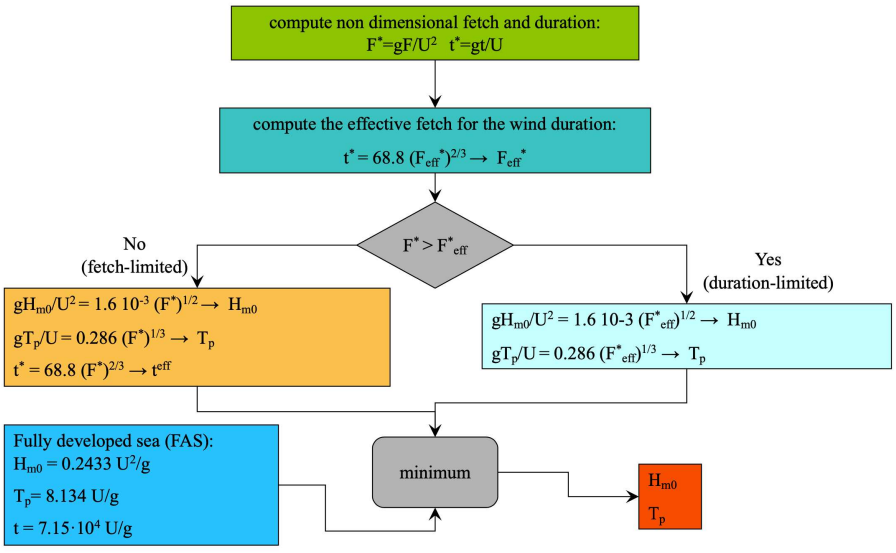

Figure 3.14: Block diagram for the JONSWAP method.

The proposed method for wave prediction is a simplified approach developed based on observations mainly in the North Atlantic Ocean, and it relies on certain simplifications. Therefore, it is approximate and requires proper calibration based on the climate of a specific site. It is advisable to use such a method for a rough estimate of the wave field, which should be confirmed by more sophisticated hindcasting models that numerically solve the governing equations for the energy balance of the wave field.

4

Wave hindcast in the Mediterranean sea

The use of spectral models holds paramount importance in understanding and characterizing the dynamic forces exerted on offshore structures, particularly during specific meteorological conditions. These models serve as indispensable tools in comprehending the intricate interplay of waves with marine structures, enabling engineers and researchers to assess the potential impacts and design structures resilient to these forces.

In the context of this paragraph, a comprehensive investigation is undertaken into a prominent spectral model aimed at simulating the propagation of wave motion in coastal regions. This endeavor seeks to delve deeply into the intricacies of the selected model, probing its efficacy and applicability in capturing the nuanced behavior of waves near the shoreline.

4.1 Introduction

This chapter illustrates an application of the SWAN spectral model for wind-wave hindcasting. The study area is a coastal region located south of the Sicily near Mazara del Vallo, Italy. This choice allows for model validation by comparing hindcasted results with measurements from the wave meter station at Mazara del Vallo (see Fig. 4.1). The wave buoy is positioned offshore of Capo Granitola at a nominal depth of 85 meters and is part of the Italian wave-meter buoy network. It has been operational for at least 40 years, and its measurements, including sea state, significant wave height, spectral period and direction, as well as wind measurements, are freely available to the public. To validate the model, a storm event lasting 24 hours is reproduced.

Figure 4.1: Measuring buoy.

4.2 Preprocessing

As discussed in Section 2.5, model setup requires grids related to bathymetry, wind, and computational grid. For simplicity, in this context, the nodes of these grids are coincident.

4.2.1 Computational Grid

The case is situated in a real region, and a geographical information program is utilised for this purpose. The geographical position of the wave buoy at Mazara del Vallo is marked with a red cross (Fig. 4.2). It is crucial to align the coordinate system of the project with that of the buoy's position. In this scenario, the Cartesian projection EPSG:3857 is employed. A set of points, spaced 1x1 km apart, is then generated in the study area. After generating these points, they are adjusted so that one grid point matches the position of the wave buoy. This process is illustrated in Fig. 4.2, where the initially generated grid (purple dots) is shifted (orange dots) to align one point with the position of the wave buoy (red cross). The coordinates of the orange points constitute the computational grid.

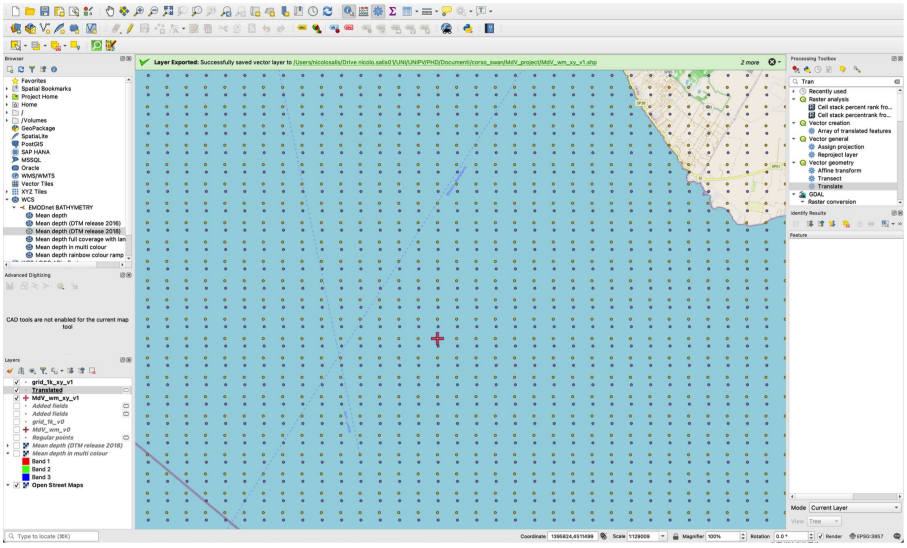

Figure 4.2: Position of the wave buoy (red cross), initially placed grid points (purple dots), computational grid points (orange dots).

4.2.2 Bathymetry Grid

Bathymetric data for the Mediterranean basin is freely accessible from EMODnet. EMODnet Bathymetry offers a service for viewing and downloading the best available harmonised Digital Terrain Model (DTM) for European sea regions, along with various other bathymetric data, products, and services. Figure 4.3 presents the coloured bathymetry of the Mediterranean basin, ranging from red (shallow water) to blue (deep water), with the study region highlighted by a pink ellipse.

The bathymetry grid required as input for the SWAN model is obtained by assigning depths from the DTM to each node of the previously defined computational grid.

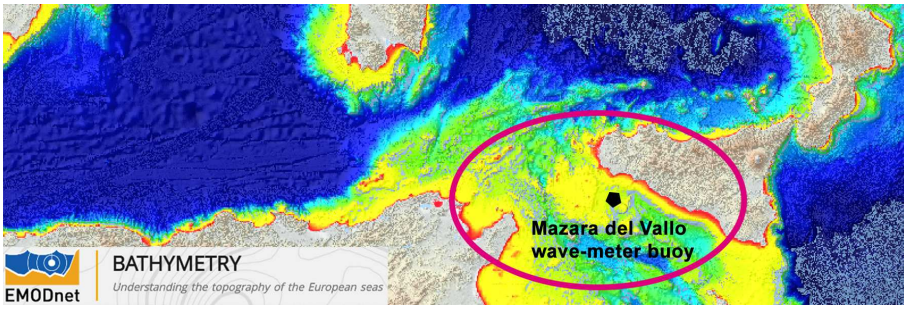

Figure 4.3: Bathymetry of the Mediterranean Seas, with the study area and the position of the Mazara del Vallo wave-meter buoy marked.

4.2.3 Wind Grid

Although the buoy can provide measurements of wind, this local information is insufficient for generating waves over a large computational grid spanning several kilometres. A single point measurement cannot be considered valid for a large region due to the significant spatial variability of wind. The ERA5 reanalysis dataset from the Copernicus project of the European Union is utilised for this purpose. ERA5 is the fifth generation ECMWF reanalysis for global climate and weather over the past eight decades, with data available from 1940 onwards. The data is provided as a geo-referenced vector image with a grid of 5x5 km. Once imported into the graphics information system program, wind velocity and direction values can be assigned to each point of the previously defined grid. In this case, 48 grids are defined, 24 each for the x-direction and y-direction. These grids correspond to each hour of simulation.

Figure 4.4 compares the measured and forecasted wind velocities at the measuring buoy. While there is slight variation between the forecast and measurement, it is necessary to use forecasted wind data as it provides spatially distributed information rather than punctual measurements, which is essential for accurate simulations.

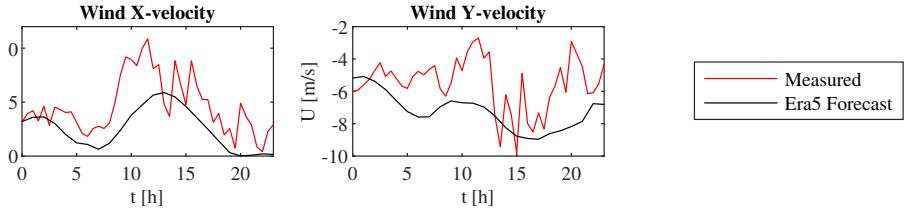

Figure 4.4: Wind velocity comparison between forecasted data and measured data in the location of the measuring buoy.

4.3 Input File

The input file is configured using the Cartesian convention, with water density set to 1023 kg/m^3 and gravity to 9.81 m/s^2. Figure 4.5 illustrates the region of interest for this study. The northeastern part of the figure depicts the Sicily coast, delineated by the pink line, with bathymetry and wind vectors indicated. The axes display the geographical coordinates of the study area, utilizing the Cartesian projection EPSG:3857.

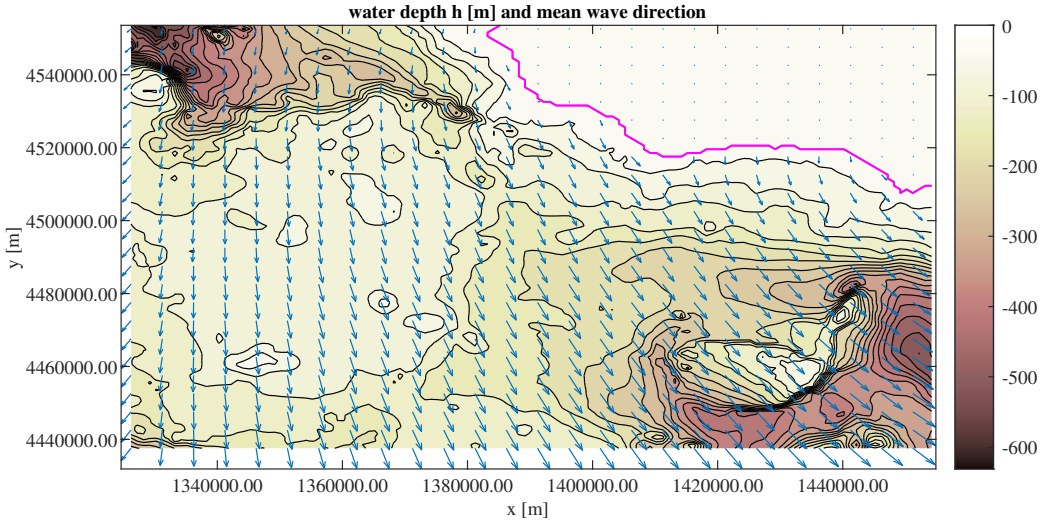

Figure 4.5: Bathymetry and mean wave direction of the study region.

The initial sea state is not provided; at the beginning of the simulation the water surface is at rest. The model execution is non-stationary as it focuses on hindcasting waves generated by wind. Due to these two aspects, the initial part of the simulation (first 10 hours) is required to generate the sea state. The computational grid is

established in geographical coordinates, with a grid size of 128 km in the x-direction and 116 km in the y-direction, and a spacing of 1 km in both directions. The grid comprises 14,848 computational nodes. The grids of bathymetry and wind velocity have the same size as the computational grid and are uploaded as text files.

The wind-wave generation parameters are configured, with type 3 generation based on the Komen method being the default. SWAN operates in third-generation mode for wind input, quadruplet interactions, and whitecapping. The Komen wave generation relies on linear growth [40], with wave generation occurring only if the keyword AGROW is present, indicating exponential growth [41]. In non-stationary runs, SWAN starts with INIT ZERO (flat water surface), and wave energy remains zero unless wave energy penetrates over the boundary or AGROW is activated.

The simulation is set up to consider all physical processes with standard values:

- QUADRUPL: Nonlinear wave-wave interactions.
- WCAPPING: Steepness-induced wave-breaking.
- BREAKING: Depth-induced wave breaking in shallow water.
- FRICTION: Bottom friction.
- TRIAD: Nonlinear wave-wave interaction redistributing wave energy within the spectrum due to resonance.
- LIMITER: This command allows the user to permanently deactivate quadruplets when the actual Ursell number exceeds 10. Additionally, as soon as the actual fraction of breaking waves exceeds 1, the action limiter will not be used in case of decreasing action density.

Next, numerical parameters are set for non-stationary computation with implicit time integration, a stop criterion with a maximum of 30 iterations per time step, and output control introduced for the entire computational grid, including the point of the wave-meter buoy. Results are saved at hourly intervals for comparison with the measured data.

The non-stationary computation begins for a duration of 24 hours, starting from May 25, 2021, at 00:00 to May 25, 2021, at 23:00.

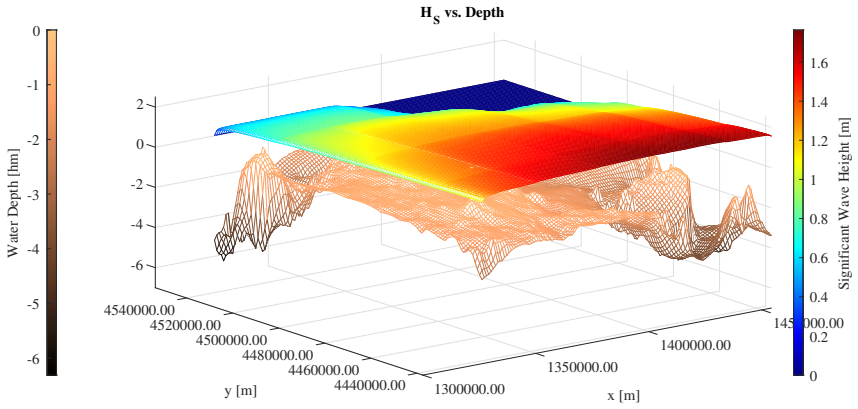

Figure 4.6: Bathymetry of the study area with significant wave height at hour 20:00.

4.4 Results

As previously said, no wave spectrum has been assigned at the beginning of the simulation. The model takes about 10 hours to develop a sea state in equilibrium with the wind forcing. After that time, results are compared with observed data. Hence, the results will be considered starting from hour 10 onward. Figure 4.6 displays the significant wave height and the bottom depth. It's worth mentioning that the North and West boundaries (Fig. 4.5) exhibit reduced wave heights. This aspect is related to the lack of spectral information for the incoming wave entering the computational domain trough these boundaries, leading to some errors in the significant wave height calculation

(Fig. 2.11). Within the region of interest, the wave height varies with water depth, ranging from 0.8-1.0 m in shallow water, while it ranges between 1.6-1.7 m in deep water.

Figure 4.7 illustrates the directional wave spectrum at the location of the wave-meter buoy at t=19:00h and t=20:00h. In both cases, the waves are directed southwest, with directions between 200° and 360°. The directional wave spectrum indicates that the simulated waves lie in the low-frequency spectrum, corresponding to relatively long wavelengths. For instance, a wave with a $f = 0.2$ Hz would have a wavelength of 39 m. The spectral energy undergoes slight changes from hour 19:00 to hour 20:00, with the wave energy slightly lower at hour 20:00. The waves exhibit similar lengths, while the direction undergoes a slight change, nearing 360°.

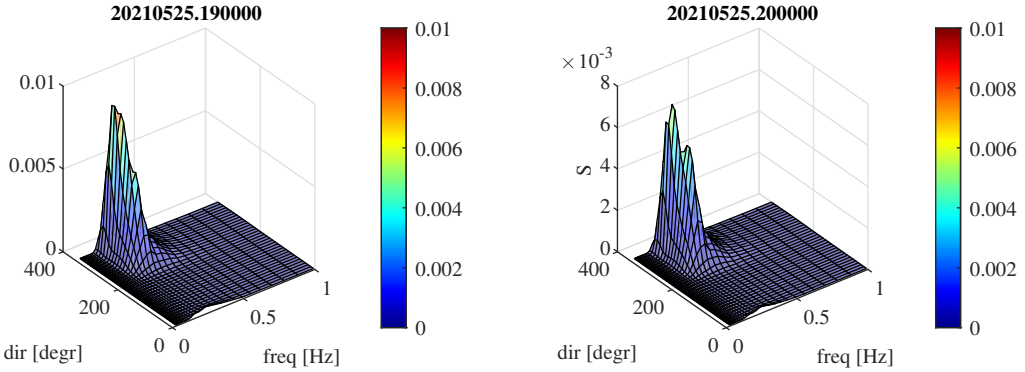

Figure 4.7: Directional wave spectrum S $(m^2/(Hz \quad deg))$ at the location of the wave-meter buoy. Left panel: hour 19:00; Right panel: hour 20:00.

Figure 4.8 depicts the hindcasted significant wave height, wave direction, peak spectral period, and mean spectral period at the Mazara del Vallo wave-meter buoy. As mentioned earlier, at least 10 hours of physical time are required to establish a sea state. This is evident in all the sub-figures, where measured data begins from a specific value, whereas simulated data initiates from zero except the wave direction•. After these 10 hours, it can be observed that the simulated trends of significant wave height, peak and mean spectral period closely resemble the measured data. While the wave direction exhibits slight discrepancies, it's noteworthy that the simulated waves are directed southwest, consistent with the measured data. This constitutes the validation of the model, albeit limited to the analysed storm event.

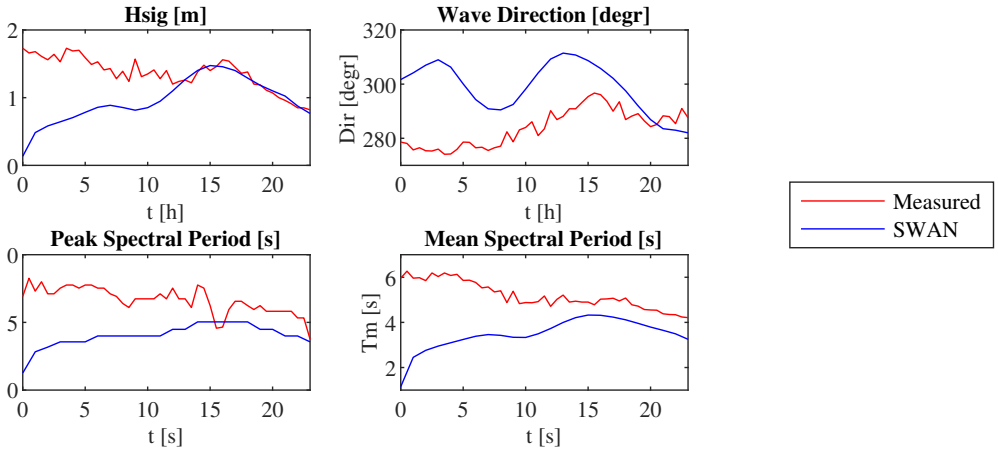

Figure 4.8: Comparison of hindcasted significant wave height, wave direction, peak spectral period, and mean spectral period with measured data at the Mazara del Vallo wave-meter buoy.

4.5 Final Remarks

This chapter presents a real-scale application of a spectral model used to hindcast a sea state. The southeast coast of Sicily was selected, particularly due to the presence of a wave-meter buoy in the region. A SWAN model was constructed and executed to replicate a storm event lasting 24 hours. The results were compared with measured data, validating the model on the selected storm event. Further testing is necessary to evaluate the model's reliability for wave hindcasting based on forecasted wind data. However, as the model input is affected by uncertainties (e.g., wind characteristics and model parameters), global sensitivity analysis and parameter optimization could enhance the model's description, though these aspects will be the subject of future studies.

Up until now, wave hindcasting at a large scale has been presented. This approach is useful for identifying the sea state of a site of interest, but it only considers time-averaged quantities such as significant wave height and spectral period. However, identifying the sea state is only the first step toward the analysis of impulsive waves impacting onto offshore structures. Time-averaged quantities are insufficient to describe these phenomena. Therefore, in the next chapter, time evolution of wave generation, propagation and wave-structure impact in a channel are studied developing and using Lagrangian particle methods.

5

Improvements to the single phase SPH model

5.1 Introduction

The modelling of regular and focused waves began in the master's thesis [42], where the SPHERA v.9.0.0 code (RSE S.p.A.) [43] was employed to simulate various linear waves. However, the model exhibited excessive numerical dissipation, resulting in reduced wave heights and velocities, particularly noticeable for higher frequency waves. During the first year of the doctoral program, efforts were focused on addressing these numerical dissipations. After an extensive literature review, the renormalisation scheme was chosen as a potential solution. Initially introduced in [44] and [45] to achieve first-order consistency in kernel derivatives, the renormalisation scheme was implemented to improve the accuracy of the SPHERA equations. The subsequent sections present the specific equations of SPHERA, with a focus on the renormalisation of kernel derivatives.

5.1.1 Original Numerical Model

In this context, SPHERA v.9.0.0 is utilised to solve the WCSPH (Weakly Compressible Smoothed Particle Hydrodynamics) approximation of the governing equations for a Newtonian fluid. The boundary treatment includes a semi-analytic approach for solid walls [46] and a scheme for solid bodies [47]. The continuity equation is as follows:

$$\begin{aligned}\left\langle \frac{d\rho}{dt} \right\rangle_i = &\sum_j \rho_j (u_{b,j} - u_{0,j}) \frac{\partial W}{\partial x_j} \varpi_j \\ &+ 2\rho_i \int_{V_h'} [(\underline{u}_w - \underline{u}_i) \cdot \underline{n}] n_j \frac{\partial W}{\partial x_j} dx^3 + C_s\end{aligned} \tag{5.1}$$

where C_s is introduced to represent the fluid-body interaction term. The notation "$\left\langle \right\rangle$" denotes the SPH particle discrete approximation. The momentum balance equation is:

$$\begin{aligned}\left\langle \frac{du_i}{dt} \right\rangle_i = &-\delta_{i3} g + \sum_j \left(\frac{p_j}{\rho_j^2} - \frac{p_i}{\rho_i^2}\right) W_j' m_j + 2\frac{p_i}{\rho_i} \int_{V_h'} \frac{\partial W}{\partial x_i} dx^3 + \\ &- \alpha_M \sum_j \frac{m_j}{\rho_i r_{ij}^2} (\underline{u}_j - \underline{u}_i) \cdot (\underline{x}_j - \underline{x}_i) \frac{\partial W}{\partial x_j}\Big|_j + \\ &- \alpha_M (\underline{u}_w - \underline{u}_i) \int_{V_h'} \frac{1}{r_{0w}^2} (\underline{x} - \underline{x}_i) \frac{\partial W}{\partial x_i} dx^3 + \underline{a}_s\end{aligned} \tag{5.2}$$

In Eq. 5.1 and Eq. 5.2, δ_{ij} represents the Kronecker delta, a_s denotes an acceleration term due to fluid-body interactions, α_M stands for artificial viscosity [48], m represents particle mass, and r_{0b} is the relative distance between the computed particle (subscript 0) and the neighbouring particle (subscript b). Here, W is the kernel function, $\mathbf{u}$ is the velocity vector, p is pressure, ρ is fluid density, g is the modulus of gravitational acceleration, $\mathbf{x}$ is the position vector, and t represents time.

The kernel support is truncated when it intersects the boundary that confines the computational domain filled by fluid particles. To address this issue, a semi-analytic technique is adopted to mimic solid boundaries. The summation extends to all fluid particles with volume ϖ (subscript b) within the kernel support of the computed fluid particle (subscript 0). The volume integral represents the boundary term, which is the convolution integral on the kernel's truncated portion with the fictitious outer volume V_h'; the subscript w denotes a generic boundary. Additionally, n represents the normal vector to the wall surface.

The system of equations is completed by the following linearised barotropic equation of state (EOS) for slightly compressible fluids:

$$p = c_{\text{ref}}^2(\rho - \rho_{\text{ref}}) \tag{5.3}$$

Here, the artificial sound speed c is set to be at least ten times higher than the maximum fluid velocity to ensure a relative density variation of at most 1% [48], and the subscript "ref" denotes the reference state. The wavemaker and the box-shaped structure are treated using the scheme of rigid body transport as solid bodies, with imposed and fixed kinematics, respectively. The time integration is performed using a second-order Leapfrog scheme. For further details on the code, readers are referred to the code documentation [43].

5.1.2 Renormalization

The renormalisation scheme is implemented to enhance the numerical accuracy in computing the kernel gradient. It mitigates non-physical dissipation of both wave height and velocity, which are more pronounced in slow dynamic phenomena. These dissipations primarily stem from higher frequency components (wave spectrum) in slow dynamics [42, 49].

Renormalization enables achieving first-order consistency of a function (zeroth order consistency for its derivative), thereby precisely reproducing the derivative of a linear function. Initially introduced in [44, 45], this technique has been consistently utilised, with minor adjustments, in free surface flows characterised by slow dynamics. In recent applications, renormalisation is employed to compute the density gradient for the diffusive term in the continuity equation (Eq. (6.15)) [50, 51, 52]. Considering the derivative of a function, as depicted in Eq. 5.4, the kernel gradient is normalised using the renormalisation matrix $\underline{\underline{L}}$.

$$\left\langle \nabla f \right\rangle_i = \left\langle \frac{\partial f}{\partial \underline{x}} \right\rangle_i \equiv \sum_j (f_j - f_i)(\underline{\underline{L}}_i \cdot \underline{\nabla W}_j)_i \frac{m_j}{\rho_j} \tag{5.4}$$

The renormalisation matrix, defined by Eq. (5.5), is applicable within the fluid and at its boundary surface, aiding in reducing truncation errors at the free surface.

$$\underline{\underline{L}}_i = \underline{\underline{B}}_i^{-1} = \left(\pm \sum_j (\underline{x}_j - \underline{x}_i) \underline{\nabla W} \frac{m_j}{\rho_j} \right)^{-1} \tag{5.5}$$

Subsequently, the normalised kernel derivative is defined as shown in Eq. 5.6.

$$\widetilde{\underline{W}'}_j = \underline{\underline{L}}_i \cdot \underline{\nabla W}_j \tag{5.6}$$

The renormalisation technique is employed in the pressure term of the momentum balance equation, in the continuity equation to normalise the kernel gradient, and for the diffusive terms (see Section 6.1.2). In Eq. (5.5), a $\pm$ sign is present. The sign of $\underline{\underline{B}}$ is positive when the renormalisation is applied to the continuity equation and diffusive term, while it is negative for the momentum balance equation, as indicated in [44].

The value of the matrix determinant ($\det(\underline{\underline{B}}_i)$) is proportional to the concentration of neighbouring particles. When the renormalisation is applied to the continuity equation and the diffusive term, there are no issues, and $\det(\underline{\underline{B}}_i) = 0$. However, problems arise when it is applied to the pressure term in the momentum balance equation, which is more sensitive. To address this, renormalisation is conducted in a case-sensitive manner using Eq. (5.7), introducing a threshold value $Btol$ for the matrix determinant. The parameter $Btol$ is chosen heuristically to ensure stability. In the investigated problems, values lower than $Btol = 0.3$ cause instabilities. In the results presented in the conference paper [49], $Btol = 0.6$ is used, representing a suitable compromise between accuracy and stability. In [49], regular

and nonlinear waves are generated in a numerical wave tank, demonstrating good accuracy compared to laboratory experiments and theoretical solutions.

$$\begin{cases} if & |det(\underline{\underline{B}}_i)| \geq Btol \qquad \widetilde{\underline{W'}}_j = \underline{\underline{B}}_i \cdot \underline{\nabla W}_j \\ if & |det(\underline{\underline{B}}_i)| < Btol \qquad W'_j = \underline{\nabla W}_j \end{cases} \tag{5.7}$$

It's important to emphasise that the renormalisation procedure, when applied to the pressure term of the motion equation, is particularly useful for enhancing the accuracy of flows characterised by slow dynamics and involving relatively large domains, as observed in wave generation scenarios in flumes.

5.2 SPH Simulation of Water Waves and Impact with a Rigid Offshore Structure in a 2D Flume

This enhancement in the single-phase model has finally enabled accurate modelling of regular waves. By reducing numerical dissipation, the waves are better able to maintain their height and velocity. This approach was validated across a wide spectrum of regular waves with varying characteristics, encompassing both short and long waves, and waves with different amplitudes. Eight regular waves with varying degrees of non-linearity, characterised by their steepness, were considered. The improved model successfully captured the behaviour of these waves. While regular waves serve as useful benchmarks for testing and validating numerical models, their relevance in real-world engineering applications is somewhat limited. In contrast, plunging or rogue waves, which greatly exceed the mean sea wave height, pose significant dangers to structures when they interact with the built environment. I began modelling these waves, generated using the focused theory. However, with the original model, components of waves in the higher frequency spectrum were not accurately reproduced. The improvements introduced now allow for the modelling of these high-frequency wave components as well. These findings were presented at the Thirty-first International Ocean and Polar Engineering Conference (ISOPE) in 2021, in a conference paper titled “SPH Simulation of Water Waves and Impact with a Rigid Offshore Structure in a 2D Flume," which details the methods and initial results obtained.

Proceedings of the Thirty-first (2021) International Ocean and Polar Engineering Conference **www.isope.org**
Rhodes, Greece, June 20 – 25, 2021

ISBN 978-1-880653-82-1; ISSN 1098-6189

SPH Simulation of Water Waves and Impact with a Rigid Offshore Structure in a 2D Flume

Nicolò Salis
University of Pavia
Pavia, PV, Italy

Alessandro Reali
University of Pavia
Pavia, PV, Italy

Min Luo
Ocean College Zhejiang University
Zhoushan, Zhejiang, China

Sauro Manenti
University of Pavia
Pavia, PV, Italy

ABSTRACT

Reliable offshore structural design deserves proper definition of the loads that a structure must bear during the life cycle. The characterization of the wave-induced action plays a key role in this context. Wave-wave interaction can cause non-linear phenomena leading to occasional wave heights much greater than the mean wave height in a sea state. When sea waves interact with an offshore structure, breaking and water sprays occur as well as two-phase flow due to air entrapment. Particle-based methods have been proven to be particularly suitable to mimic these phenomena.

This work illustrates the application of the Free/Libre and Open-Source Software (FOSS) code SPHERA v.9.0.0 (RSE S.p.A.) for the generation of regular waves, non-linear waves, and the wave impact with a fixed rigid offshore structure in a 2D wave flume. Obtained results are compared against laboratory experiments and results from other numerical models. The main advantages of the proposed modelling approach are pointed out and the aspects that deserve further improvement are discussed.

KEY WORDS:

SPH; Experimental Validation; Non-Linear Wave Generation; Offshore Structures; Wave Impact; Wave Load.

INTRODUCTION

The wave load is a key parameter in the design process to ensure reliability and longevity of offshore structures. Wave-structure interaction, is a highly complicated phenomenon as the impacting wave forces a movement to the structure which being partially constrained, generates an interference wave field. Furthermore, in the impact, wave breaking and large deformation of the continuum occur. Eulerian grid-based methods have been soundly adopted to simulate wave-structure interaction. Examples can be found in Stansberg et al. (2005) with the commercial code Flow-3D; Pákozdi et al. (2005) using the commercial code STAR CCM+; Yan et al. (2019) with a Navier-Stokes solver and Yan et al. (2020) using OpenFOAM. These highly non-linear phenomena are well estimated by means of Lagrangian particle-based methods, among which the Smoothed Particle Hydrodynamics (SPH) seems to be particularly well suited (Liu and Liu, 2003) and has therefore been recently applied to these phenomena. Gómez-Gesteira et al. (2005) analyzed green water overtopping a deck, finding the utilized SPH model to be quantitatively suitable for one-to-one comparison between numerical and experimental results. Lo and Shao (2002) adopting an Incompressible SPH (ISPH) method together with a Large Eddy Simulation (LES) successfully reproduced wave profiles of solitary wave against a vertical wall and running up a plane slope. In the matter of ISPH Liu et al. (2014) used a non-reflection internal wave maker to simulate waves and interaction with a solid wall and a submerged trapezoid backwater; the authors found that the non-reflection internal wave maker can be a quite robust tool for long time simulation of waves and wave-structures interaction. More recently Sun et al. (2019) simulated a freak wave impacting a fixed structure focusing on the suction stage. Altomare et al. (2020) simulated real sea wave impacting a large-scale structure with the open-source code DualSPHysics in a real-word engineering application. In order to test the capability of a numerical code and its accuracy, before simulating non-linear waves and wave-structure impact, it may be convenient starting with the generation of regular waves in a flume using the wavemaker theory (Biésel and Suquet, 1951). Ursell et al. (1960) investigated the regular wave generation in a flume adopting wavemaker theory for flap-type and piston-type wavemakers. Laboratory experiments focused on the wave steepness affecting the non-linear behavior of regular waves. The study results showed that the wavemaker theory is quite suitable to describe the height of small steepness generated waves whilst the amplitude is slightly overestimated for high steepness waves (non-linear effect). The experiments of Ursell et al. (1960) were reproduced adopting numerical codes in Huang et al. (1998) and in Anbarsooz et al. (2013). Huang et al. (1998) focused on the piston-type wavemaker for the simulation of non-linear wavefields. They developed a finite difference numerical method for solving the unsteady 2D Navier-Stokes equations where a modification of the SUMMAC method for treating the free-surface unknown variables was implemented. Their results are in good agreement for the low steepness waves whilst high steepness wave heights are slightly underestimated with respect to the experimental results. Anbarsooz et al. (2013) focused on laboratory experiments and numerical non-linear generation of regular waves for both piston-type and flap-type wavemaker. The used

model is a finite difference method where the Navier-Stokes equations are solved by a three-step projection method. The results are similar to Ursell et al. (1960) showing good agreement between simulations and experimental data. It is worth mentioning also the work of Lee et al. (2020), who investigated the SPH wave generation focusing on waves with short period, large relative depth, and large wave steepness. Lee's studies show that the wave tank with the mass-weighted damping zone is useful to accurately generate different waves, from linear to breaking waves. He et al. (2021) proposed a new theoretical method for the plunger-type wave maker. Results shows that solitary waves generated by plunger-type wave makers are of a comparable accuracy respect to the piston-type wave maker, provide that the plunger does not have sharp corners. Yan et al. (2019) studied the regular wave generation, non-linear wave generation, as well as the impact with a box-shaped structure. They performed laboratory experiments as well as numerical simulations, using a 2D two-phase Navier-Stokes solver with a set method (finite difference) while the structure was simulated with an improved immersed boundary method. Their results show that the front wall bears a larger impact pressure than the bottom wall. Pressure oscillations are detected due to the evolution of the air cavity. Numerical results are roughly in agreement with the experiments. Sun et al. (2018) presented a 2D two-phase δ+ Weakly Compressible Smoothed Particle Hydrodynamics (WCSPH). The δ+ correction term is a diffusive term which helps in reducing the high-frequency oscillations that usually affect the pressure field as a consequence of the weakly compressible assumptions. This numerical model was adopted in Sun et al. (2019) where they performed a numerical study on the waves presented in Yan et al. (2019). Sun et al (2019) focused on the implementation of a Tensile Instability Control (TIC) scheme preventing the occurrence of unphysical fluid voids. Results are validated through experimental data and are in good agreement. Impact pressures onto the structure are well represented by the numerical model, particularly the pressure oscillations in the suction stage.

This work is part of a wider study aiming at testing and validating the research computer code SPHERA v.9.0.0 (RSE S.p.A.) (2021) for the simulation of 2D water waves and wave impact on a fixed offshore structure. Simulations are performed using a 2D single-phase WCSPH model and the validation is carried out through analytical, experimental, and reference numerical results. The main advantages of the proposed modelling approach are pointed out, and aspects deserving further improvements are discussed, proposing remedial interventions on the source code. The paper is mainly subdivided into three parts: regular wave generation, non-linear wave generation, and impact against a fixed rigid box-shaped structure. In the first part, a parametric study on two types of waves is performed and eight waves with different period *T* from Ursell et al. (1960) are simulated. In the second part of the paper a freak wave is analyzed, while in the third part an early investigation on the impact with a box-shaped structure from Sun et al. (2019) is shown.

MATHEMATICAL FORMULATION OF THE SPHERA MODEL

SPHERA v.9.0.0 (RSE S.p.A.) (2021) is here used to solve the WCSPH approximation of the governing equations for a Newtonian fluid using the semi-analytic approach for solid walls (Di Monaco at al. 2011) and a scheme for solid bodies (Amicarelli et al., 2015) as boundary treatment schemes. The model solves, accordingly to standard WCSPH approach the following continuity equation, Eq. (1), and the momentum balance equation, Eq. (2):

$$\langle\frac{d\rho}{dt}\rangle_0 = \sum_b \rho_b\left(u_{b,j}-u_{0,j}\right)\left.\frac{\partial W}{\partial x_j}\right|_b \varpi_b + 2\rho_0 \int_{V_h'} \left[\left(\underline{u}_w-\underline{u}_0\right)\cdot\underline{n}\right]n_j\frac{\partial W}{\partial x_j}dx^3 + C_s \quad (1)$$

where the Einstein's notation is adopted to imply a summation over repeated indices, and C_s is introduced to represent a fluid-body interaction term. The notation "⟨⟩" indicates the SPH particle -discrete-approximation. According to Di Monaco et al. (2021), Amicarelli et al. (2015) and SPHERA (2021) the momentum balance formulation is:

$$\begin{aligned}\langle\frac{du_i}{dt}\rangle_0 = -\delta_{i3}g &+ \sum_b\left(\frac{p_b}{\rho_b^2}+\frac{p_0}{\rho_0^2}\right)W_b'm_b + 2\frac{p_0}{\rho_0} \\ &+ \int_{V_h'}\frac{\partial W}{\partial x_i}dx^3 \\ &- \nu_M\sum_b\frac{m_b}{\rho_0 r_{0b}^2}\left(\underline{u}_b-\underline{u}_0\right) \\ &\cdot\left(\underline{x}_b-\underline{x}_0\right)\left.\frac{\partial W}{\partial x_j}\right|_b - \nu_M\left(\underline{u}_w-\underline{u}_0\right) \\ &\cdot\int_{V_h'}\frac{1}{r_{0w}^2}\left(\underline{x}-\underline{x}_0\right)\frac{\partial W}{\partial x_i}dx^3 + \underline{a}_s\end{aligned} \quad (2)$$

where δ_{ij} is the Kronecker's delta, $\underline{a}_s$ represents an acceleration term due to the fluid body interactions, ν_M is the artificial viscosity (Monaghan 2005), m is the particle mass, and r_{0b} the relative distance between the computed particle (subscript 0) and the neighboring particle (subscript *b*). In Eq 1 and Eq 2 W is the kernel function, $\underline{u}$ is the velocity vector, p is the pressure, ρ is the fluid density, g is the modulus of gravity acceleration, $\underline{x}$ is the position vector and t time. The kernel support is truncated when it intersects the boundary that limits the computational domain filled by the fluid particles. To avoid this inconvenience, the semi-analytic technique is adopted for mimic solid boundaries. The summation is extended to all fluid particles with volume ϖ (subscript *b*) in the kernel support of the computed fluid particle (subscript *0*). The volume integral represents the boundary term, that is the convolution integral on the kernel's truncated portion with the fictitious outer volume V_h'; the subscript *w* denotes a generic frontier. Furthermore, n is the normal vector to the wall surface.

The system of equations is closed by the following linearized barotropic equation of state (EOS) for slightly compressible fluids:

$$p = c_{ref}^2(\rho-\rho_{ref}) \quad (3)$$

The artificial sound speed c is at least ten times higher than the maximum fluid velocity in order to guarantee a relative density variation at most equal to 1% (Monaghan 2005) and the subscript *ref* stands for the reference state. The wavemaker and the box-shaped structure are treated by the scheme of rigid body transport as a solid body, respectively with imposed kinematics and fixed kinematics. The time integration is performed by means of a second-order Leapfrog scheme. For further details on the code readers are referred to the code documentation (SPHERA (RSE S.p.A.) (2021)).

SIMULATION SET-UP

In this section, the Biésel transfer function is first presented, followed by a description of the regular wave generation for the parametric study and to reproduce the experiments by Ursell et al. (1960) with a constant still water depth of h=1 m. The second part of the section describes the inputs for the non-linear wave generation and the box-shaped structure wave-impact, as well as the input data for these experiments. In Biésel et al. (1951) the solutions of the analytical problems concerning different wave generators are presented. Given a particular wavemaker, a transfer function allows to link the wavemaker displacement to the generated wave amplitude. Considering the piston-type wavemaker as the upstream boundary condition in the wave boundary value problem, Biésel et al. (1951) found the following solution for the transfer function:

$$\frac{H}{S_0} = \frac{4\sinh^2(kh)}{\sinh(kh) + 2kh} \tag{4}$$

In Eq (4), H is the wave height, S_0 is the wavemaker stroke and kh is the relative depth, k is the wave number related to the wavelength L.

Regular Wave Generation

In Fig. 1 the adopted domain for the regular waves is sketched. The domain has a flat part and a sloped beach with 1/10 slope ratio to reduce wave reflection. This configuration has been carefully selected based on a previous study (Salis 2019) where the sloped beach is found to produce similar results to a flat bottom domain whilst reducing computational time.

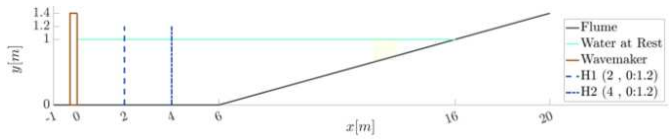

Figure 1: Wave flume with water at rest (regular waves).

The piston-type wavemaker is placed on the left-hand side of the flume. Two wave gauges H1 and H2 for measuring wave heights are positioned respectively at x_p= 2m and at x_p= 4m away from the wavemaker. Two wave types are generated, relevant characteristics are listed in Tab. 1. Wave types T1 and T2 serve to perform a parametric study that allows evaluating the influence of relevant model parameters, such as particle resolution, artificial viscosity, *CFL*, as well as the model convergence.

Table 1: Parameters Adopted for Simulating Regular Waves.

Wave	*T (s)*	*L (m)*	*S₀ (m)*	*kh*	*h (m)*	*H/L*	*H/S₀*
T1	1.13	1.99	0.1	2.14	1.00	0.097	1.195
T2	1.4	2.97	0.1	3.16	1.00	0.058	1.729

After some early simulations in Salis (2019), the following optimal set of numerical parameters has been defined: particle size dx=0.01m, artificial viscosity α_M=0.01, and *CFL*=0.2. The probe resolution of dx_p=0.0025m is found to be sufficiently accurate. Either the free-slip or the no-slip condition can be utilized. These parameters seem to guarantee a good compromise between numerical accuracy and computational cost with a run-time of approximately 18h for a simulation time of 20s on a machine with 2×18-core Intel Xeon E5-2697 v4 (Broadwell) @2.30 GHz, 128 GB of Ram. All simulations presented in this paper are executed on this machine. The optimal resolution, artificial viscosity and *CFL* parameters are then utilized to simulate the experiments by Ursell et al. (1960). To reproduce these waves, the same wave steepness (*H/L*), the same relative depth (*kh*), and the same wave height to stroke ratio (*H/S₀*) as seen in Ursell et al. (1960) are imposed. A constant still water depth (h) is adopted and therefore the wavemaker stroke S_0 and the wave period T are determined with the following procedure:

1. Knowing h and kh the wavelength L is obtained.
2. Given the wave steepness H/L the wave height H is determined.
3. The wavemaker stroke S_0 is determined with the wave height to stroke ratio H/S_0, Eq. (4).
4. The wave period T is determined with the dispersion equation knowing kh and L.

Once the stroke S_0 and period T have been determined for each testing wave, the time evolution of the wavemaker velocity can be obtained, Tab. 2 summarizes the relevant parameters for the studied waves.

Table 2: Regular waves parameters from Ursell et al. (1960)

Wave	*T (s)*	*L (m)*	*S₀ (m)*	*kh*	*h (m)*	*H/L*	*H/S₀*
Low steepness waves							
09	1.070	1.78	0.021	3.52	1.00	0.0488	1.970
13	1.294	2.58	0.022	2.44	1.00	0.0485	1.820
15	3.010	8.37	0.120	0.72	1.00	0.0439	0.700
17	1.785	4.42	0.032	1.42	1.00	0.0409	1.320
High steepness waves							
21	1.006	1.16	0.039	3.98	1.00	0.2300	1.990
22	1.264	2.46	0.065	2.55	1.00	0.1530	1.850
23	1.714	4.16	0.131	1.51	1.00	0.0094	1.390
24	2.152	5.76	0.225	1.09	1.00	0.0096	1.050

The input for each simulation is the wavemaker velocity and is determined with Eq. (5) where ω is the angular frequency and t is the time variable. Furthermore, the sinusoidal terms are multiplied by an exponential term to damp the wavemaker velocity at the beginning of simulation thus avoiding numerical instabilities due inertial effects.

$$u_x(t) = \frac{1}{2}S_0\omega \cdot \cos(\omega t) \cdot \left(1 - \exp\left(-\frac{t}{T}\right)\right) + \frac{S_0}{2}\sin(\omega t) \cdot exp^{\left(-\frac{t}{T}\right)}\Big/_T \tag{5}$$

The input velocity for each wave type described in Tab. 1 and Tab. 2 can be obtained from Eq. (5). Figure 2 shows the wavemaker displacement and velocity for wave-type 09 in Tab. 2.

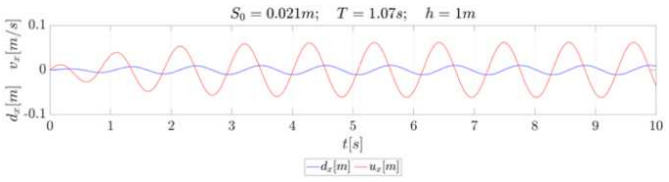

Figure 2: Wavemaker displacement and velocity for test case 09.

Non-linear Freak Wave Generation and Wave-Structure Impact

The non-linear wave to be simulated is generated with the focused wave theory as a superimposition of 32 linear wave components. Their crest meets simultaneously at a specific point, referred to as the focusing point, in space x_f and in time t_f, producing a large-amplitude wave which will develop into a plunging breaker subsequently (Yan et. al. 2019). The profile of the wave can be described as:

$$\eta(x,t) = \sum_{i=1}^{N} a_i \cos\left[k_i(x_p - x_f) - 2\pi f_i(t - t_f)\right] \qquad (6)$$

The wave has N =32 linear components. The *i-th* subscript index refers to each linear component. The amplitude a_i=0.0061m is constant throughout the frequencies which are equally spaced from f_{min} = 0.32Hz to f_{max} = 0.96Hz. The wavenumber k_i is computed, for each linear wave component with the dispersion equation (based on linear wave theory). The domain configuration is set accordingly to the freak wave test case with h=0.7m in Sun et al. (2019). The flume in Fig. 3 is a slight modification of the domain in Fig. 1, where the flat bottom has been extended whilst the beach slope ratio remains unchanged.

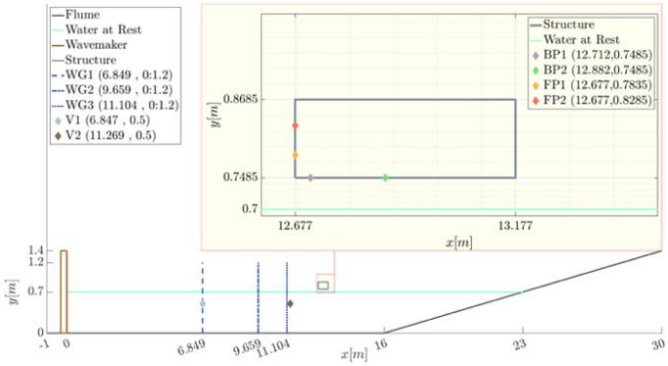

Figure 3: Wave flume with water at rest (freak wave).

Simulations are performed with the optimal particle resolution and artificial viscosity. The non-linear wave is first studied without the structure, thus allowing to keep control of the model results and to tune model parameters (e.g., artificial viscosity and particle resolution). The wave height is evaluated at the wave gauges WG1, WG2 and WG3 and the velocity is measured at the probes V1 and V2. Then the box-shaped structure is introduced for the analysis of wave-structure impact. Four additional probes have been added: BP1 and BP2 placed on the bottom of the structure; FP1 and FP2 placed on the front of the structure. Fig. 4 shows the time plot of the wavemaker input velocity utilized for all the simulations.

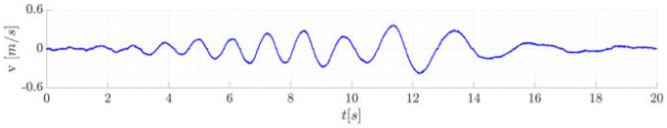

Figure 4: Experimental Wavemaker Velocity

ANALYSYS OF RESULTS

In this section, the results of the parametric study on regular wave generation in a numerical flume are first briefly discussed. Furthermore, the results relative to the modelling of the eight waves from Ursell et al. (1960) are analyzed. The second subsection, instead, deals with the results of the non-linear wave generation in a flume, and the section is concluded with the first insights of wave-structure impact reproducing the experiments of Sun et al. (2019).

Regular Wave Generation

The parametric study on wave types T1 and T2 is subdivided in an investigation on artificial viscosity, particle resolution, and the *CFL* convergence study. The influence of artificial viscosity to the model considers four values of artificial viscosity α_M: 0.01, 0.02, 0.03, and 0.06. Simulations are carried out with the optimal set of parameters (particle resolution dx=0.01m and the optimal CFL = 0.2).

Figure 5 shows the free surface elevation for wave T1 (upper panel) and T2 (lower panel) at wave gauge H1 compared with Biésel reference solution. It can be seen that the phase is well represented, while some wave height dissipation can be noticed. Such a wave height dissipation is more emphasized for wave type T1. Artificial viscosity seems to influence wave type T1 more than T2, and the top panel of Fig. 5 highlights that using a higher artificial viscosity gives more numerical dissipation.

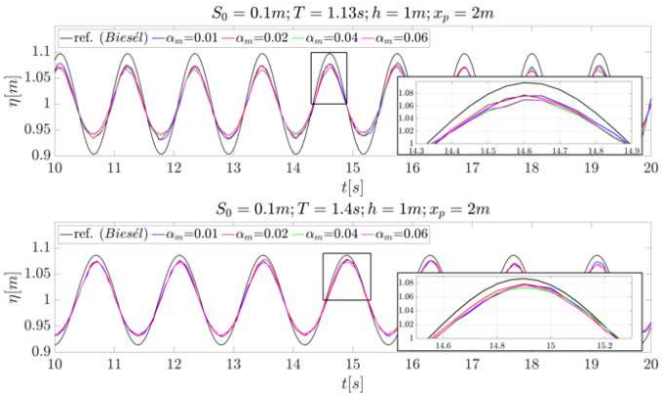

Figure 5: Artificial viscosity. Free surface comparison at x_p=2m.

Figure 6 reports the contour of velocity magnitude at t=15s of wave-type T2 for different values of artificial viscosity. Higher artificial viscosity shows, as said for Fig. 5, higher numerical dissipation.

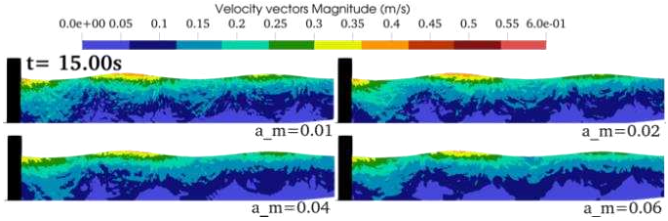

Figure 6: Artificial viscosity. Contour of velocity magnitude for wave-type T2.

In Fig. 7 the free surface elevation time plot at 4m from the wavemaker shows that the wave height reduction grows as the probe distance from the wavemaker is increased.

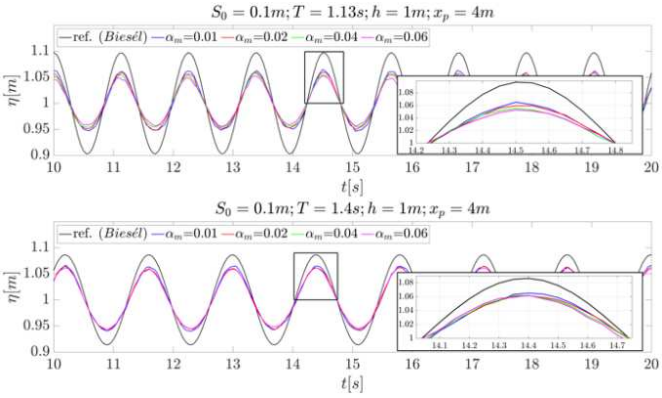

Figure 7: Artificial viscosity. Free surface comparison at x_p=4m.

Considering the reference solution of Biésel, wave heights are underestimated by the model. Numerical dissipation can be controlled (to some extent) by lowering the artificial viscosity and considering a lower artificial viscosity value seems appropriate for this purpose. However, further lowering the artificial viscosity gives noisy and less overall stable results. A first-order consistency scheme could help in reducing numerical dissipation for regular waves. Wave height dissipation could also be related to non-linear effects such as the wave steepness.

In Salis (2019), the particle dimension dx is set to be a multiple of the still water height thus avoiding errors in the free-surface position. Three particle sizes are investigated, since simulation run-time is highly dependent on the particle resolution through the numerical stability condition and significantly drops when particle size is increased. The simulation run time is 18h, 0.9h, and 0.38h, respectively, for particle dimensions dx=0.01m, dx=0.02m, and dx=0.025m and a constant simulation time of t=20s. The reference parameters for this study are α_M=0.01 and CFL=0.2.

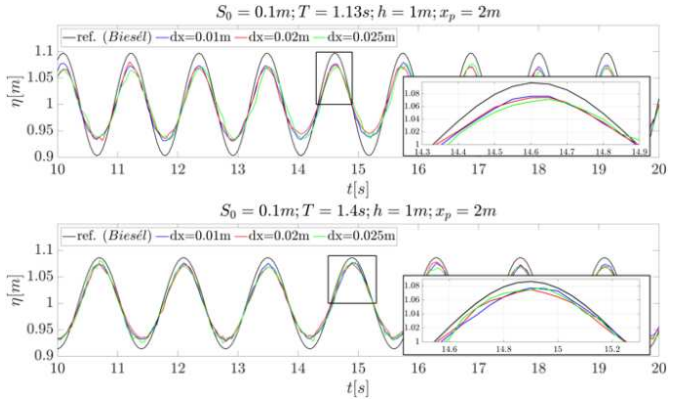

Figure 8: Particle resolution. Free surface comparison at x_p=2m.

All three investigated particle sizes in Fig. 8 give similar results, however, it can be seen that those from the higher resolution simulation are more regular and seem more consistent throughout the whole simulation time. As the resolution decreases, one can notice less consistency in wave height profiles, with a more pronounced wave height reduction as the particle dimension grows. Based on the present results, the most appropriate resolution is dx=0.01m.

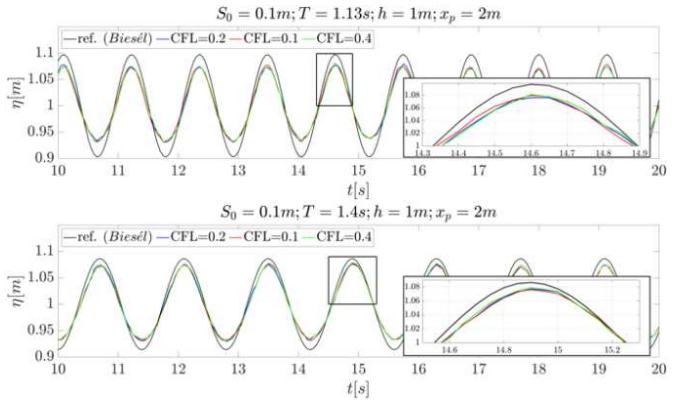

Figure 9: Temporal convergence. Free surface comparison at x_p=2m.

The temporal convergence of the model is studied by varying the CFL value. As CFL is doubled the simulation run-time is halved. The following different CFL values are considered: 0.1 with a run time of 36h, 0.2 with a run time of 18h, and 0.4 with a run time of 9h. Particle dimension and artificial viscosity remain constant at dx=0.01m, α_M=0.01. Figure 9 shows that, in the investigated range of values, the CFL condition does not significantly modify the simulation results. CFL=0.2 seems the most appropriate as it grants a suitable accuracy whilst reducing computational time.

Figure 10 shows the pressure contours at t = 10s in regular wave cases T1 and T2. Pressure fields in the two snapshots are generally smooth and there is not numerical noise. In the SPHERA model the diffusion term in the continuity equation is substituted by the partial smoothing of the pressure field (Di Monaco et al. (2011)).

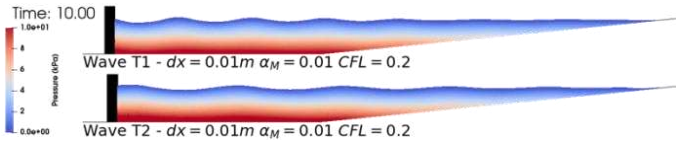

Figure 10: Pressure contours at t = 10s in two regular wave cases.

Since the model suffers from wave height dissipation it is worth investigating the non-linear aspects of regular waves to assess how much the numerical dissipation affects the model. To verify the SPHERA code eight waves from Ursell et al. (1960) are reproduced. All presented simulations are carried out with the optimal values of parameters: particle resolution dx=0.01m, artificial viscosity α_M=0.01, and CFL=0.2.

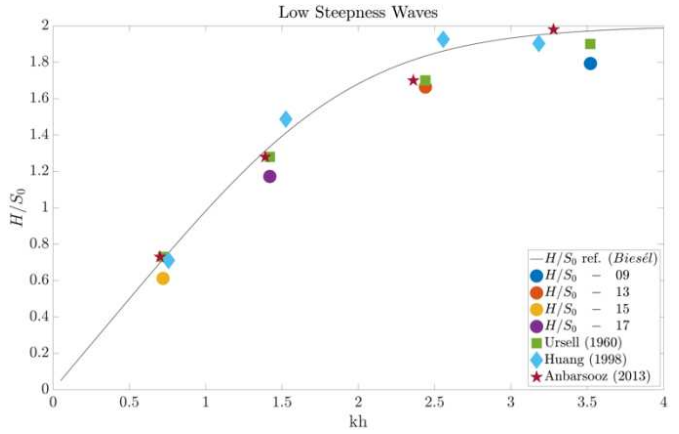

Figure 11:Wave height to stroke ratio vs. relative depth (low steepness waves). Probe at 2 m from the wavemaker.

Figure 11 shows the wave height to stroke ratio, i.e., H/S_0, in dependence of the relative depth kh for the low-steepness waves. It can be said that, on average, the wave to stroke ratios appear to be quite close to the reference solution and the experiments. For wave-type 13 simulation results are comparable with the experiments of Ursell et al. (1960) and Anbarsooz et al. (2013) whilst appearing a little far from the reference solution.

Figure 12 shows the wave height to stroke ratios for the simulated high steepness waves. For waves of higher relative depth (kh>2), the wave height to stroke ratio H/S_0 results underestimated. For lower relative depth waves (kh<2), H/S_0 results are very similar to literature results, whilst being underestimated with respect to the reference analytical solution. In Tab. 2, it can be seen that wave-types 21 and 22 have the higher frequency ($1/T$) than wave-types 23 and 24. As previously discussed for wave types T1 and T2, it can be observed that the wave

height numerical dissipation increases with the wave frequency. Based on the results for low and high steepness waves, the H/S_0 reduction with respect to literature data should be attributed to numerical dissipation.

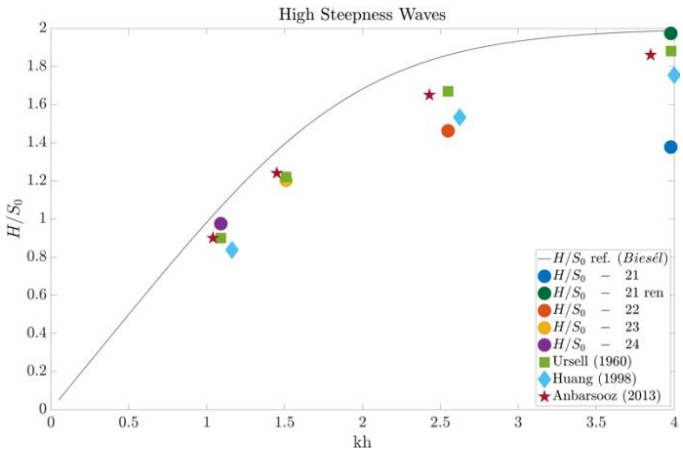

Figure 12: Wave hight to stroke ratio vs. relative depth (high steepness waves). Probe at 2 m from the wavemaker.

In general, the accuracy of the model in generating waves needs further improvement. A first order consistency scheme e.g., the renormalization scheme (Randles and Libersky, 1996; Johnson and Beissel, 1996; Vila 1999; Amicarelli et al. 2011) could damp numerical dissipation. In Fig. 12 the wave height to stroke ratio of wave type 21 is much lower than those of both experimental and others' numerical results. Figure 12 includes the results of a preliminary simulation (H/S_0 – 21 ren) adopting the renormalization scheme, indicated as "ren", (Randles and Libersky, 1996) for the momentum equation, i.e., Eq. (2). This result seems adequate for the early investigation of the non-linear wave and the impact on the fixed structure, presented in the following.

Non-Linear Wave Generation

Table 3 summarizes the adopted parameters for simulating the non-linear wave. It seems to be in general a good strategy to run test simulation with a low *CFL* value to ensure convergence; thus, run12 is assumed to be the reference simulation. In run11 and run10 the *CFL* is increased. Run10, despite a constant simulation time of t=20s, has a much lower computational run time (10h) than regular wave simulations (18h) mainly due to the lower number of particles contained in the computational domain (see Fig. 3).

Table 3: Summary of relevant parameters adopted for non-linear wave simulations.

2Dnlw	*dx [m]*	α_M	*CFL*	*slip*	Total elapsed time *[hh:mm:ss]*
10	0.01	0.02	0.2	free	10:35:36
11	0.01	0.02	0.1	free	21:01:09
12	0.01	0.02	0.05	free	43:02:45
13	0.007	0.02	0.05	free	234:56:06
14	0.007	0.01	0.05	free	242:51:20

When considering the higher particle dimension dx=0.01m the *CFL* value, in the investigated range does not seem to affect the simulation stability. However, if the particle dimension is reduced to dx=0.007 numerical instability appears. This instability can be controlled either by reducing *CFL*=0.05 or by increasing the artificial viscosity at a value higher than α_M=0.02. The adoption of *CFL*=0.05 allows reducing the artificial viscosity to α_M=0.01 with controlled numerical instability.

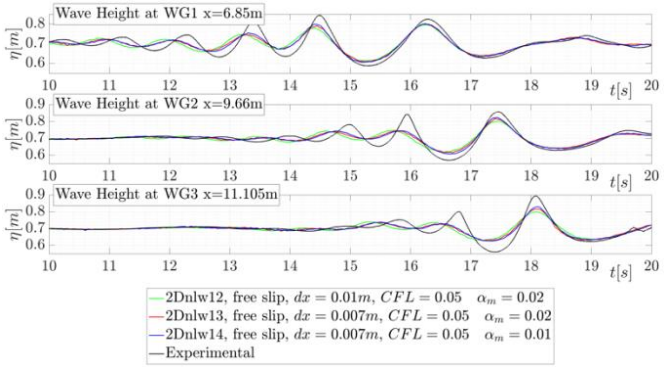

Figure 13: Non-linear wave elevation at WG1, WG2 and WG3.

Figure 13 shows the free surface time plot. At WG1 the wave height of the last crest, at about t=16.2s, is very close to the experimental wave height, while crests at early time are slightly underestimated. At gauges WG2 and WG3 the numerical dissipation of wave height is higher and increases with the distance of the gauge from the wavemaker. It should be noted that the phase of the simulated wave shows a delay with respect to the experimental result in all three gauges. In Fig. 13 it can be noticed the improvement in reproducing the wave height with respect to the reference simulation (run12). Improvement is obtained by increasing the particle resolution (run13) and combining the increased resolution with a lower artificial viscosity (run14). Particularly at WG1 the wave height increase is higher on the third and fourth crest. In WG2 and WG3 the wave height increase is significant in the last crest. The best result in term of simulating the experimental maximum wave height is obtained with run14. It can be noticed that for all three gauges the phase is again better represented by run14, with combined increased particle resolution and lowered artificial viscosity.

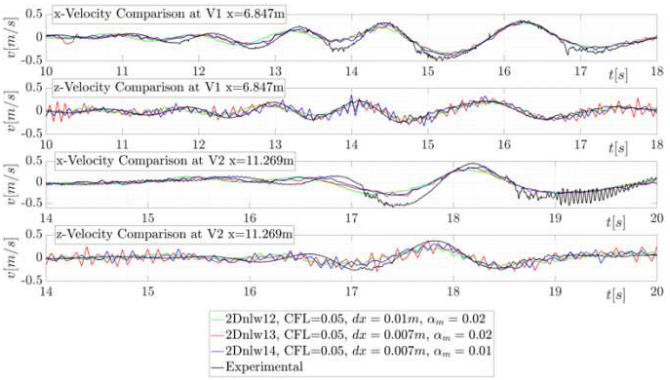

Figure 14: Non-linear wave velocity at V1 and V2.

The time histories of fluid velocity at the probes V1 and V2 in Fig. 14 shows that numerical dissipation affects the fluid velocity at V2 more than that at V1. The time plot of the x-velocity at both probes V1 and V2 is quite smooth while the z-velocity time plot appears to be affected by non-physical higher order oscillations. It is to be noted that the oscillation frequency increases in run13 and run14 with respect to run12. Figure 15 reports the contour of velocity magnitude at 18.0s, 18.5s, and 19s, respectively, for run12, run13, and run14. It can be seen that in the higher resolution simulations (e.g., run13 and run14) the highest crest is faster than that in the coarser-resolution simulation of run12. When the higher resolution is combined with the lower artificial viscosity (run14), velocity magnitude increases with respect to run12 and run13 of about 0.1 m/s in the higher crest.

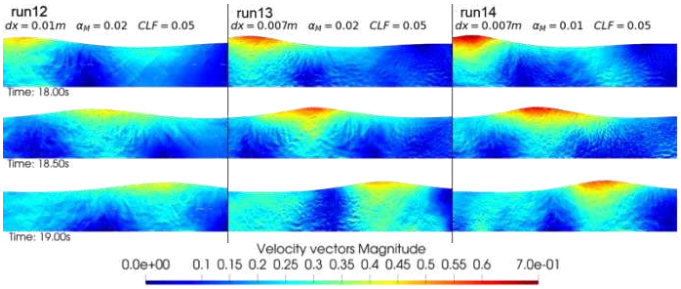

Figure 15: Contour of velocity magnitude at time 18s, 18.5s and 19s.

Figure 16 shows the wave height of a test simulation, executed with the proposed renormalization scheme. It can be seen that in the simulation with the renormalization scheme, the kinematics of the non-linear wave (height and phase) are more adherent to the experimental data.

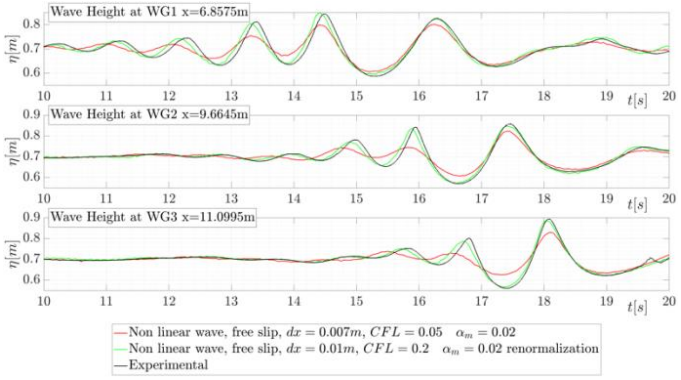

Figure 16: Wave elevations at WG1, WG2 and WG3 for the non-linear wave case.

Non-linear Freak Wave Impact on a Rigid Box-Shaped Structure

In this section, a preliminary investigation of wave-structure impact is briefly discussed.

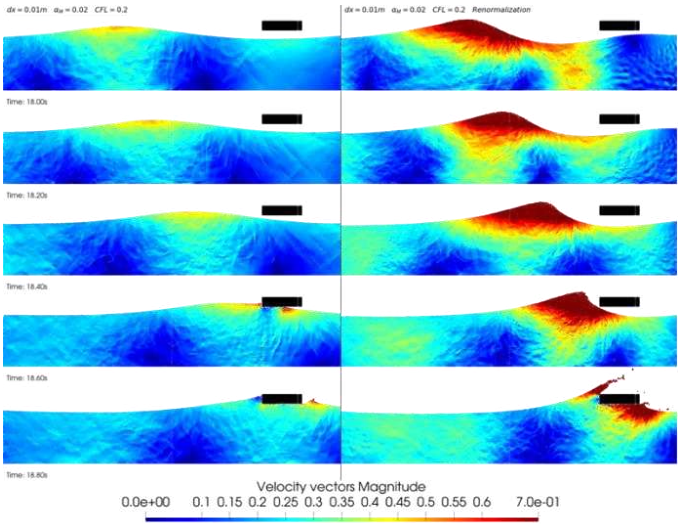

Figure 17: Contours of velocity magnitude at time instants close to and during the wave-structure interaction. Left panels: results without renormalization. Right panels: results with renormalization.

The relevant parameters are dx=0.01, α_M=0.02, CFL=0.2 with a free-slip boundary condition and a simulation time of t=20s; using such choices, numerical instability can be controlled while obtaining a suitable result accuracy and computational time of 10h. The contours of velocity magnitude in Fig. 17 show that the predicted velocity field is generally smooth. Moreover, when renormalization is applied, wave height and phase are better predicted and wave breaking is successfully captured (right hand panels).

CONCLUSIONS

The SPHERA code has been applied to simulate regular waves, a non-linear wave packet, and the wave impact on a fixed rigid structure. For the regular wave simulation, the phase is always well represented by the model. It is however to be noted that the model is affected by numerical dissipation, leading to a wave height reduction that increases with the probe distance from the wavemaker. Nevertheless, SPHERA results are in accordance with the literature data, in particular when simulating low steepness waves. The numerical dissipation seems larger in the simulation of regular waves of higher frequencies. However, numerical dissipation can be controlled via the renormalization scheme. The generated non-linear wave height is affected by numerical dissipation. Velocities are well represented and the z-velocity shows some oscillations (reason for which needs further investigation). A finer particle resolution gives better results, particularly when a smaller artificial viscosity is adopted. The simulation of freak wave impact on a rigid structure, thanks to the damping of numerical dissipation by the renormalization, produces reasonably good results. The adopted model allows obtaining a suitable accuracy and proper representation of both the linear and non-linear wave kinematics (i.e. wave height and phase) when including the renormalization procedure. These results demonstrate that SPHERA is promising in simulating ocean wave related problems. Reducing numerical dissipation is very important for this study, and this goal can be achieved through the renormalization scheme (Randles and Libersky, 1996; Johnson and Beissel, 1996; Vila, 1999; Amicarelli et al. 2011) to damp numerical dissipation. Future perspectives of this study are therefore the generalization of the 2D renormalization scheme in SPHERA and its validation. Concerning the non-linear wave impact onto the structure, pressure field representation needs to be improved. This task can be accomplished by subsequent steps with increasing complexity that will be considered in the future: (i) applying the renormalization scheme to the continuity equation; (ii) managing the tensile instability caused by negative pressure; (iii) including the air phase to account for the air cushion that affects the slamming pressure.

ACKNOWLEDGEMENTS

We acknowledge the CINECA award under the ISCRA initiative, for the availability of High Performance Computing resources and support". In fact, SPHERA simulations of the present study have also been financed by means of the following instrumental funding HPC projects: HPCNHLW2, HSPHER20, HSPHER21.

The partial support by the MIUR-PRIN project XFAST-SIMS (no. 20173C478N) is also gratefully acknowledged.

Finally, the authors would like to deeply thank Dr. Andrea Amicarelli (RSE S.p.A.) for several fruitful discussions on the topic of the present paper.

REFERENCES

Altomare, C., Tafuni, A., Domínguez, J. M., Crespo, A. J., Gironella, X., & Sospedra, J. (2020). SPH simulations of real sea waves impacting a large-scale structure. *Journal of Marine Science and Engineering*, *8*(10), 826.

Amicarelli, A., Marongiu, J.-C., Leboeuf, F., Leduc, J., Neuhauser, M., Fang, L., and Caro, J. (2011). SPH truncation error in estimating a 3d derivative. International journal for numerical methods in engineering, 87(7):677–700.

Amicarelli, A., Albano, R., Mirauda, D., Agate, G., Sole, A., & Guandalini, R. (2015). A Smoothed Particle Hydrodynamics model for 3D solid body transport in free surface flows. *Computers & fluids*, *116*, 205-228.

Anbarsooz, M., Passandideh-Fard, M., and Moghiman, M. (2013). Fully nonlinear viscous wave generation in numerical wave tanks. Ocean Engineering, 59:73–85.

Biesel, F., & Suquet, F. (1951). Les appareils générateurs de houle en laboratoire. *La houille blanche*, (2), 147-165.

De Padova, D., Dalrymple, R., Mossa, M., and Petrillo, A. (2009). SPH simulations of regular and irregular waves and their comparison with experimental data. arXiv preprint arXiv:0911.1872.

Di Monaco, A., Manenti, S., Gallati, M., Sibilla, S., Agate, G., & Guandalini, R. (2011). SPH modeling of solid boundaries through a semi-analytic approach. *Engineering Applications of Computational Fluid Mechanics*, *5*(1), 1-15.

Lo, E. Y., & Shao, S. (2002). Simulation of near-shore solitary wave mechanics by an incompressible SPH method. *Applied Ocean Research*, *24*(5), 275-286.

Gómez-Gesteira, M., Cerqueiro, D., Crespo, C., and Dalrymple, R. (2005). Green water overtopping analyzed with a SPH model. Ocean Engineering, 32(2):223–238.

He, M., Khayyer, A., Gao, X., Xu, W., & Liu, B. (2021). Theoretical method for generating solitary waves using plunger-type wavemakers and its Smoothed Particle Hydrodynamics validation. *Applied Ocean Research*, *106*, 102414.

Huang, C.-J., Zhang, E.-C., and Lee, J.-F. (1998). Numerical simulation of nonlinear viscous wavefields generated by piston-type wavemaker. Journal of engineering mechanics, 124(10):1110–1120.

Johnson, G. R., & Beissel, S. R. (1996). Normalized smoothing functions for SPH impact computations. *International Journal for Numerical Methods in Engineering*, *39*(16), 2725-2741.

Lee, S., & Hong, J. W. (2020). A Semi-Infinite Numerical Wave Tank Using Discrete Particle Simulations. *Journal of Marine Science and Engineering*, *8*(3), 159.

Liu, G. R., & Liu, M. B. (2003). *Smoothed particle hydrodynamics: a meshfree particle method*. World Scientific.

Liu, X., Lin, P., & Shao, S. (2015). ISPH wave simulation by using an internal wave maker. *Coastal Engineering*, *95*, 160-170.

Monaghan, J. J. (2005). Smoothed particle hydrodynamics. *Reports on progress in physics*, *68*(8), 1703.

Pákozdi, C., Österman, A., Stansberg, C. T., Peric, M., Lu, H., & Baarholm, R. (2015, July). Estimation of wave in deck load using CFD validated against model test data. In *The Twenty-fifth International Ocean and Polar Engineering Conference*. International Society of Offshore and Polar Engineers.

Randles, P. W., & Libersky, L. D. (1996). Smoothed particle hydrodynamics: some recent improvements and applications. *Computer methods in applied mechanics and engineering*, *139*(1-4), 375-408.

Salis, N. (2019). Numerical Modelling of Waves in a 2D Flume. Master's thesis, University of Pavia., Faculty of Engineering Department of Civil Engineering and Architecture.

SPHERA (RSE SpA) (2021). https://github.com/AndreaAmicarelliRSE.

Stansberg, C. T., Baarholm, R., Kristiansen, T., Hansen, E. W. M., & Rortveit, G. (2005, January). Extreme wave amplification and impact loads on offshore structures. In *Offshore Technology Conference*. Offshore Technology Conference.

Sun, P. N., et al. "Multi-resolution Delta-plus-SPH with tensile instability control: Towards high Reynolds number flows." *Computer Physics Communications* 224 (2018): 63-80.

Sun, P.-N., Luo, M., Le Touzé, D., and Zhang, A.-M. (2019). The suction effect during freak wave slamming on a fixed platform deck: Smoothed particle hydrodynamics simulation and experimental study. Physics of Fluids, 31(11):117108.

Ursell, F., Dean, R. G., and Yu, Y. (1960). Forced small-amplitude water waves: a comparison of theory and experiment. Journal of Fluid Mechanics, 7(1):33–52.

Vila, J. P. (1999). On particle weighted methods and smooth particle hydrodynamics. *Mathematical models and methods in applied sciences*, *9*(02), 161-209.

Wang, W., Kamath, A., Pakozdi, C., and Bihs, H. (2019). Investigation of focusing wave properties in a numerical wave tank with a fully nonlinear potential flow model. Journal of Marine Science and Engineering, 7(10):375.11.

Windt, C., Davidson, J., Schmitt, P., and Ringwood, J. V. (2019). On the assessment of numerical wave makers in CFD simulations. Journal of Marine Science and Engineering, 7(2):47.

Yan, B., Luo, M., and Bai, W. (2019). An experimental and numerical study of plunging wave impact on a box-shape structure. Marine Structures, 66:272–287.

Yan, M., Ma, X., Bai, W., Lin, Z., & Li, Y. (2020). Numerical Simulation of Wave Interaction with Payloads of Different Postures Using OpenFOAM. *Journal of Marine Science and Engineering*, *8*(6), 433.

5.3 Final remarks

The model has now been validated to accurately reproduce both regular waves and focused plunging waves. In Figure 17 of the initial paper, the first attempt to model a wave-structure impact was depicted. However, the initial results of this phenomenon were slightly unstable. Furthermore, it became evident that something crucial was missing from the model. The inclusion of the air phase is essential for a comprehensive modelling of the physical phenomena involved. Recognizing this necessity, I commenced the development of a high-density ratio multiphase scheme.

6

Development of a high density ratio multiphase scheme

This chapter delineates the numerical intricacies of a Free and Open Source Software (FOSS) derived code, accomplished by incorporating significant modifications into the original SPHERA v.9.0.0 (RSE SpA) code.

6.1 Introduction

Extensive modifications were made to the original SPHERA v.9.0.0 model. Henceforth, the multiphase model will be referred to as derived model. Analyzing the impact of waves on structures and the induced loads is inherently complex due to air entrapment between the wavefront and the structure. Figure 6.1 illustrates the instability at the interface observed during the simulation of a hydrostatic case with a different Weakly Compressible Smoothed Particle Hydrodynamics (WCSPH) model [53]. Two main factors contribute to this instability: the discontinuity of both density and pressure derivatives at the interface.

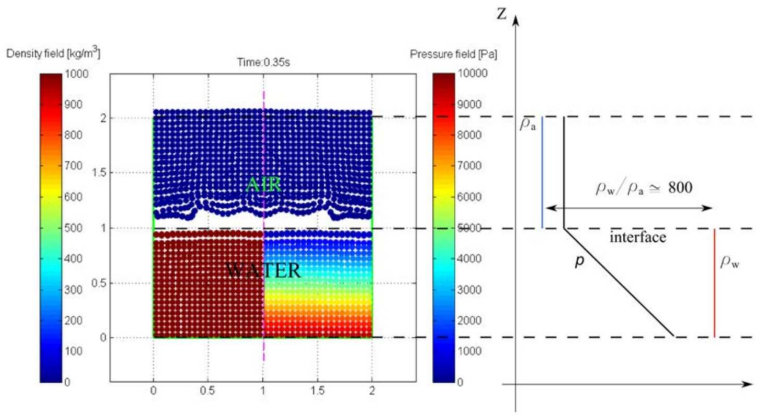

Figure 6.1: SPH numerical instability in still water. [53]

Numerous models in the technical literature have been proposed to address these issues [54, 55, 53, 52]. Each of these models employs different approaches to mitigate instabilities at the fluid interface. Herein, a relatively simple and accurate alternative approach is presented to eliminate instabilities caused by the high density discontinuity. The strategy involves replacing particle density with particle volume in the kernel summation. While density is discontinuous at the interface, particle volume remains continuous (assuming there is no multi-particle resolution). Pressure and viscous terms in the momentum balance equation must be accordingly modified. For the pressure term in the momentum equation, a symmetric formulation with volume-weighted summation is implemented. Initial results reveal some residual instabilities associated with the pressure field. Therefore, pressure smoothing, based on Shepard filtering, is replaced by a diffusive term in the continuity equation, which provides greater stability. These aforementioned modifications were incorporated into the original SPHERA v.9.0.0 code.

6.1.1 Two-phase WCSPH Formulation

Several two-phase WCSPH models for high density ratio have been proposed in the technical literature. Colagrossi et al. [54] presented a simple model for treating interfacial flows, while Grenier et al. [55] introduced a new Hamiltonian interface SPH formulation that achieved good agreement between simulations and reference results [53]. Rezavand et al. [56] proposed a new standard WCSPH by substituting the density (which is discontinuous at the interface) with the inverse of the particle volume inside the kernel summation. Colagrossi et al. [52] overcame WCSPH instabilities by solving a Riemann problem at the interface. Additionally, based on the approach of Grenier et al. [55], they found a new formulation of WCSPH with the continuity equation written in terms of evolving volume rather than density. In standard WCSPH, there are two alternative approaches that may lead to different discretisations of the continuity and momentum equation [57]. Equation (6.1) illustrates the application of the SPH approximation, considering only the velocity divergence.

$$\frac{D\rho_i}{Dt} = \rho_i \sum_j \frac{m_j}{\rho_j} \underline{u}_j \cdot \nabla W \tag{6.1}$$

Considereing the partition of kernel in Eq.(6.2) allows to write Eq. (6.3).

$$\nabla 1 = \int 1 \nabla W = \sum_j \frac{m_j}{\rho_j} \cdot \nabla W = 0 \tag{6.2}$$

$$\rho_i \sum_j \frac{m_j}{\rho_j} \underline{u}_i \cdot \nabla W = \rho_i \underline{u}_i \sum_j \frac{m_j}{\rho_j} \cdot \nabla W \tag{6.3}$$

Adding Eq. (6.3), which is zero, to the right hand side of (6.1) gives Eq. (6.4) which represents the first approach to obtain the continuity equation.

$$\frac{D\rho_i}{Dt} = \rho_i \sum_j \frac{m_j}{\rho_j} (\underline{u}_j - \underline{u}_i) \cdot \nabla W \tag{6.4}$$

The second approach, which is the most widely used for defining the continuity equation, is represented by Eq. 6.6. This approach is also employed in the Smoothed Particle Hydrodynamics (SPH) approximation of the continuity equation in the official release of SPHERA, and it relies on the identity presented in Eq. 6.5.

$$-\rho \nabla \underline{u} = -(\nabla(\rho \underline{u}) - \underline{u} \cdot \nabla \rho) \tag{6.5}$$

$$\frac{D\rho_i}{Dt} = \rho_i \sum_j m_j (\underline{u}_j - \underline{u}_i) \cdot \nabla W \tag{6.6}$$

This last approach allows us to “hide" the density of the neighbouring particles. Thus, the summation of relative velocities is weighted with the mass of the neighbouring particle. For a single-phase scenario, this is not a problem since the particle mass is constant across the entire domain. However, for two-phase simulations, the mass differences between particles can be very high, as is the case with water and air.

Taking a step back and not applying the identity in Eq. 6.5 leads to the relative velocity being multiplied by the neighbor’s mass over the density, i.e., the volume, which is continuous, as shown in Eq. 6.4. With this formulation of the continuity equation, it is possible to treat two-phase flows with high-density ratios. This continuity equation must be in accordance with the momentum equation. Similarly to (6.6), the most widely used momentum equation, where $\underline{\underline{\sigma}}$ is a generic stress tensor, is given by Eq. 6.7.

$$\frac{D\underline{u}_i}{Dt} = \sum_j m_j \Big(\frac{\underline{\underline{\sigma}}_i}{\rho_i^2} + \frac{\underline{\underline{\sigma}}_j}{\rho_j^2} \Big) \cdot \nabla W \tag{6.7}$$

This formulation (Eq. 6.7) is obtained by applying the following identity Eq. 6.8.

$$-\frac{1}{\rho} \nabla \underline{\underline{\sigma}} = -\Big(\nabla \Big(\frac{\underline{\underline{\sigma}}}{\rho} \Big) + \frac{\underline{\underline{\sigma}}}{\rho^2} \nabla \rho \Big) \tag{6.8}$$

Also in this case, it is found that the stress tensor is “weighted" with mass, which is not ideal for simulating two fluids with a high density ratio and is not compatible with (6.4). Without the substitution of these mathematical identities

(Eqs. 6.5 and 6.8), the continuity and momentum equations are valid for treating two phases with a high density ratio. Further details can be found in [57] and [58]. Based on the above developments, the standard SPH balance equations can be written as shown in Eq. (6.9).

$$\begin{cases} \frac{d\rho_i}{dt} = \rho_i \sum_j \frac{m_j}{\rho_j} \cdot (\underline{u}_j - \underline{u}_i) \cdot \nabla W = \rho_i \sum_j V_j (\underline{u}_j - \underline{u}_i) \cdot \nabla W \\ \frac{d\underline{u}_i}{dt} = \sum_j m_j \frac{\underline{\underline{\sigma}}_i + \underline{\underline{\sigma}}_j}{\rho_j \rho_i} \nabla W = \frac{1}{\rho_i} \sum_j \frac{m_j}{\rho_j} (\underline{\underline{\sigma}}_j + \underline{\underline{\sigma}}_i) \nabla W = \frac{1}{\rho_i} \sum_j V_j (\underline{\underline{\sigma}}_j + \underline{\underline{\sigma}}_i) \nabla W \end{cases} \tag{6.9}$$

The new two-phase model is obtained by modifying the original Eqs. (5.1) and (5.2) according to Eq. (6.9). The continuity equation of the model is therefore given by Eq. (6.10). This formulation needs to accommodate the semi-analytic approach for boundary treatment [46]. The formulation of integral terms for the semi-analytic boundary treatment does not encounter any issues since the particle mass doesn't appear in the fluid-body interaction terms, which depend solely on the geometry of boundaries.

$$\begin{aligned} \left\langle \frac{d\rho}{dt} \right\rangle_i = & \sum_j \rho_i (u_j - u_i) \cdot \nabla W \frac{m_j}{\rho_j} \\ & + 2\rho_i \int_{V_h'} [(\underline{u}_w - \underline{u}_i) \cdot \underline{n}] \underline{n} \cdot \nabla W dx^3 + C_s \end{aligned} \tag{6.10}$$

The momentum balance equation is modified accordingly, resulting in Eq. (6.11), which represents the new two-phase momentum balance equation. The only altered terms are the pressure term and the artificial viscosity term. The pressure term remains symmetric but now incorporates the volume rather than the mass in the neighbour summation.

$$\begin{aligned} \left\langle \frac{du_i}{dt} \right\rangle_i = & -\delta_{i3} g + \frac{1}{\rho_i} \sum_j (p_j - p_i + p_r) \nabla W \frac{m_j}{\rho_j} + 2\frac{p_i}{\rho_i} \int_{V_h'} \frac{\partial W}{\partial x_i} dx^3 + \\ & - \rho_{0in} \cdot \upsilon_m \sum_j \frac{m_j}{\rho_j} \frac{1}{r_{ij}^2} (\underline{u}_j - \underline{u}_i) \cdot (\underline{x}_j - \underline{x}_i) \nabla W + \\ & - 2\upsilon_m (\underline{u}_w - \underline{u}_i) \cdot \int_{V_h'} \frac{1}{r_{0_w}^2} (\underline{x} - \underline{x}_i) \nabla W dx^3 + \underline{a}_s + \\ & + 2\nu_i (\underline{u}_w - \underline{u}_i) \int_{V_h'} \frac{1}{r} \frac{\partial W}{\partial r} dx^3 \end{aligned} \tag{6.11}$$

The artificial viscosity term has also been modified. Now, the artificial viscosity is calculated only if the neighbouring particle and the computational particle 0 belong to the same phase.

$$\upsilon_m = \frac{\alpha \cdot h \cdot c}{\rho_i} \tag{6.12}$$

The factor υ_m is adjusted in accordance with [52], resulting in Eq. (6.12), where ρ_{0in} is the initial density of particle 0, c is the velocity of the medium, h is the smoothing length, and α is the Monaghan alpha parameter ranging between 0.01 and 0.1 depending on the specific simulation case.

6.1.2 Diffusive Term

In WCSPH, the pressure field requires numerical treatment to avoid non-physical noise. This is due to the weakly compressible assumption and the fact that pressure is computed with a stiff equation of state, meaning small changes in density result in high pressure changes. In SPHERA, the noisy pressure field is addressed with pressure smoothing:

$$p_i = p_i + \theta \sum_{b=1}^{N} \Delta P \frac{\nabla W}{r_{ij}} \tag{6.13}$$

Here, θ is defined as:

$$\theta = \theta_p c_i \frac{dt}{h} \tag{6.14}$$

where θ_p is a user-defined constant ranging between 0.1 and 0.3, c_i is the sound speed of the medium, dt is the time step, and h is the smoothing length.

To apply pressure smoothing, three loops are required: two loops over all particles and one nested loop over the neighbours of the computational particle 0. It's important to note that pressure smoothing is not applied every time step. However, this method is robust and yields good results.

In some WCSPH models [59, 60], this method is replaced by the addition of a diffusive term in the continuity equation:

$$D_i = 2\delta c_i h \sum_{b=1}^{N} \psi_{ij} \frac{r_{ij} \cdot \nabla W}{\|r_{ij}\|^2} V_j \tag{6.15}$$

The diffusive term must satisfy Eq. 6.16 for consistency with global mass conservation [60]:

$$\sum_i D_i V_i = 0 \qquad \psi_{ij} = -\psi_{b0} \tag{6.16}$$

This approach is more robust and less computationally demanding than pressure smoothing. The definition of the term ψ_{ij} affects the formulation. The formulation by [59] is simple:

$$\psi_{ij}^{Mol} = \rho_j - \rho_i \tag{6.17}$$

However, it leads to non-physical behaviour in certain scenarios characterised by slow particle motion and long-time dynamics, such as sloshing problems and gravity wave propagation.

The formulation by [60] is stable and consistent with both hydrostatic and dynamic cases:

$$\psi_{ij}^{Ant} = \rho_j - \rho_i - \frac{1}{2}(\langle \nabla \rho \rangle_j^L + \langle \nabla \rho \rangle_i^L) \cdot r_{ij} \tag{6.18}$$

$$\langle \nabla \rho \rangle_i^L = \sum_j (\rho_j - \rho_i) \underline{\underline{L}}_i \cdot \underline{\nabla W}_i \frac{m_j}{\rho_j} \tag{6.19}$$

The formulation proposed by [60] is preferred because it is compatible with slow dynamics and long simulation times. This is demonstrated in [61], where after a long simulation time, particles near the free surface spread and rise above the expected free surface.

6.2 Wave Generation and Wave–Structure Impact Modelling with WCSPH

The multiphase model was initially tested by reproducing a dam break scenario. It's important to highlight that renormalisation was not compatible with the dam break simulation and was consequently disabled. However, renormalisation was consistently applied for computing the diffusive term in the continuity equation. The results of the multiphase dam break simulation were quite accurate. Nevertheless, the model exhibited instabilities at the interface, primarily stemming from tensile instability and the formation of numerical voids.

Given the extensive changes in the governing equations compared to those of SPHERA v.9.0.0, the model required a new round of study and validation in single-phase scenarios. The selected cases for validating the new model were the eight regular waves and the plunging wave-structure impact. It's noteworthy that renormalisation in these cases could also introduce instabilities. To address this, a limiter was applied to the renormalisation process. The limiter, a constant, determined whether renormalisation was applied based on the determinant of the $\mathbf{B}$ matrix. This approach enabled the use of renormalisation while avoiding both numerical dissipation and instabilities.

The results of these validations are detailed in the paper titled "Wave generation and wave–structure impact modelling with WCSPH," published in the journal Ocean Engineering.

Ocean Engineering 266 (2022) 113228

Contents lists available at ScienceDirect

Ocean Engineering

journal homepage: www.elsevier.com/locate/oceaneng

Wave generation and wave–structure impact modelling with WCSPH

Nicolò Salis [a,*,1], Min Luo [b,2], Alessandro Reali [a,c,3], Sauro Manenti [a,c,4]

[a] Department of Civil Engineering and Architecture DICAr, University of Pavia, via Ferrata 3, Pavia, 27100, Italy
[b] Ocean College, Zhejiang University, Zhoushan, 316021, Zhejiang, China
[c] Water Research Center CRA, University of Pavia, via Ferrata 3, Pavia, 27100, Italy

ARTICLE INFO

Keywords:
WCSPH
Wave–structure impact
Dam break
Regular wave
Non-linear wave
Wave generation
Wave breaking
Multiphase SPH

ABSTRACT

The reliable prediction of plunging wave induced load, which represents a challenging task in offshore engineering, is of key relevance for the safety of existing offshore structures as well for the reliable design of new ones. This work shows the early advances in the development of a FOSS derived model, obtained by independently introducing relevant modifications in the original model SPHERA v.9.0.0 (RSE SpA) based on the Weakly Compressible Smoothed Particle Hydrodynamics (WCSPH) method. This derived model is validated on single-phase laboratory flume tests from technical literature (i.e., dam break and regular waves) and on a laboratory flume test of plunging wave impacting an offshore structure. The derived model allows modelling two-phase flows with a large density ratio, as shown by an additional two-phase dam break simulation. Therefore it seems promising for application to two-phase plunging impact to improve the prediction of impact load on the structure.

1. Introduction

In recent years, the world has seen the increase of the frequency in climate-generated calamities as well as of the severity of the induced consequences. For this reason, wave height and slamming forces acting on offshore structures are meant to grow, and thus the issue of their safety is strategic and deserves to be carefully analysed on the basis of expected changes. This is even more important considering the fact that the offshore structure population is considerable and more structures are being built. Even if some climate change models are being developed to forecast the relevant characteristics of wave forcing, reliable wave load prediction on the offshore structure is very challenging. The phenomenon is highly non-linear, because of the impulsive interaction between water, air and a structure with complex geometry.

1.1. Modelling approaches in literature

Experimental campaigns are quite expensive and can still have some intrinsic uncertainties related to scale effects (Johnson, 1949). Empirical methods may be unsuitable when applied to cases that strongly differ from those for which these methods have been obtained. In this framework, numerical modelling may be more versatile and can represent a trade-off between effort and accuracy, overcoming the limitations due to scale effects, but they need calibration and validation making use of experimental results. The numerical modelling of wave generation and structure interaction may be carried out following several approaches, each one with its own advantages and disadvantages. Eulerian grid-based methods are the most widely used computational fluid dynamics (CFD) tool in engineering (Liu and Liu, 2003). Wave generation and wave–structure interaction have been investigated widely with Eulerian grid-based methods. Stansberg et al. (2005) simulated wave-deck impacts with a commercial Volume-of-Fluid (VOF) tool (Flow-3D), achieving promising results of load time series against test data. Pákozdi et al. (2015) studied wave-deck loads on a gravity-based structure caused by 5th order Stokes regular waves in a laboratory model, the air–water simulation being carried out with a commercial model (STAR CCM+), solving a VOF method that accounts for wave breaking and air entrapment. Both Stansberg et al. (2005) and Pákozdi et al. (2015) reported that greater loads are generated by non-linear waves. Recently, Yan et al. (2020), used the open-source model OpenFOAM to study the non-linear interaction of regular waves with floating payloads. However, modelling free surface flows

* Corresponding author.
E-mail addresses: nicolo.salis01@universitadipavia.it (N. Salis), min.luo@zju.edu.cn (M. Luo), alessandro.reali@unipv.it (A. Reali), sauro.manenti@unipv.it (S. Manenti).
[1] Ph.D. Student.
[2] Research Professor, Ph.D..
[3] Professor of Solid and Structural Mechanics, Ph.D..
[4] Associate Professor of Fluid Mechanics, Ph.D..

https://doi.org/10.1016/j.oceaneng.2022.113228
Received 4 October 2022; Received in revised form 13 November 2022; Accepted 17 November 2022
Available online 28 November 2022

Notation

Subscript 0	Computational particle.
Subscript b	Neighbour of the computational particle 0.
ρ	Density of the neighbouring. (kg m^{-3})
t	Time variable. (s)
$\underline{u}$	Velocity vector. (m s^{-1})
∇	Gradient operator.
W	Kernel function.
ϖ	Particle volume. (m^3)
$\underline{n}$	Normal vector to the wall surface.
V_h'	Fictitious wall boundary volume.
C_s	Fluid-body interaction term (continuity equation).
$\underline{g}$	Gravitational acceleration vector. (m s^{-2})
p	Particle pressure. (Pa)
υ_m	Artificial viscosity multiplication term.
m	Particle mass. (kg)
r_{0b}	Distance between computational and neighbouring particle. (m)
$\underline{x}$	Particle position. (m)
$\underline{a}_s$	Acceleration term due to fluid-body interactions. (m s^{-2})
α	Artificial viscosity factor. (–)
h	Smoothing length. (m)
c_s	Artificial sound speed (celerity). (m s^{-1})
$\underline{\underline{B}}_0$	Neighbour concentration matrix on computational particle.
$\underline{\underline{L}}_0$	Renormalization matrix on computational particle.
$\overline{\nabla W}$	Kernel gradient.
$\overline{\widetilde{\nabla W}}$	Renormalized Kernel gradient.
λ	Renormalization threshold value. (–)
δ_{i3}	Kronecker's delta function.
θ	Multiplying factor for pressure smoothing. (–)
ΔP	Pressure variation. (Pa)
D_0	Diffusive term in the continuity equation.
δ	Multiplying factor for the continuity diffusive term. (–)
ψ	Continuity diffusive summation term. (–)
$\nabla \rho_0^B$	Renormalized density gradient.

with an Eulerian approach introduces some challenging aspects to be handled, such as boundary conditions to determine the free surface, simulation of jets, sprays and wave breaking. Large grid distortion that may occur can affect the solution accuracy, and therefore it must be properly treated with expensive re-meshing techniques. Owing to its intrinsic properties, Lagrangian particle methods have proven to be a reliable tool for the simulation of free surface flows with impacts (Luo et al., 2021). The lack of any topological connection between particles allows to model large and rapid deformation of the domain, fluid splitting and particle coalescence. The Lagrangian formulation of the fluid governing equations lacks the advection terms, thus avoiding numerical diffusion and making particle methods more suitable to model advection-dominated flows. Furthermore, the particle discretization allows tracking implicitly fluid interfaces when dealing with multiphase interaction problems. Among Lagrangian particle methods, the Smoothed Particle Hydrodynamics (SPH) provides a good framework for the analysis of free surface impulsive flows (Monaghan, 2005; Gomez-Gesteira et al., 2010; Lind et al., 2020; Lyu et al., 2022). SPH allows the straightforward inclusion of a different medium to study multiphase flows (Manenti, 2018; Colagrossi et al., 2020; Gu et al., 2022; Gong et al., 2016). SPH has proven to be suitable for generating regular and non-linear waves in a Numerical Wave Tank (NWT) using either a plunging wave-maker (He et al., 2021), or a piston-type wave-maker (Lee et al., 2020), or an internal wave-maker algorithm (Liu et al., 2015) or via the interaction with external rigid or deformable bodies (Gallati et al., 2005), such as landslides (Manenti et al., 2018). Also SPH techniques have been proved suitable to investigate wave-impacts. Lo and Shao (2002) adopted ISPH with Large Eddy Simulation (LES) to reproduce near-shore solitary waves and impacts with vertical and sloped walls. Gómez-Gesteira et al. (2005) simulated the impact of a single wave with a flat horizontal deck finding results that both qualitatively and quantitatively match experimental results, although the used particle dimension was quite rough. Altomare et al. (2020) applied the open-source model DualSPHysics to a real-scale engineering application simulating a sea wave impacting the "Pont del Petroli" deck. Results showed higher forces than those considered in design phase and demonstrated the failure mechanism that led to severe damage of the piers.

1.2. Purpose of this research

The contributions introduced by this research are summarized in the following. An alternative standard WCSPH formulation to treat multiphase flows with high-density ratio is proposed. To the authors knowledge this research shows for the first time a thorough SPH analysis of the generation and propagation of a wide variety (from low to high steepness) of regular waves in a flume. Furthermore, a reliable tool has been set up for the investigation of non-linear waves in a flume with impact load to a marine structure providing accurate results using a single-phase approach. The work contributes to the development and validation of a FOSS model. The FOSS model here described "Derived code" (2022) is obtained by independently introducing relevant modifications in the original model (SPHERA v9.0.0 (RSE SpA), 2022) to obtain stable and accurate simulations of the analysed problems. An alternative formulation of the continuity and momentum equation is proposed where the kernel summation is weighted by the particle volume that, unlike the density, is continuous at the air–water interface. For the same reason, the momentum equation is reformulated adopting a symmetric formulation of the pressure term. Renormalization of kernel derivatives is also adopted to avoid excessive numerical dissipation of wave energy (Gomez-Gesteira et al., 2010). The computed renormalization matrix allows to replace Shepard filtering in the continuity equation with a diffusive term which is suitable even for slow-dynamics (Molteni and Colagrossi, 2009; Antuono et al., 2010). The model is validated, thus showing its capability to simulate the relevant aspects of these flows, although some aspects still need further study to improve the model. The layout of the paper is the following: the relevant modifications introduced into the original model (SPHERA v9.0.0 (RSE SpA), 2022) to obtain the (Derived code, 2022) are described; then, the benchmarks performed to validate the model are introduced; simulation results are illustrated and discussed; finally, conclusions are drawn.

2. Mathematical formulations

This section illustrates the relevant modifications introduced into the original model (SPHERA v9.0.0 (RSE SpA), 2022) to obtain the (Derived code, 2022) for application to non-linear wave generation and impact onto a fixed structure.

2.1. Original model

This subsection briefly recalls the governing equations for a Newtonian fluid of the original model SPHERA v.9.0.0 (RSE S.p.A.) that were modified to obtain the derived model described in the following subsection. The adopted boundary treatment schemes are the semi-analytic approach for solid walls (Di Monaco et al., 2011) and the scheme for solid bodies (Amicarelli et al., 2015). These schemes are reported in Section 2.1.1. Other numerical schemes of SPHERA that were not used in this work are described in Amicarelli et al. (2020) and the user guide of SPHERA (SPHERA v9.0.0 (RSE SpA), 2022).

$$\begin{aligned}\left\langle \frac{d\rho}{dt} \right\rangle_0 &= \sum_b \rho_b \left(\underline{u}_b - \underline{u}_0\right) \cdot \nabla W \varpi_b \\ &+ 2\rho_0 \int_{V'_h} \left[\left(\underline{u}_\gamma - \underline{u}_0\right) \cdot \underline{n}\right] \left(\underline{n} \cdot \nabla W dx^3\right) \\ &+ C_s\end{aligned} \tag{1}$$

$$\begin{aligned}\left\langle \frac{d\underline{u}}{dt} \right\rangle_0 =& \underline{g} + \sum_b \left(\frac{p_b}{\rho_b^2} + \frac{p_0}{\rho_0^2}\right) \nabla W m_b \\ &+ 2\frac{p_0}{\rho_0} \int_{V'_h} \nabla W dx^3 \\ &- \upsilon_m \sum_b \frac{m_b}{r_{0b}^2} \left(\underline{u}_b - \underline{u}_0\right) \cdot \left(\underline{x}_b - \underline{x}_0\right) \nabla W \\ &- \upsilon_m \left(\underline{u}_\gamma - \underline{u}_0\right) \cdot \int_{V'_h} \frac{1}{r_{0_\gamma}^2} \left(\underline{x} - \underline{x}_0\right) \nabla W dx^3 \\ &+ \underline{a}_s + 2\nu_0 \left(\underline{u}_\gamma - \underline{u}_0\right) \int_{V'_h} \frac{1}{r} \left|\frac{\partial W}{\partial r}\right| dx^3\end{aligned} \tag{2}$$

$$\upsilon_m = \frac{\alpha \cdot h \cdot \widetilde{c}}{\widetilde{\rho}} \tag{3}$$

Eq. (1) is the continuity equation where C_s is introduced to represent the fluid-body interaction term. The notation "⟨⟩" indicates the SPH particle -discrete- approximation; Eq. (2) is the momentum balance formulation, where: $\underline{a}_s$ represents an acceleration term due to the fluid body interactions. υ_m is the artificial viscosity, which mimics the physical viscosity of water providing consistent and accurate results, and it is defined in Eq. (3) (Monaghan, 2005) where $\widetilde{\rho} = 2\rho_0 h$, $\widetilde{c} = 2c_i$ and c_i is the medium celerity; h is the smoothing length, α is the Monaghan parameter ranging between 0.01 and 0.1 depending on the simulated case study. m is the particle mass, and r_{0b} the relative distance between the computational particle (subscript 0) and the neighbouring particle (subscript b). In Eqs. (1) and (2) W is the kernel function, $\underline{u}$ is the velocity vector, p is the pressure, ρ is the fluid density, $\underline{g}$ is the gravity acceleration, $\underline{x}$ is the position vector and t is the time variable. The summation is extended to all fluid particles with volume ϖ (subscript b) that are in the kernel support of the computed fluid particle (subscript 0). The kernel support becomes truncated when it intersects the boundary surface. To avoid this inconvenience, the semi-analytic technique is adopted for mimic solid boundaries (Section 2.1.1). $\underline{n}$ is the normal vector to the wall surface. The system of equations is closed by the following linearized barotropic equation of state (EOS) for slightly compressible fluids:

$$p = c_{ref}^2 \left(\rho - \rho_{ref}\right) + p_0 \tag{4}$$

The artificial sound speed c must be assumed at least ten times higher than the maximum fluid velocity in order to assure a relative density variation at most equal to 1% (Monaghan, 2005); the subscript ref stands for the reference state. In WCSPH approximation, the pressure is computed with a stiff equation of state where small changes in density correspond to high pressure variations. Therefore, the pressure field requires numerical treatment to avoid numerical noise. In SPHERA v9.0.0 a pressure smoothing is applied based on Shepard filtering according to Eq. (5).

$$p_0 = p_0 + \theta \sum_{b=1}^{N} \Delta P \frac{\nabla W}{r_{0b}} \tag{5}$$

θ is defined in Eq. (6) where θ_p is a user defined parameter ranging between 0.1 and 0.3, dt is the time step.

$$\theta = \theta_p c_0 \frac{dt}{h} \tag{6}$$

To apply the pressure smoothing three loops are needed: two loops over all particles and one nested loop over the neighbours of the computational particle 0. It is worth noting that the pressure smoothing is not applied on every time step. Moreover, it can be said that this method is robust and give good results. For a complete description of the model features, readers are referred to the model documentation (SPHERA v9.0.0 (RSE SpA), 2022).

2.1.1. Boundary conditions

Solid walls are treated with the semi-analytic approach (Vila, 1999). The inner domain is filled with particles while at the boundaries the kernel support is not truncated and it can partially lie outside the fluid domain. The boundary contributions, owing to the semi analytic approach in Eqs. (1) and (2) are expressed through the integral terms. These terms represent the convolution integral on the portion of the kernel support V'_h that lies outside of the domain. Flow variables e.g. pressure, velocity and density are linearized accordingly to Di Monaco et al. (2011). Eq. (7) shows the linearization for the pressure and density. Values of these "$_{SA}$" functions are assigned to represent a null normal gradient of reduced pressure at the frontier interface (Amicarelli et al., 2020).

$$\begin{aligned}p_{SA} =& p_0, \quad \left\langle \frac{\partial p}{\partial x_i} \right\rangle_{SA} = \underline{g} \\ \rho_{SA} =& \rho_0, \quad \left\langle \frac{\partial \rho}{\partial x_i} \right\rangle_{SA} = 0\end{aligned} \tag{7}$$

The velocity vector is considered uniform outside of the domain. At the boundary, the velocity vector is divided in normal $\underline{u}_{SA,n}$ and tangential $\underline{u}_{SA,\tau}$ components. The normal component is expressed as a linearization of the fluid particle velocity, the tangential component is set equal to the analogous vector of the computational particle (subscript 0). Eq. (8) shows such linearization where subscript γ refers to a generic domain frontier.

$$\begin{aligned}\underline{u}_{SA,n} =& [(2\underline{u}_\gamma - \underline{u}_0) \cdot \underline{n}]\underline{n} \\ \underline{u}_{SA,\tau} =& \underline{u}_{0,\tau}, \quad \left\langle \frac{\partial u_i}{\partial x_i} \right\rangle_{SA} = 0 \\ & therefore \\ \underline{u} - \underline{u}_0 =& \underline{u}_{SA} - \underline{u}_0 = 2[(\underline{u}_\gamma - \underline{u}_0) \cdot \underline{n}]\underline{n}\end{aligned} \tag{8}$$

In Eqs. (1) and (2), the terms C_s and $\underline{a}_s$ account for fluid-body interaction respectively. This scheme has been firstly introduced by Adami et al. (2012) and in this research is used to model the wavemaker in the cases of wave generation and the structure in the case of wave–structure impact. This method can be interpreted as a discretization of the semi analytic approach. The outer domain is not truncated but filled with the body particles. Eq. (9) shows the fluid-body interaction term for the continuity equation. This represents a discretization of the analogues semi-analytic term for the solid boundary contribution. Eq. (10) shows the acceleration introduced by the fluid–solid interface, which influences the estimation of body particle pressure. The subscript s refers to the generic neighbouring surface body particle. Amicarelli et al. (2015)

$$C_s = 2\rho_0 \sum_s [(\underline{u}_s - \underline{u}_0) \cdot \underline{n}_s] \nabla W_s \varpi_s \tag{9}$$

$$\underline{a}_s = \sum_s \left(\frac{p_s + p_0}{\rho_0^2}\right) \nabla W_s m_s \tag{10}$$

Further details on the derivation of boundary conditions can be found in Di Monaco et al. (2011) and Amicarelli et al. (2015, 2020). Moreover, it is worth noting that these schemes apply also to the "Derived code" (2022).

2.1.2. Time propagation scheme

A second-order Leapfrog scheme is used to integrate in time the governing equations. Amicarelli et al. (2020)

$$\begin{aligned}\underline{x}_{|t+dt} &= \underline{x}_{|t} + \underline{u}_{|t+dt/2}dt \\ \underline{u}_{|t+dt/2} &= \underline{u}_{|t-dt/2} + \left\langle \frac{d\underline{u}}{dt} \right\rangle\Big|_t dt \\ \rho_{|t+dt} &= \rho_{|t} + \left\langle \frac{d\rho}{dt} \right\rangle\Big|_{|t-dt/2} dt\end{aligned} \tag{11}$$

Eq. (12) shows the stability criteria for the time integration.

$$dt = min_0\left\{0.05\frac{2h^2}{\nu}; CFL\frac{2h}{c+|\underline{u}|}\right\} \tag{12}$$

The described integration scheme is used without modification in the (Derived code, 2022).

2.2. Derived model

This subsection reports the independent modifications introduced in the original WCSPH model (SPHERA v9.0.0 (RSE SpA), 2022) to obtain the (Derived code, 2022). These modifications are introduced in the governing equations adopting the standard WCSPH formulation which suffer from some intrinsic problems when simulating two fluids with large density ratio. Several two-phase WCSPH models have been proposed in the literature in order to overcome these problems. Colagrossi and Landrini (2003) presented a relatively simple and effective model to treat interfacial flows. Grenier et al. (2009) introduced a new Hamiltonian interface SPH formulation obtaining good agreement between simulations and reference results. Manenti et al. (2018) proposed a new standard WCSPH substituting the density (discontinuous at the interface) with the inverse of the particle volume inside the kernel summation. Rezavand et al. (2020) overcame the instabilities of WCSPH by solving a Riemann problem at the interface. Colagrossi et al. (2020), based on the approach of Grenier et al. (2009), introduced a new formulation where the continuity equation is written evolving volume rather than density. Writing the continuity and momentum equation in a proper formulation (see for instance Liu and Liu (2003), Violeau (2012)), the following equivalent discretized WCSPH equations can be obtained:

$$\begin{aligned}\left\langle \frac{d\rho}{dt} \right\rangle_0 &= \sum_b \rho_0 \left(\underline{u}_b - \underline{u}_0\right)\cdot\nabla W\frac{m_b}{\rho_b} \\ &+ 2\rho_0\int_{V'_h}\left[\left(\underline{u}_\gamma - \underline{u}_0\right)\cdot\underline{n}\right]\underline{n}\cdot\nabla W dx^3 \\ &+ C_s\end{aligned} \tag{13}$$

$$\begin{aligned}\left\langle \frac{d\underline{u}}{dt} \right\rangle_0 &= \underline{g} + \frac{1}{\rho_0}\sum_b \left(p_b - p_0\right)\nabla W\frac{m_b}{\rho_b} \\ &+ 2\frac{p_0}{\rho_0}\int_{V'_h}\nabla W dx^3 \\ &- \rho_{0in}\upsilon_m\sum_b \frac{m_b}{\rho_b}\frac{1}{r_{0b}^2}\left(\underline{u}_b - \underline{u}_0\right)\cdot\left(\underline{x}_b - \underline{x}_0\right)\nabla W \\ &- 2\upsilon_m\left(\underline{u}_\gamma - \underline{u}_0\right)\cdot\int_{V'_h}\frac{1}{r_{0_\gamma}^2}\left(\underline{x} - \underline{x}_0\right)\nabla W dx^3 \\ &+ \underline{a}_s + 2\nu_0\left(\underline{u}_\gamma - \underline{u}_0\right)\int_{V'_h}\frac{1}{r}\left|\frac{\partial W}{\partial r}\right| dx^3\end{aligned} \tag{14}$$

Eqs. (13)–(14) are suitable to perform stable simulations of multi-phase flows with high density ratio because the kernel summation is carried out assuming the particle volume instead of their mass which varies abruptly between the phases leading to unbalanced fictitious forces. Therefore, the (Derived code, 2022) is obtained by modifying (SPHERA v9.0.0 (RSE SpA), 2022) mass and momentum balance Eqs. (1) and (2). The integral terms of the semi analytic boundary treatment depend solely on the geometry of boundaries, not on the particle mass. Therefore, in the momentum balance equation the only modified terms are the pressure term and the artificial viscosity term. The pressure term is still symmetric but the kernel summation is carried out on particle volume rather than on mass. The artificial viscosity term has been modified to obtain particle b volume instead of mass.

$$\upsilon_m = \frac{\alpha\cdot h\cdot c}{\rho_{0in}} \tag{15}$$

The υ_m factor defined in (3) is modified in accordance with Colagrossi et al. (2020) becoming Eq. (15), where ρ_{0in} is the initial density of the particle 0. In order to reduce non-physical dissipation of both wave-height and velocity which are more pronounced for slow dynamic phenomena, a kernel derivative renormalization is adopted to obtain first order consistency of the kernel function. This technique was first introduced in Randles and Libersky (1996) and Vila (1999), and has been utilized since then, with minor modifications, in free surface flows with slow dynamics. In most recent applications (Gomez-Gesteira et al., 2010; Antuono et al., 2010; Sun et al., 2019b; Antuono et al., 2012; Colagrossi et al., 2020) the renormalization is used to compute the density gradient for the diffusive term in the continuity equation (see following). Since this technique may be applied to the renormalization of the SPH gradient of several flow variables, such as p, ρ and $\underline{u}$, the general formulation (16) if given for the generic variable f.

$$\langle\nabla f\rangle_0 = \left\langle\frac{\partial f}{\partial\underline{x}}\right\rangle_0 \equiv \sum_b \left(f_b - f_0\right)\left(\underline{\underline{L}}_0\cdot\underline{\nabla W}_b\right)_i\frac{m_b}{\rho_b} \tag{16}$$

The renormalization matrix $\underline{\underline{L}}_0$ is defined by the formulation in Eq. (17) which is valid inside the fluid and at its boundary surface. According to Randles and Libersky (1996), the sign of $\underline{\underline{B}}_0$ is positive when the renormalization is applied to the continuity equation and the diffusive term, while it is negative for the momentum balance equation.

$$\underline{\underline{L}}_0 = \underline{\underline{B}}_0^{-1} = \left(\pm\sum_b \left(\underline{x}_b - \underline{x}_0\right)\underline{\nabla W}\frac{m_b}{\rho_b}\right)^{-1} \tag{17}$$

Hereafter the normalized kernel derivative, when the renormalization scheme is activated, will be defined as in Eq. (18) and it replaces the kernel gradient in the summations of Eqs. (13) and (14).

$$\widetilde{\underline{\nabla W}}_b = \underline{\underline{L}}_0\cdot\underline{\nabla W}_b \tag{18}$$

The renormalization is used in the pressure term of the momentum balance equation, in the continuity equation applied to the kernel gradient and for the diffusive terms (see following). To calculate $\underline{\underline{L}}_0$ a key parameter is the determinant of matrix B_0, which is always different from zero but can get very close to zero, because its value is proportional to the concentration of neighbouring particles. If this happens, the pressure term in the momentum balance equation may become unstable. For this reason, renormalization is carried out with a conditional statement through Eq. (19), introducing a threshold value λ for the matrix determinant.

$$\begin{cases}|\underline{\underline{B}}_0| \geq \lambda & \rightarrow \quad \widetilde{\underline{\nabla W}}_b \quad replace \quad \underline{\nabla W}_b \\ |\underline{\underline{B}}_0| < \lambda & \rightarrow \quad keep \quad \underline{\nabla W}_b\end{cases} \tag{19}$$

The parameter λ is chosen heuristically to achieve stability. In the investigated problems it has been found that values lower than $\lambda = 0.4$ create instabilities. Results presented in Salis et al. (2021) adopted $\lambda = 0.6$ which represents a good compromise between accuracy and stability. It is worth remarking that the renormalization procedure, applied to the continuity equation, is useful to improve the accuracy of those flows with slow dynamics and involving relatively large domain, as in the case of wave generation in the flume. In some WCSPH models the Shepard filtering is substituted by a diffusive term (Eq. (20) in the continuity equation), similarly to the artificial viscosity (Molteni and Colagrossi, 2009; Antuono et al., 2010).

$$D_0 = 2\delta c_0 h\sum_{b=1}^{N}\psi_{0b}\frac{r_{0b}\cdot\nabla W}{\|r_{0b}\|^2}V_b \tag{20}$$

To assure the consistency with the global mass conservation, the diffusive term must satisfy the following condition (Antuono et al., 2010) to enforce that the summation of the diffusive terms D_0 on all particles is zero:

$$\sum_0 D_0 V_0 = 0 \qquad \psi_{0b} = -\psi_{b0} \tag{21}$$

The adoption of diffusive term in the continuity equation can be more robust and less computationally demanding than the pressure smoothing. Its definition depends on the formulation of the term ψ_{0b}. Molteni and Colagrossi (2009) suggested a quite simple formulation given by Eq. (22):

$$\psi_{0b}^{Mol} = \rho_b - \rho_0 \tag{22}$$

The major benefit of this formulation is its low computational cost, since no extra loop is needed for computing this term. The drawback of this formulation is the incompatibility with the hydrostatic solution that leads to a non-physical motion of the fluid particles. This issue also affects those phenomena characterized by a slow particle motion and a long-time dynamics as, for example, sloshing problems and gravity wave propagation. The formulation by Antuono et al. (2010) is given in Eq. (23)

$$\psi_{0b}^{Ant} = \rho_b - \rho_0 - \frac{1}{2}\left(\langle\nabla\rho\rangle_b^L + \langle\nabla\rho\rangle_0^L\right)\cdot r_{0b} \tag{23}$$

$$\langle\nabla\rho\rangle_0^L = \sum_b \left(\rho_b - \rho_0\right)\underline{\underline{L}}_0 \cdot \nabla W_0 \frac{m_b}{\rho_b} \tag{24}$$

This formulation is stable and consistent with the hydrostatic and dynamic cases. In the latter case the re-normalization is needed to compute the density gradient at the computational particle 0 and its neighbour b. Computationally it is less expensive than the pressure smoothing as it needs only one extra loop to compute the renormalized density gradient in Eq. (24). Nevertheless, in the present work the formulation of Antuono et al. (2010) is adopted since it is compatible with slow dynamics and guarantees stability at the free surface.

3. Results and discussion

The derived model is first validated on two laboratory flume tests from technical literature: the dam break and the regular waves. Results are compared to the original model to show improvements. The results of simulation where is employed the original model, SPHERA v9.0.0 (RSE SpA) (2022), are referred to as "SPHERA-master".[5] Then the derived model, hereafter referred to as "Present model" is validated on a laboratory flume test of plunging wave impacting an offshore structure which is simulated neglecting air phase at this early stage of development. It is worth noting that derived model allows modelling two-phase flows with large density ratio, as shown by the two-phase dam break simulation illustrated in the subsequent section.

3.1. Dam break

The dam break test case is widely adopted to test numerical models. In technical literature, there is wide availability of reference results for comparison. The interest to this test case concerns the relative simple set up and implementation and the low computational cost. For the above-mentioned reasons the dam break is here used to validate the derived code considering both single and two-phase simulations. Obtained results are compared with SPHERA-master to show improvements. SPHERA v9.0.0 (RSE SpA) has already been validated to reproduce dam-break test cases (Amicarelli et al., 2020) and allows a straightforward comparison with the present model. Fig. 1 shows the domain for the dam-break test case (Zhou et al., 1999). The domain has a length of 3.22 (m) and a height of 1.8 (m). The water body in the left-hand side of the domain is 0.6 (m) deep and 1.2 (m) long. In the domain there are three gauges: water gauge 1 (WG1) and water gauge 2 (WG2) which measure the water height or the interface location for two-phase simulations; the third gauge is a pressure gauge (pg) located on the downstream vertical wall at a height of 0.16 (m). The initial condition consists of water column at rest with hydrostatic pressure distribution. The water body is free to collapse under gravity force inside the domain. The wave propagates on a dry bed with free slip conditions. For the multiphase simulation no boundary condition is applied on the air free surface. The closed top condition has been momentarily excluded to avoid non-physical pressure in the air phase due to particle settlement. The same numerical parameters are assumed in the master and the independently derived model. The particle dimension is $dx = 0.005$ (m) for single-phase simulations, while for the multiphase simulation is $dx = 0.01$ m. The Monaghan's parameter is $\alpha = 0.02$ and the $CFL = 0.05$ to ensure convergence. The artificial sound speed, defined by Eq. (25a), is set to $c = 54.77$ (m s^{-1}), since the expected highest fluid velocity is $\approx$5 (m s^{-1}). The ratio between the sound speed of air and water can be obtained with Eq. (25b) and the sound speed in the air phase should always be higher than that in water (Manenti, 2018). The adopted air artificial sound speed is $c_a = 699.85$ (m s^{-1}).

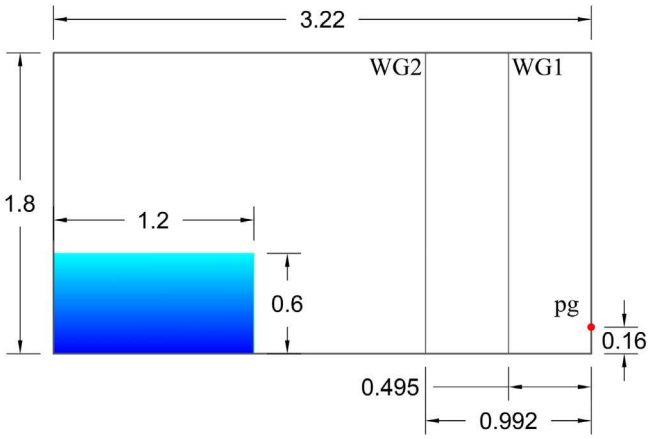

Fig. 1. Dam-break simulation set-up.

Table 1
Dam-break run time.

Code	Particles	Pressure	Run time (hh:mm:ss)	Simulated time (s)
SPHERA-master	28 800	Shepard filtering	02:54:18	4.00
Present model	28 800	δ-SPH (Antuono)	04:46:22	4.00
Present model multiphase	57 960	δ-SPH (Antuono)	86:16:51	4.00

$$c = \sqrt{\frac{\rho}{k}} \tag{25a}$$

$$\frac{c_a}{c_w} = \sqrt{0.2\frac{\rho_w}{\rho_a}} \tag{25b}$$

In the simulations performed with SPHERA-master the pressure smoothing parameter is set to $\theta_p = 0.25$ while in the present model is used $\delta = 0.1$. Table 1 shows the run time and simulated time. The simulations presented in this paragraph are carried out on the HPC cluster available at the Department of Mathematics of the University of Pavia, equipped with 68 cores (Intel(R) Xeon(R) Gold SkyLake 6130 CPU @ 2.10 GHz) and 128 Gb of memory. The high number of air particles combined with the high artificial sound speed results in high simulation time in Table 1.

[5] All simulations are held with commit b443656 published on 29 Mar 2021.

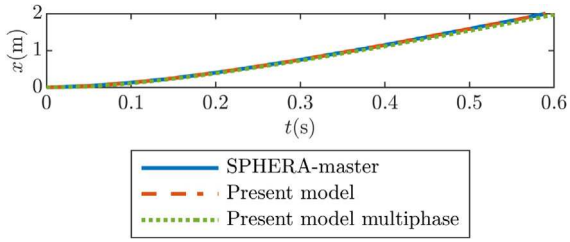

Fig. 2. Dam-break wave-front kinematics.

Fig. 2 shows the comparison of wave-front evolution for the dam break simulations. The ordinate shows the water tongue position after the water column collapse. The abscissa show the physical time until the downstream wall impact. This figure shows negligible differences between the curves. The wave fronts advance with the same speed in single-phase simulations while the multiphase wave front is slightly slower due to the presence of the air particles that are accelerated by the leading water front.

Fig. 3 shows the pressure and magnitude velocity contour plots. Single-phase results are quite similar with each other, the pressure contours are slightly different due to the different pressure treatment and may present some oscillation owing to the media compressibility. There are negligible changes in the contour and shape for the single-phase and the multiphase model. The wave front impacts the downstream wall at the same time (t = 0.59 (s)); the maximum water height at the downstream wall is the same and the reflected wave impact occurs almost simultaneously (t = 1.47 (s)) with a negligible change. The generated spray (t = 1.80 (s)) is also similar. Negligible difference in the shape of the air pocket can be observed. The multiphase model shows good results of pressure and velocity contours. Although some transient instabilities, the multiphase model is stable and produces acceptable results.

Fig. 4 shows the free surface elevation at the two water gauges. WG1 is closer to the right-hand side wall than WG2. The recorded free surface at WG1 (Fig. 4(a)) is similar to the experimental curve from t = 0.5 (s) to t = 1.5 (s). After that time, the simulated water height rises to the maximum value before the experimental curve while reaching similar height. The air–water interface, reaches similar height to the single-phase model at t = 1.5 (s). Between t = 1.5 (s) and t = 2 (s) the two-phase interface is lower than the single-phase height. From t = 2 (s) the simulated water height start descending in all simulations, showing a higher slope than the experimental curve. From t = 2.5 (s) the water height shows a second relative peak which is more pronounced for the single-phase simulations. From this time on, the multiphase model interface reproduces better the experimental height of this second peak. At WG2 (Fig. 4(b)) the trends of the simulated free surface is closer to the experimental curve. It is worth noting that just after the time t = 1.5 (s) the single-phase simulated water height grows faster and higher than the experimental water height. In the same time interval, the trend of the multiphase model, allows obtaining an interface height which is lower than the single-phase and is much closer to the experimental data. This behaviour can be explained by the fact that, during the descending phase of the water tongue, a cavity is progressively formed inside the backward plunging wave. The compressibility of the entrapped fluid affects the wave front dynamics (Colagrossi and Landrini, 2003). In the single-phase models, where there is no air inside the cavity, the collapse of plunging wave is faster than in the two-phase model, where the collapse of the backward plunging wave is slightly damped by the entrapped air cushion which is going to be compressed by the plunging wave; hence, the obtained surface elevation at WG2 is closer to the experimental data. This can also be noticed in Fig. 3 at t = 1.99 (s) where the wave elevation evolution which is obtained with the multiphase model is lower than

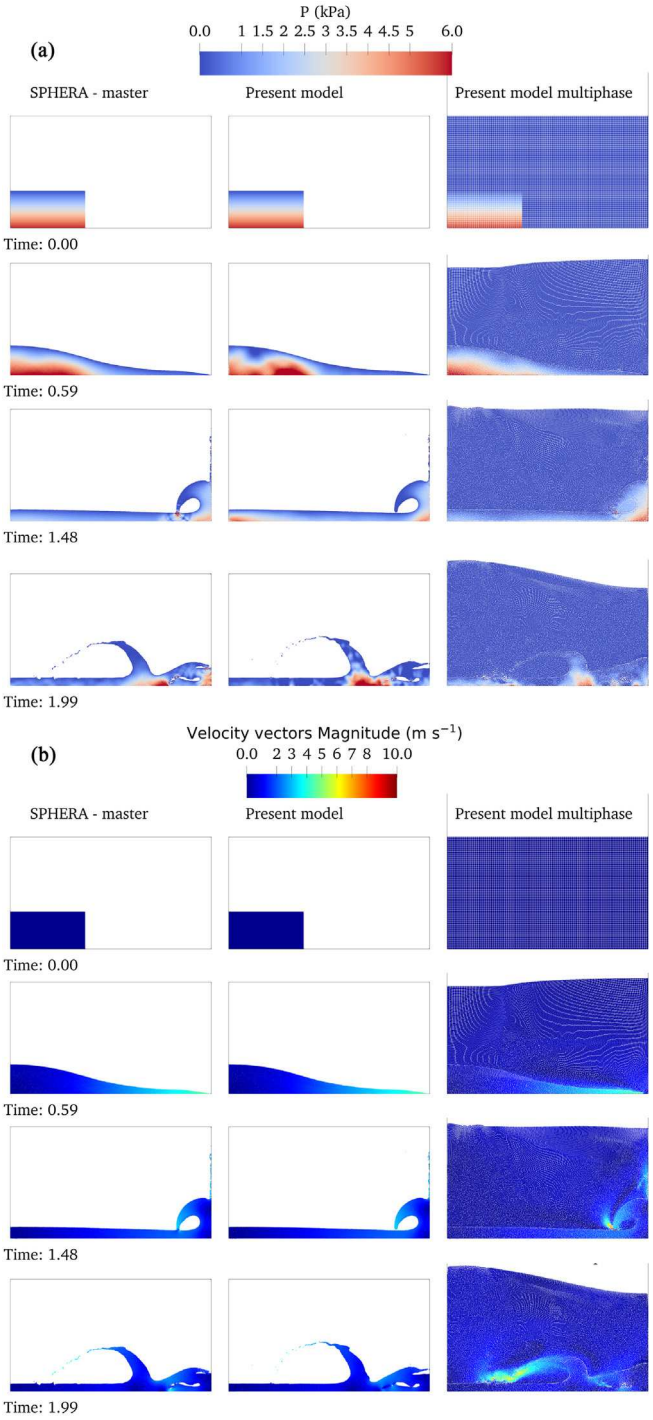

Fig. 3. Dam-break pressure contour (a) velocity contour (b). Left column: SPHERA master, centre column: present model, right column: present model multiphase.

the single-phase ones and close to the experimental result. After t = 2 (s) the simulated water height decreases following the slope of the experimental result. Only slight differences appear between the models and the experimental results, so they can be considered validated in this aspect.

Fig. 5 shows the pressure time series at the pressure gauge "pg". The simulated pressure signals are post-processed with a lowpass filter, to smooth out the high frequency spurious oscillations owing to fluid compressibility. This is carried with the signal analyser in Matlab (version R2022a). Parameters utilized are: Passband frequency $1 \cdot 10^{-6} \cdot \pi$

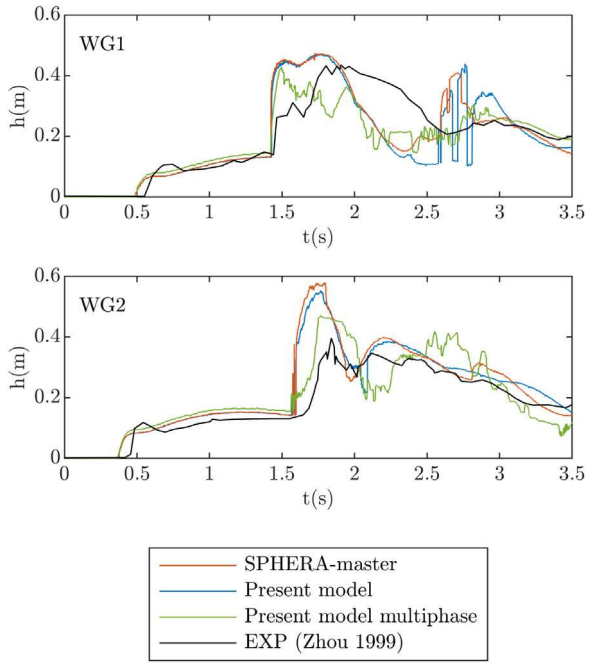

Fig. 4. Free surface elevation at the water gauges. Water gauge 1 (a), water gauge 2 (b).

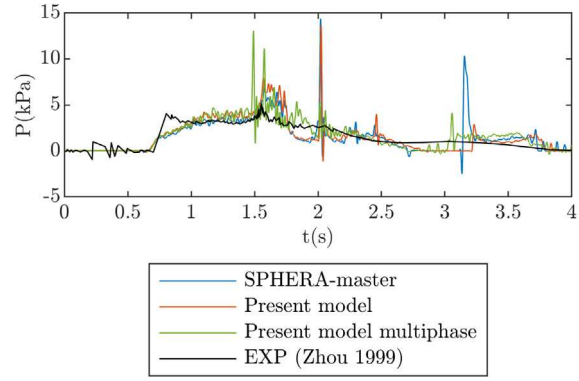

Fig. 5. Dam-break: Pressure time series at the pressure gauge pg on the right-hand side wall.

(rad samples^{-1}) with a sample frequency $f = 1000$ (Hz); steepness is set to 0.85 and the stopband attenuation is 60 (dB). It is worth specifying that this procedure has no significant effects on high and low values of pressure signal. It can be seen that the pressure rises at $t = 0.65$ (s), simulations show a milder slope than the experimental data (probably owing to fluid compressibility) while reaching similar pressure values. At $t = 1.5$ (s) there is a second peak of the pressure in the experiment. This is captured by both single-phase models with a slightly higher pressure for a time of 0.2 (s). The multiphase simulation, at $t = 1.5$ (s) better reproduces the experimental pressure. After $t = 1.8$ (s) the pressure starts descending in accordance with the experiment. At $t = 2$ (s) the single-phase simulations, both master and present model, produce a very high peak not shown by the experimental result. In the multiphase simulation such a pressure peak is much more damped and the computed pressure profile is closer to the experimental curve. Luo et al. (2016) investigated the behaviour of pressure field, and the evolution of air pockets in the dam break. At $t = 2$ (s) it forms a full closed air pocket, the entrapped air (vacuum) region collapses and impacts on the main water body, which induces a non-physical violent pressure peak. The diffusive term utilized still displays some travelling

Table 2
Summary of regular wave parameters. Ursell et al. (1960).

Wave	T (s)	H (m)	L (m)	S (m)	c (m s^{-1})	h (m)	kh	H/L	H/S
U09[a]	1.07	0.041	1.78	0.02	1.67	1.00	3.52	0.023	1.97
U13[a]	1.29	0.039	2.58	0.02	1.99	1.00	2.44	0.0153	1.82
U15[a]	3.01	0.084	8.73	0.12	2.9	1.00	0.72	0.0096	0.7
U17[a]	1.78	0.042	4.42	0.03	2.48	1.00	1.42	0.0094	1.32
U21[b]	1.01	0.077	1.58	0.04	1.57	1.00	3.98	0.0488	1.99
U22[b]	1.26	0.12	2.46	0.06	1.95	1.00	2.55	0.0485	1.85
U23[b]	1.71	0.183	4.16	0.13	2.43	1.00	1.51	0.0439	1.39
U24[b]	2.15	0.236	5.76	0.22	2.68	1.00	1.09	0.0409	1.05

[a]Low steepness wave.
[b]High steepness wave.

sound waves after the impact at the right wall causing such spurious pressure fluctuation (Antuono et al., 2012). This comparative analysis between the present model (both single-phase and multiphase) with the experimental data shows suitable results. Therefore the present model is validated against the experimental result in Zhou et al. (1999). Similar consideration holds for SPHERA-master.

3.2. Regular wave generation

Fig. 6 shows a sketch of the adopted domain for the generation of regular waves. On the left-hand side of the flume, there is the piston-type wave maker. On the right-hand side, there is a 1:10 sloped beach. This domain comes from previous investigations, where the configuration had been tested to reduce wave reflection at the boundaries (Salis, 2019; Salis et al., 2021). Wave heights are measured with two wave gauges, placed in the flat part of the flume bottom respectively at 2 and 4 meters from the wavemaker. The piston-type wavemaker and the box-shaped structure are treated by the scheme for rigid body transport, respectively with imposed kinematics and fixed kinematics. The still water height is kept constant to $h_{still} = 1$ (m) for all the simulated regular waves. Biésel and Suquet (1951) obtained the analytical solution for different wavemakers types. Eq. (26) relates the wave height H to the wavemaker stroke S_0 for the piston-type wavemaker:

$$\frac{H}{S_0} = \frac{4sinh^2(kh)}{sinh(kh) + 2kh} \tag{26}$$

The regular waves in Ursell et al. (1960) have been generated with various still water heights, ranging from $h_{still} = 0.18$ (m) to $h_{still} = 0.73$ (m). To reproduce these waves in the numerical flume, the wave steepness (H/L), the relative depth (kh), and the wave height to stroke ratio (H/S_0) are imposed in accordance with the laboratory experiments of Ursell et al. (1960). The wavemaker stroke S_0 and the wave period T are determined through the following procedure: L is obtained first by knowing h and kh; wave height H is determined knowing wave steepness H/L; wavemaker stroke S_0 is calculated knowing the wave height to stroke ratio H/S_0, Eq. (26); the wave period T is computed by solving the dispersion equation. For each wave type, the piston-type wavemaker velocity is determined with Eq. (27) knowing the stroke S_0 and period T. In this equation ω is the angular frequency and t is the time variable.

$$u_x(t) = \frac{1}{2}S_0\omega \cdot cos(\omega t) \cdot \left(1 - exp\left(-\frac{t}{T}\right)\right) + \frac{S_0}{2}sin(\omega t) \cdot exp\frac{\left(-\frac{t}{T}\right)}{T} \tag{27}$$

In Eq. (27) the piston velocity is initially damped with an exponential coefficient to avoid numerical instabilities due to inertial effects. Table 2 summarizes the regular waves parameters obtained with the illustrated procedure. Optimal simulation parameters have been previously investigated in Salis (2019) and Salis et al. (2021). Some numerical parameters are further tuned to better reproduce the

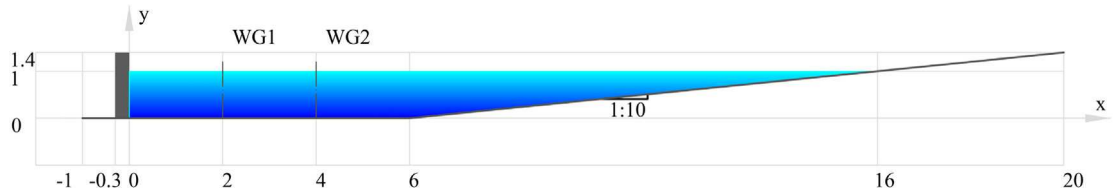

Fig. 6. Wave flume with water at rest for regular wave generation.

Table 3
Regular wave generation run-time.

Wave	Run-time (hh:mm:ss)		Increase (%)
	SPHERA-master	Present model	
U09[a]	10:45:41	12:01:14	12
U13[a]	10:24:31	11:13:18	8
U15[a]	10:03:55	12:08:37	21
U17[a]	10:04:39	10:44:53	7
U21[b]	09:41:41	11:16:33	6
U22[b]	09:39:01	10:52:18	13
U23[b]	10:10:21	11:38:21	14
U24[b]	10:18:39	11:49:26	15

[a]Low steepness wave.
[b]High steepness wave.

Table 4
Amplitude (A), amplitude Lowering (L), Error (E) and Improvement (I).

Wave	Aa (m)	Am (m)	Lm (%)	Em (%)	Ap (m)	Lp (%)	Ep (%)	I (%)
U09[a]	0.0207	0.0144	69.75	30.25	0.0158	76.42	23.58	9.56
U13[a]	0.0202	0.0167	82.66	17.34	0.0191	94.68	5.32	14.54
U15[a]	0.043	0.0372	86.54	13.46	0.0404	94	6	8.63
U17[a]	0.0214	0.0185	86.8	13.2	0.0207	96.93	3.07	11.67
U21[b]	0.0388	0.023	59.39	40.61	0.0288	74.28	25.72	25.07
U22[b]	0.0605	0.0446	73.79	26.21	0.0537	88.85	11.15	20.41
U23[b]	0.0917	0.0765	83.44	16.56	0.0856	93.34	6.66	11.86
U24[b]	0.1196	0.104	86.97	13.03	0.1101	92.02	7.98	5.81

[a]Low steepness wave.
[b]High steepness wave.

experiments. The particle dimension is set to ensure that $H/dx \gtrsim 8$. For wave-type 09, 13 and 17 the particle dimension is $dx = 0.005$ (m) while for all other wave-types is $dx = 0.01$ (m). The CFL is set to 0.05 to ensure convergence, although higher values may be used without losing stability. A free slip condition is utilized as boundary condition. The artificial sound speed is set to be at least 10 time higher of the wave celerity. Is employed a single value for all the simulations that is $c = 31.62$ (m s^{-1}). These parameters are adopted in both models. The pressure stabilization method is different for the two models, in simulations held with SPHERA-master, $\theta_p = 0.25$ is used while in the present model $\delta = 0.1$ is used. The alpha coefficient was used to reduce the numerical dissipations. With the introduction of the new features, (renormalization and diffusive terms) it is found that a low value of alpha is not necessary. The simulations held with the SPHERA-master have $\alpha = 0.01$ while in the simulations held with the new model $\alpha = 0.06$ is used. All simulations are run on a node of the High-Performance Computing machine Galileo100 with 2 × CPU Intel CascadeLake 8260 (24 cores each) @2.4 GHz and 384 GB RAM. For each simulation 48 threads are utilized, so only one of the two CPU in the computing node is used. The number of particles and the simulation time are constant for all wave-types respectively $N_p = 110\,000$ and $t = 20$ (s). Table 3 summarizes the run time for the regular wave generation. Run times between the two models are similar, with the present model slightly more computationally expensive than the master, due to the renormalization procedure. The increase in run time is between 6% and 21% and can be considered acceptable.

Fig. 7 shows the non-dimensional wave elevation time series for all the simulated waves, recorded at WG1 and WG2. The wave dynamics is well reproduced by both models. Wave height is slightly underestimated by the SPHERA-master. The present model shows decreased numerical dissipation and simulated wave height is better represented. Both models present a slight phase displacement with respect to the linear solution. However, in the present model the phase displacement is reduced with respect to SPHERA-master. These two aspects are more noticeable for the higher frequency waves, and are related to numerical dissipation (Salis et al., 2021). The numerical dissipation increases with the distance from the wavemaker. This aspect is more pronounced for high frequency waves, e.g., U09 and U21 whose wave length is smaller than the distance between the wavemaker and WG1. The second wave gauge (WG2) is at a distance from the wavemaker twice that one of WG1, that is about one wave length (for wave types U17 and U23) or more (for wave types U09, U13, U21 and U22). The adopted set-up is therefore suitable to detect the numerical dissipation. For wave-type U23 and U24, the wave elevation and phase-displacement are slightly better when simulated with SPHERA-master model. It is worth noting that for wave U09 and U13 the particle dimension is too high to correctly simulate the waves. The utilized particle dimension is $dx = 0.01$ (m) while U09 and U13 wave heights are respectively $H = 0.041$ m and $H = 0.039$ m. To achieve a similar H/dx ratio to the other waves, the particle dimension should be $dx = 0.005$ (m). This comes with a substantial increase in simulation time; ≈10 (s) need ≈72 CPU hours. Fig. 8 shows these two waves, simulated with the refined particle dimension. The present model is more adherent to the linear solution and the wave height time series is smoother than the master. The disturbances in the normalized free surface profile computed with SPHERA-master can be probably reduced increasing the value of the artificial viscosity coefficient α even if this would lead to higher numerical dissipation.

The fast Fourier transform of the wave signal allows to compute the amplitude of the simulated wave. Eq. (28) is employed to study the wave spectrum (Rahman et al., 2011).

$$\widetilde{g}\left(\frac{n}{2lN}\right) = \sum_{k=0}^{N-1} \gamma(2lk)\, e^{\frac{-2\pi i n k}{N}} \qquad n = 0, 1, 2, \ldots, N-1 \tag{28}$$

Fig. 9 shows the fast Fourier transform of the wave elevation, recorded at WG1, for all the simulated waves. In Fig. 9 the y-axis can represent either the wave amplitude or the wave energy spectral density and the x-axis sees the frequencies (Rahman et al., 2011). Despite the slight phase displacement, experienced in both models, the analytical frequency is always captured by both models. For all wave-types, plots show negligible numerical oscillations around the peak frequency. Figs. 7 and 8 show that the simulated wave profile is always close to the relative maxima (wave crest) and slightly far-off than the relative minima (wave through). The Fourier transform of the signal allows to evaluate the wave amplitude rather than the wave height. Furthermore, Fig. 9 shows that the wave amplitude simulated with the present model is higher than SPHERA-master and always closer to the linear solution.

Table 4 summarizes the results from the fast Fourier transforms of the regular waves presented in Fig. 9. The second column Aa shows the maximum amplitude of the analytical transform. Columns from three to five show for SPHERA-master the maximum amplitude Am, the

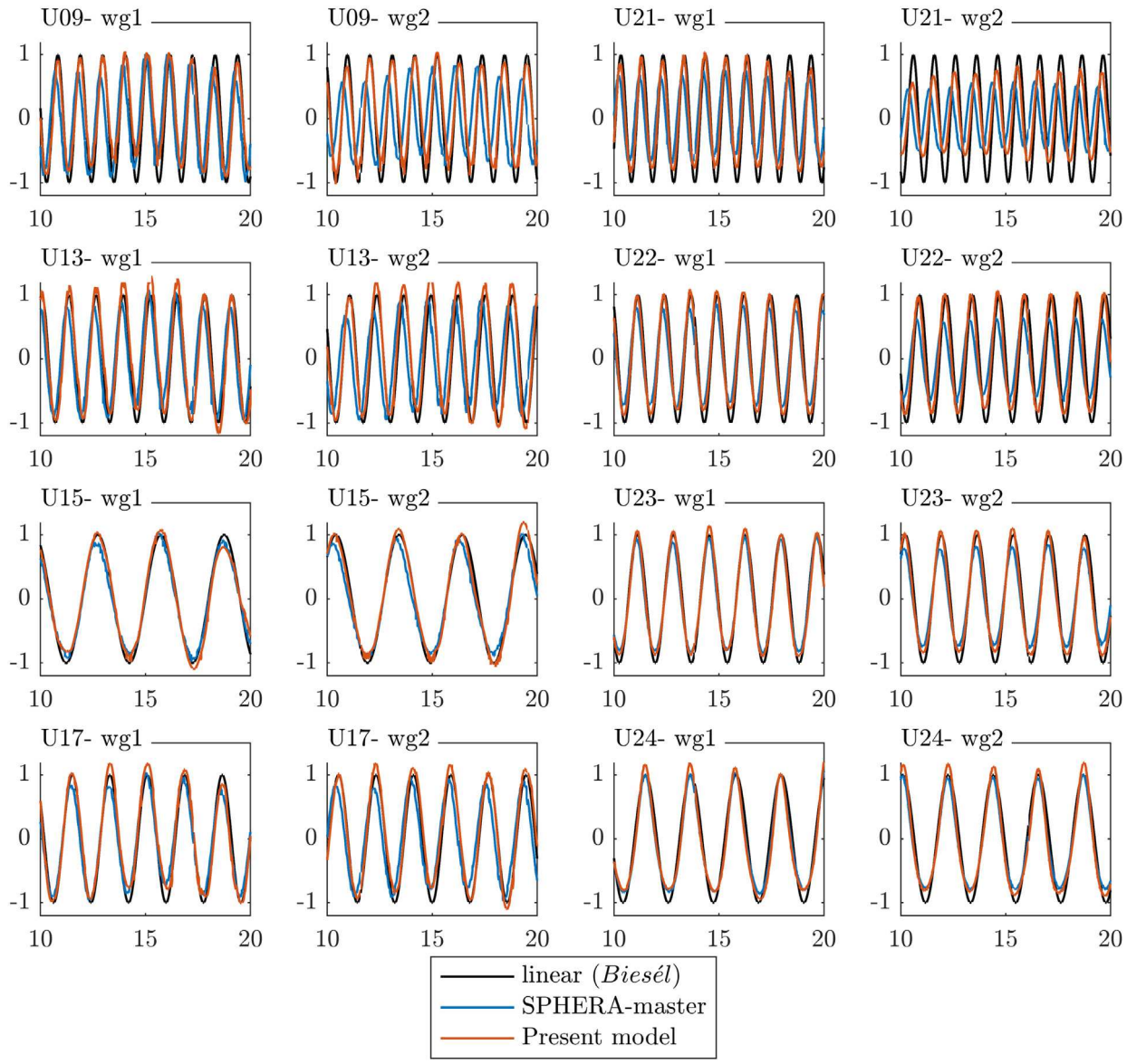

Fig. 7. Simulated wave elevation time series, recorded at WG1 and WG2. For each sub-figure: the ordinate axis shows the wave elevation over the amplitude for each wave-type η/a_0 (–); the abscissa shows time t (s). Low steepness waves are U09, U13, U15 and U17. High steepness waves are U21, U22, U23 and U24.

amplitude lowering Lm and the error Em of the master maximum value with respect to the analytical solution. The columns from six to eight show for the present model the maximum amplitude Ap, the amplitude lowering Lp and the error Ep of the present model maximum value with respect to the analytical solution. The last column reports the improvement I of the present model with respect to the SPHERA-master. These quantitative result shows that the SPHERA master amplitude reaches at least 59% of the analytical value while the present model reaches at least the 74%, with an improvement of 25%. The SPHERA-master always shows bigger errors than the present model which guarantees improvements between 5% and 25%. The highest error are made by both models simulating the two waves that have the higher frequency. However, the present model improves the master amplitude of 9.5% for U09 and 25% for U21. Fig. 10 shows the vertical profiles of velocity and pressure, at characteristic locations which are representative of the velocity fields below: through A, node B, crest C and node D. Fig. 10(a) shows these four locations highlighted for the three curves. It is worth noting that, due to the slight phase displacement with respect to the analytical solution, the locations do not overlap in the figure. For each wave signal it is found the time t_0 at which the free surface elevation is zero, representative of node B with a tolerance of 0.1% due to sampling interval. From node B the through at the time of $t = t_0 - T/4$ and the crest at the time of $t = t_0 + T/4$ are determined, while node D is found at $t = t_0 + T/2$ (T is the wave period). The velocity profiles are computed with the regular wave theory (Dean and Dalrymple, 1991). Fig. 10(b) and (c) show that the simulated velocity profiles are in good accordance with the analytical solution. For the x-velocity profiles Fig. 10(b) at location A and C the present model shows higher velocity, near the free surface, than the SPHERA-master. Present model velocities are closer to the maximum analytical values. As the depth increases, both models show smaller differences with respect to the analytical profile. At points B and D, both models correctly represent the analytical velocity profile. Similar consideration can be made for the z-velocity profiles Fig. 10(c), where the present model profile is closer, near the free surface, to the maximum analytical values and both models well represent the profiles at locations A and C. The vertical velocity profile dynamics is correctly represented by both models. The present model shows, near the free surface, a reduced difference from the analytical maximum values with respect to the SPHERA-master. Fig. 10(d) shows the non-dimensional pressure. Both models well represent the analytical pressure vertical

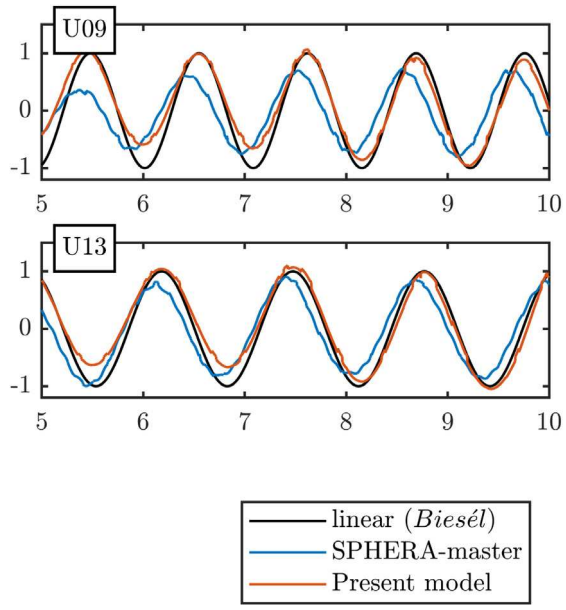

Fig. 8. Wave elevation time series with refined particle dimension $dx = 0.005$ (m), recorded at WG1. For each sub-figure: the ordinate axis shows the wave elevation over the amplitude for each wave-type η/a_0 (–); the abscissa shows time t (s).

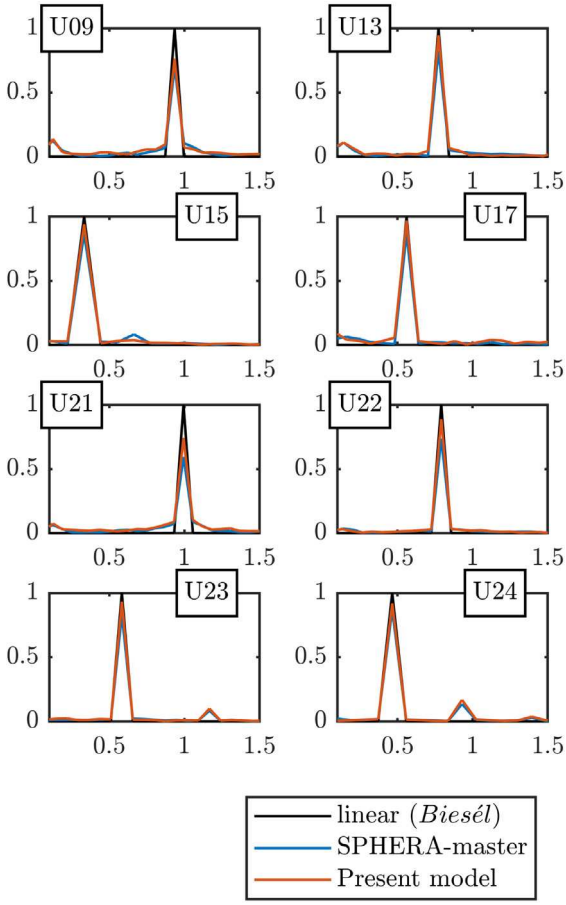

Fig. 9. Fast Fourier transforms of wave elevations recorded at WG1. For each sub-figure: the ordered axis shows the simulated amplitude over the analytical amplitude a/a_0 (–); in the abscissa there is the frequency f (Hz).

profile. It is worth noting that the present model, for increasing depths, shows values closer to the analytical solution while the SPHERA-master shows slightly higher values. This difference, although present, is however negligible and both models can approximate the pressure profiles.

Fig. 11(a) shows the pressure contours for wave U23 at some representative instant. These are smooth and free from numerical noise, the maximum pressure at the flume bottom is representative of the quasi-hydrostatic pressure in a flume. Pressure contours of the two models is similar with SPHERA-master showing slightly higher values at the flume bottom. This confirms the validity of both methods of stabilization for the pressure, i.e., Shepard filtering and the (continuity) diffusive term are adequate and equivalent. Fig. 11(b) reports the velocity magnitude contours. The comparison of the two models shows that SPHERA-master is affected by numerical dissipations as velocities are significantly reduced near the free surface. This aspect has been already discussed for the vertical velocity profiles (Fig. 10(b) and (c)). Even if velocity contours near the wavemaker are quite similar for the two models, the present model retains the velocity in all crests over the flat bottom. Instead, the SPHERA-master model presents significant velocity reduction, starting approximatively two meters from the wavemaker onwards.

In order to compare results with laboratory experiments, the wave height to stroke ratio are computed considering the mean wave height as follows:

$$H_{mean} = \frac{1}{N}\sum_{n=1}^{N}\eta\left(t\left(n\right)\right) - \frac{1}{N}\sum_{n=1}^{N}\eta\left(t\left(n\right)+\frac{T}{2}\right) \tag{29}$$

where η represents the free surface elevation, $n = 1$ represents the first relative maximum (crest) position, T is the wave period. The second relative maximum $n = 2$ is one period from n = 1 while the subsequent relative minimum (trough) is found at half a period. To compute the wave number of the simulated wave the fast Fourier transform is applied according to the following procedure. The simulated wave period is obtained as $T = 1/f(A_{max})$, where $f(A_{max})$ is the frequency found at the peak of amplitude spectrum. Once the period is obtained the wave number is computed with the dispersion equation from linear theory.

SPH results of the eight wave-types are compared, in terms of wave height to stroke ratio, with the laboratory experiments of Ursell et al. (1960), Huang et al. (1998) and Anbarsooz et al. (2013). The black curves in Fig. 12 represents the linear solution of Biesél Eq. (26). Fig. 12 shows two sub-figures, one for low steepness waves (LSW) and one for high steepness waves (HSW). Low steepness wave height to stroke ratio is slightly underestimated by the SPHERA-master with respect to the linear solution, to the experimental result of Ursell et al. (1960) and the numerical results (Huang et al., 1998; Anbarsooz et al., 2013). This is noticeable particularly for waves with higher frequency and small wave height (U09, U13 and U17). The present model presents an increased accuracy as the wave height to stroke ratio is closer to the experimental reference results (green squares). The only exception is U09 for which, as discussed earlier, the particle dimension should be probably enhanced to capture the small wave height. Results with the refined particle dimension are not presented due to the short simulation time and consequent small number of waves. For high steepness waves, the wave height to stroke ratio is closer to the experiments for both models. In this sub-figure, the difference between low frequency (U23 and U24) and high frequency (U21 and U22) is clearer. The model SPHERA-master is more dissipative in regards of the simulated higher frequency waves. The results of wave height to stroke ratio for the lower frequency waves is closer to the experiments, showing that numerical dissipation is greater for the simulated higher frequency waves. With the present model, for the low frequency waves, the obtained results show a higher wave height to stroke ratio with respect to the experiments of Ursell. It is worth noting that these results are closer to the analytical solution as the simulated wave height is greater.

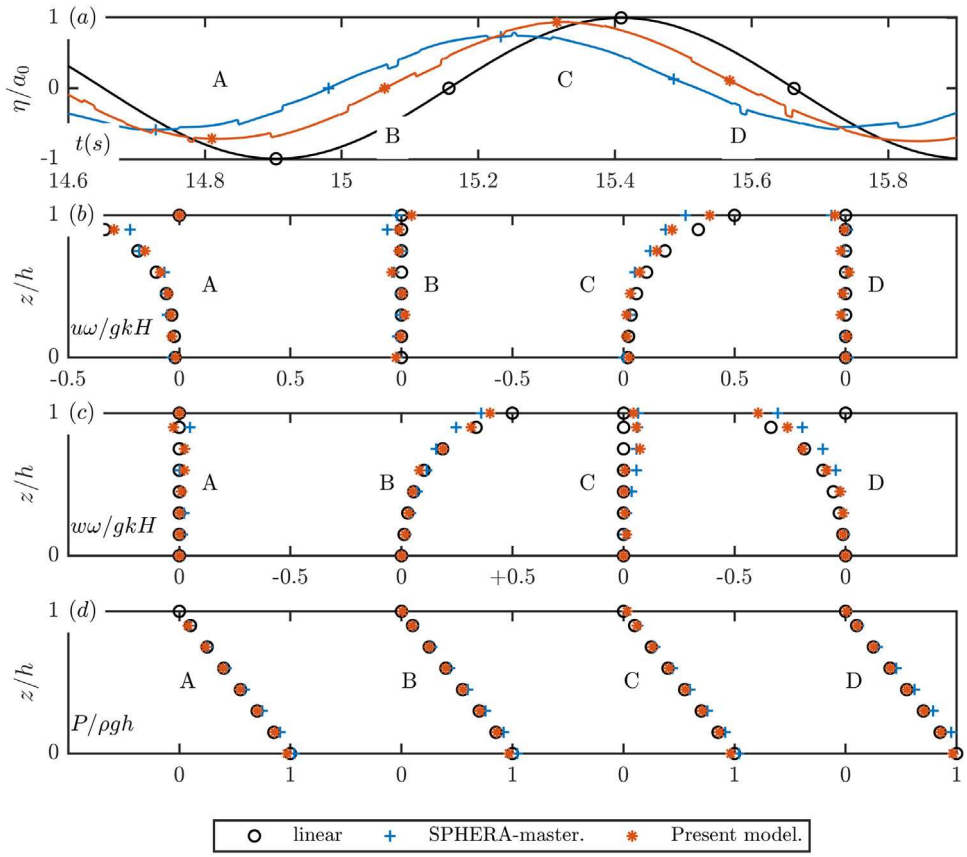

Fig. 10. Wave elevation and vertical profiles under wave-type U23, recorded at WG1. (a) wave elevation with highlighted points. (b) non dimensional x-velocity. (c) non-dimensional z-velocity. (d) non-dimensional pressure. Points A are through, B and D are nodes and C are crest.

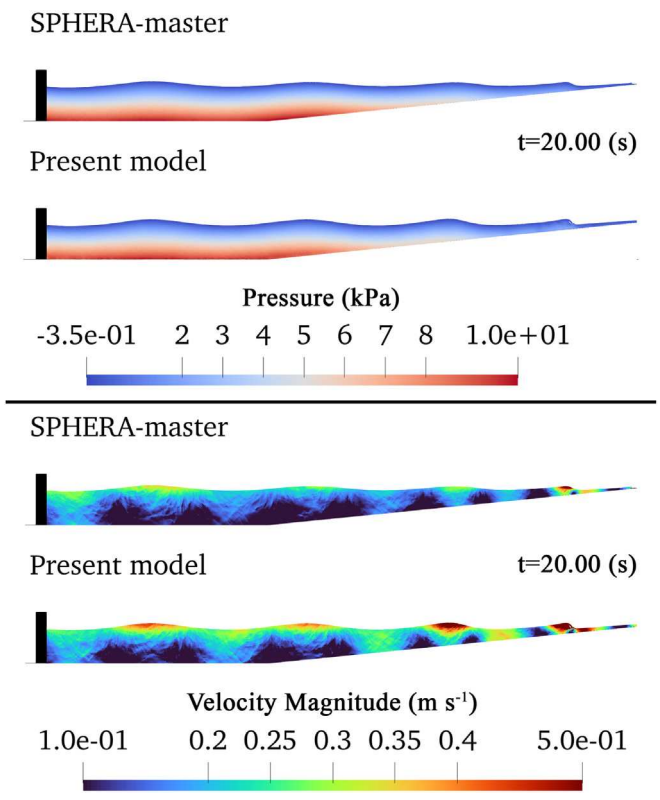

Fig. 11. Pressure contour (a) and velocity magnitude contour (b) for regular wave-type U23. For each time SPHERA-master on the top, derived model at the bottom.

For the higher frequency waves, with the present model, substantially higher values of wave height to stroke ratio are achieved. For the wave U22 the results are adherent to the experiment however, U21 shows a slightly lower value. The relative depth of simulated waves is in close proximity with the relative depth of the experiments and the numerical results. The kh distance with respect to the experiments is negligible, with a slightly greater distance shown in the case of high frequency waves (U09, U13, U21 and U22).

Fig. 12 shows that the error in relative depth is always acceptable, exception made for the higher frequency wave (i.e., U09) which is characterized by similar wave height (i.e., similar particle dimension) but higher steepness (more than twice) than simulation U17. If simulation U13 is considered, which has almost the same wave height of simulation U17 but lower steepness than simulation U09, the error in relative depth is quite acceptable. Therefore, simulation U09 would probably benefit from an increase of particle resolution to account for higher steepness relative to wave height. From Fig. 12 it seems that the relative depth best captured when the wave steepness to wave height ratio is below 0.4, as in the case of the simulations U15 and U17 (for LSW) and the simulations U23 and U24 (for HSW). Concerning the error on the prediction of wave height to stroke ratio, the worst results are obtained for the simulations U09 (LWS) and U21 (HSW) that shows both the higher ratio between wave steepness and wave height. As discussed above, an increase of particle resolution may help lowering the relative error. Therefore, obtained results can be considered acceptable in reproducing regular waves. It is worth noting that numerical parameters could be calibrated for each wave-type in order to reduce the error. However, retaining constant numerical parameters across this variety of wave-types with different characteristics such as wave height, period, steepness, allows validating the present model.

On the basis of the results obtained for the simulation of eight regular waves illustrated above, the wave dynamics is well reproduced

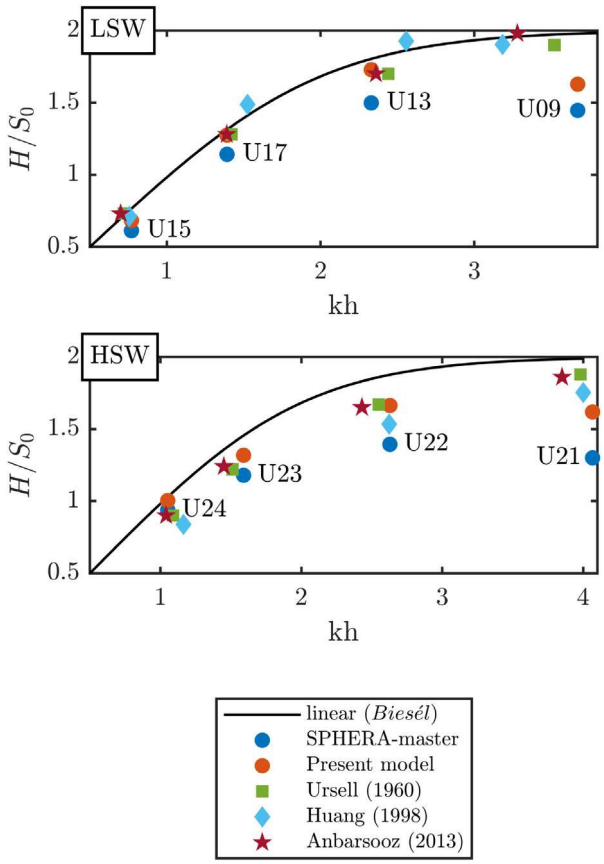

Fig. 12. Wave height to stroke ratio H/S_0 vs. relative depth kh. (LSW) low steepness waves, (HSW) high steepness waves. Wave elevation recorded at WG1, all results are simulated with $dx = 0.01$ (m) (Ursell et al., 1960; Huang et al., 1998; Anbarsooz et al., 2013). (For interpretation of the references to colour in this figure legend, the reader is referred to the web version of this article.)

by both models that were tested. However, wave heights and amplitude of the derived model are generally better than the SPHERA-master. The frequency of each wave is captured by both models. The vertical velocity and pressure profiles of both models are very close to the analytical solution. However, the SPHERA-master shows a significant velocity dissipation at the free surface, with respect to the derived model. This is further shown in the velocity contours. SPHERA-master near the free surface, at a distance greater than two meters from the wavemaker, shows a reduced velocity with respect to the derived model. Finally, derived model results are compared with the experiments of Ursell showing significant error reduction with respect to the SPHERA-master. Based upon these considerations, the present model can be considered validated to generate regular waves in a numerical flume.

3.3. Non-linear wave generation and structure impact

A modified wave flume is adopted to simulate the experiment from Yan et al. (2019) and Sun et al. (2019b). The non-linear wave-type S3 is generated with the focusing wave theory by superimposing 32 linear wave components. The larger wave amplitude is produced at the focusing point, at the spatial position x_p and time t_p, where all crest components meet simultaneously. The wave profile is described at any point of space and time by Eq. (30). The sum is extended to $N = 32$ wave components of constant amplitude $a_i = 0.0061$ (m). The reproduced frequency bandwidth (f_i) ranges from $f_{min} = 0.32$ (Hz) to $f_{max} = 0.96$ (Hz) and the wavenumber k_i is computed with the dispersion equation (linear wave theory) for each wave component.

$$\eta(x,t) = \sum_{i=1}^{N} a_i cos\left[k_i\left(x_p - x_f\right) - 2\pi f_i\left(t - t_f\right)\right] \tag{30}$$

Table 5
Wave–structure impact simulations run times and parameters summary.

Run	Run-time (hh:mm:ss)	dx/dx_b	c (m s^{-1})	α	λ
A	49:14:25	1	31.62	0.06	0.7
B	153:18:13	2	22.36	0.06	0.7
C	36:33:54	1	22.36	0.06	0.7
D	16:38:24	1	10	0.06	0.4
E	17:46:36	1	10	0.06	0.5
F	16:10:50	1	10	0.06	0.7
H	18:35:54	1	10	0.04	0.7
I	17:02:22	1	10	0.02	0.7
L	16:00:34	1	10	0.08	0.7

Fig. 13 shows a sketch of the numerical flume for the non-linear wave generation and wave–structure impact. The flat part which extends beyond the box is stretched from 6 (m) (in the previous configuration) to 16 (m); the still water height is set to $h_{still} = 0.7$ (m) and the beach slope is 1:10. The piston-type wavemaker and the box-shaped structure are treated by the scheme for rigid body transport, with an imposed and a fixed kinematics, respectively. The numerical probes and the fixed structure are set according to Sun et al. (2019b). There are three wave gauges WG1, WG2 and WG3 respectively at a distance from the wavemaker of 6.849 (m), 9.659 (m) and 11.104 (m) at the focusing point. Two velocity probes V1 and V2 are placed at a height of 0.5 (m) with a distance from the wavemaker respectively of 6.845 (m) and 11.296 (m). The red box in Fig. 13 shows a detail of the box-shaped fixed structure. The bottom left corner is at coordinates $x = 12.677$ (m) and $y = 0.7485$ (m) with a still water–structure clearance of 0.0458 m. The structure has a height of 0.12 (m) and length of 0.5 (m). In the structure there are four probes, denoted by red dots (Fig. 13), named respectively FP1 and FP2 in the front of the structure and BP1 and BP2 at the bottom.

Fig. 14 shows the wavemaker input velocity. The particle resolution is $dx = 0.007$ (m) with a h/dx ratio of 100. In Sun et al. (2019b) this particle resolution is found to be adequate to reproduce the experiment. To guarantee convergence the CFL is set to 0.05 and the free slip boundary condition is adopted. Different values of the artificial viscosity have been investigated, the results showing that $\alpha = 0.06$ is appropriate for this experiment. In this section all presented results are simulated with the proposed model, independently derived from SPHERA v9.0.0 (RSE SpA). In this section, all simulations run on a node of the High-Performance Computing machine Galileo100 with 2 x CPU Intel CascadeLake 8260 (24 cores each) @2.4 GHz and 384 GB RAM. For each simulation 48 threads are utilized, so only one of the two CPUs in the computing node is used. Table 5 summarizes simulation run times and parameters. For the non-linear wave impacting the fixed box structure, the model sensitivity to its parameters is assessed. The investigated parameters are the ratio between the fluid particle size and body particle size (dx/dx_b), the artificial sound speed (c), the artificial viscosity coefficient (α) and the renormalization threshold (λ). Runs are named from A to L, the reference run being F to which other simulation results are compared, with the exception of the parameter dx/dx_b investigated in early simulation stage. The number of particles is constant $N_p = 278\,600$ and the simulation time is $t = 20$ (s). The run time varies significantly. Since the $CFL = 0.05$ is constant, run time is influenced mainly from two parameters: dx/dx_b and c.

The first is relevant to avoid fluid-body (wavemaker and structure) particle penetration, since a lower body particle dimension i.e., a higher particle concentration, prevents this issue. However, for the presented simulations, the fluid–solid penetration is negligible with no significant influence on the results. The run time is 4.2 times higher with the lower body particle dimension. For this reason, it is more convenient to have

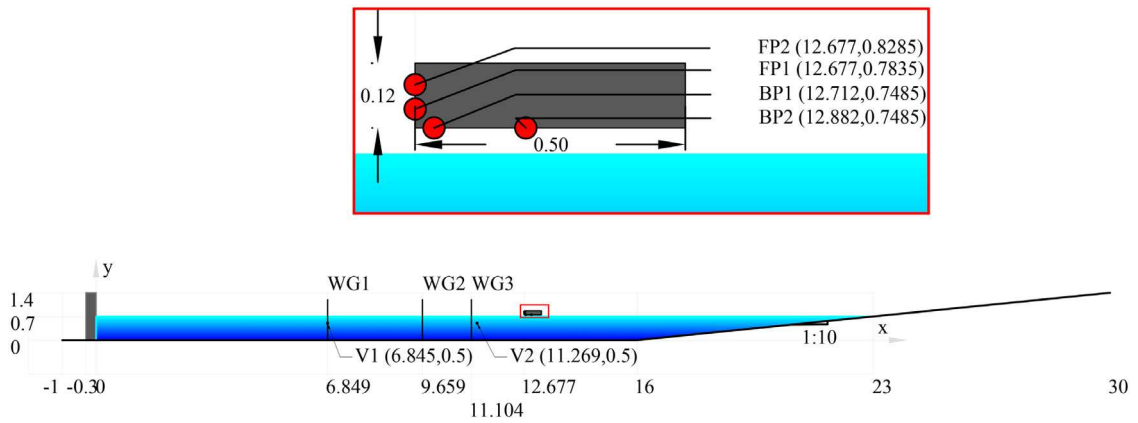

Fig. 13. Wave flume with water at rest for non-linear wave generation and wave–structure impact. Magnification of the box-shaped structure (top panel). (For interpretation of the references to colour in this figure legend, the reader is referred to the web version of this article.)

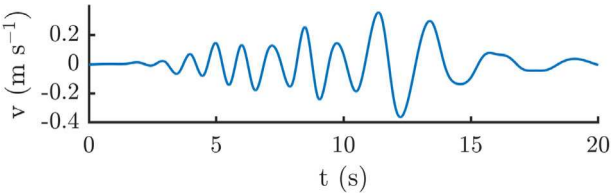

Fig. 14. Wavemaker input for the non-linear wave generation.

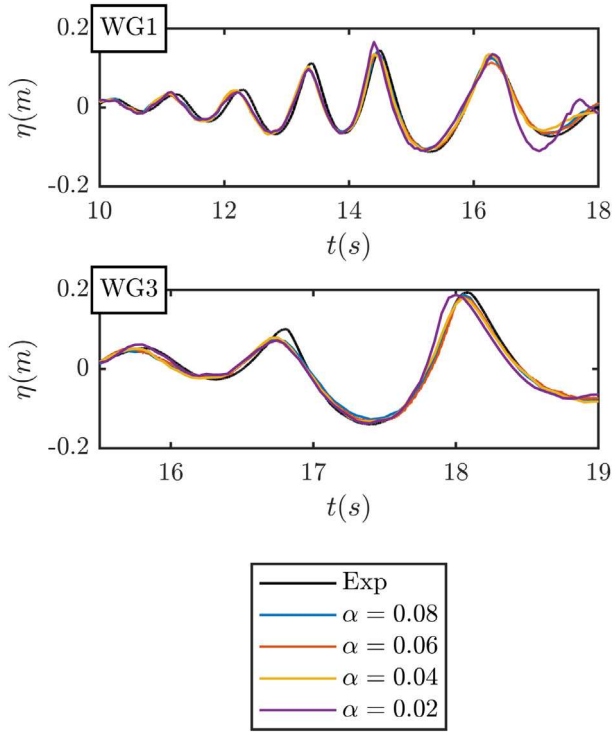

Fig. 15. Wave elevation recorded and simulated at WG1 and WG3, sensitivity to artificial viscosity. (For interpretation of the references to colour in this figure legend, the reader is referred to the web version of this article.)

the structure particle dimension equal to the fluid particle dimension. To achieve faster run-times the artificial sound speed has been reduced, implying higher fluid compressibility. For regular waves the artificial sound speed was assumed ten times the wave celerity in order to reduce density oscillations. For the non-linear wave generation, the characteristic wave celerity $c_w = 2.11$ (m s^{-1}) could be used, and therefore the artificial sound speed must be higher than $c = 21.10$ (m s^{-1}) which implies high computational cost for this set-up. However, results show that with c being 5 times the characteristic wave celerity, simulations are stable even when sharp gradients of pressure and velocity occur. Moreover, numerical results are in good agreement with the experimental results. Once the artificial sound speed is assigned, the influence of the artificial viscosity may be analysed. The usual range of this parameter is from 0.01 to 0.1. Values close to 0.1 are slightly more dissipative (lower wave height) with a greater simulation stability; on the contrary with values close to the lower limit (0.01) the numerical dissipation is reduced but numerical noise may appear. Fig. 15 shows the wave elevation at WG1 and WG2 for different values of α. With the lower α values, namely, 0.02 and 0.04, wave heights are overestimated and non-physical wave breaking occurs (purple wave at $t = 14.4$ (s) recorded at WG1). The higher tested values show similar results. The value of α is 0.06 represents a compromise between stability and suitable wave heights, particularly at WG3 and the wave crest at $t = 18.2$ (s) (the time and point before the wave–structure impact).

The threshold λ for the determinant of the matrix $|\underline{\underline{B}}_0|$ controls the application of the renormalization procedure. The matrix determinant has the physical meaning of spatial particle concentration. Low values of the determinant mean that the interaction domain of computational particle 0 has a low number of neighbours i.e., is close to the free surface or boundary. With values close to 1 instead, the interaction domain of computational particle 0 is almost full of neighbours. Fig. 16 shows the typical contour plot of $|\underline{\underline{B}}_0|$. It can be seen that close to the free surface and the bottom boundary values are close to 0.2 while inside the water these values range between 0.6 to 1.0. The renormalization is not applied to those particles that have $|\underline{\underline{B}}_0|$ lower than the threshold value λ. Three values of λ are herein considered, namely, 0.4, 0.5 and 0.7. With values lower than 0.4 the simulation is not accurate. For this value, in fact, the numerical dissipation is quite negligible but the wave elevation is higher than expected, reaching a greater steepness i.e., waves are closer to instability and non-physical wave breaking occurs, preventing the correct wave generation. With values from 0.5 to 0.7 results are similar and it is found that a greater accuracy is reached. The renormalization is not applied to particles at or near free surface, including jets or splashing particles.

Fig. 17 shows the wave elevation time series at the three wave gauges for different λ values. For the lowest considered value, higher wave heights are achieved. These are closer to the experimental ones in all crests except the crest at $t = 18.1$ (s) recorded at WG3. It can be seen that, for some crests, there is a significant phase displacement between the simulation and the experimental result. The second negative aspect

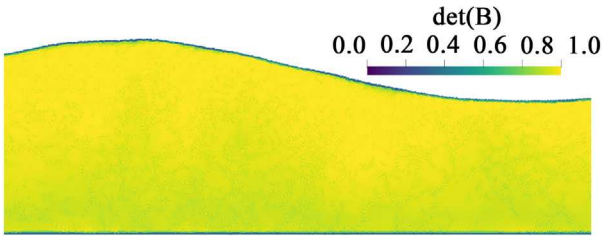

Fig. 16. Contour plot of the determinant of $\underline{\underline{B}}_0$.

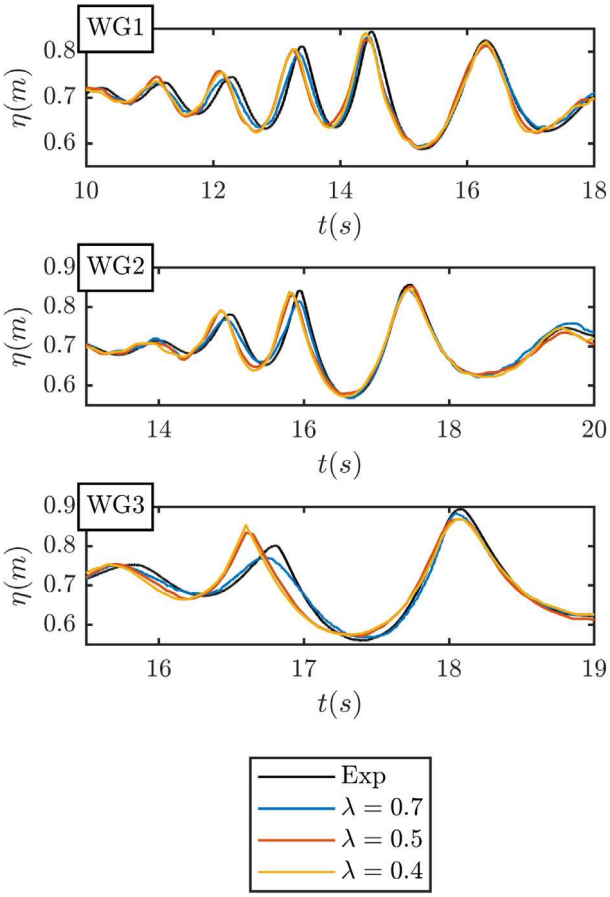

Fig. 17. Wave elevation recorded and simulated at the three wave gauges, sensitivity to λ.

is that some wave components break, prior reaching the focusing point (i.e., crest at $t = 18.1$ (s) at WG3). For the low considered λ values, at WG3 the crests at $t = 16.6$ (s) break and subsequently reduce the wave height at the focusing point.

The most appropriate value of λ seems to be 0.7 since this value provides a good balance between numerical dissipation and wave height at the focusing point. From this parametric analysis the appropriate parameters to reproduce the wave–structure impact can be determined. The reference simulation, which will be compared to the experimental results, is run F in Table 5. Fig. 18 compares the wave elevation, recorded at three wave gauges. SPH results, at WG1 are close to the experimental result. The wave height is close to that of the experiment while there is a negligible phase displacement in all crests except at $t = 16.3$ (s). Similarly, at WG2 there is a phase displacement in all crests and the wave height is slightly lower than the experimental one. At WG3 $t = 16.8$ (s) the wave height of the simulation is lower than the experimental one, and occurs slightly earlier. In the crest at $t = 18.1$

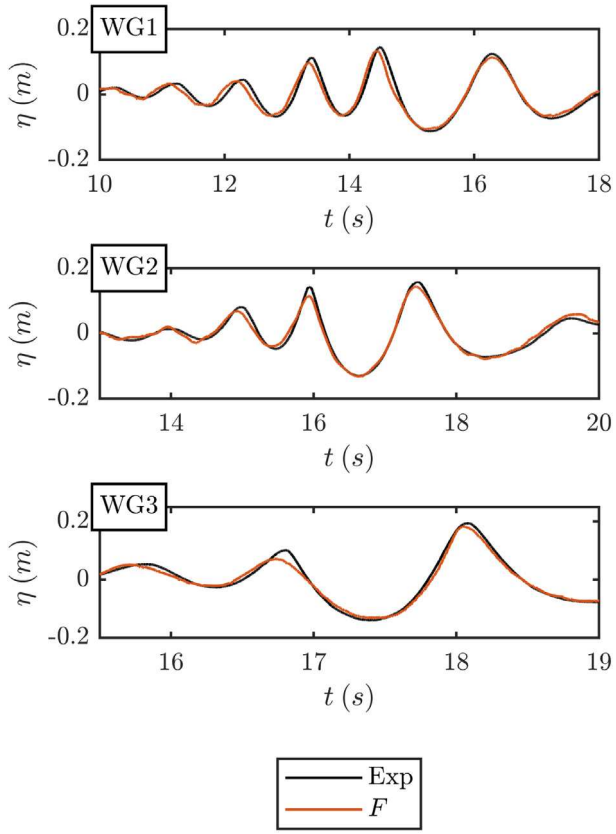

Fig. 18. Wave elevation recorded and simulated at the three wave gauges.

(s), the wave height is quite close to the experimental one and slightly in advance. This means that, although small, the phase displacement affects the wave–structure impact. This will be further discussed later on, as the numerical pressure gauges at the structure have a delay of $\Delta t \approx 0.03$ (s) with respect to the experimental one.

Fig. 19 shows the fast Fourier transform of the surface elevation signal at the three wave gauges. The frequency spectrum of the SPH simulation is in good agreement with the experimental wave spectrum. Wave amplitude is close to the experimental values; it is worth noting that at WG3 there is a slightly underestimation in the frequencies from $f = 0.4$ (Hz) to $f = 0.8$ (Hz). Fig. 20 shows the velocity magnitude and pressure contours around the impact instants. Before the impact (Fig. 20(a)), the highest velocity is at the crest top and it progressively reduces along the depth. When the impact occurs (Fig. 20(b) and (c)), in the area of contact between wave and structure, velocity comes to a sudden reduction while pressure increases. After the impact (Fig. 20(d) and (e)) it can be observed the formation of a jet that rapidly overcomes the structure deck. In all snapshots, the pressure is quasi hydrostatic excluding the impacting wave. The velocity field shows the presence of secondary waves. Fig. 21 shows the x and z velocity components (u and w respectively) recorded at the two velocity probes V1 and V2 at a height of $z = 0.5$ (m). For the probe V1 the u and w components are quite close to the experiment values. The simulated u is adherent to the laboratory result in both phase and magnitude. The simulated w shows a slight phase displacement of the peak at $t = 16.9$ (s) with a lower velocity; the crest at $t = 17.9$ (s) shows smaller phase displacement while the velocity is higher than the experiment one. At V2 the simulated velocity is slightly different than the experimental velocity. The simulated u velocity, before $t = 15.0$ (s), presents a series of oscillations whereas in the experiment one these are less prominent. After $t = 15.0$ (s), the simulated u velocity approximates well the experimental time series. The w velocity instead is quite close to the

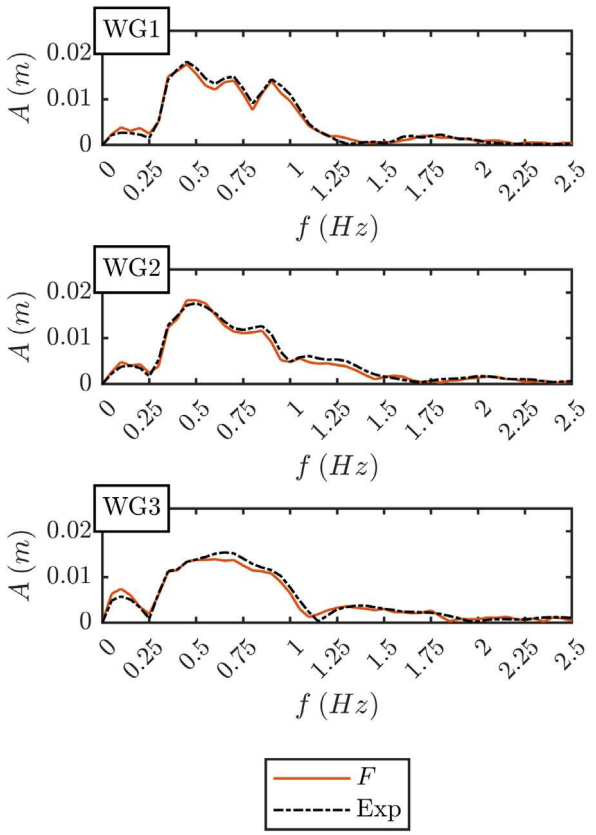

Fig. 19. Fast Fourier transform of the surface elevation signal at the three wave gauges.

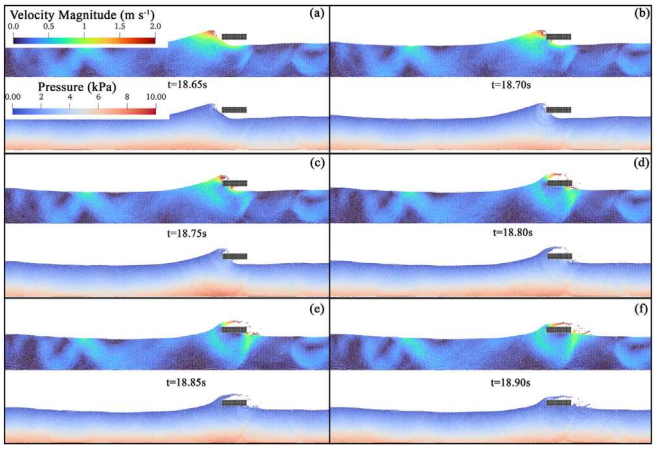

Fig. 20. Velocity magnitude and pressure contours for the wave–structure impact.

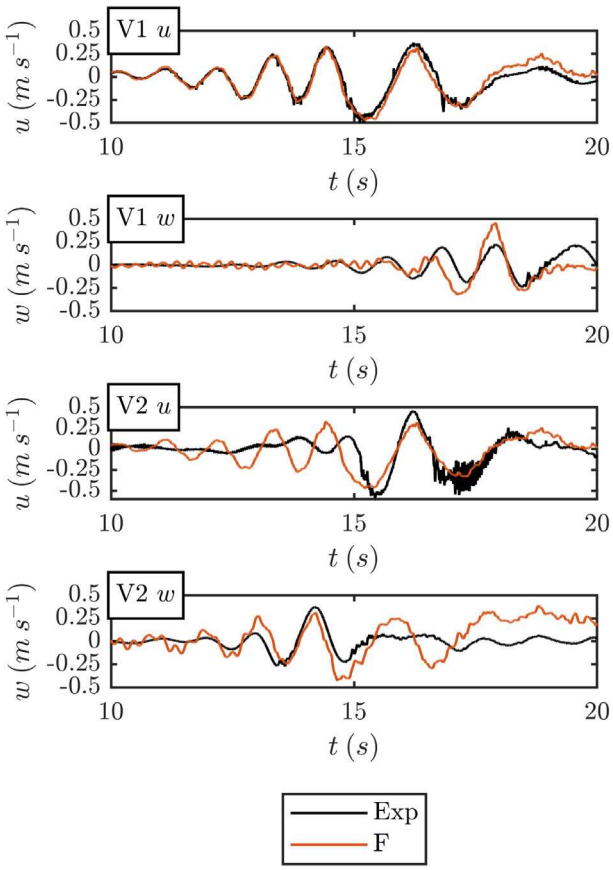

Fig. 21. x-velocity (u (m s^{-1})) and z-velocity (w (m s^{-1})) time series recorded at the two velocity probes V1 and V2.

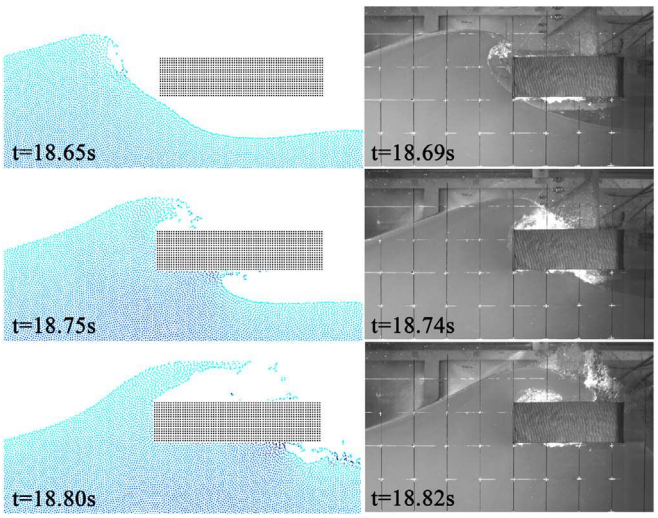

Fig. 22. Wave–Structure impact. SPH simulation, left panels. Experimental snapshots, right panels.

experimental time series before $t = 15.0$ (s) while, after this time, it overestimates the expected experimental velocity values. Overall, the present model seems suitable to reproduces the relevant kinematic features of the experiment.

Fig. 22 shows three snapshots of the wave–structure impact, comparing the SPH results to the laboratory experiments of Sun et al. (2019b). As anticipated, the numerical impact it is slightly delayed with respect to the experiment. Moreover, the sampling of SPH result has been done every $t_{sample} = 0.05$ (s) thus they are not available at the exact laboratory frames. For this reason, the delay between the SPH and laboratory snapshots can be considered negligible. The frame just before the impact at $t = 18.65$ (s) shows that the wave is breaking as the experimental one. The shape of the impacting crest is slightly different, with the plunging wave crest in the laboratory frame slightly moved forward. The curvature of the experimental frame at $t = 18.69$ (s) is higher than in the numerical result at 18.65 (s). This aspect slightly affects the pressures at the sensors. At $t = 18.75$ (s) the SPH and the laboratory results are very similar both over and under the decks. Over the deck the wave is closing onto the structure while breaking with several particles detaching. At $t = 18.80$ (s) the shapes of the curves

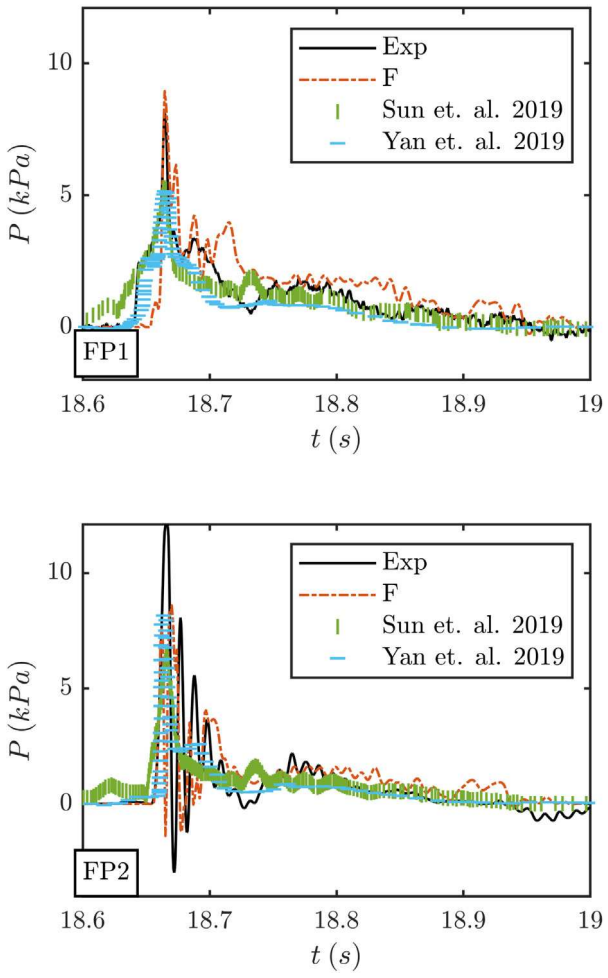

Fig. 23. Pressure time series at the structure front sensors FP1 and FP2 (Sun et al., 2019b; Yan et al., 2019).

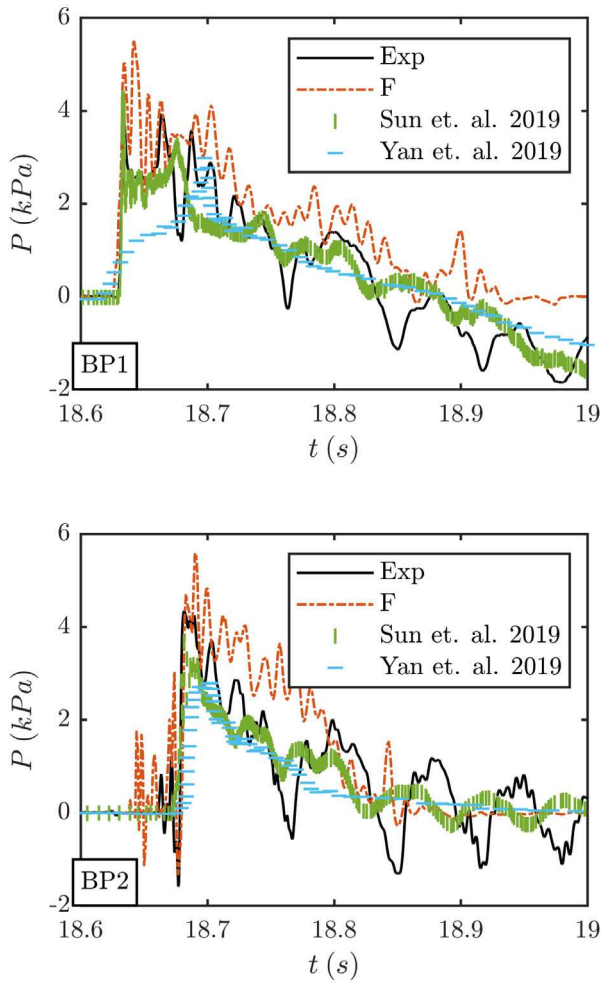

Fig. 24. Pressure time series at the structure bottom sensors BP1 and BP2 (Sun et al., 2019b; Yan et al., 2019).

of the SPH simulation and of the experiment is slight difference. The SPH wave carries slightly higher velocity thus the jet reaches a higher elevation than the experimental one which envelopes completely the structure deck. The relevant impact characteristics are, anyway, well reproduced by the present model. It is worth noting that the model is single-phase and cannot reproduce the effects of air entrapment and suction stage where strong negative pressures appear in the structure bottom.

As discussed earlier there is a slight phase displacement in the last crest (Fig. 19, WG3 at $t = 18.1$ (s)) thus also the simulated pressure time series is slightly delayed. As a result, in both Figs. 23 and 24 the SPH pressures plots are shifted forward in time with respect to the experimental ones. It is worth noting that the time delay is always small ($\Delta t \approx 0.03$ (s)). In Fig. 23 the SPH result at the structure front sensors FP1 and FP2 is close to the experimental one. At sensor FP1 the SPH pressure peak is slightly higher than the experimental one, but the overall trend is suitably reproduced. The model reproduces the compression–decompression stages at early times in FP2, with reduced amplitude than the experimental one. Fig. 24 shows the pressure time series at the bottom structure pressure probes. The first half of the pressure time series at BP1 is well reproduced, with similar values of pressure and a similar descending trend. From $t = 18.85$ (s) on, the experimental strong negative pressures values are not captured by the present model where an non-physical void forms at the measuring point, and the suction effect is not captured. At the sensor BP2 the pressure increment is captured by the present model, while in the descending phase some differences appear. This could be due to the difference between the simulated impacting wave and the laboratory one previously described.

Also, the multiphase simulation in Sun et al. (2019b) and in Yan et al. (2019) are reported for comparison purposes. Even though the presented model is single-phase, its results are similar to those ones from more complex models and the relevant aspects of the laboratory test can be captured.

4. Conclusions

In this paper, a model derived from SPHERA v.9.0.0 (RSE SpA) has been presented. The model equations are modified with the possibility to treat multiphase flows with high density ratio which will be further investigated in a future study. The diffusive term in the continuity equation is added and the renormalization is used to reduce numerical dissipation. The model has been tested and validated on three cases: (i) dam-break, (ii) generation of regular waves in a 2D flume, and (iii) generation of non-linear wave in a 2D flume and structure impact. Dam-break results obtained with the original code SPHERA and with the derived model, both single-phase and multiphase, are quite close to the laboratory experiments. The main limitation of the proposed multiphase formulation is the formation of a very small interface gap between the two media, that however do not affect the accuracy of the results. Non-physical air voids can be momentarily generated by local pressure/velocity gradients with negligible influence on model results.

In the case of the generation of regular waves, the present model is less dissipative than SPHERA and adequately reproduces the kinematic and dynamics aspects. Moreover, with the present model the error in wave height, with respect to the laboratory experiment of Ursell et al. (1960) is significantly reduced, showing similar accuracy to other numerical models presented in the literature. The generation of the non-linear wave shows that the present model accurately reproduces the wave height, the amplitude spectrum and velocity field with respect to the laboratory data. When applied to wave generation, the model requires fine calibration of the model parameters, to accurately reproduce the different wave-types. The wave–structure impact reproduces satisfactorily the relevant aspects of the phenomenon. The shape of the impacting wave is very similar to the laboratory one, even if it is slight delayed. Thanks to the reduction of the artificial sound speed, pressures at the structure probe are in the same range of values with the experimental one. The suction stage at BP1 cannot be reproduced. Nevertheless, the obtained results are quite satisfactory considering the relative simplicity of the presented model. The present model can be extended to the analysis of two-phase flows with high density ratio. This will be the subject of future investigations.

5. Future perspectives

The future perspectives of this research are the application of the multiphase model to the wave–structure impact. The drawbacks (e.g. interface gap, particle cluster) of the multiphase model should be overcome with a particle shifting technique (PST). A PST, based on the Fick's law, can be used to regularize the particle distribution in the domain, shifting particles from a zone with high particle density, to a zone with low particle density. Particle shifting techniques, based on this law have proven to be a reliable tool to model multiphase flows with high density ratios (Sun et al., 2019a; Wang et al., 2019; Krimi et al., 2020).

CRediT authorship contribution statement

Nicolò Salis: Conceptualization, Software, Simulations, Validation, Writing – original draft. **Min Luo:** Conceptualization, Writing – review & editing. **Alessandro Reali:** Conceptualization, Writing – review & editing. **Sauro Manenti:** Conceptualization, Writing – original draft, Supervision.

Declaration of competing interest

The authors declare that they have no known competing financial interests or personal relationships that could have appeared to influence the work reported in this paper.

Data availability

No data was used for the research described in the article.

Acknowledgements

The authors would like to deeply thank Dr. Andrea Amicarelli (RSE S.p.A.) for his support with the code SPHERA v.9.0.0 (RSE SpA). SPHERA v.9.0.0 is realized by RSE SpA thanks to the funding "Fondo di Ricerca per il Sistema Elettrico" within the frame of a Program Agreement between RSE SpA and the Italian Ministry of Economic Development (Ministero dello Sviluppo Economico).

The authors acknowledge the CINECA award under the ISCRA initiative, for the availability of High Performance Computing resources and support (Italian National HPC Research Project). HPC simulations refer to the following HPC research projects (instrumental funding based on competitive calls, ISCRA-C project at CINECA, Italy): HSPHER21_ 1, HPCNHLW3.

The EOS HPC cluster of the Department of Mathematics "Felice Casorati" at the University of Pavia is gratefully acknowledged.

Funding

The partial support by the MIUR-PRIN project XFAST-SIMS (no. 20173C478N) is also gratefully acknowledged.

References

Adami, S., Hu, X.Y., Adams, N.A., 2012. A generalized wall boundary condition for smoothed particle hydrodynamics. J. Comput. Phys. 231 (21), 7057–7075.

Altomare, C., Tafuni, A., Domínguez, J.M., Crespo, A.J., Gironella, X., Sospedra, J., 2020. SPH simulations of real sea waves impacting a large-scale structure. J. Mar. Sci. Eng. 8 (10), 826.

Amicarelli, A., Albano, R., Mirauda, D., Agate, G., Sole, A., Guandalini, R., 2015. A smoothed particle hydrodynamics model for 3D solid body transport in free surface flows. Comput. & Fluids 116, 205–228.

Amicarelli, A., Manenti, S., Albano, R., Agate, G., Paggi, M., Longoni, L., Mirauda, D., Ziane, L., Viccione, G., Todeschini, S., et al., 2020. SPHERA v. 9.0. 0: A computational fluid dynamics research code, based on the smoothed particle hydrodynamics mesh-less method. Comput. Phys. Comm. 250, 107157.

Anbarsooz, M., Passandideh-Fard, M., Moghiman, M., 2013. Fully nonlinear viscous wave generation in numerical wave tanks. Ocean Eng. 59, 73–85.

Antuono, M., Colagrossi, A., Marrone, S., 2012. Numerical diffusive terms in weakly-compressible SPH schemes. Comput. Phys. Comm. 183 (12), 2570–2580.

Antuono, M., Colagrossi, A., Marrone, S., Molteni, D., 2010. Free-surface flows solved by means of SPH schemes with numerical diffusive terms. Comput. Phys. Comm. 181 (3), 532–549.

Biésel, F., Suquet, F., 1951. Les appareils générateurs de houle en laboratoire. Houille Blanche (2), 147–165.

Colagrossi, A., Landrini, M., 2003. Numerical simulation of interfacial flows by smoothed particle hydrodynamics. J. Comput. Phys. 191 (2), 448–475.

Colagrossi, A., Marrone, S., Hammani, I., Oger, G., Le Touzé, D., 2020. δ-SPH model for multi-phase flow: how to correctly select the sound speeds of the different phases. In: SPHERIC Harbin 2020.

Dean, R.G., Dalrymple, R.A., 1991. Water Wave Mechanics for Engineers and Scientists, Vol. 2. world scientific publishing company.

Derived code, 2022. https://github.com/ncsalis/SPHERA/tree/SPHERA_v_9_0_0_NS_2P.

Di Monaco, A., Manenti, S., Gallati, M., Sibilla, S., Agate, G., Guandalini, R., 2011. SPH modeling of solid boundaries through a semi-analytic approach. Eng. Appl. Comput. Fluid Mech. 5 (1), 1–15.

Gallati, M., Braschi, G., Falappi, S., 2005. SPH simulations of the waves produced by a falling mass into a reservoir. Il Nuovo Cimento C 28 (2), 129–140.

Gómez-Gesteira, M., Cerqueiro, D., Crespo, C., Dalrymple, R., 2005. Green water overtopping analyzed with a SPH model. Ocean Eng. 32 (2), 223–238.

Gomez-Gesteira, M., Rogers, B.D., Dalrymple, R.A., Crespo, A.J., 2010. State-of-the-art of classical SPH for free-surface flows. J. Hydraul. Res. 48 (sup1), 6–27.

Gong, K., Shao, S., Liu, H., Wang, B., Tan, S.-K., 2016. Two-phase SPH simulation of fluid–structure interactions. J. Fluids Struct. 65, 155–179.

Grenier, N., Antuono, M., Colagrossi, A., Le Touzé, D., Alessandrini, B., 2009. An Hamiltonian interface SPH formulation for multi-fluid and free surface flows. J. Comput. Phys. 228 (22), 8380–8393.

Gu, S., Zheng, W., Wu, H., Chen, C., Shao, S., 2022. DualSPHysics simulations of spillway hydraulics: a comparison between single-and two-phase modelling approaches. J. Hydraul. Res. 60 (5), 835–852.

He, M., Khayyer, A., Gao, X., Xu, W., Liu, B., 2021. Theoretical method for generating solitary waves using plunger-type wavemakers and its smoothed particle hydrodynamics validation. Appl. Ocean Res. 106, 102414.

Huang, C.-J., Zhang, E.-C., Lee, J.-F., 1998. Numerical simulation of nonlinear viscous wavefields generated by piston-type wavemaker. J. Eng. Mech. 124 (10), 1110–1120.

Johnson, J.W., 1949. Scale effects in hydraulic models involving wave motion. EOS Trans. Am. Geophys. Union 30 (4), 517–525.

Krimi, A., Jandaghian, M., Shakibaeinia, A., 2020. A WCSPH particle shifting strategy for simulating violent free surface flows. Water 12 (11), 3189.

Lee, S., Ko, K., Hong, J.-W., 2020. Comparative study on the breaking waves by a piston-type wavemaker in experiments and SPH simulations. Coast. Eng. J. 62 (2), 267–284.

Lind, S.J., Rogers, B.D., Stansby, P.K., 2020. Review of smoothed particle hydrodynamics: towards converged Lagrangian flow modelling. Proc. R. Soc. Lond. Ser. A Math. Phys. Eng. Sci. 476 (2241), 20190801.

Liu, X., Lin, P., Shao, S., 2015. ISPH wave simulation by using an internal wave maker. Coast. Eng. 95, 160–170.

Liu, G.-R., Liu, M.B., 2003. Smoothed Particle Hydrodynamics: A Meshfree Particle Method. World scientific.

Lo, E.Y., Shao, S., 2002. Simulation of near-shore solitary wave mechanics by an incompressible SPH method. Appl. Ocean Res. 24 (5), 275–286.

Luo, M., Khayyer, A., Lin, P., 2021. Particle methods in ocean and coastal engineering. Appl. Ocean Res. 114, 102734.

Luo, M., Koh, C., Bai, W., Gao, M., 2016. A particle method for two-phase flows with compressible air pocket. Internat. J. Numer. Methods Engrg. 108 (7), 695–721.

Lyu, H.-G., Sun, P.-N., Huang, X.-T., Zhong, S.-Y., Peng, Y.-X., Jiang, T., Ji, C.-N., 2022. A review of SPH techniques for hydrodynamic simulations of ocean energy devices. Energies 15 (2), 502.

Manenti, S., 2018. Standard WCSPH for free-surface multi-phase flows with a large density ratio. Int. J. Ocean Coast. Eng. 1 (02), 1840001.

Manenti, S., Amicarelli, A., Todeschini, S., 2018. WCSPH with limiting viscosity for modeling landslide hazard at the slopes of artificial reservoir. Water 10 (4), 515.

Molteni, D., Colagrossi, A., 2009. A simple procedure to improve the pressure evaluation in hydrodynamic context using the SPH. Comput. Phys. Comm. 180 (6), 861–872.

Monaghan, J.J., 2005. Smoothed particle hydrodynamics. Rep. Progr. Phys. 68 (8), 1703.

Pákozdi, C., Österman, A., Stansberg, C.T., Peric, M., Lu, H., Baarholm, R., 2015. Estimation of wave in deck load using CFD validated against model test data. In: The Twenty-Fifth International Ocean and Polar Engineering Conference. OnePetro.

Rahman, M., Riordan, D., Susilo, A., Mousavizadegan, S., 2011. The Fast Fourier Transform Applied to Estimate Wave Energy Spectral Density in Random Sea State. WITPRESS LTD.

Randles, P., Libersky, L.D., 1996. Smoothed particle hydrodynamics: some recent improvements and applications. Comput. Methods Appl. Mech. Engrg. 139 (1–4), 375–408.

Rezavand, M., Zhang, C., Hu, X., 2020. A weakly compressible SPH method for violent multi-phase flows with high density ratio. J. Comput. Phys. 402, 109092.

Salis, N., 2019. Numerical Modelling of Waves in a 2D Flume (Master's thesis). University of Pavia. Faculty of Engineering - Department of Civil Engineering and Architecture.

Salis, N., Luo, M., Reali, A., Manenti, S., 2021. SPH simulation of water waves and impact with a rigid offshore structure in a 2D flume. In: The 31st International Ocean and Polar Engineering Conference. OnePetro.

SPHERA v9.0.0 (RSE SpA), 2022. https://github.com/AndreaAmicarelliRSE.

Stansberg, C.T., Baarholm, R., Kristiansen, T., Hansen, E., Rortveit, G., 2005. Extreme wave amplification and impact loads on offshore structures. In: Offshore Technology Conference. OnePetro.

Sun, P., Colagrossi, A., Marrone, S., Antuono, M., Zhang, A.-M., 2019a. A consistent approach to particle shifting in the δ-plus-SPH model. Comput. Methods Appl. Mech. Engrg. 348, 912–934.

Sun, P.-N., Luo, M., Le Touzé, D., Zhang, A.-M., 2019b. The suction effect during freak wave slamming on a fixed platform deck: Smoothed particle hydrodynamics simulation and experimental study. Phys. Fluids 31 (11), 117108.

Ursell, F., Dean, R.G., Yu, Y., 1960. Forced small-amplitude water waves: a comparison of theory and experiment. J. Fluid Mech. 7 (1), 33–52.

Vila, J., 1999. On particle weighted methods and smooth particle hydrodynamics. Math. Models Methods Appl. Sci. 9 (02), 161–209.

Violeau, D., 2012. Fluid Mechanics and the SPH Method: Theory and Applications. Oxford University Press.

Wang, P.-P., Meng, Z.-F., Zhang, A.-M., Ming, F.-R., Sun, P.-N., 2019. Improved particle shifting technology and optimized free-surface detection method for free-surface flows in smoothed particle hydrodynamics. Comput. Methods Appl. Mech. Engrg. 357, 112580.

Yan, B., Luo, M., Bai, W., 2019. An experimental and numerical study of plunging wave impact on a box-shape structure. Mar. Struct. 66, 272–287.

Yan, M., Ma, X., Bai, W., Lin, Z., Li, Y., 2020. Numerical simulation of wave interaction with payloads of different postures using OpenFOAM. J. Mar. Sci. Eng. 8 (6), 433.

Zhou, Z., De Kat, J., Buchner, B., 1999. A nonlinear 3D approach to simulate green water dynamics on deck. In: Proceedings of the Seventh International Conference on Numerical Ship Hydrodynamics, Nantes, France. pp. 1–15.

6.3 Final remarks

As previously mentioned, the multiphase model exhibited some issues, notably the formation of non-physical voids in the domain and a small gap between the two phases. These voids manifest when significant deformation with a very high velocity gradient occurs. In Section 9, several ideas are proposed to address these instabilities. Given that these instabilities arise from high-velocity gradients, a particle shifting PS scheme is proposed to mitigate tensile instability. Additionally, the small particle gap is addressed by solving the Riemann problem at the interface for particles of different densities.

7

Comparison on two Lagrangian particle methods

In March 2022, I embarked on my first Erasmus exchange abroad, which lasted for four months. In alignment with my group, I chose to join CIMNE - “Centro Internacional de Métodos Numéricos en la Ingeniería" in Barcelona, Spain. During this period, my focus remained on the development of the multiphase SPH model, particularly refining the PS scheme, as detailed further in Section 9. Additionally, I began learning and utilising the free and open-source model “Kratos multiphysics," specifically exploring the particle finite element method (PFEM).

7.1 Introduction

Following an initial learning phase, I commenced testing the model with various cases. Initially, I attempted to simulate a multiphase collapsing water column impacting a bottom-fixed structure. Figure 7.1 displays snapshots of this simulation, comparing the results obtained from the PFEM model (top panels) with those from the SPH-derived model (bottom panels). The water (heavy phase) is represented in blue, while the air (light phase) is depicted in red.

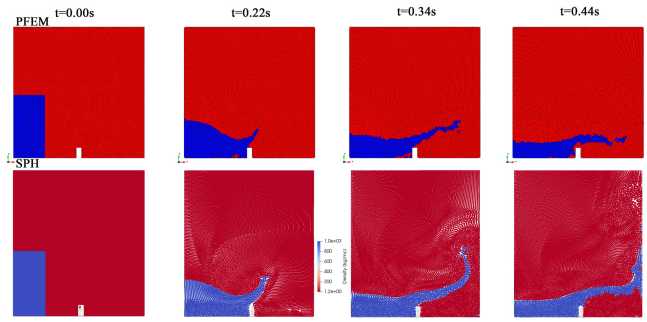

Figure 7.1: Multiphase collapsing water column and impact with bottom structure. A comparison between PFEM (top panels) and SPH (bottom panel).

The model encountered challenges in accurately simulating these flows, particularly when a heavier phase jet penetrated the lighter phase, resulting in a loss of mass conservation. Rectifying these issues necessitated significant modifications and the development of new strategies to ensure mass conservation.

Upon consultation with my supervisor at CIMNE, we decided to pivot away from this approach. Consequently, I shifted my focus to modelling regular waves. Initial tests were conducted using the same flume configuration as previous simulations. The PFEM model, leveraging finite element methods and implicit integration, demonstrated high accuracy from the outset.

Upon closer examination, it was observed that the recorded wave height at the measuring gauges was affected by reflected waves from the beach on the right-hand side. Figure 7.2 presents the fast Fourier transform of the recorded wave height, highlighting the presence of low-frequency waves reflected by the beach. Notably, resonant frequencies at approximately 0.9 and 1.4 Hz were observed, with minimal influence on the results.

To address wave reflection issues, various domain configurations were explored. Utilizing a longer domain effectively mitigated wave reflection. After successfully modelling regular waves, I proceeded to simulate solitary waves and the wave impact with a box-shaped structure. Notably, no critical issues arose during this simulation with the PFEM model.

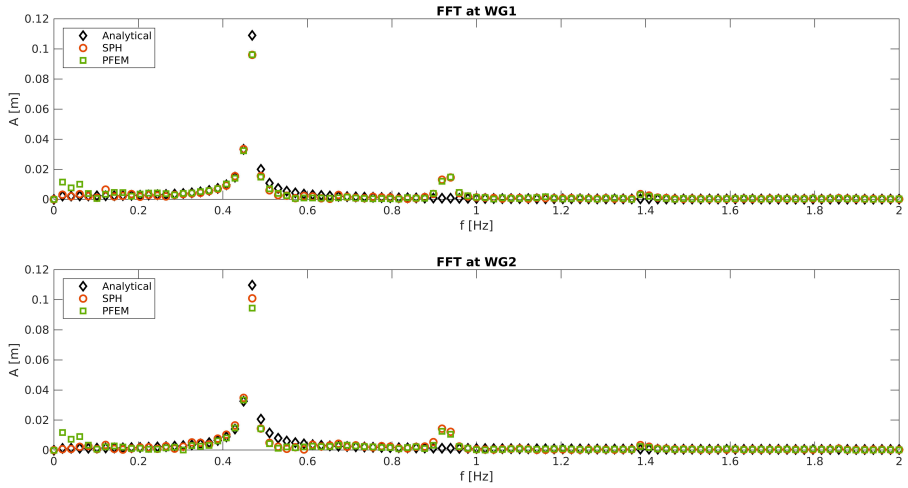

Figure 7.2: Fast Fourier transform of a regular wave, comparison between the PFEM and SPH model.

7.2 Lagrangian Particle-Based Simulation of Waves: a Comparison of SPH and PFEM Approaches

The objective of this publication is to provide an overview of two Lagrangian particle models: the SPH-derived model discussed in Section 6, and the PFEM model implemented in the multiphysics code Kratos. The aim is not only to compare the mathematical formulations of these methods but also to explore their potential applications in real engineering problems, particularly in the context of waves and wave-structure interactions.

The selected cases for comparison lie at an intermediate level between the two models. Solitary waves, as discussed in the paper, had previously been studied using the PFEM model but were new to the SPH model. Conversely, regular waves and plunging wave-structure impacts had been investigated using the SPH model but were novel to the PFEM approach.

The resulting publication, titled “Lagrangian particle-based simulation of waves: a comparison of SPH and PFEM approaches," has been featured in the journal “Engineering with Computers."

Engineering with Computers
https://doi.org/10.1007/s00366-023-01831-w

ORIGINAL ARTICLE

Lagrangian particle-based simulation of waves: a comparison of SPH and PFEM approaches

Nicolò Salis[1] · **Alessandro Franci**[2,3] · **Sergio Idelsohn**[2,4] · **Alessandro Reali**[1,5] · **Sauro Manenti**[1,5]

Received: 26 February 2023 / Accepted: 24 April 2023

Abstract
Lagrangian numerical methods are particularly suitable to reproduce flows involving large and rapid deformation of the domain, fluid splitting and coalescence, jets and sprays. The absence of the convective terms in the governing equations avoids numerical diffusion. This paper provides a comparative study between two Lagrangian particle models based on the Smoothed Particle Hydrodynamics (SPH) and the Particle Finite Element Method (PFEM). The description of the methods is provided; features and drawbacks of each method are compared and discussed. The introduced models, which represent widely used advanced analysis tools, are compared and validated in the simulation of five test cases: Two solitary waves, two regular wave trains and a non-linear wave-structure impact. Results from each model are similar and quite close to reference data. Therefore, both models have been validated against new test cases never simulated before, showing that these models can be effectively used for the analysis of regular and non-linear wave with structure impact.

Keywords SPH · PFEM · Particle methods · Solitary waves · Regular waves · Non-linear waves · Breaking waves

1 Introduction

Extreme wave events are of great concern in coastal and ocean engineering. Furthermore, these events are expected to grow in number and severity owing to climate change. Wave-structure impacts may cause severe damages to offshore and coastal structures, besides causing human and economic losses. Moreover, bores that may originate can be highly risky for seaside urban areas. Numerical simulation can be of strategic relevance to predict the effects of wave-structure impact. With the recent developments in computational capabilities, simulations are much faster, cheaper and more accessible than an experimental campaign. Moreover, numerical simulation allows the investigation of several test configuration with relative ease. Furthermore, numerical methods allow a full-scale simulation of a real event thus overcoming scale effect-induced problems, though they may need to be validated with the aid of experimental or field data. Numerical wave generation and wave-structure interaction, although widely investigated in literature with both Eulerian and Lagrangian strategies, still represent a challenging task. On the one hand, Eulerian methods need an *ad-hoc* treatment for dealing with evolving free-surface, such as the use of Level Set functions, and may suffer from numerical diffusion in the simulation of advection-dominated flows. Despite these inconveniences, Eulerian methods have been successfully employed for the generation of regular waves [1, 2], solitary and non-linear waves [3, 4] and wave-structure interaction [5, 6]. On the other hand, Lagrangian strategies allow for a natural tracking of the deforming fluid domain and modelling of the convective term. However, in mesh-based Lagrangian methods, the progressive deterioration of the mesh limits the application of these methods to small deformation problems. Lagrangian particle methods overcome this limitation either by avoiding the use of the mesh, such as in the Smoothed Particle Hydrodynamics (SPH) method [7], or by combining the use of material

✉ Nicolò Salis
nicolo.salis01@universitadipavia.it

[1] Department of Civil Engineering and Architecture DICAr, University of Pavia, 27100 Pavia, Italy

[2] International Center for Numerical Methods in Engineering, (CIMNE), 08034 Barcelona, Spain

[3] Universitat Politècnica de Catalunya, (UPC), 08034 Barcelona, Spain

[4] Institució Catalana de Recerca i Estudis Avançats, (ICREA), 08034 Barcelona, Spain

[5] Water Research Center CRA, University of Pavia, 27100 Pavia, Italy

Published online: 11 May 2023

particles with a fixed solving mesh, such as in the Material Point Method (MPM) [8] or in the Particle Finite Element Method of second generation (PFEM-2) [9], or by using an efficient remeshing procedure, such as in the Particle Finite Element Method (PFEM) [10].

In this comparative analysis, we focus our attention on the application to wave generation and structure impact of two particle-based methods, namely the SPH and the PFEM.

The SPH was introduced in [7, 11] to solve astrophysical problems. Subsequently, it has been also adapted to simulate continuum solid and fluid mechanics problems [12, 13] along with alternative methods, such as the Moving Particle Method (MPS) [14], the Consistent Particle Method [15] and the Incompressible SPH [16]. Applications of the SPH to wave propagation and fluid-solid interaction can be found in [17–21]. In this work, we will use the weakly-compressible SPH formulation presented in [20].

Since its pioneering works [10, 22], the PFEM has been applied to complex fluid dynamics problems in presence of free-surface flows and fluid–structure interaction phenomena. Previous PFEM works in the context of wave propagation problems can be found in [23–25]. In more recent publications [26, 27], complex fluid–structure interaction phenomena involving strong wave impact and structural failure were also considered. In this work, we will use the weakly-compressible PFEM formulation presented in [28].

SPH and PFEM have some common features. Both numerical techniques are classified as particle methods, since they discretise the computational domain into a discrete set of particles that move according to the equation of motion. Despite this continuous nature, both methods allow sprays formation which subsequently splash onto the main water body, thus allowing wave-breaking analysis. However, while the SPH is a mesh-less method, wihout a connection between particles, the PFEM solution is computed using a FEM mesh. In particular, the SPH embraces the concept of integral representation of functions using a kernel function (Fig. 1(a)) that mimics the Dyrac's delta but is continuous and differentiable. Instead, in the PFEM, a computational mesh is generated using the particles as mesh nodes. Then, after the appropriate definition of shape functions (Fig. 1(b)), this mesh is used for the finite element solution of the Lagrangian governing equations. To circumvent mesh distortion in large-deformation problems, the PFEM regenerates the mesh continuously via an efficient remeshing technique based on a Delaunay triangulation algorithm [29, 30].

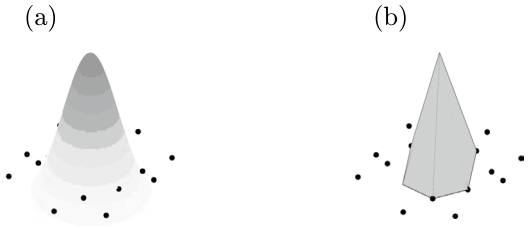

Fig. 1 Graphical representation of SPH kernel (**a**) and PFEM (FEM) (**b**) shape functions for a cloud of points

In this work, two distinct frameworks are used for the SPH and PFEM solvers. For the SPH solution, is adopted a Free and Open-Source Software (FOSS) derived from SPHERA v.9.0.0 (RSE SpA) by introducing relevant modifications of the research code [31]. Instead, for the PFEM, the formulation implemented in the PfemFluidDynamicsApplication module of the open-source code Kratos Multiphysics [32] is used.

In this work, two models based on SPH and PFEM are applied to the analysis of regular, non-linear and solitary waves with structure impact in two-dimensional flumes. Some of the investigated test cases have never been performed before and represent a validation of these models. To the best of the authors' knowledge, this document represents the first comparison (and result discussion) between these two particle methods.

The layout of the paper is described in the following. In Sect. 2, the governing equations of the problem are presented. In Sects. 3 and 4, the mathematical models and solution algorithms of the SPH and the PFEM are briefly described. In Sect. 5, the models are validated on three significant test cases. The first test concerns solitary waves, where simulation results are validated with laboratory results for two different experimental campaigns. These test cases are new for the SPH model. The second test is the generation of regular waves in a flume and the validation with the linear wave theory [33]. The third test represents a non-linear wave impacting on a fixed box-shaped structure validated with experimental results. These last two test cases are new for the PFEM model.

2 Governing equations

The Navier–Stokes equations are solved by both the SPH and the PFEM. In Eqs. (1a) and (1b), the strong form of the governing equations (momentum and mass balance equations, respectively) for a Newtonian fluid are written in an updated Lagrangian framework.

$$\rho\frac{\partial \mathbf{u}}{\partial t} - \nabla\cdot\left(2\mu\left(\frac{1}{2}\left(\nabla\mathbf{u}+\nabla\mathbf{u}^T\right) - \frac{1}{3}(\nabla\cdot\mathbf{u})\mathbf{I}\right) - p\mathbf{I}\right) = \mathbf{b} \qquad \text{in } \Omega_t\times(0,\tau) \tag{1a}$$

$$\frac{\partial \rho}{\partial t} + \rho\nabla\cdot\mathbf{u} = 0 \qquad \text{in } \Omega_t\times(0,\tau) \tag{1b}$$

Where $\mathbf{u}$ is the velocity vector, p is the pressure, $\mathbf{b}$ is the body force per unit volume, μ is the fluid dynamic viscosity, ρ is the density, t is the time, Ω_t is the updated computational

domain, τ is the total time duration, and $\mathbf{I}$ is the identity second-order tensor. We remark that both the SPH and the PFEM strategies used in this work are based on a quasi-incompressible formulation. We also remark that Eq. (1b) can be re-written by substituting the density with the pressure as follows

$$\frac{\partial p}{\partial t} + \kappa \nabla \cdot \mathbf{u} = 0 \qquad \text{in } \Omega_t \times (0, \tau) \tag{2}$$

where κ is the material bulk modulus which is defined as $\kappa = \rho c^2$, being c the speed of sound in the medium. System (1) is complemented by the following boundary conditions

$$\mathbf{u} = \hat{\mathbf{u}} \qquad \text{on } \Gamma_v \tag{3a}$$

$$\boldsymbol{t} = \hat{\mathbf{t}} \qquad \text{on } \Gamma_t \tag{3b}$$

being $\boldsymbol{t}$ the normal projection of the stress tensor on the fluid boundaries, $\hat{\mathbf{u}}$ the prescribed velocities on the Dirichlet boundary (Γ_v), and $\hat{\mathbf{t}}$ the tractions acting on the Neumann boundary (Γ_t), with $\Gamma_v \cup \Gamma_t = \partial\Omega_t$ and $\Gamma_v \cap \Gamma_t = \varnothing$.

3 SPH formulation

The SPH model utilised in this work has been obtained by independently introducing relevant modifications in the original code SPHERA v.9.0.0 (RSE SpA) [31]. This derived code [34] is redistributed on Github (bound to the GNU-GPL license and in respect of SPHERA copyright terms). For a full description of the derived model, the reader is referred to [20]. For further information, interested readers are referred to the documentation of the original SPHERA model [31, 35–38].

3.1 SPH approximation of governing equations

The SPH approximation of the mass balance equation (Eq. (1b)) reads

$$\begin{aligned}\left\langle \frac{d\rho}{dt} \right\rangle_0 &= \sum_b \rho_0 (\mathbf{u}_b - \mathbf{u}_0) \cdot \nabla W \frac{m_b}{\rho_b} \\ &+ 2\rho_0 \int_{V'_h} [(\mathbf{u}_w - \mathbf{u}_0) \cdot \mathbf{n}]\mathbf{n} \cdot \nabla W dx^3 \\ &+ C_s + 2\delta c_0 h \sum_{b=1}^{N} \psi_{0b} \frac{\mathbf{r_{0b}} \cdot \nabla W}{||r_{0b}||^2} \frac{m_b}{\rho_b}\end{aligned} \tag{4}$$

where the notation "$\langle\rangle$" indicates the SPH particle -discrete-approximation. In this equation the computational particle has subscript 0 while the neighbouring particle has subscript b. ρ is the particle density, m is the particle mass, W is the kernel function and r_{0b} the relative distance between the computational particle and the neighbouring one. $\mathbf{n}$ is the outward normal vector to the boundary surface, c_0 is the artificial sound celerity, and h is the smoothing length. δ is the diffusive coefficient and ψ_{0b} is the diffusive term formulated accordingly to [39]. The subscripts s and w refer, respectively, to the generic neighbouring surface body particle and the solid boundary [37]. In Eq. (4), the term C_s represents the fluid-body interaction contribution for the mass balance equation and is defined as

$$C_s = 2\rho_0 \sum_s [(\mathbf{u}_s - \mathbf{u}_0) \cdot \mathbf{n}_s] \nabla W_s \varpi_s \tag{5}$$

where ϖ_s is the body particle volume. This scheme first introduced in [40] can be interpreted as a discretisation of the semi-analytic approach. We also remark that the last term of Eq.(4) represents a diffusive contribution that it is needed to obtain a stable pressure field solution [39]. Using the same notation as Eq. (4), the SPH approximation of the momentum balance equation (Eq. (1a)) reads

$$\begin{aligned}\left\langle \frac{d\mathbf{u}}{dt} \right\rangle_0 &= -\mathbf{g} + \frac{1}{\rho_0} \sum_b (p_b + p_0) \nabla W \frac{m_b}{\rho_b} \\ &+ 2\frac{p_0}{\rho_0} \int_{V'_h} \nabla W dx^3 \\ &- \nu_m \sum_b \frac{m_b}{\rho_b} \frac{1}{r_{0b}^2} (\mathbf{u}_b - \mathbf{u}_0) \cdot (\mathbf{x}_b - \mathbf{x}_0) \nabla W \\ &- 2\frac{\nu_m}{\rho_{0in}} (\mathbf{u}_w - \mathbf{u}_0) \cdot \int_{V'_h} \frac{1}{r_{0_w}^2} (\mathbf{x} - \mathbf{x}_0) \nabla W dx^3 \\ &+ \mathbf{a}_s + 2\nu_0 (\mathbf{u}_w - \mathbf{u}_0) \int_{V'_h} \frac{1}{r} \frac{\partial W}{\partial r} dx^3\end{aligned} \tag{6}$$

where $\mathbf{g}$ is the gravity acceleration, $\mathbf{x}$ is the position vector of the particle, ρ_{0in} is the initial density of particle 0. The artificial viscosity is defined as $\nu_m = \rho_{0in} \frac{\alpha \cdot h \cdot c}{\rho_0}$ where α is the artificial viscosity coefficient ranging between 0.01 and 0.1. Artificial viscosity introduced by [11] bears no relation to real fluid viscosity, while it mimics its behaviour [41]. Moreover, its design allows the simulation of shock phenomena and stabilises the numerical algorithm [42]. For a thorough study on the influence of the artificial viscosity coefficient, the reader is referred to [19, 20].

The term a_s of Eq.(6) is the fluid-body interaction contribution for the momentum balance equation and is defined as

$$\mathbf{a}_s = \sum_s \left(\frac{p_s + p_0}{\rho_0^2} \right) \nabla W_s m_s \tag{7}$$

we remark that the artificial viscosity term of Eq. (6) has been modified to depend on particle volume instead of mass. This allows to obtain stable simulations of multiphase flows with high density ratio. The system of equations (4) and (6)

is closed by the linearised barotropic equation of state for slightly compressible fluids, which reads

$$p = c_{ref}^2(\rho - \rho_{ref}) + p_0 \tag{8}$$

In SPH, the artificial sound speed c_{ref} must be assumed at least ten times higher than the maximum fluid velocity to guarantee a relative density variation at most equal to 1% [42] and the subscript *ref* stands for the reference state. Concerning the boundary conditions, we remark that no constraints are needed to define the free surfaces. Solid walls are treated with the semi-analytic approach [36] where at the boundaries, the kernel support can partially lie outside the fluid domain. The integral terms in Eqs. (4) and (6) express these boundary contributions. Such terms represent the convolution integral on the portion of the kernel support V_h' that lies outside of the domain and is filled with body particles. A second-order staggered Leapfrog scheme is used to integrate in time the governing equations [38]. The stability criterion for the time integration is given by:

$$dt = min_0 \left\{ 0.05\frac{2h^2}{\nu}; CFL\frac{2h}{c_{ref} + |\mathbf{u}|} \right\} \tag{9}$$

Where the utilised viscosity ν is the real fluid viscosity.

3.2 SPH solution scheme

The momentum and the mass balance equations are solved as described below. After the first initialisation of the particles in the domain, i.e., neighbouring search and computations of: $\mathbf{r_{0b}}$, W, ∇W for the background grid, at each time step the procedure is given by the following steps

1. Evaluation of the integrals for the solid neighbouring surface contour
2. Computation of the momentum balance equation and body dynamics by Eq. (6)
3. Leapfrog integration scheme applied to momentum balance equation
4. Update the particle position (Lagrangian trajectory)
5. Neighbouring search and computations of: $\mathbf{r_{0b}}$, W, ∇W
6. Evaluation of the integrals for the solid neighbouring surface contour
7. Computation of the mass balance equation (4)
8. Leapfrog integration scheme applied to mass balance equation
9. Pressures computations via the equation of state (8)

4 PFEM formulation

In this work, the PFEM solution is obtained through the velocity-pressure solver for Newtonian fluids presented in [28]. As in standard PFEM formulations, equal order of interpolation (linear) for both the velocity and the pressure unknowns. The Finite Calculus (FIC) stabilisation [28] is adopted to avoid spurious oscillations due to the unfulfillment of the so-called *inf-sup* condition [43]. The formulation is implemented in the open-source code Kratos Multiphysics [32]. In the following sections, the basic features of the method are presented.

4.1 FEM discretisation

In the PFEM, the balance equation system (1) is discretised according to the standard Galerkin Finite Element Method (FEM). The full derivation of the FEM solution scheme is considered out of the scope of this work and only the final discretised, FIC-stabilised form is given.

Following the variational equation approach in [28], the governing equations (1a) and (2) can be written in matrix form as

$$\boldsymbol{M}_0\dot{\bar{\boldsymbol{u}}} + \boldsymbol{K}\bar{\boldsymbol{u}} + \boldsymbol{Q}\bar{\boldsymbol{p}} = \boldsymbol{f} \tag{10}$$

$$\boldsymbol{M}_1\dot{\bar{\boldsymbol{p}}} + \boldsymbol{Q}^T\bar{\boldsymbol{u}} = \boldsymbol{S}_\tau \tag{11}$$

where $\boldsymbol{M}_0$ is the mass matrix, $\boldsymbol{K}$ is the viscous matrix, $\boldsymbol{Q}$ is the gradient matrix, $\boldsymbol{f}$ is the external force vector, $\boldsymbol{M}_1$ is the bulk matix, and $\boldsymbol{S}_\tau$ includes all terms arising from the FIC stabilisation procedure. The vectors $\bar{\boldsymbol{u}}$ and $\bar{\boldsymbol{p}}$ contain respectively the nodal velocities and nodal pressures. The notation $\dot{\bar{\boldsymbol{a}}}$ stands for the first material derivative of vector $\bar{\boldsymbol{a}}$. The definition of all the matrices introduced in Eqs. (10) and (11) is provided in appendix A. For the full mathematical development of the discretised equations the reader is referred to [28].

4.2 PFEM solution scheme

At each time step $[^n t; ^{n+1} t]$ of duration Δt, the linear momentum and the mass balance equations are solved iteratively for the nodal velocities and pressures. In the following, the main steps of this implicit PFEM scheme are summarised.

At each non-linear iteration i:

1. Compute the nodal velocities $\bar{\boldsymbol{u}}^{i+1}$ from Eq.(10)
2. Update the nodal coordinates: $^{n+1}\bar{\boldsymbol{x}}^{i+1}$
3. Compute the nodal pressures $\bar{\boldsymbol{p}}^{i+1}$ from Eq.(11)

4. Check the convergence: $\frac{\|\bar{\boldsymbol{u}}^{i+1} - \bar{\boldsymbol{u}}^{i}\|}{\|^{n}\bar{\boldsymbol{u}}\|} \leq e_u$, $\frac{\|\bar{\boldsymbol{p}}^{i+1} - \bar{\boldsymbol{p}}^{i}\|}{\|^{n}\bar{\boldsymbol{p}}\|} \leq e_p$
   with e_u and e_p prescribed error norms for velocities and pressures.
   If condition 4 is not fulfilled, return to 1 with $i \leftarrow i + 1$.

The nodal positions, thus the mesh, are continuously updated in a Lagrangian fashion according to the solution of the governing equations. To maintain a good quality of the discretisation in large deformation problems, such as the ones considered in this work, the mesh is continuously rebuilt. This is done by erasing all the elements of the previous (distorted) mesh but maintaining the nodes. The new mesh is built over this distribution of nodes by combining the Delaunay triangulation [44] and the Alpha-Shape [45] method. The main steps of the PFEM remeshing are summarised in the following.

At each remeshing step:

1. Erase the elements of the previous mesh and maintain the nodes
2. Create a Delaunay triangulation
3. Do Alpha-Shape check to rebuild the boundaries

On one hand, the Delaunay triangulation guarantees a good quality of the elements for the given cloud of nodes, on the other hand, the Alpha-Shape method allows recovering the physical contours of the computational domain with good accuracy. The result is a good-quality mesh ready to be used for the FEM solution of the following computational step. We also remark that in the PFEM, as for the SPH, the fluid-free contours are automatically tracked by the solution algorithm. More details about the PFEM remeshing procedure and its implications on the PFEM solution are provided in [29].

5 Results and discussion

5.1 Solitary waves

Two solitary wave types generated by piston wave-maker are considered for testing the SPH and PFEM models. In Fig. 2, a sketch of the two numerical wave tanks is plotted. For both domains, on the left-hand side there is a piston-type wave-maker. Figure 2 (a) shows the domain for the so-called wave-type A. On the right-hand side of the domain, there are two beaches with a 1:10 slope ratio that are connected by a flat bottom. The wave height is measured at the toe of the upper beach ($x = 90m$) with the gauge *WM*. In the reference laboratory experiments [46], the wave impacted and damaged a reinforced concrete wall that was placed at the right-hand side of the flume. The 3D wave-wall interaction has been fruitfully reproduced with the PFEM method in [26].

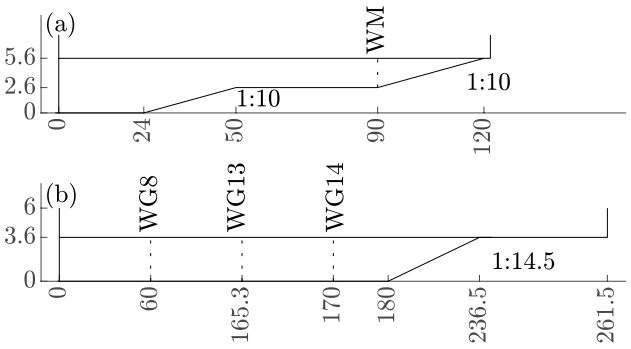

Fig. 2 Numerical wave tanks for solitary waves. **a** Domain for wave-type A [26, 46] **b** domain for wave-type B [27, 47, 48]. In this figure, all measures are in meters

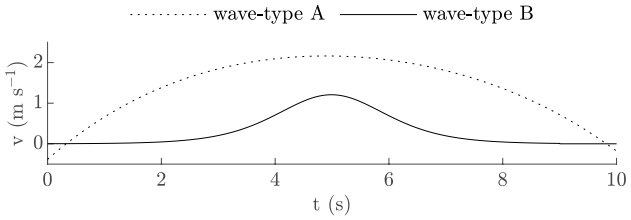

Fig. 3 Velocity input for paddle wave-maker. **a** Solitary wave-type A, **b** solitary wave-type B

Figure 2 (b) shows the domain for wave-type B. This wave type reproduces the laboratory experiment carried out in the large wave flume at the Coastal Research Centre in Hannover [47–49]. At the right-hand side of the domain there is a sloped beach with a 1:14.5 ratio. The sloped beach is followed by a flat part where a bore originates from the solitary wave breaking. The wave height is monitored at three *WG* gauges. This experiment has been reproduced in [27] coupling an Eulerian method and the PFEM method. This is the first attempt to reproduce these wave generation and propagation with SPH. Figure 3 shows the velocity input for the wave-maker for both wave types. While both waves are generated in ten seconds, the propagation in the channel is different: wave-type A propagates in ten seconds while wave-type B propagates in forty seconds. Table 1 shows the spatial resolution and the particle/node number for each wave-type. The wave type is defined in the first column of the table while on the second column the run number is reported to distinguish simulations with different spatial resolution. The third and fourth columns show the particle spacing **dx** respectively for the SPH and PFEM model. The fifth column shows

Table 1 Simulation nodes at different resolutions - solitary waves

Wave	run	dx (m)		End time (s)	N (-)	
		SPH	PFEM		SPH	PFEM
A	1	0.25	0.25	20.00	6451	8174
A	2	0.1	0.1	20.00	41120	48315
A	3	0.05	0.05	20.00	164480	191661
B	1	0.1	0.1	50.00	75510	88395
B	2	0.05	–	50.00	302040	–

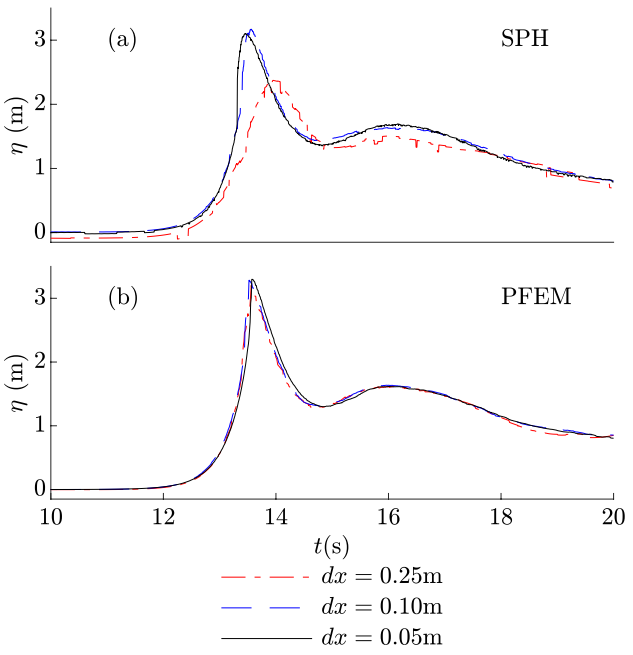

Fig. 4 Solitary wave-type A: wave elevation at wave gauge WM obtained with spatial discretisation $dx = 0.25\,m$, $dx = 0.1\,m$, and $dx = 0.05m$. **a** SPH solution, **b** PFEM solution

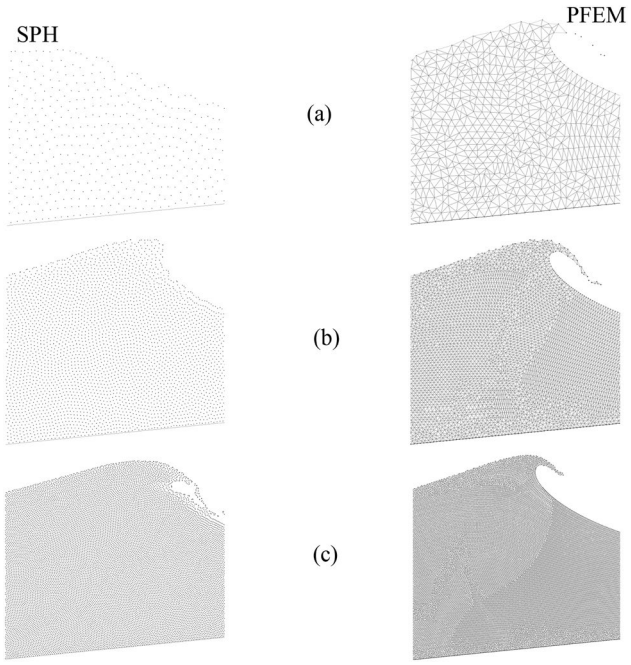

Fig. 5 Solitary wave-type A: domain discretisation at $t = 14.0s$. Left-hand panels SPH, right-hand panels PFEM. **a** $dx = 0.25m$, **b** $dx = 0.1m$, **c** $dx = 0.05m$

the physical simulation end time. On the sixth and seventh columns the particle number (number of nodes) **N** is reported respectively for the SPH and PFEM model.

5.1.1 Solitary wave-type A

This solitary wave, due to the lower particle number and simulation time, is chosen to perform a sensitivity analysis on the particle/mesh size. Table 1 shows the simulation runs where three different spatial resolutions have been considered. Figure 4 shows wave elevation at *WM* obtained with the SPH and the PFEM models for three different resolutions. These graphs show that the change in resolution has a greater impact on the SPH (Fig. 4 (a)) model than on the PFEM (Fig. 4 (b)). In fact, negligible differences in the wave elevation are exhibited with the PFEM model for the selected mesh sizes. Instead, the wave elevation obtained with the SPH model grows significantly from the coarse to fine resolutions and a very fine mesh is needed to obtain a convergent result. The best result being achieved with the fine spatial resolution. The trough, the second crest and the subsequent descending part of the wave elevation are close to the PFEM model and the experimental wave elevation.

Figure 5 shows a detail of the SPH and PFEM particles/nodes at $t = 14.0s$ (wave breaking point) for the three different resolutions. As discussed before, the effect of resolution increase on the numerical results is more significant in the SPH than in the PFEM. Although the number of particles is similar between models (Table 1), at the coarsest resolution (Fig. 5 (a)) the finite element discretisation allows to obtain a more faithful representation of the wave breaking than SPH, and the wave evolves into a plunging breaker. With the middle spatial resolution (Fig. 5 (b)), the accuracy of SPH is greatly improved but the wave breaking is still not so accurately reproduced. At the higher spatial resolution analysed

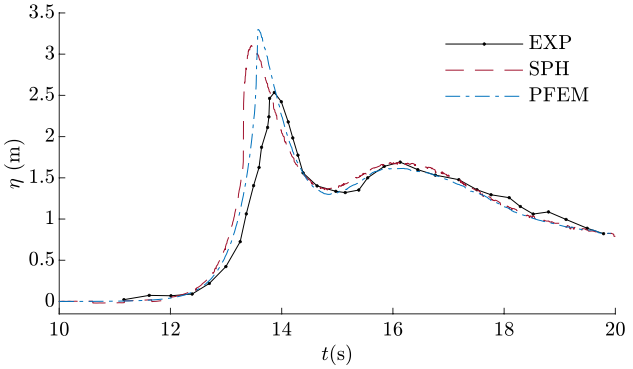

Fig. 6 Solitary wave-type A: wave elevation at wave gauge WM obtained experimentally [46] and numerically with SPH and PFEM

(Fig. 5 (c)) the discretisation is finally sufficient to model the breaking wave with the SPH. Figure 5 also confirms that in the SPH model the wave breaks before the PFEM model. In Fig. 5 (c), the SPH plunging breaker is falling and closing onto the main water body. With the PFEM model, the breaking point is much less influenced by different resolutions. Moreover, the crest gets tighter when resolution increases and with the highest resolution analysed no particles detach from the crest.

Figure 6 shows the wave elevation at *WM*. Numerical results with the resolution of $dx = 0.05m$ are compared with the experimental results of [46]. The first SPH peak in Fig. 6 is slightly shifted to the left. The SPH wave breaks slightly earlier than the wave generated with the PFEM model. Therefore the first SPH peak is slightly lower than the PFM one. Both models overestimate the experimental peak at $14s$. The wave gauge *WM* is placed at the toe of the upper slope change where the solitary wave becomes a plunging breaker, thus affecting the experimental measure of the wave elevation at the peak. Both models produce a wave profile with negligible differences from the experimental wave. This is particularly evident in the trough and during the descending part of the wave from $t = 14.5s$ to $t = 20s$.

5.1.2 Solitary wave-type B

The original experiment [48] focused on the propagation of the wave in the flat beach and subsequent impact with fixed structures. Based on the previous results, for the PFEM mesh, a resolution coarser than the one adopted for the SPH is used. In particular, with the PFEM, suitable results are achieved with $dx = 0.1m$, while the SPH needs a particle size of $dx = 0.05m$. Even though mesh/particle resolutions are different, the models produce similar results. Figure 7 shows the wave elevation obtained numerically and experimentally at the three gauges *WG*8, *WG*13, and *WG*14. In this figure, two SPH wave

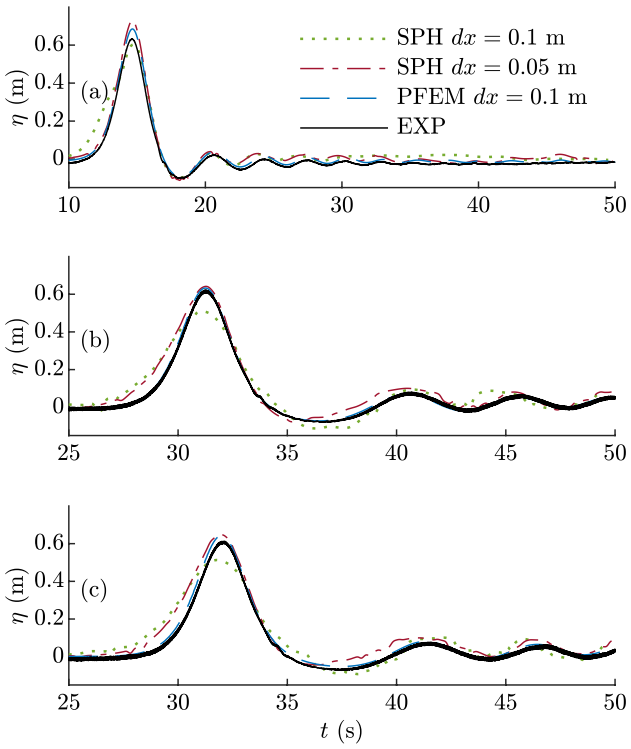

Fig. 7 Solitary wave-type B: wave elevation at sensors: **a** *WG*8, **b** *WG*13, **c** *WG*14 [48]

elevations are shown with $dx = 0.1$ m and with $dx = 0.05$ m. The first one has the same resolution as the PFEM simulation. As discussed for Fig. 4 at this resolution the SPH model does not converge. Once spatial convergence is achieved by both models (with different discretisation) a fair comparison can be maid, showing that results are similar and rather close to the experiment. At *WG*8, Fig. 7 (a) both models gives a slightly higher wave elevation at the $t = 15.0s$ crest. The models capture the wave train from $t = 18.0s$ to $t = 35.0s$ in both phase and height. For WG13, and WG14, corresponding to Fig. 7 (b) and (c), similar considerations can be made. The wave crest at $t \approx 32.0\,s$ and the following wave train of smaller amplitude are well estimated with negligible differences between both models and the experiment.

Figure 8 shows the velocity magnitude contour of the solitary wave propagating in the channel. In the PFEM model the highest velocities are centred under the wave crest moving in the channel. In the SPH model, the highest velocities seem diffused in front of and behind the wave crest. The maximum velocity captured at the crest top is $\approx 1ms^{-1}$. Close to the bottom, the SPH velocity is attenuated, while the PFEM contours show higher velocities.

Figure 9 shows the pressure contour. Both models show a quasi hydrostatic distribution, with the PFEM contour

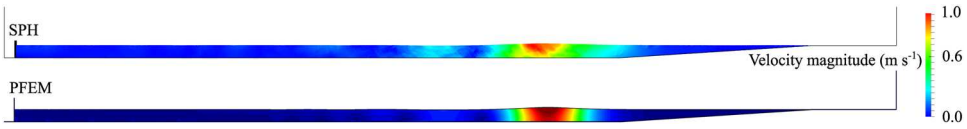

Fig. 8 Solitary wave-type B: velocity magnitude contour at $t = 30.0s$. SPH $dx = 0.05$ m, PFEM $dx = 0.1$ m

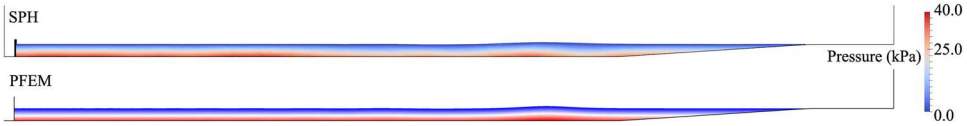

Fig. 9 Solitary wave-type B: pressure contour at $t = 30.0s$. SPH $dx = 0.05$ m, PFEM $dx = 0.1$ m

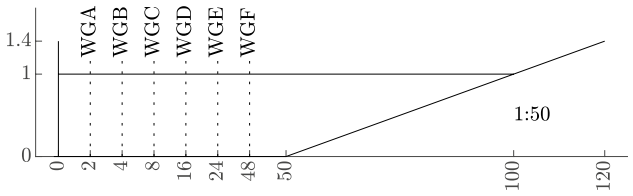

Fig. 10 Numerical wave tank for regular waves. In this figure, all measures are in meters

being slightly more consistent than the SPH one. The pressure increase under the wave crest is detected by both models and is consistent with the increase of free surface height in shallow water.

5.2 Regular waves

The domain is a slight modification of that used in previous SPH simulations [19, 20] to avoid wave reflection due to the sloped beach. Figure 10 shows a sketch of the updated domain, with a milder beach slope 1:50 that allows to reduce wave reflection at measuring gauges. The flat part of the domain has been extended to 50 m. On the left-hand side, there is the piston-type wave-maker. Wave heights are monitored with six wave gauges placed at an increasing distance from the wave-maker with imposed kinematic. This is the first time that the PFEM model is tested on the generation and propagation of regular wave trains in a flume.

Biŕsel [50] derived the analytical solution for different wave-maker types. The wave-maker stroke is set to obtain the target wave height. Equation (12) shows the time-velocity law imposed on the wave-maker. S_0 is the maximum displacement (stroke) of the wave-maker, ω is the angular frequency related to the wave period T, and t is the time variable. The following exponential terms are introduced to avoid inertial effects at early simulation stages:

$$u_x(t) = \frac{1}{2} S_0 \omega cos(\omega t) \cdot \left(1 - exp\left(-\frac{t}{T}\right)\right) + \frac{S_0}{2} sin(\omega t) \cdot exp\left(-\frac{t}{T}\right)/T \tag{12}$$

The still water height is $h_{still} = 1m$ and is constant in both experiments; wave parameters are obtained with the procedure illustrated in [19, 20]. Two wave types, from Ursell [51] are reproduced. Table 2 summarises the target characteristics of the waves. **T** is the wave period, **H** is the wave height, **L** is the wavelength, **S** is the maximum paddle stroke, **c** is the wave celerity, $\mathbf{h_{still}}$ is the still water height in the flume, **kh** is the wave relative depth, **H/L** is the wave steepness, **H/S** is the wave height to stroke ratio. One may refer to [19, 20] for a short theoretical description of wave generation. Table 3 shows the adopted dx, the simulation time and the node / particle number for the two models. Figure 11 shows the wave elevation at the wave gauges in the numerical flume for wave-type U15 and U24. Regular wave-types are compared with their respective analytical solution. With both models, the phase and wave heights are accurately reproduced. This numerical flume, with the 1:50 sloped beach, prevents wave reflection. Moreover, this sloped beach prevents mass losses in the PFEM model. In the flat part of the channel both models show negligible wave height reduction with respect to the analytical solution.

Figure 12 (a) shows the magnitude velocity contours for both models at $t = 50s$. The results of the two models are comparable. The velocity at wave crests, through, and nodes is well simulated. Slightly lower velocities are obtained with the PFEM model than with the SPH one. It is worth noting that the SPH velocity field is affected by negligible

Table 2 Regular waves characteristics

Wave	T(s)	H (m)	L (m)	S(m)	c (m s−1)	h_{still} (m)	kh	H/L (–)	H/S (–)
U15	3.01	0.084	8.73	0.12	2.9	1.00	0.72	0.0096	0.7
U24	2.15	0.236	5.76	0.22	2.68	1.00	1.09	0.0409	1.05

Table 3 Simulation nodes - regular waves

Wave	dx (m)		End time (s)	N (-)	
	SPH	PFEM		SPH	PFEM
U15	0.025	0.025	51.0	187500	143325
U24	0.025	0.025	56.0	187500	143325

numerical noise. The dashed box is magnified in Fig. 12 (b) where the velocity vector field under the wave is shown. On the left-hand side, there is the node before the wave crest, where the horizontal component of velocity is null and the vertical component is directed downwards. Under the wave crest the vertical component of velocity is null and the horizontal component is directed along the wave propagation

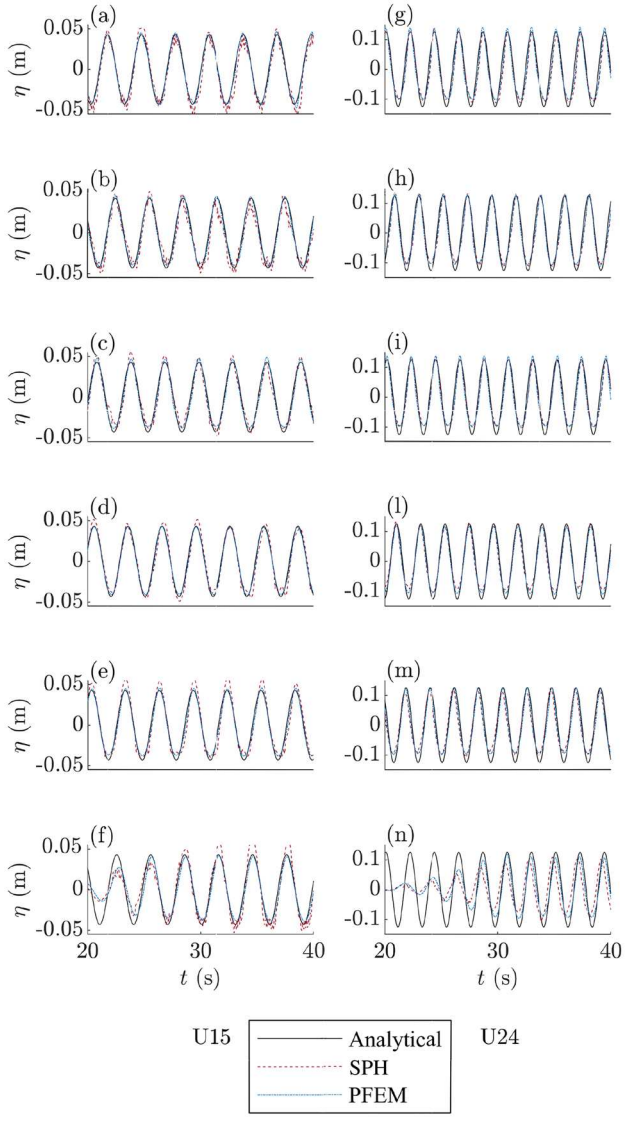

Fig. 11 Regular wave elevation at measurement gauges. Wave-type U15: left panels; wave-type U24: right panels. (**a**) (**g**) WGA, (**b**) (**h**) WGB, (**c**) (**i**) WGC, (**d**) (**l**) WGD, (**e**) (**m**) WGE, (**f**) (**n**) WGF

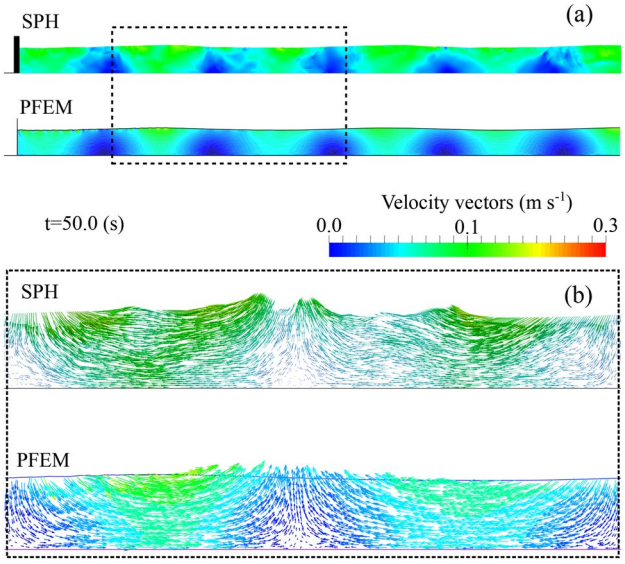

Fig. 12 Regular wave-type U15. **a** Magnitude velocity contours. **b** Velocity vectors

direction. In the node between the wave crest and the wave through, the horizontal component of the velocity vector is null while the vertical component is directed upwards. Under the wave through, the vertical velocity component is null and the horizontal velocity component is directed against the direction of wave propagation. The obtained results from both models are in accordance with the linear wave theory [33].

5.3 Non-linear wave-structure impact

The original laboratory experiment [52] was carried out in the flume at the hydraulic laboratory at the National University of Singapore. The freak wave was designed according to the focusing wave theory (13). $N = 32$ small amplitude waves meet simultaneously at a focusing point in space x_f and time t_f producing a large amplitude wave, which becomes a plunging breaker subsequently. This test case is applied here for the first time to the PFEM model and therefore used for validation.

$$\eta(x,t) = \sum_{i=1}^{N} a_i \cos[k_i(x - x_f) - 2\pi f_i(t - t_f)] \tag{13}$$

In Eq. (13), the index i refers to each linear wave component with a constant amplitude of $a_i = 0.0061m$. Frequency components f_i are equally spaced in the frequency bandwidth ranging from $f_{min} = 0.32Hz$ to $f_{max} = 0.96Hz$. The wave number k_i is computed for each linear wave component with the dispersion equation (linear theory). The characteristic wavelength is $L = 3.312m$ and the characteristic wave

celerity is $c = 2.11\ ms^{-1}$. The experimental velocity input for the wave-maker can be found in [20]. The adopted domain is shown in Fig. 13. The flat bottom is $16m$ long allowing the simulation of the non-linear wave at the focusing point $x_f = 11.104m$ (WG3). The wave is generated through a piston type wave-maker (left-hand boundary). A 1:10 sloped beach (right-hand side) prevents reflected waves. A $0.7m$ still water height is used and the wave elevation is recorded at three wave gauges WG1, WG2, and WG3. The bottom left corner of the fixed box-shaped structure is placed at $x = 12.677m$ and $y = 0.7458m$. Impact pressure time series are recorded at four probes, two on the bottom side and two on the front.

With the SPH, a resolution of $h/dx = 100$ is required to achieve accurate results for both the wave propagation and the fluid-solid impact. Instead, with the PFEM a coarser resolution would be sufficient to reproduce accurately the wave generation and propagation phenomena. However, a coarse discretisation would be not adequate to simulate satisfactorily the wave-structure impact. This is because contact elements connecting the solid obstacle and the free surface of the fluid at rest would be built during the PFEM remeshing. We remark that the distance between the water and the structure is less than $5cm$. Therefore, for both SPH and PFEM models a resolution of $h/dx = 100$, i.e., a discretisation size of $0.007m$ is used. The adopted SPH artificial viscosity parameter $\alpha = 0.7$, is slightly higher than the one used in [20]. Table 4 shows the spatial resolution dx and the computational nodes/particles utilised for each model. It is worth noting that with the PFEM model a decreased simulation time can be achieved by adopting a variable mesh size with a consequent node number reduction.

Figure 14 shows the wave elevation at the three wave gauges. The models show similar results accurately reproducing the experimental wave elevation time series at each gauge. In Fig. 14 (c) the only difference between both models and the experimental wave elevation is at $t \approx 16.5s$. In this crest both numerical models show a reduced elevation with respect to the experimental data. However, the wave height at the subsequent crest ($t \approx 18.0s$) is more accurate. The PFEM model shows slightly higher accuracy than the SPH at some crests.

Table 4 Simulation nodes - non-linear wave

dx (m)		End time (s)	N (–)	
SPH	PFEM		SPH	PFEM
0.007	0.007	20.00	278600	322764

Figure 15 shows the impact pressures. At the front probes (Fig. 15 (a) and (b)) both models reproduce adequately the positive impact pressures. Peak values are similar to the experimental one for FP1 (Fig. 15 (a)) while they are slightly underestimated for FP2 (Fig. 15 (a)). The trend of the impact load is suitably reproduced by both models. At FP1 (Fig. 15 (a)) the SPH shows some secondary oscillations that are not shown in the results of the PFEM and the experiment. At FP2 (Fig. 15 (b)) the PFEM pressure time series is quite regular. At $t = 18.78s$, a secondary pressure increase is exhibited in the experimental signal that is well captured by the SPH model. Figure 15 (c) and (d) shows the bottom pressure probes. The positive impact pressures are well reproduced by both models even if the SPH overestimates the peaks. At the bottom probes, the SPH shows some oscillations as in the experimental signal but does not capture negative values. The PFEM model shows a regular trend with no oscillations and values close to the averaged

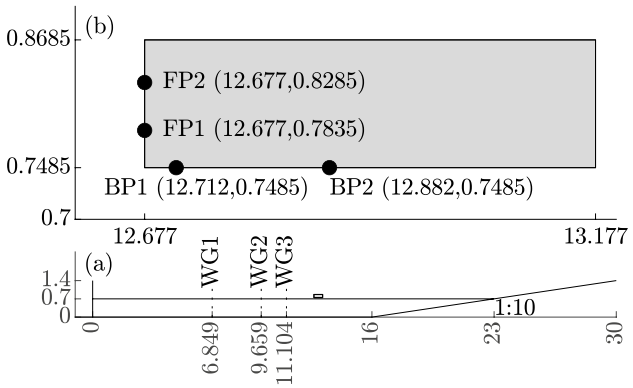

Fig. 13 Non-linear wave-structure impact. **a** Numerical flume. **b** Structure close-up.In this figure, all measures are in meters

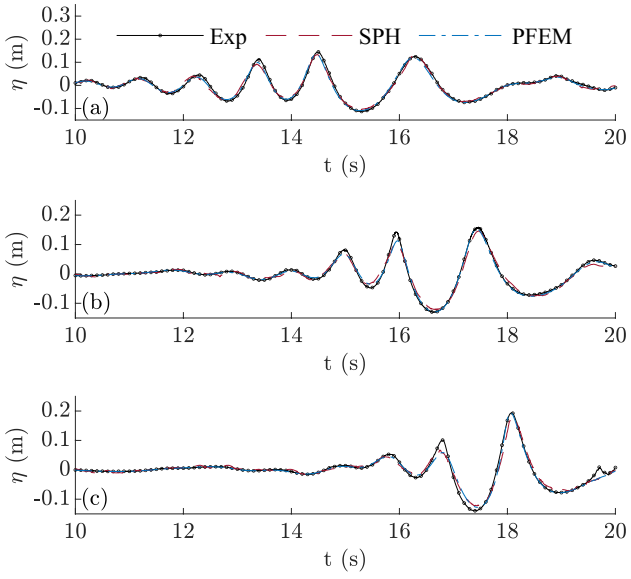

Fig. 14 Non-linear wave elevation at the gauges: **a** WG1, **b** WG2, **c** WG3

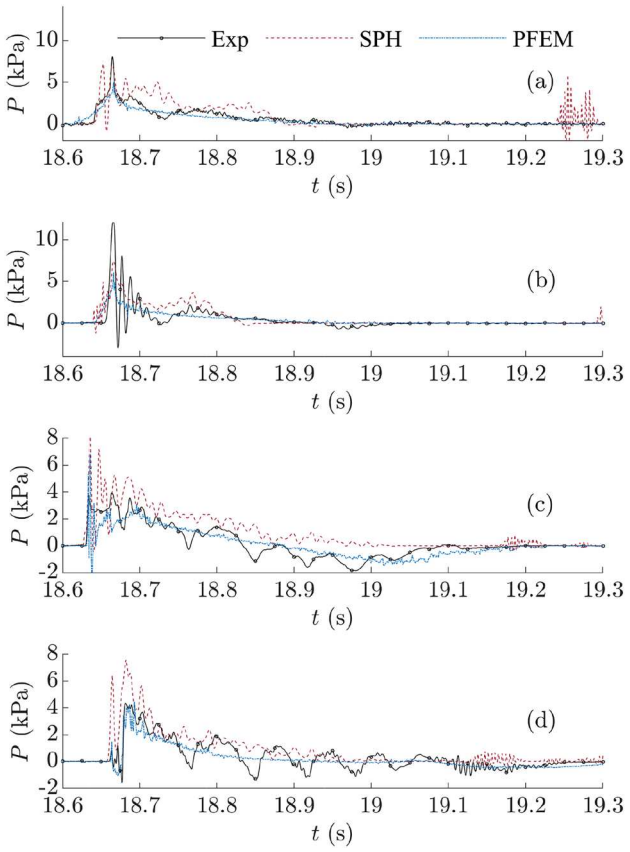

Fig. 15 Non-linear wave-structure impact pressure time series at the structure probes [52]. **a** FP1 **b** FP2 **c** BP1 **d** BP2

experimental signal. The time series of both models shows, on average, a similar trend to the experimental time series. At the bottom probes, the SPH computes slightly higher pressure values than the experiment and PFEM model. At BP1 (Fig. 15 (c)) from $t \approx 18.85s$ to $t \approx 19.1\,s$ strong suction pressures are recorded [53]. While the SPH model cannot capture these negative pressures due to tensile instability, the PFEM model reproduces the average suction pressures adequately. Similar considerations can be made for BP2 (Fig. 15 (d)). It is worth noting that other SPH models can reproduce the negative pressures [53] when the tensile instability is properly controlled.

Figure 16 shows the pressure contours of the non-linear wave impact with the box shaped structure. The SPH and the PFEM results are shown on the left-hand and right-hand sides, respectively. In the centre, the experimental snapshots are given for comparison purposes. For each frame, pictures refer to the indicated time. The pressure contours produced by each model are quite similar. At $t = 18.69s$, just before the impact, the pressure distribution is quasi-hydrostatic. On the bottom left corner of the structure, there is a slight pressure increase, with a similar magnitude for both models. Both models produce a wave whose shape is similar to the experimental results. At $t = 18.74s$, the SPH model produces higher pressure distribution around the wetted part of the structure than the PFEM, as shown in Fig. 15. In this frame the experimental wave is plunging onto the structure, this behaviour is captured by both models obtaining a similar behaviour. At $t = 18.77s$, the PFEM pressure contour is smooth with the highest pressures around the bottom centre of the structure. The SPH shows pressure peaks in the same area, but there are some minor oscillations (owing to the fluid–structure boundary treatment). At this time the SPH wave is more similar to the experimental frame where the leading edge turns downwards. The PFEM model shows a different dynamics of the wavefront collapse. At $t = 18.82s$, the SPH model produces slightly higher pressures to the bottom of the structure than PFEM model.

6 Conclusions

This work dealt with a comparative study among two Lagrangian particle-base numerical models, namely, SPH and PFEM, applied to the simulation of regular and non-linear waves in a flume with impact onto rigid structures. The analysed test cases were two solitary waves, two regular waves and a non-linear wave. Some of these test cases are investigated here for the first time and allow validation of the models. Results show that choosing the appropriate resolution, the wave elevation and the kinematic properties of the studied waves are adequately reproduced by both models. The PFEM wave elevation is not affected by relatively coarse mesh size. Instead, the SPH wave elevation is greatly improved with a higher spatial resolution. The SPH method needs a high number of neighbouring particles to obtain reliable results with the kernel approximation. The PFEM model instead is less influenced due to the FEM discretisation, which provides good results even for coarse resolutions. This aspect was highlighted in the analysis of solitary wave-type A where the influence of particle/mesh resolution was investigated. The non-linear wave impact result also shows that to model accurate impact pressures both models require a high spatial resolution. With higher resolution, both models can reproduce the pressure time history of the non-linear wave-structure impact. The SPH models slightly higher pressures than the experimental signal. The PFEM shows a regular trend with no oscillations and values close to the averaged experimental signal. Although the models are characterised by different Lagrangian approaches, they produce very similar results. The kinematic and dynamic properties of the analysed waves are reproduced adequately by both models and the achieved results are close to the experimental / analytical results of analysed waves. Given

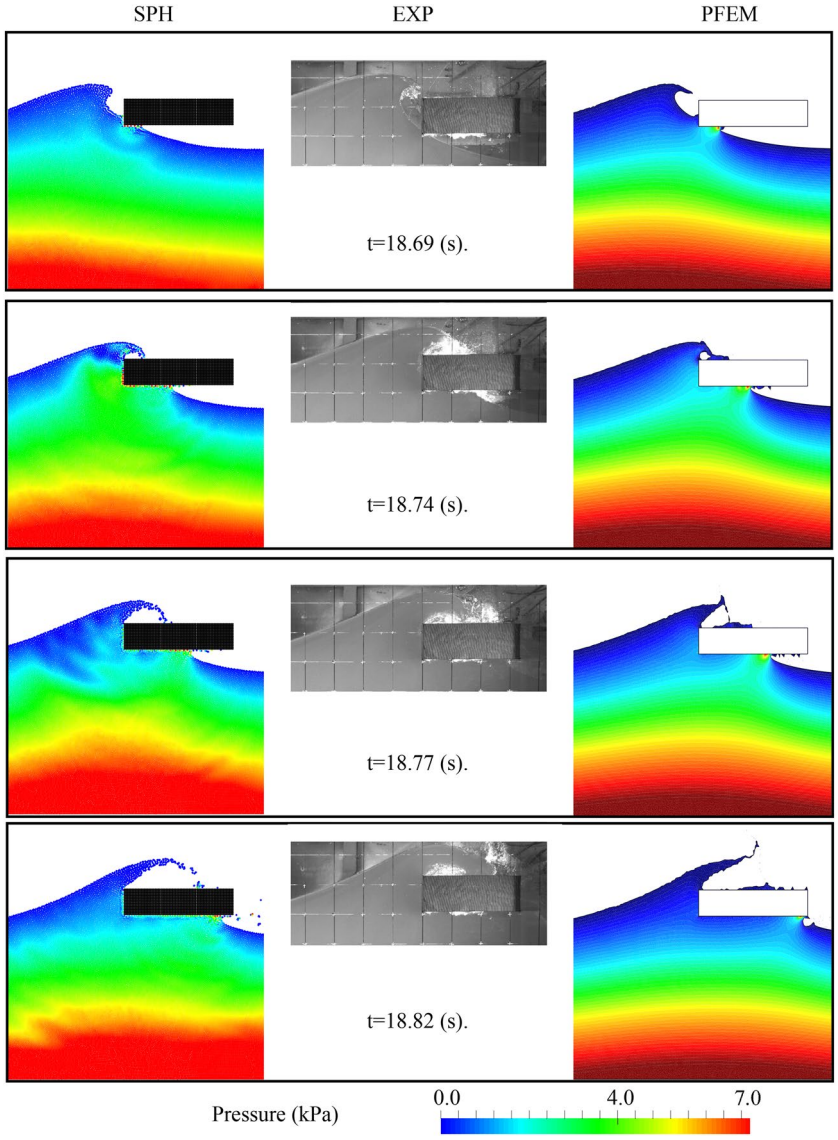

Fig. 16 Non-linear wave-structure impact pressure contours. Left-hand column SPH, right-hand column PFEM. Comparison with experimental snapshots [52]

the appropriate parameter choice and mesh / particle sizes, both models can be considered validated to reproduce a wide range of waves.

Appendix A FEM discretization

In this appendix, we give the discretised form of the FIC-stabilised Navier-Stokes equations [28], briefly introduced in Sect. 4.1.

Let us consider a computational domain discretised into N_e finite elements with n nodes. For 2D problems, as those considered in this work, linear triangles are considered, therefore $n = 3$. Linear shape functions N_i^e are defined for each node i ($i = 1, n$) of the element e, both for the velocity and the pressure field. [54–56]. Following the variational equation approach in [28], the governing equations (1a) and (1b) can be written in matrix form as

$$\boldsymbol{M}_0\dot{\bar{\boldsymbol{u}}} + \boldsymbol{K}\bar{\boldsymbol{u}} + \boldsymbol{Q}\bar{\boldsymbol{p}} = \boldsymbol{f} \tag{A1}$$

$$\boldsymbol{M}_1\dot{\bar{\boldsymbol{p}}} + \boldsymbol{M}_2\ddot{\bar{\boldsymbol{p}}} + \boldsymbol{Q}^T\bar{\boldsymbol{u}} + (\boldsymbol{L} + \boldsymbol{M}_b)\bar{\boldsymbol{p}} = \boldsymbol{f}_p \tag{A2}$$

The tensors of Eqs. (A1) and (A2) are defined as follows:

- $\boldsymbol{M}^e_{0ij} = \int_{\Omega^e} \rho N_i^e N_j \boldsymbol{I} d\Omega$
- $\boldsymbol{K}^e_{ij} = \int_{\Omega^e} \boldsymbol{B}_i^{eT} \boldsymbol{D} \boldsymbol{B}_j^{eT} d\Omega$
- $\boldsymbol{Q}^e_{ij} = \int_{\Omega^e} \boldsymbol{B}_i^{eT} \boldsymbol{m} N_j^e d\Omega$
- $M^e_{1ij} = \int_{\Omega^e} \frac{1}{k} N_i^e N_j^e d\Omega$

- $M^e_{2ij} = \int_{\Omega^e} \frac{\tau}{c^2} N^e_i N^e_j d\Omega$
- $M^e_{bij} = \int_{\Omega^e} \frac{2\tau}{h_n} N^e_i N^e_j d\Gamma$
- $L^e_{ij} = \int_{\Omega^e} \tau(\nabla^T N^e_i)\nabla N^e_j d\Omega$
- $f^e_i = \int_{\Omega^e} N^e_i \boldsymbol{b} d\Omega + \int_{\Gamma_t} N^e_i \boldsymbol{t} d\Omega$
- $f^e_{pi} = \int_{\Gamma^t} \tau N^e_i [\rho \dot{u}_n - \frac{2}{h_n}(2\mu\epsilon_n - t_n)] d\Gamma - \int_{\Omega^e} \tau \nabla^T N^e_i \boldsymbol{b} d\Omega$

These integral are defined on the element domain Ω^e or at the frontier Γ^t. The sub-index n refers to the normal component, h is the mesh size, and the stabilisation parameter τ arising from the FIC procedure is defined as follows.

$$\tau = \left(\frac{8\mu}{h^2} + \frac{2\rho}{\delta} \right)^{-1} \tag{A3}$$

being h and δ a characteristic space and time lengths, respectively.

The tensors introduced in Eqs.(A1) and (A2) are listed below.

- $\boldsymbol{D} = \mu \begin{pmatrix} 4/3 & -2/3 & 0 \\ -2/3 & 4/3 & 0 \\ 0 & 0 & 2 \end{pmatrix}$
- $\boldsymbol{B}^e_i = \begin{pmatrix} \frac{\partial N_i}{\partial x} & 0 \\ 0 & \frac{\partial N_i}{\partial y} \\ \frac{\partial N_i}{\partial y} & \frac{\partial N_i}{\partial x} \end{pmatrix}$
- $\boldsymbol{N}^e_i = N^e_i \boldsymbol{I}$
- $\nabla = \left(\frac{\partial}{\partial x}, \frac{\partial}{\partial y} \right)^T$
- $m = [1, 1, 0]^T$

Acknowledgements The authors would like to deeply thank Prof. Luo Min for his partial support for the Non-linear wave-structure impact test case. The EOS HPC cluster of the Department of Mathematics "Felice Casorati" at the University of Pavia is gratefully acknowledged.The authors acknowledge the contribution of the National Recovery and Resilience Plan, Mission 4 Component 2 - Investment 1.4 - NATIONAL CENTER FOR HPC, BIG DATA AND QUANTUM COMPUTING (project code: CN 00000013) - funded by the European Union - NextGenerationEU, as well as the support from the Italian Ministry of University and Research through the MIUR-PRIN project "XFAST-SIMS" (no. 20173C478N).

Author Contributions NS Conceptualisation, Software, Simulations, Validation, Writing-Original Draft. AF Conceptualisation, Software, Writing-Review, Supervision. SI Writing-Review & Editing AR Conceptualisation, Writing-Review & Editing SM Conceptualisation, Writing-Original Draft, Supervision.

Funding Open access funding provided by Università degli Studi di Pavia within the CRUI-CARE Agreement. The partial support by the MIUR-PRIN project XFAST-SIMS (no. 20173C478N) is gratefully acknowledged.

Code availability SPHERA v.9.0.0 derived modelhttps://github.com/ncsalis/SPHERA/tree/SPHERA_v_9_0_0_NS_2PKratos https://github.com/KratosMultiphysics/KratosGiD https://github.com/ncsalis/GiDInterface.

Declarations

Conflict of interest The authors declare that they have no known competing financial interests or personal relationships that could have appeared to influence the work reported in this paper.

References

1. Huang C-J, Zhang E-C, Lee J-F (1998) Numerical simulation of nonlinear viscous wavefields generated by piston-type wavemaker. J Eng Mech 124(10):1110–1120
2. Anbarsooz M, Passandideh-Fard M, Moghiman M (2013) Fully nonlinear viscous wave generation in numerical wave tanks. Ocean Eng 59:73–85
3. Mohapatra SC, Islam H, Hallak TS, Soares CG (2022) Solitary wave interaction with a floating pontoon based on boussinesq model and cfd-based simulations. J Mar Sci Eng 10(9):1251
4. Yan M, Ma X, Bai W, Lin Z, Li Y (2020) Numerical simulation of wave interaction with payloads of different postures using openfoam. J Mar Sci Eng 8(6):433
5. Pákozdi C, Österman A, Stansberg CT, Peric M, Lu H, Baarholm R (2015) Estimation of wave in deck load using cfd validated against model test data. In: The Twenty-fifth International Ocean and Polar Engineering Conference. OnePetro
6. Stansberg CT, Baarholm R, Kristiansen T, Hansen E, Rortveit G (2005) Extreme wave amplification and impact loads on offshore structures. In: Offshore Technology Conference. OnePetro
7. Lucy LB (1977) A numerical approach to the testing of the fission hypothesis. Astron J 82:1013–1024
8. Sulsky D, Chen Z, Schreyer HL (1994) A particle method for history-dependent materials. Comput Methods Appl Mech Eng 118(1–2):179–196. https://doi.org/10.1016/0045-7825(94)90112-0
9. Idelsohn SR, Nigro N, Gimenez J, Rossi R, Marti J (2013) A fast and accurate method to solve the incompressible navier-stokes equations. Eng Comput 30(3):197–222
10. Idelsohn SR, Oñate E, Pin FD (2004) The particle finite element method: a powerful tool to solve incompressible flows with free-surfaces and breaking waves. Int J Numer Meth Eng 61(7):964–989
11. Gingold RA, Monaghan JJ (1977) Smoothed particle hydrodynamics: theory and application to non-spherical stars. Mon Not R Astron Soc 181(3):375–389
12. Monaghan JJ (1994) Simulating free surface flows with sph. J Comput Phys 110(2):399–406

13. Monaghan J, Kocharyan A (1995) Sph simulation of multi-phase flow. Comput Phys Commun 87(1–2):225–235
14. Koshizuka S, Oka Y (1996) Moving-particle semi-implicit method for fragmentation of incompressible fluid. Nucl Sci Eng 123(3):421–434
15. Koh C, Gao M, Luo C (2012) A new particle method for simulation of incompressible free surface flow problems. Int J Numer Meth Eng 89(12):1582–1604
16. Lind SJ, Xu R, Stansby PK, Rogers BD (2012) Incompressible smoothed particle hydrodynamics for free-surface flows: A generalised diffusion-based algorithm for stability and validations for impulsive flows and propagating waves. J Comput Phys 231(4):1499–1523
17. Liu X, Lin P, Shao S (2015) Isph wave simulation by using an internal wave maker. Coast Eng 95:160–170
18. Altomare C, Tafuni A, Domínguez JM, Crespo AJ, Gironella X, Sospedra J (2020) Sph simulations of real sea waves impacting a large-scale structure. J Mar Sci Eng 8(10):826
19. Salis N, Luo M, Reali A, Manenti S (2021) Sph simulation of water waves and impact with a rigid offshore structure in a 2d flume. In: The 31st International Ocean and Polar Engineering Conference. OnePetro
20. Salis N, Luo M, Reali A, Manenti S (2022) Wave generation and wave-structure impact modelling with wcsph. Ocean Eng 266:113228. https://doi.org/10.1016/j.oceaneng.2022.113228
21. Luo M, Reeve DE, Shao S, Karunarathna H, Lin P, Cai H (2019) Consistent particle method simulation of solitary wave impinging on and overtopping a seawall. Eng Anal Bound Elem 103:160–171
22. Oñate E, Idelsohn SR, Del Pin F, Aubry R (2004) The particle finite element method. an overview. Int J Comput Methods 2:267–307. https://doi.org/10.1142/S0219876204000204
23. Oliveira T, Sánchez-Arcilla A, Gironella X (2012) Simulation of wave overtopping of maritime structures in a numerical wave flume. J Appl Math. https://doi.org/10.1155/2012/246146
24. Oliveira TCA, Sanchez-Arcilla A, Gironella X, Madsen OS (2017) On the generation of regular long waves in numerical wave flumes based on the particle finite element method. J Hydraul Res 55(4):538–556. https://doi.org/10.1080/00221686.2016.1275047
25. Mulligan R, Franci A, Celigueta M, Take W (2020) Simulations of landslide wave generation and propagation using the particle finite element method. J Geophys Res Oceans 125:2019–015873. https://doi.org/10.1029/2019JC015873
26. Oñate E, Cornejo A, Zárate F, Kashiyama K, Franci A (2022) Combination of the finite element method and particle-based methods for predicting the failure of reinforced concrete structures under extreme water forces. Eng Struct 251:113510
27. Franci A, Masó M, Cornejo A (2022) A lagrangian-eulerian procedure for the coupled solution of the navier-stokes and shallow water equations for landslide-generated waves. Adv Model Simul Eng Sci 9(1):15
28. Oñate E, Franci A, Carbonell JM (2014) Lagrangian formulation for finite element analysis of quasi-incompressible fluids with reduced mass losses. Int J Numer Meth Fluids 74(10):699–731
29. Cremonesi M, Franci A, Idelsohn S, Oñate E (2020) A state of the art review of the particle finite element method (pfem). Arch Comput Methods Eng 27(5):1709–1735
30. Meduri S, Cremonesi M, Perego U (2019) An efficient runtime mesh smoothing technique for 3d explicit lagrangian free-surface fluid flow simulations. Int J Numer Meth Eng 117(4):430–452
31. SPHERA (RSE SpA) (2023) https://github.com/GiordanoAgateRSE/SPHERA
32. KratosMultiphysics (2022) https://github.com/KratosMultiphysics/Kratos
33. Dean RG, Dalrymple RA (1991) Water wave mechanics for engineers and scientists, vol 2. World scientific publishing company
34. "Derived code" (2022) https://github.com/ncsalis/SPHERA/tree/SPHERA_v_9_0_0_NS_2P
35. Amicarelli A, Marongiu J-C, Leboeuf F, Leduc J, Neuhauser M, Fang L, Caro J (2011) Sph truncation error in estimating a 3d derivative. Int J Numer Meth Eng 87(7):677–700
36. Di Monaco A, Manenti S, Gallati M, Sibilla S, Agate G, Guandalini R (2011) Sph modeling of solid boundaries through a semi-analytic approach. Eng Appl Comput Fluid Mech 5(1):1–15
37. Amicarelli A, Albano R, Mirauda D, Agate G, Sole A, Guandalini R (2015) A smoothed particle hydrodynamics model for 3d solid body transport in free surface flows. Comput Fluids 116:205–228
38. Amicarelli A, Manenti S, Albano R, Agate G, Paggi M, Longoni L, Mirauda D, Ziane L, Viccione G, Todeschini S et al (2020) Sphera v. 9.0. 0: A computational fluid dynamics research code, based on the smoothed particle hydrodynamics mesh-less method. Comput Phys Commun 250:107157
39. Antuono M, Colagrossi A, Marrone S (2012) Numerical diffusive terms in weakly-compressible sph schemes. Comput Phys Commun 183(12):2570–2580
40. Adami S, Hu XY, Adams NA (2012) A generalized wall boundary condition for smoothed particle hydrodynamics. J Comput Phys 231(21):7057–7075
41. Manenti S, Sibilla S, Gallati M, Agate G, Guandalini R (2012) Sph simulation of sediment flushing induced by a rapid water flow. J Hydraul Eng 138(3):272–284
42. Monaghan JJ (2005) Smoothed particle hydrodynamics. Rep Prog Phys 68(8):1703
43. Brezzi F, Fortin M (1991) Mixed and hybrid finite element methods. Springer, New York
44. Edelsbrunner H, Tan TS (1993) An upper bound for conforming delaunay triangulations. Discret Comput Geom 10(2):197–213
45. Edelsbrunner H, Mucke EP (1999) Three dimensional alpha shapes. ACM Trans Graph(TOG) 13(1):43–72
46. Arikawa T (2009) Structural behavior under impulsive tsunami loading. J Disaster Res 4(6):377–381
47. Krautwald C, Stolle J, Hitzegrad J, Niebuhr P, Goseberg N, Nistor I, Sieder M (2020) Large-scale physical modelling of a broken solitary wave impact on rigid and non-rigid box-like structures. Coast Eng Proceed. https://doi.org/10.9753/icce.v36v.structures.19
48. Krautwald C, Stolle J, Robertson I, Achiari H, Mikami T, Nakamura R, Takabatake T, Nishida Y, Shibayama T, Esteban M et al (2021) Engineering lessons from september 28, 2018 indonesian tsunami: Scouring mechanisms and effects on infrastructure. J Waterw Port Coast Ocean Eng 147(2):04020056
49. Krautwald C, Von Häfen H, Niebuhr P, Vögele K, Schürenkamp D, Sieder M, Goseberg N (2022) Large-scale physical modeling of broken solitary waves impacting elevated coastal structures. Coast Eng J 64(1):169–189
50. Biésel F, Suquet F (1951) Les appareils générateurs de houle en laboratoire. La houille blanche
51. Ursell F, Dean RG, Yu Y (1960) Forced small-amplitude water waves: a comparison of theory and experiment. J Fluid Mech 7(1):33–52
52. Yan B, Luo M, Bai W (2019) An experimental and numerical study of plunging wave impact on a box-shape structure. Mar Struct 66:272–287
53. Sun P-N, Luo M, Le Touzé D, Zhang A-M (2019) The suction effect during freak wave slamming on a fixed platform deck: Smoothed particle hydrodynamics simulation and experimental study. Phys Fluids 31(11):117108
54. Zienkiewicz, O.C., Taylor, R.L.: The finite element method, volume i. Fluid dynamics (2000)
55. Oñate E (2013) Structural Analysis with the Finite Element Method. Linear Statics: Volume 2: Beams, Plates and Shells. Springer,

56. Zienkiewicz OC, Taylor RL, Zhu JZ (2005) The finite element method: its basis and fundamentals. Elsevier

7.3 Final remarks

This study demonstrates that both models yield accurate results when simulating various types of free surface waves. It strikes a good balance between the mathematical underpinnings of the models and their practical applications in engineering contexts.

8

3D modelling of wave interaction with floating tension leg moored platform

In February 2023, I embarked on my second Erasmus period, which also lasted four months. In collaboration with my research group, I chose to visit TUM -“Technische Universität München" in Munich, Germany. During this period, I advanced the development of the multiphase SPH model, including the Riemann scheme to treat the interface. Additional information can be found in Section 9. Simultaneously, I began learning, using, and contributing to the free and open-source SPH model SPHinXsys.

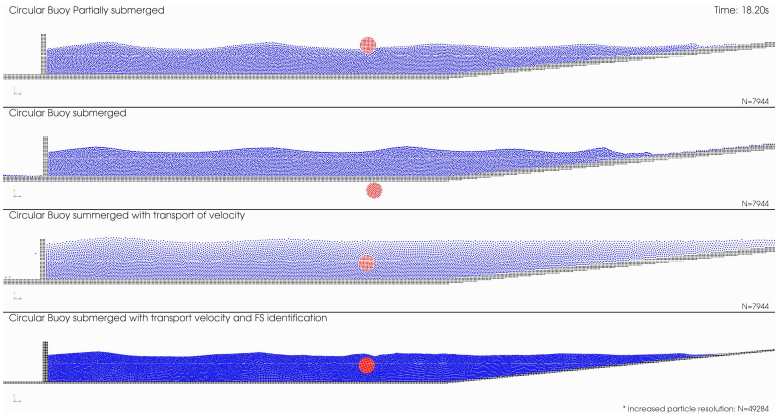

Figure 8.1: Simulation of regular waves interaction with partially submerged or submerged tethered buoy.

8.1 Introduction

During the first month and a half, my primary focus was on enhancing the SPH multiphase model outlined in Section 6. However, detailed discussions regarding these enhancements are provided in Chapter 9, and will not be covered in this chapter.

Modeling ropes in a 3D framework presents considerable challenges. My initial aim was to simulate the interaction of a plunging wave with a tension leg floating platform in 3D. Within SPHinXsys, there was already integration with a multibody model called Simbody, which is utilised for simulating the motion of rigid bodies. Simbody includes a rope model that can be used as a constraint for a rigid body. While this feature was intriguing, modelling a structure in 3D, supported by four cables, proved to be quite complex. It was essential to gain control over the model through simpler simulations.

To start, I conducted simulations involving a rope interacting with regular waves and a circular buoy. Achieving numerical stability was a significant concern throughout this process. Figure 8.1 displays snapshots from these simulations. Initially, there was an unexpected behaviour where the circular buoy was overrun by water. Once fully submerged, the buoy exhibited erratic movement. After several attempts, focusing on a submerged buoy, the model began producing satisfactory results. The transport velocity technique was particularly useful in these simulations.

However, it required careful handling to prevent the free surface from rising uncontrollably. This aspect was managed through the implementation of free surface identification, which excluded particles near the free surface from the transport of velocity.

Next, I sought to increase the complexity by modelling a structure with a complex shape, tethered with two cables. However, I encountered strange behaviour, as depicted in Figure 8.2, where the structure exhibited unexpected rotation early in the simulation.

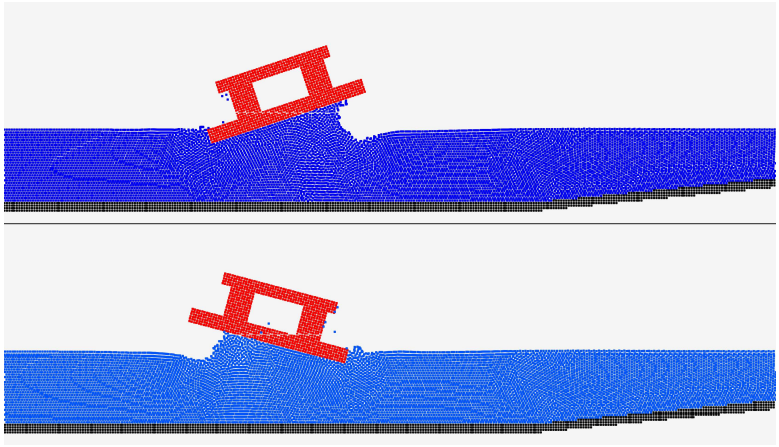

Figure 8.2: Complex shape structure rotating casually.

Upon investigation, I discovered that the inertia of the structure was not properly configured. Once the inertia was correctly set and coupled with the removal of the transport of velocity and free surface identification, the model yielded improved results. It became apparent that the utilisation of these schemes was unnecessary and computationally inefficient for this simulation, as tensile instability was not a significant issue.

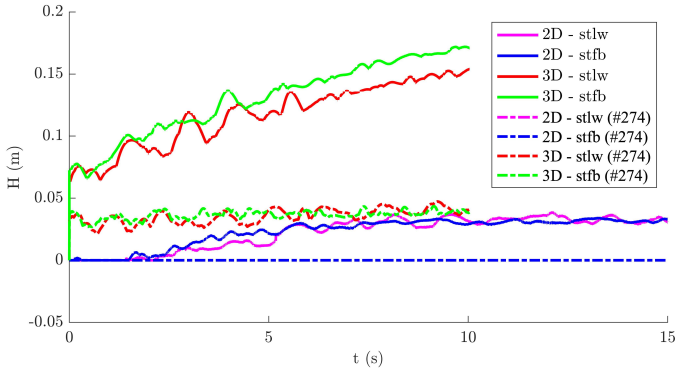

Figure 8.3: Free surface rising bug. Solid line shows the bug with free surface non-physically risyng, dashed lines (pull #274) show the fixed issue. Legend stlw stands for still water, stfb stands for still water with floating body.

While the wave-structure interaction was adequately modelled, another issue surfaced: the free surface rose above its expected level. To address this, I conducted four cases—two in 2D and two in 3D—simulating still water and a free-floating box in still water. The improper initialization of density was identified as the cause of this issue. Figure 8.3 illustrates the free surface elevation in still water and with a floating body before and after the bug fix, showing a marked improvement following the resolution of this issue.

8.2 3D SPH Analysis of Focused Waves Interacting with a Floating Structure

This publication presents one of the initial real engineering applications of plunging wave interaction with a floating moored tension-leg platform. Here, SPHinXsys is coupled with Simbody to simulate three waves with varying focusing times in 3D. Accurate results regarding the overall aspects such as movement, impact pressures, and tether tension in the fluid-structure interaction are achieved with relatively low particle resolution and no parameter tuning. The publication, titled “3D SPH Analysis of Focused Waves Interacting with a Floating Structure," is featured in the journal “Applied Ocean Research."

Applied Ocean Research 144 (2024) 103885

Contents lists available at ScienceDirect

Applied Ocean Research

journal homepage: www.elsevier.com/locate/apor

Research paper

3D SPH analysis of focused waves interacting with a floating structure

Nicolò Salis [a,*,1], Xiangyu Hu [b,2], Min Luo [c,2], Alessandro Reali [a,d,3], Sauro Manenti [a,d,4]

[a] Department of Civil Engineering and Architecture DICAr, University of Pavia, via Ferrata 3, Pavia, 27100, Italy
[b] School of Engineering and Design, Technical University of Munich, Garching, 85748, Germany
[c] Ocean College, Zhejiang University, Zhoushan, 316021, Zhejiang, China
[d] Water Research Center CRA, University of Pavia, via Ferrata 3, Pavia, 27100, Italy

ARTICLE INFO

Keywords:
3D
CFD
WCSPH
Wave-structure interaction
Floating structure
Plunging wave
SPHinXsys
Simbody

ABSTRACT

In recent years, the number of offshore floating structures has been growing and is expected to continue growing. Due to climate change, the frequency and severity of extreme waves are increasing. Numerical models can be a strategic tool in the reliable design and optimization of marine structures. However, the number of numerical parameters to be tuned plays a crucial role, as they could limit the model's applicability and reliability. Furthermore, there are many challenges in modelling wave-structure interaction. Among these challenges, the simulation of one-dimensional tethers is of great concern when dealing with moored floating structures. In this study, a 3D numerical model is developed based on the Smoothed Particle Hydrodynamics (SPH) technique. This hydrodynamic model is coupled with a multi-body solver for the dynamic analysis of moorings and structures. In a three-dimensional numerical flume, focused ocean waves are generated with a piston-type wave-maker and propagated until impact with the floating structure. The developed model predicts the wave profile, impact forces, and structural dynamics, and is validated by comparing numerical results against experimental data.

1. Introduction

Impacts of waves onto marine structures are of high concern. The population of marine structures is increasing, along with the probability of natural disasters, which is also related to climate change. Freak or rogue waves are among the most dangerous, characterized by a wave height that exceeds those expected by the sea state (Dysthe et al., 2008). Moreover, their formation is random and can occur in ocean areas with various depths (Kharif and Pelinovsky, 2003). Three-dimensional wave focusing is a mechanism that contributes to the occurrence of these rogue waves (Fochesato et al., 2007). Rogue waves interacting with offshore floating structures (e.g., ships, offshore wind turbines, oil platforms) can pose a serious threat, and impacts are often catastrophic. Field recordings of freak waves show significant heights, e.g., 18.49 m for the Draupner wave (Karin Magnusson and Donelan, 2013). The occurrence and consequences of these waves have been highlighted by research communities. Moreover, they emphasize the importance of accounting for these waves in structural design (Bitner-Gregersen and Gramstad, 2016). These waves have been investigated both experimentally and numerically (Yan et al., 2020; Salis et al., 2021). A wave-structure impact with a fixed box-shaped structure has been considered (Sun et al., 2019; Salis et al., 2022, 2023).

1.1. Challenges in numerical modelling

Wave-structure impacts are particularly violent and involve large domain deformation of the fluid phase, air entrapment, rapidly varied flow, and sprays. The numerical modelling of flows with the aforementioned characteristics is quite challenging. Eulerian grid-based methods are widely adopted in computational fluid dynamics problems. Wave-structure impacts with fixed structures have been investigated using Eulerian grid-based methods, even though these methods are not particularly suited to model these phenomena (Chen et al., 2014; Westphalen et al., 2014). Modelling free surfaces requires additional boundary conditions and must simulate wave breaking. Some of these issues can be solved by employing Lagrangian methods, which could be advantageous: the advection is implicitly modelled, simulation of free surface,

* Corresponding author.
E-mail addresses: nicolo.salis@unipv.it (N. Salis), xiangyu.hu@tum.de (X. Hu), min.luo@zju.edu.cn (M. Luo), alessandro.reali@unipv.it (A. Reali), sauro.manenti@unipv.it (S. Manenti).
[1] PhD Student.
[2] Research Professor, Ph.D.
[3] Professor of Solid and Structural Mechanics, Ph.D.
[4] Associate Professor of Fluid Mechanics, Ph.D.

https://doi.org/10.1016/j.apor.2024.103885
Received 20 September 2023; Received in revised form 9 January 2024; Accepted 10 January 2024

sprays, jets, fluid splitting/merging do not need additional treatment. The Lagrangian discretization of the governing equations could be investigated with mesh-based or mesh-free approaches. Lagrangian grid-based methods, e.g., the material point method (Larese et al., 2019; Soga et al., 2016), and the particle finite element method (Cremonesi et al., 2020; Carbonell et al., 2010), require computationally expensive re-meshing techniques to guarantee high-quality meshes. The capabilities of mesh-free Lagrangian particle methods in ocean and coastal engineering have been highlighted in Luo et al. (2021).

Among mesh-free particle methods, the Smoothed Particle Hydrodynamics (SPH) technique (Lucy, 1977; Gingold and Monaghan, 1977; Monaghan, 1994) has been successfully employed in this research field (Altomare et al., 2020; Zhang et al., 2021c; Marrone et al., 2019; Shimizu et al., 2020). The majority of research has focused on wave loads on cylinders (Deng et al., 2016; Yan et al., 2020), vertical rigid walls (Chan and Melville, 1988; Oñate et al., 2022), or fixed structures (Stansberg et al., 2005; Gómez-Gesteira et al., 2005). Wave-structure interaction is much more complicated, as it requires two-way coupling between the fluid and solid; the structure displacement has to be coupled with the fluid phase, and the force exchange between fluid and structure must be accounted for Verbrugghe et al. (2018), Manenti et al. (2008) and Zhang et al. (2021c). In real ocean applications, deep-sea founded floating structures (e.g., wind turbines and oil platforms) are moored to the seabed. This aspect introduces a further complication as the structure moorings are one-dimensional elements in a three-dimensional domain. The small cable diameter, compared to the simulation scale, would require a very fine domain discretization. Coupling a fluid-dynamic model with a multi-body solver overcomes this issue. Several approaches that model floating structures with moorings are proposed in Tagliafierro et al. (2022), Domínguez et al. (2019), Moreno et al. (2020) and Altomare et al. (2020, 2021). However, they only consider regular waves with either simple structures or without including tether tension. Moreover, in most of these works, the impact pressures are not shown, or the air-cushion effect is not mentioned.

In Tagliafierro et al. (2023), an open-source SPH code is validated against experimental data for three configurations of a floating platform subjected to several wave conditions (regular, bi-chromatic, and JONSWAP). Simulated and measured model responses are compared in terms of water surface elevation, run-up wave elevation, surge, and heave forces. The surge decay test shows the model's potential precision, even if excessive numerical dissipation is induced by the adopted SPH implementation. Investigation of hydrodynamic loads on the floating offshore structure yielded good accuracy for both regular and spectral wave forcing. Two ensembles of focused wave trains are also investigated, which could be relevant for ultimate limit state analysis, but the model has not been validated against experimental data.

Recently, Cai et al. (2023) modelled a non-linear wave interacting with a moored floating structure. They found precise simulation of wave generation and propagation using high particle resolution. However, only one wave condition is considered, and the structure dynamic interaction and impact pressures are in weak accordance with the experimental data.

1.2. Novelties and outline

In this work, three irregular focused wave types are generated in a 3D numerical flume, subsequently plunging onto a complex three-dimensional floating offshore structure. The main aim of this work is to validate an SPH model for the analysis of wave-structure interaction, predicting wave and structure dynamics, hydrodynamic impact pressure, and tension on the tethers. Wave height, structure displacement, and mooring tension are accurately computed. Numerical results are successfully validated with experimental data (Luo et al., 2020).

To the best of the authors' knowledge, this research represents the first attempt to validate an open-source SPH code against three plunging focused wave types impacting onto a floating moored 3D structure.

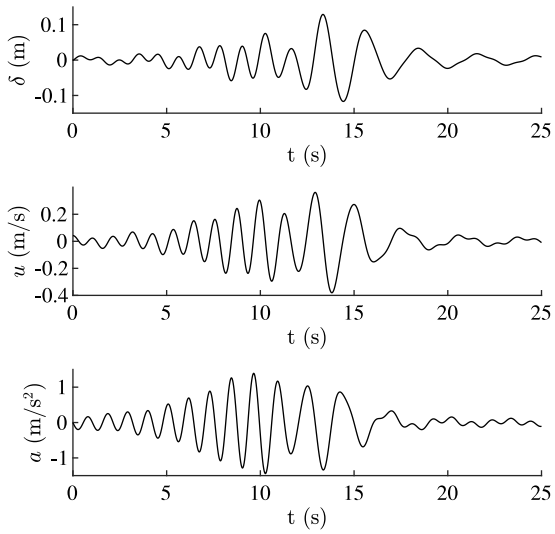

Fig. 1. WC2 wave-maker's displacement δ, velocity u, and acceleration a.

Besides validating the time series of wave kinematics, hydrodynamic pressure on the structure, and its displacement components, the time representation of stress tension on the tethers is computed.

All the aforementioned works (Tagliafierro et al., 2022; Domínguez et al., 2019; Moreno et al., 2020; Altomare et al., 2020, 2021; Tagliafierro et al., 2023) employ the numerical code DualSPHysics (Domínguez et al., 2022) coupled with MoorDyn (Hall, 2020), while in this paper, the multi-physics library SPHinXsys (Zhang et al., 2021b) is coupled with Simbody (Sherman et al., 2011). SPHinXsys is used to model fluid dynamics, while structure movement and moorings are modelled with Simbody. This work features the first use of SPHinXsys coupled with Simbody to model the structure anchor cables. The SPHinXsys library has been extensively applied to model a wide variety of test cases, e.g., fluid–structure interaction (Han and Hu, 2018; Zhang et al., 2023), sloshing interaction with an elastic baffle (Ren et al., 2023a), wave interaction with an oscillating surge converter (Zhang et al., 2021c), oscillating beams, and elastic objects (Wu et al., 2023).

The paper is structured as follows. In the section "Materials and Methods", the test cases are defined, the SPHinXsys and Symbody libraries are introduced, and the modelling chain of the developed model is presented. The Kernel gradient correction parameter and the spatial convergence studies are performed, showing high accuracy and efficiency at relatively low resolutions. Results of three focused waves are discussed, and numerical results are validated with laboratory measurements.

2. Materials and methods

2.1. Test cases

In a numerical wave tank, three different wave conditions are reproduced. In each testing condition, the same geometrical properties, still water depth, and equilibrium position of the floating structure are assumed. Using a piston-type wave-maker, three focused wave types are generated, impacting and interacting with the floating structure.

2.1.1. Wave conditions

The considered non-linear waves are generated adopting the focused wave theory (Rapp and Melville, 1990). In the frequency range of the spectrum, $0.32 < f < 96$ (Hz), $N_w = 32$ small linear waves are generated with a constant amplitude $a_i = 0.0068$ (m). The wave-wave interaction produces a rogue wave at a specific focusing time t_f and spatial position y_f.

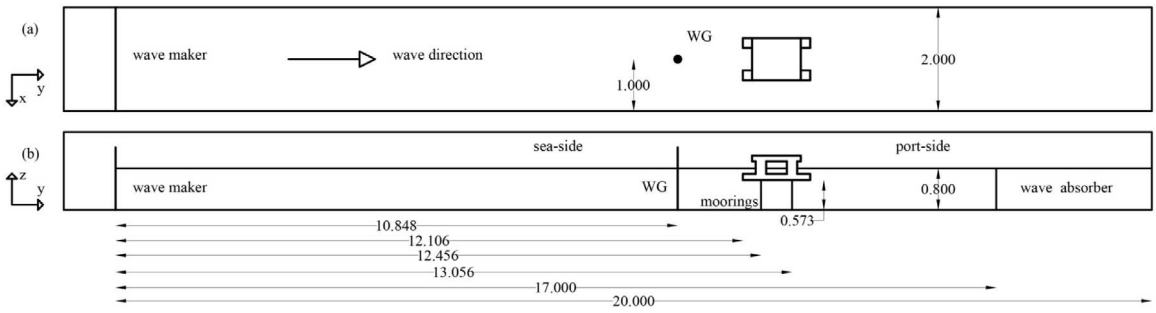

Fig. 2. Schematic of the three-dimensional numerical wave flume, dimensions in meters. (a) Top view. (b) Side view.

Table 1
Simulated wave conditions: focusing spatial position and time.

Condition	y_f (m)	t_f (s)
WC1	11.800	20.360
WC2	12.000	20.480
WC3	12.300	20.620

The test cases reproduce three wave conditions from the laboratory experiments in Luo et al. (2020). Each wave condition is imposed, specifying the focusing spatial position y_f and time t_f. Table 1 shows, for each wave condition, the focusing spatial position and time. WC1 is highly-breaking, tongue impacts with the deck vertical wall; WC2 is breaking, tongue impacts with the vertical wall; WC3 is slightly/non-breaking.

Considering the linear transfer function (Biésel and Suquet, 1951) to define the piston-type wave-maker stroke S_i as a function of the wave characteristics, the displacement δ, the velocity u, and the acceleration a of the wave-maker are defined:

$$\begin{cases} \delta = \sum_i^N \frac{1}{2} S_i \cos(-k_i y_f - \omega_i (t - t_f)) \\ u = \sum_i^N \frac{1}{2} S_i \omega_i \sin(-k_i y_f - \omega_i (t - t_f)) \\ a = \sum_i^N -\frac{1}{2} S_i \omega_i^2 \cos(-k_i y_f - \omega_i (t - t_f)) \end{cases} \quad (1)$$

where $\omega_i = 2\pi f_i$ is the angular frequency and k_i is the wavenumber of the ith regular wave component. Fig. 1 shows for WC2 the displacement, velocity, and acceleration of the wave-maker.

2.1.2. Numerical wave flume

Fig. 2 shows a sketch of the numerical flume with still water depth $d = 0.80$ m. The left-hand side of the floating structure is assumed as the sea side, while the right-hand side is assumed as the port side. At the sea-side boundary, the piston-type wave-maker is used to generate the waves. Waves propagate from left to right towards the moored floating structure. The wave height is recorded at the wave gauge WG. On the port side, there is a wave-absorbing region where the particle fluid velocity is reduced at each time step, with quadratic decay depending on particle position (Zhang et al., 2021c). This region prevents wave reflection from the port-side vertical wall.

2.1.3. Floating structure

The floating moored structure is characterized by a complex geometry, composed of nine parts: two partially submerged pontoons, four pillars, one deck, and two strengthening rods. Fig. 3 shows the dimensions of the floating structure. The structure is considered as a rigid body with uniform density. Table 2 shows the parameters adopted to model the structure. The structure's volume and weight match the experimental ones (Luo et al., 2022).

In the laboratory experiment, the structure is anchored to the flume bed with four steel tethers (Fig. 2) aligned with the geometrical centre of each pillar. Table 3 shows the adopted mooring parameters. In the laboratory flume, the moorings are anchored to steel bars at the bottom. In the numerical flume, these anchoring bars are not considered. Therefore, the tethers have a greater length l_t than the experimental ones (0.447 m). Although the length differs from the experiment, the axial stiffness of the tethers is assumed to be equal to the laboratory one.

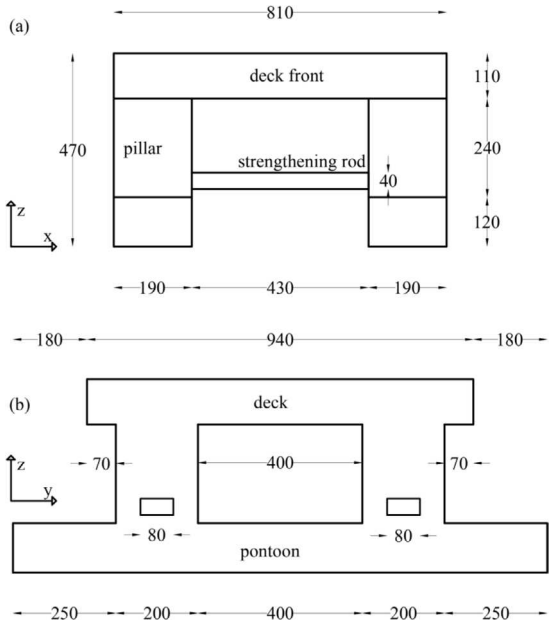

Fig. 3. Floating structure dimensions (mm). (a) Front view. (b) Side view.

Table 2
Structure parameters.

Parameter	Description	Value	Units
m_s	Mass	62.036	kg
V_s	Volume	0.182	m^3
ρ_s	Density	340.360	kg/m^3
x_G	Center of mass	1.000	m
y_G	Center of mass	12.756	m
z_G	Center of mass	0.833	m
I_{xx}	Inertia	7.803	m^4
I_{yy}	Inertia	6.422	m^4
I_{zz}	Inertia	10.987	m^4

Table 3
Mooring parameters.

Parameter	Description	Value	Units
l_t	Length	0.573	m
s_{ax}	Axial stiffness	316.3	kN/m

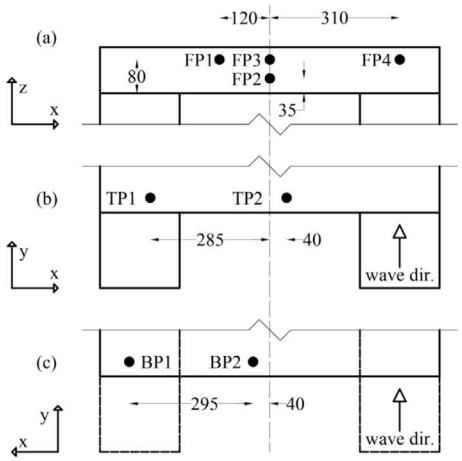

Fig. 4. Position of deck pressure probes (mm). (a) Vertical deck front wall (b) Deck top (c) Deck bottom.

Fig. 4 shows the position of the eight pressure probes: two at the top of the structure deck, two at the bottom of the structure deck, and four at the deck vertical wall. Length and tension of the four tethers are monitored as well.

After defining the geometrical properties and wave conditions of the problem, the mathematical formulation is introduced.

2.2. SPHinXsys library

SPHinXsys (https://github.com/Xiangyu-Hu/SPHinXsys) is an open-source multi-physics SPH library (Zhang et al., 2020b, 2021b). The following subsections illustrate: the governing equations for weakly compressible fluids; the kernel gradient correction; the wall boundary treatment; the dual-criteria time-stepping and the coupling with Simbody (https://github.com/simbody/simbody).

2.2.1. Governing equation for a weakly compressible fluid

The governing equations are based on a low-dissipation Riemann solver (Zhang et al., 2017) that allows the simulation of free surfaces. SPHinXsys is used to solve the discretized governing equations for a weakly compressible fluid continuum (2).

$$\begin{cases} \frac{d\rho_i}{dt} = 2\rho_i \sum_j \frac{m_j}{\rho_j}(U^* - \mathbf{v}_i \cdot \mathbf{e}_{ij})\frac{\partial W_{ij}}{\partial r_{ij}} \\ \frac{d\mathbf{v}_i}{dt} = -\sum_j m_j \frac{2P^*}{\rho_i \rho_j}\nabla_i W_{ij} + 2\sum_j m_j \frac{\mu}{\rho_i \rho_j}\frac{\mathbf{v}_{ij}}{|\mathbf{r}_{ij}|}\frac{\partial W_{ij}}{\partial r_{ij}} + \boldsymbol{g} \end{cases} \tag{2}$$

The mass m_i of the ith computational particle is assumed to be invariant. The particle volume is defined as $V_i = m_i/\rho_i$, where ρ_i is the particle density. W_{ij} is the 5th-order Wendland Kernel (Wendland, 1995) used with a smoothing length of $h = 1.3\,dx$ and a cut-off radius of $2.6\,dx$ where dx is the particle dimension. The velocity of the computational particle is $\mathbf{v}_i$. U^* and P^* are the solutions of the Riemann problem between the neighbouring particle j and the computational particle i. According to Ren et al. (2023b), P^* is normalized with the kernel gradient correction, see Section 2.2.2. The Riemann problem is solved along the direction between the two particles $\mathbf{e}_{ij} = \mathbf{r}_{ij}/|\mathbf{r}_{ij}|$ (Zhang et al., 2017), where $\mathbf{r}_{ij}$ is the relative particle position. The shear term for viscous flows is defined according to Hu and Adams (2006), where μ is the dynamic viscosity. A density reinitialization scheme (Zhang et al., 2020a) is used at the beginning of a new time step to stabilize the density field updated through the mass balance equation in free surface flows:

$$\rho_i = \max\left(\rho^*, \rho^0 \frac{\sum_j W_{ij}}{\sum_j W^0_{ij}}\right) \tag{3}$$

where ρ^* is the density prior to reinitialization, and the superscript 0 refers to the kernel computed with the initial particle distribution.

Note that recent schemes preventing the generation of pressure oscillation have been proposed in Sun et al. (2023) and Khayyer et al. (2023), showing promising results. However, in this work, we adopt a density reinitialization scheme. The density re-initialization allows for the modelling of slow-dynamics cases, such as still water, without non-physical rising of the free surface (Antuono et al., 2012). Although simultaneous uses of density diffusion in Riemann SPH and a density reinitialization scheme would raise concerns about excessive smoothing, this framework has been proven to provide stable and smooth pressure distributions in previous publications (Zhang et al., 2021b, 2020a). In this paper, the simulations are performed without particle shifting or transport velocity schemes.

2.2.2. Kernel gradient correction

The kernel gradient correction is adopted to avoid the over-attenuation of small waves, thereby improving energy conservation (Salis et al., 2022; Wen et al., 2018; Zago et al., 2021; Khayyer et al., 2017). This correction on the normalization matrix can lead to numerical instability that may be induced by the inversion of the matrix $\boldsymbol{A}_i$ when its determinant approaches zero. Several formulations have been proposed to mitigate these numerical instabilities (Salis et al., 2022; Lyu et al., 2023; Vila, 2005). In this work, the scheme proposed in Ren et al. (2023b) is adopted. The normalization matrix is corrected with two weighting factors w_1 and w_2. The corrected normalization matrix reads:

$$\widetilde{\mathbf{B}}_i = w_1 \mathbf{B}_i + w_2 \mathbb{I} \tag{4}$$

where $\mathbb{I}$ is the identity matrix, and $\mathbf{B}_i$ is:

$$\mathbf{B}_i = \left(\boldsymbol{A}_i\right)^{-1} = \left(\sum_j \mathbf{r}_{ij} \otimes \nabla_i W_{ij} V_j\right)^{-1} \tag{5}$$

The weighting factors w_1 and w_2 depend on $|\boldsymbol{A}_i|$, which is the determinant of matrix $\boldsymbol{A}_i$, and $\kappa_i = \max(\alpha - |\boldsymbol{A}_i|, 0)$ with α ranging from 0 to 1.

$$w_1 = \frac{|\boldsymbol{A}_i|}{|\boldsymbol{A}_i| + \kappa_i} \quad \text{and} \quad w_2 = \frac{\kappa_i}{|\boldsymbol{A}_i| + \kappa_i} \tag{6}$$

When $\kappa_i = 0$, the correction on the normalization matrix is not applied; therefore, $\widetilde{\mathbf{B}}_i = \mathbf{B}_i$. If the ith particle has an irregular particle distribution in its neighbour, $|\boldsymbol{A}_i|$ can approach zero. In this case, $\widetilde{\mathbf{B}}_i \approx \mathbb{I}$; therefore, the kernel gradient correction is not applied. κ_i depends on the concentration matrix determinant and a parameter α. In Ren et al. (2023b), values ranging between 0 and 1 are suggested, with the general indication that the value 0.1 is effective.

2.2.3. Wall boundary

For fluid particles near solid wall particles is solved with a one-sided Riemann problem (Zhang et al., 2017) along the wall normal direction. The left state, subscript L, of the Riemann problem is defined as

$$(\rho_L, U_L, P_L) = (\rho_f, -\mathbf{n}_w \cdot \mathbf{v}_f, P_f) \tag{7}$$

where $\mathbf{n}_w$ is the normal to the wall, and the subscript f refers to the fluid particles. In accordance with the wall boundary conditions, the right state of the Riemann problem is defined in Eq. (8), where u_w is the wall velocity. The right state pressure P_R, is defined similarly to (Adami et al., 2012):

$$\begin{cases} U_R = -U_L + 2u_w \\ P_R = P_L + \rho_f \mathbf{g} \cdot \mathbf{r}_{fw} \end{cases} \tag{8}$$

where $\mathbf{r}_{fw} = \mathbf{r}_w - \mathbf{r}_f$ is obtained by applying the equation of state $p = c^2(\rho - \rho^0)$.

2.2.4. Dual-criteria time stepping

Following Zhang et al. (2020a), the governing equations for fluids are relaxed with two time-step size criteria. The advection criterion is defined as:

$$\Delta t_{ad} = CFL_{ad} \min\left(\frac{h}{|\mathbf{v}|_{max}}, \frac{h^2}{\nu}\right) \tag{9}$$

where h is the smoothing length. The acoustic criterion is defined according to:

$$\Delta t_{ac} = CFL_{ac} \frac{h}{c + |\mathbf{v}|_{max}} \tag{10}$$

In (9) and (10), $CFL_{ad} = 0.25$ and $CFL_{ac} = 0.6$, while $|\mathbf{v}|_{max}$ is the maximum anticipated flow particle advection velocity, and ν denotes the kinematic viscosity. It is worth noting that the computation of $|\mathbf{v}|_{max}$ may take into account external forces, e.g., gravity. The advection criterion controls the updating rate for neighbouring particles, while the acoustic criterion determines the updating rate for pressure and density.

2.2.5. Coupling with simbody

Simbody is an open-source library to model multi-body dynamics (Sherman et al., 2011). The hydrodynamic force on rigid bodies is computed by SPHinXsys. These forces define a Simbody state that is solved with the Newton–Euler equation, providing the body motion. The solution of the kinematic state are stored in Simbody and outputted to SPHinXsys, which updates the position, velocity, and normal direction of the structure particles (Zhang et al., 2021c). In SPHinXsys, fluid and solid bodies are discretized into a set of numerical particles. The total force induced onto the solid bodies by the fluid is computed as:

$$\begin{aligned}\mathbf{F} = \sum_{a\in N_s} \mathbf{f}_a = \sum_{a\in N_s} \Big(&-2\sum_{i=1} V_i V_a \frac{p_i\rho_a^d + p_a^d\rho_i}{\rho_i + \rho_a^d} \nabla_a W_{ai} \\ &+ 2\sum_{i=1} \nu V_i V_a \frac{\mathbf{v}_i - \mathbf{v}_a^d}{r_{ai}} \frac{\partial W_{ai}}{\partial \mathbf{r}_{ai}} \Big)\end{aligned} \tag{11}$$

The summation extends to the N_s structure's particles. Subscripts a and i point respectively to the solid body and to the fluid one. The right-hand side terms of Eq. (11) express the pressure and viscous forces. The fictitious pressure and velocity read as follows:

$$\begin{cases} p_a^d = p_i + \rho_i \max\left(0, \left(\mathbf{g} - \frac{d\mathbf{v}_a}{dt}\right)\cdot \mathbf{n}\right)(\mathbf{r}_{ai}\cdot\mathbf{n}) \\ \mathbf{v}_a^d = 2\mathbf{v}_i - \mathbf{v}_a \end{cases} \tag{12}$$

where $\mathbf{n}$ is the outward normal to the solid body. The total torque $\boldsymbol{\tau}$ acting on the solid body can be written as:

$$\boldsymbol{\tau} = \sum_{a\in N} (\mathbf{r}_a - \mathbf{r}_G) \times \mathbf{f}_a \tag{13}$$

where $\mathbf{r_G}$ is the position vector for the solid body mass centre at the end of each time step. The force and torque are now the input for a Simbody state. The Newton-Euler equation solved by Simbody reads:

$$\begin{pmatrix}\mathbf{F}\\ \boldsymbol{\tau}\end{pmatrix} = \begin{pmatrix} m\mathbb{I} & \mathbf{0} \\ \mathbf{0} & \mathbf{I}\end{pmatrix}\begin{pmatrix} d\mathbf{v}/dt \\ d\boldsymbol{\Omega}/dt\end{pmatrix} + \begin{pmatrix}\mathbf{0}\\ -k_d\boldsymbol{\Omega}\end{pmatrix} \tag{14}$$

where m is the mass of the solid body, $\mathbb{I}$ is the identity matrix, $\mathbf{I}$ is a vector containing the inertia moments for the three rotation axes of the solid body. $\boldsymbol{\Omega}$ is the angular velocity, and k_d is the damping coefficient. To satisfy the momentum balance from fluid to structure and vice versa, on the right hand side of Eq. (2) the reaction terms from the structure are included according to the multi-resolution FSI coupling described in Zhang et al. (2021b). In detail, the coupling with Simbody is executed as follows. At the beginning of the advection step, Eq. (3) is used to reinitialize the density. The viscous force from the fluid body is computed, and the pressure relaxation is executed several times (Zhang et al., 2020a) using a position-based Verlet scheme (Zhang et al., 2021a):

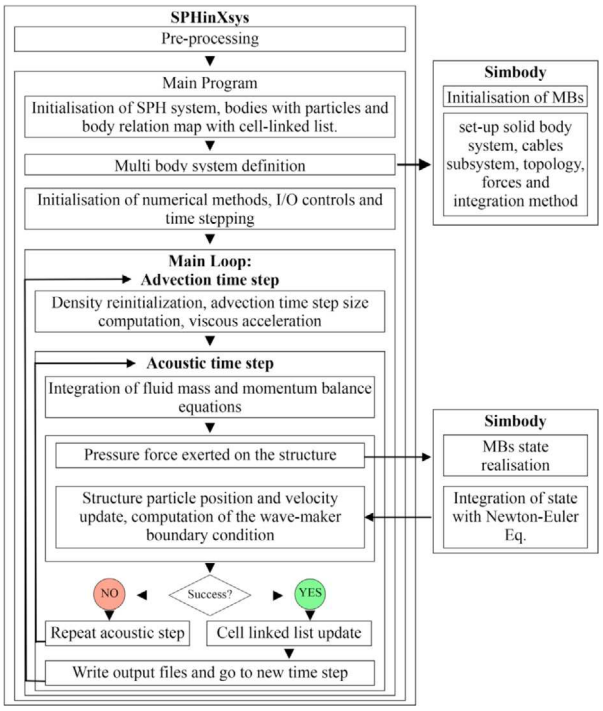

Fig. 5. Block diagram of the modelling chain.

$$\begin{cases} \rho_i^{n+\frac{1}{2}} = \rho_i^n + \frac{1}{2}\Delta t_{ac}\left(\frac{d\rho_i}{dt}\right)^{n+\frac{1}{2}} \\ \mathbf{r}_i^{n+\frac{1}{2}} = \mathbf{r}_i^n + \frac{1}{2}\Delta t_{ac}\mathbf{v}_i^n \end{cases} \tag{15}$$

The fluid particle density and position are integrated and updated in the middle point. The particle velocity is subsequently updated to the new time step:

$$\mathbf{v}_i^{n+1} = \mathbf{v}_i^n + \Delta t_{ac}\left(\frac{d\mathbf{v}_i}{dt}\right)^{n+1} \tag{16}$$

Now the particle's position and density can be updated to the new time step as:

$$\begin{cases} \rho_i^{n+1} = \rho_i^{n+\frac{1}{2}} + \frac{1}{2}\Delta t_{ac}\left(\frac{d\rho_i}{dt}\right)^{n+\frac{1}{2}} \\ \mathbf{r}_i^{n+1} = \mathbf{r}_i^{n+\frac{1}{2}} + \frac{1}{2}\Delta t_{ac}\mathbf{v}_i^{n+1} \end{cases} \tag{17}$$

The pressure and viscous force on the structure is computed; so the total force and torque are given to Simbody and the Newton-Euler equation is solved. The result is imported back to SPHinXsys, and the position, velocity, and normal direction of the solid body particles are updated.

2.3. Modelling chain

This section illustrates the model development implementing the mathematical algorithms previously described. Fig. 5 shows a schematic representation of the proposed modelling chain using the open-source libraries SPHinXsys and Simbody.

2.3.1. Preprocessing

In the preprocessing step, all the quantities needed in the main program are defined. The material properties of the fluid are defined: $\rho_f = 1000$ (kg/m^3), $\mu_f = 0.001$ (Pa s). The considered characteristic velocity is $U_f = 2\sqrt{gz_w}$ where $g = 9.81$ (m/s^2) is the gravity acceleration

modulus, z_w is the initial water depth, and the reference sound speed is $c = 10U_f$. The dimensions of the bodies (fluid and solid) are defined either with binary shapes or by importing a CAD model. The topology of the four tethers is defined considering the structure centre of mass. The boundary conditions for the wave generation and wave absorbing are introduced.

2.3.2. Main program

In the main program, the SPHsystem (SPHs) is initialized. The bodies are all discretized with numerical particles. According to a level-set function (Yu et al., 2023), the particle resolution of the structure body is refined near the faces. Therefore, the particle resolution of the structure is independent of the particle dimension of the other bodies. The monitoring bodies (e.g., FP1, BP2, etc.) are defined in their initial position and initialized.

The body relation map (contact map) is specified. The contact map defines the numerical connections between the bodies (e.g., the water has a topological connection with both the wall and the structure).

The Simbody multi-body system (MBs) is initialized; the structure body is imported into the MBs. The structure is modelled as a rigid free-moving body with six DOF. The cable subsystem is used to model the tethers inside the MBs. The force subsystem is initialized for the MBs. The structure will float under the hydrodynamic forces (from the SPHs). The tethers behave similarly to elastic springs, with the prescribed axial stiffness. A Runge–Kutta Merson integration method with suitable accuracy is adopted.

The numerical methods, introduced in 2.2, are initialized as well as the input/output methods to write output files. The basic control parameters for the time stepping are defined. The simulation is configured with the Verlet cell-linked list (Zhang et al., 2021a).

2.3.3. Main loop

The main loop of the program can be summarized into six points:

1. A fluid time step is initialized with the density reinitialization. In the advection time step: the advection time step size as well as the water viscous acceleration with the wall and structure are computed.
2. In the acoustic time step: the acoustic time step size is defined, and the governing equations for the fluid are integrated. The mass and momentum balance equation are computed.
3. The pressure force exerted by the water to the structure is computed.
4. The MBs state is realized and integrated with the Newton-Euler equation.
5. Structure particle position and velocity are updated, and the wave-maker boundary condition is executed.
6. If the SPHs and MBs integration process is successfully concluded, the cell-linked list and particle-interaction configuration are updated. The output files for the measuring devices are written for the current time step. A new advection time step can start (point 1), and the simulation time is updated. If the SPHs and MBs integration process is not satisfied, the acoustic time step is repeated (point 2).

3. Results and discussion

In this section, the model results for the three wave conditions are discussed and validated with laboratory experiments. An investigation on the kernel gradient correction parameter α and a subsequent spatial convergence study have been carried out. The spatial resolution d/dx is defined as the still water depth d divided by the particle dimension dx. For the spatial convergence study, WC2 is investigated at various resolutions ranging from $d/dx = 10$ to $d/dx = 50$ with a step size of 10. Despite the model with lower particle resolution being very fast and yielding acceptable physical results, the higher resolution of $d/dx = 50$ is adopted to reproduce the three wave characteristics with greater accuracy.

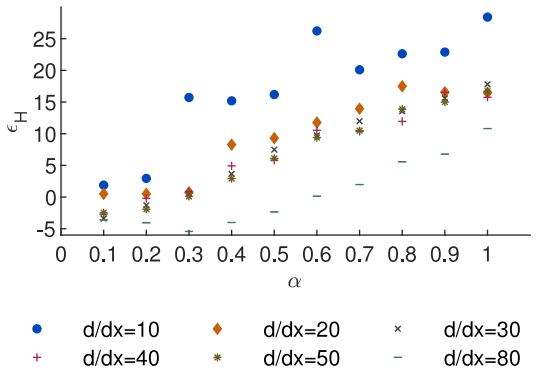

Fig. 6. 2D WC2: Influence of α. Wave height error ϵ_H at different spatial resolutions d/dx.

3.1. Analysis on the kernel gradient correction

The effect of the kernel gradient correction parameter α on the simulation results is investigated. This study focuses on the wave height of WC2 simulated in 2D. Ten values of α in the range suggested by Ren et al. (2023b) are investigated at different spatial resolutions d/dx. In this document, unless otherwise specified, the error is relative to the experimental signal with:

$$\epsilon_{\mathbb{f}} = 100\frac{\mathbb{f}_e - \mathbb{f}_s}{\mathbb{f}_e} \tag{18}$$

The subscript e refers to the experimental signal, while the subscript s refers to the simulated signal. Eq. (18) will be used in the following, where $\mathbb{f}$ is a dummy function, here represents the wave height $H = \max(\eta) - \min(\eta)$, where η is the wave elevation. With $\alpha = 0$, the simulations show numerical instabilities, while for values from 0.1 to 1, the error ranges from −3% (simulated wave height is higher than the experimental one) to 25% (simulated wave height is lower than the experimental one). Fig. 6 shows that simulation results are affected by the value of α in combination with the particle dimension. The 2D analysis suggests that low values of α can produce accurate results.

WC2 is reproduced in 3D by analysing the α values suggested by Fig. 6. The target spatial resolution for 3D simulations is $d/dx = 50$. With this spatial resolution, the following α values are investigated: 0.1, 0.2, 0.25, and 0.3.

Fig. 7 shows for WC2 the shape of η obtained for different α values at the resolution $d/dx = 50$. With $\alpha = 0.1$, non-physical numerical breaking at the ≈18 (s) crest is induced. Fig. 6 suggests that, at this spatial resolution, the error would be reduced close to zero with $\alpha = 0.3$. However, Fig. 7 shows that the crest height is unchanged while the experimental trough is underestimated with both α equal to 0.25 and 0.3. In conclusion, the choice of $d/dx = 50$, $\alpha = 0.2$ provides a good compromise between accuracy and numerical stability. Therefore, in the following simulations, $\alpha = 0.2$ is adopted.

3.2. Convergence analysis

The convergence analysis is carried out to show that meaningful quantitative results can be achieved with a relatively small particle number in a short computational time. Table 4 shows the number of fluid nodes N and the computational time.

SPHinXsys is parallelized with OpenMP, which allows single-node multicore simulation using shared memory. The lowest particle resolution $d/dx = 10$, with $N = 56\,000$ computational particles, is computed in $T_s = 10$ min (see Table 4). The higher resolution, with $N = 7.01$ million particles, is computed in circa 2.7 days. The model exhibits high computational efficiency, with a relatively small computational time required to obtain a reliable representation of such a complex physical problem.

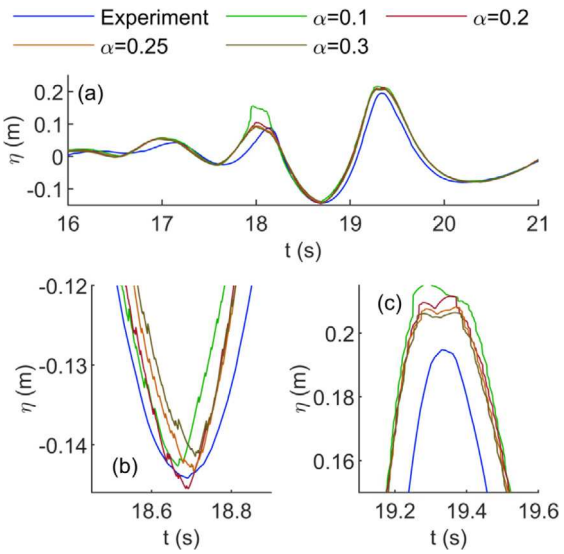

Fig. 7. 3D wave height of WC2 at $d/dx = 50$: Influence of parameter α. (a) Wave elevation, (b) $t = 18.7$ (s) through, (c) $t = 19.3$ (s) crest.

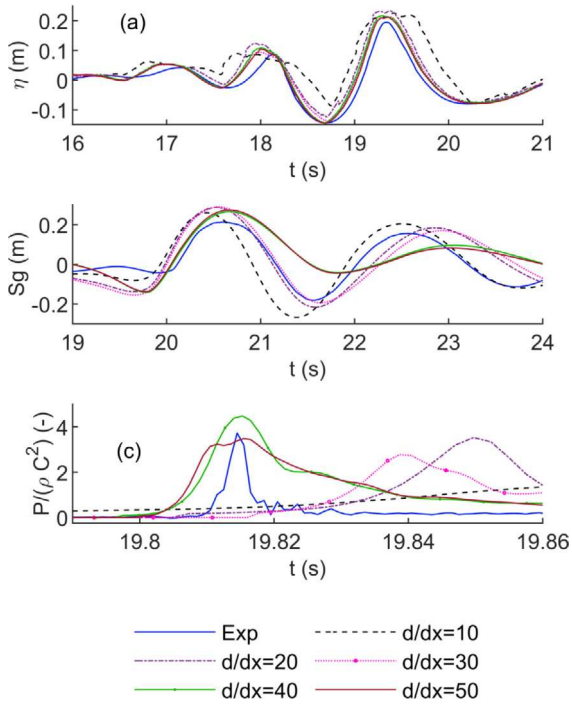

Fig. 8. Convergence study for WC2. (a) Wave elevation, (b) surge displacement, (c) normalized pressure at probe FP2.

Table 4
Number of fluid particles N against computational time. Computational Time (T_s) for the simulation time of $t = 25.00$ (s) executed on 2 × 16 cores CPUs (Intel(R) Xeon(R) Gold SkyLake 6130 CPU @ 2.10 GHz) at the HPC cluster of the Mathematics Department at the University of Pavia.

d/dx	N	T_s (d-hh:mm:ss)
10	$56.01 \cdot 10^3$	0:10:17
20	$448.7 \cdot 10^3$	01:44:01
30	$1.51 \cdot 10^6$	08:19:15
40	$3.59 \cdot 10^6$	1-03:20:10
50	$7.01 \cdot 10^6$	2-18:15:53

Table 5
Error produced at different d/dx resolution measured for: wave height ϵ_H, surge amplitude ϵ_S, and pressure peak ϵ_P.

d/dx	ϵ_H (%)	ϵ_S (%)	ϵ_P (%)
10	7.67	33.51	61.34
20	5.33	27.34	5.32
30	3.77	22.24	25.51
40	6.40	6.68	20.21
50	5.35	6.44	6.57

Fig. 8 shows the results of a convergence study for WC2. For different spatial resolutions, the time series of wave elevation (a), platform surge (b), and pressure at probe FP2 (c) are shown. Table 5 shows the error produced by the model at different resolutions, in the estimation of wave height, surge amplitude, and peak pressure. The errors are computed with respect to the experimental signals. The error at $d/dx = 50$ for the wave height is 5%, the difference between the crest of the numerical model and the experiment is $\Delta\eta = 0.017$ (m), which is circa the particle size dx.

At the lowest resolution $d/dx = 10$, the model shows a higher duration of the peak than the experiment with a comparable wave height at the focusing point. In this context, it is worth highlighting that the lower resolution has a particle size of $dx = 0.08$ (m), which is approximately 11 times bigger than the amplitude of one linear wave component $a_i = 0.0068$ (m) of the focused wave. At the lower analysed resolutions, the surge amplitude and the frequency are higher with larger and faster structure oscillations. At the higher resolution, the surge amplitude error is significantly lower ≈6%. The pressure estimation error at probe FP2 is ≈6%. It is worth noting that in this impact the air phase plays a crucial role, as it will be discussed in Section 3.4.3. Based on the results of the convergence analysis, the resolution of $d/dx = 50$ is adopted to model the three wave conditions in 3D. This resolution, which is relatively low considering the problem, gives accurate results in terms of wave height, structure displacement, and pressure.

3.3. Wave generation

Fig. 9 shows the magnitude velocity contour for three rogue waves before the structural impact. The simulation frames are compared with the laboratory images in Luo et al. (2020). The three wave conditions yield different wave shapes upon impact: In WC1, the wave crest breaks and impacts the vertical wall; in WC2, the wave crest is very close to the breaking point and breaks while impacting the structure; in WC3, the wave crest does not break before impact, thus showing slightly lower height and velocity. For each one of the three conditions, the wave shape at the impact is quite close to the experimental one. The comparison with the experimental snapshots highlights that the model accurately reproduces the wave design characteristics upon impact. The experimental snapshots show that a large air cavity interposes between the wave front and the structure. The air influence on the impact pressures will be discussed in Section 3.4.3.

Fig. 10 shows the wave elevation, for the three wave conditions, at the wave gauge WG. As previously explained, the three waves are focused in three different spatial and temporal points. WC1 shows the highest wave height, WC2 and WC3 show progressively smaller wave heights. Although the waves are characterized by the same linear components, WC1 has the focusing point closer to the wave-maker. This means that the WC1 wave develops into a plunger breaker before the others; therefore, slightly higher wave heights and velocities are expected at the impact with the structure. Table 6 shows the maximum and minimum wave elevation measured (subscript e) and simulated (subscript s), the difference between the experimental and the simulated results, and the error produced by the numerical model for the wave height. The numerical model slightly overestimates the wave

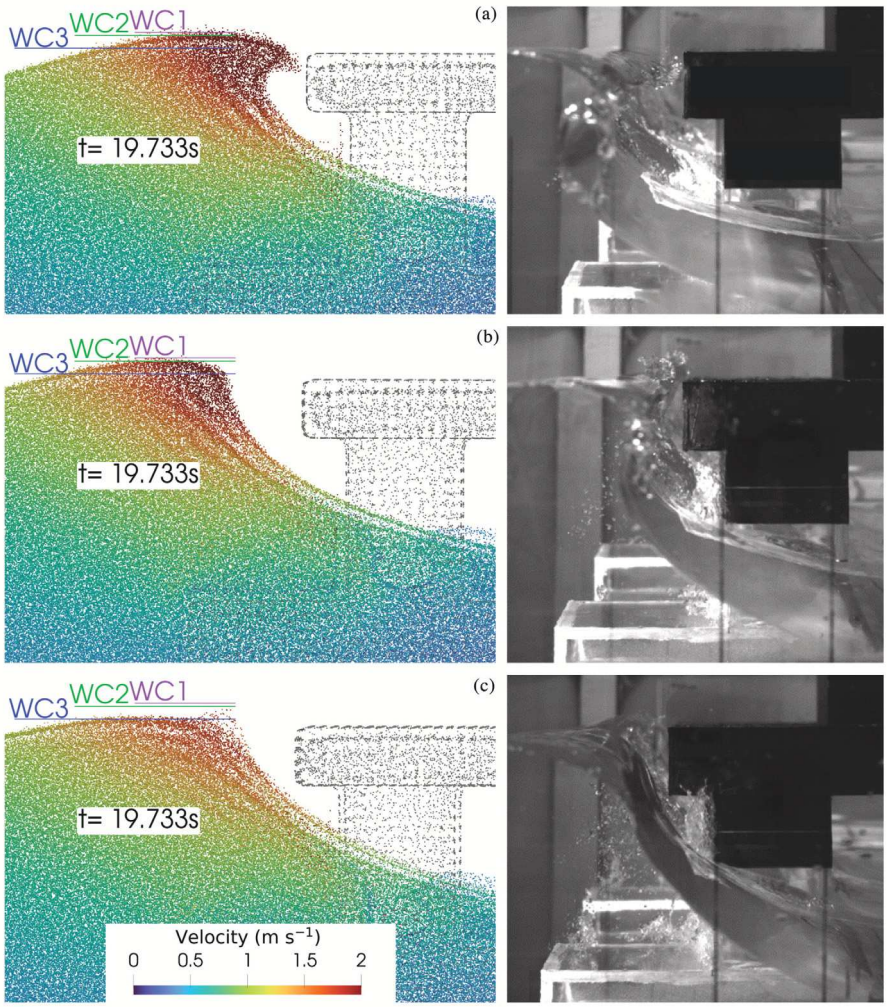

Fig. 9. Magnitude velocity contour of the wave crest before the impact, left-hand panels. Laboratory experimental snapshots (Luo et al., 2020), right-hand panels. (a) Wave condition 1, (b) wave condition 2, (c) wave condition 3.

Table 6
Wave height error. For the wave trough $min(\eta)$ and crest $max(\eta)$.

WC	1	2	3
$max(\eta_e)$ (m)	0.202	0.195	0.182
$max(\eta_s)$ (m)	0.221	0.212	0.193
$\Delta_{\max}$ (m)	0.018	0.017	0.012
$min(\eta_e)$ (m)	−0.143	−0.144	−0.141
$min(\eta_s)$ (m)	−0.143	−0.146	−0.146
$\Delta_{\min}$ (m)	0.0002	0.0016	0.0046
ϵ_H (%)	5.16	5.35	4.83

height, $\Delta_{\max}$ is circa the dimension of one particle $dx = 0.016$ (m) for all three wave conditions. The error produced for the wave amplitude is ≈ 5% for all three waves, which is acceptable for engineering purposes. In conclusion, the model accurately reproduces the mechanics of focused non-linear wave generation and propagation. For the three simulated conditions, the numerical model accurately reproduces the laboratory wave phase and height, showing wave heights slightly higher than the experiment.

Fig. 11 shows the focused wave generation for WC1, where small amplitude waves are generated by the piston-type wave-maker. The propagation of the linear wave components before the impact is visualized from $t = 0.00$ (s) to $t = 19.73$ (s). The linear wave components' focus occurs near the structure sea-side at $t \approx 19.0$ (s). In Cai et al. (2023), WC2 is modelled with DualSPHysics at higher spatial resolution (higher computational cost); nevertheless, wave heights similar to those presented in this study are obtained. Based on the above considerations, the model can accurately reproduce different wave conditions.

3.4. Floating structure interaction

The impacting wave induces pressures, displacements, and tension in the moorings on the structure. In the following sections, the fluid–structure interaction results are discussed.

3.4.1. Structure dynamics

Fig. 12 shows, for WC1, the wave-structure impact. The structure undergoes large displacements in the y-direction. At the port-side, the structure slightly sinks while the hydrodynamic buoyancy forces on the pontoons keep the structure afloat. As the wave impacts and excites the structure, the anchor cables pull the structure back to the undisturbed configuration, resulting in dynamic transitoriness during which the structure oscillates around its static equilibrium position. The numerical model shows a faster decay of the oscillation amplitude than the experimental results. Fig. 13 shows the structure displacement in the y-direction (surge) and in the z-direction (heave). The simulated structure displacement is close to the experimental results for all three wave conditions. The surge amplitude is slightly higher than the experiment. For all three wave conditions, the simulations show that the structure

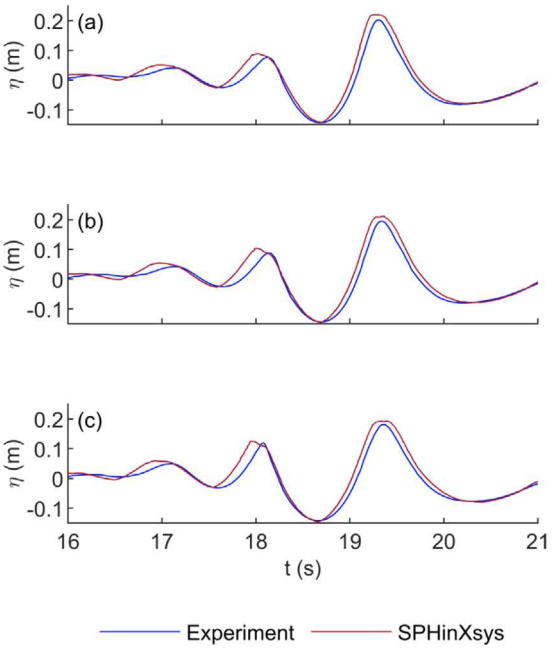

Fig. 10. Wave elevation at gauge WG. Numerical simulation against experimental measurement (Luo et al., 2020). (a) Wave condition 1, (b) wave condition 2, (c) wave condition 3.

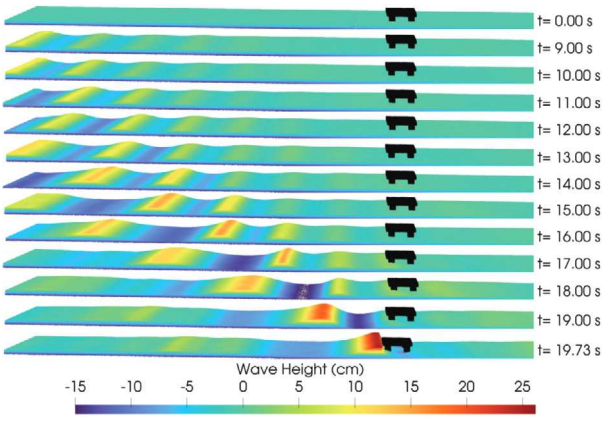

Fig. 11. WC1, wave generation and propagation. Still water surface is at $\eta = 0.0$ (cm).

is pulled toward the seaside direction. ($t \approx 19.9$ s) before a large displacement to the port-side region ($t \approx 20.5$ s). In the experiment, the structure is poorly influenced by the wave thorough (Fig. 11 at $t = 19$ s) and shows a smaller displacement in the negative y-direction. The simulated maximum positive and negative surge peaks occur roughly at the same time instant as the experimental recordings. Concerning the heave, the model can accurately reproduce the maximum submersion of the structure (i.e., maximum negative peak), while the subsequent oscillations differ from the experimental recording. In Cai et al. (2023), the WC2 structural displacement is modelled with DualSPHysics at higher spatial resolution, showing higher period with faster amplitude decay than the experiment. Table 7 shows the error of the numerical model predicting the structure displacement. The model is able to accurately reproduce the structure movement with surge amplitude errors ranging between 3 and 10% and heave errors ranging between 1 and 15%. In conclusion, the presented model can suitably reproduce the maximum and minimum peaks, introducing some discrepancies in the decay phase of dynamic oscillation. Differences in the structural

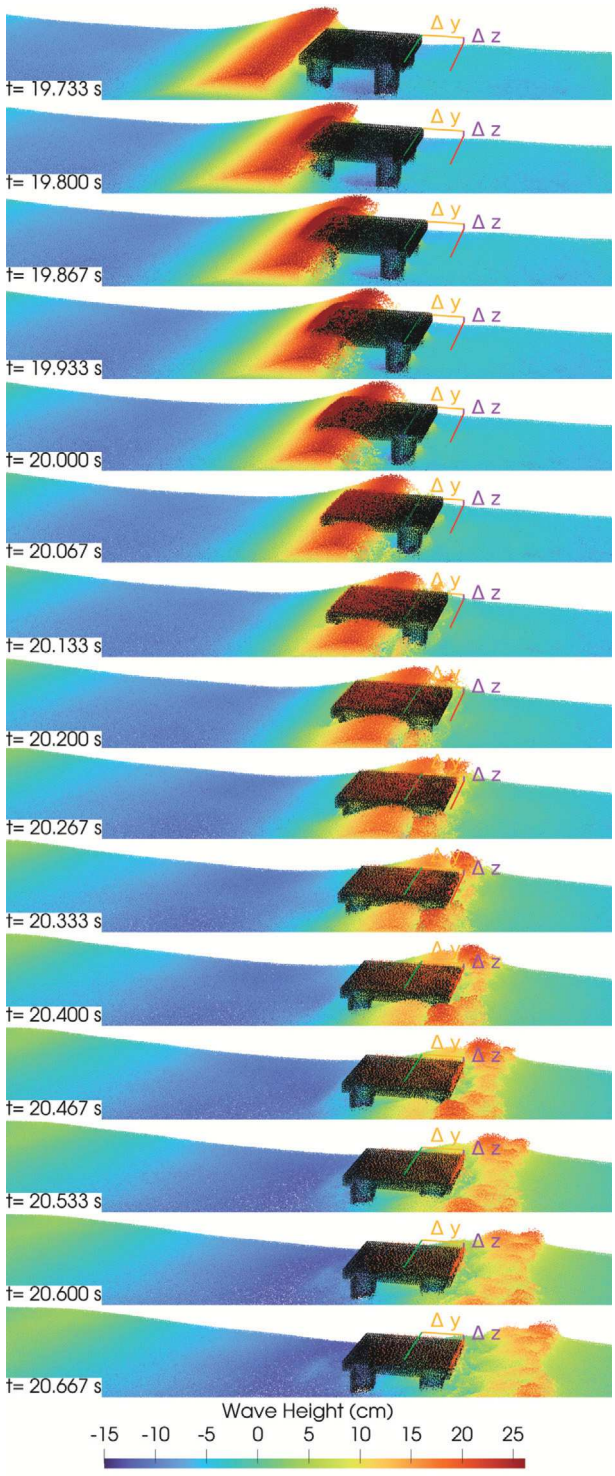

Fig. 12. WC1, wave-induced displacement on the moored floating structure. Contour of magnitude velocity.

dynamic response can be related to the differences between the experimental and simulated cables, as pointed out in the description of the numerical model.

3.4.2. Anchor cables

Fig. 14 shows the moorings' tension over time. Since the structure displacement along the x direction is negligible, only two cables are

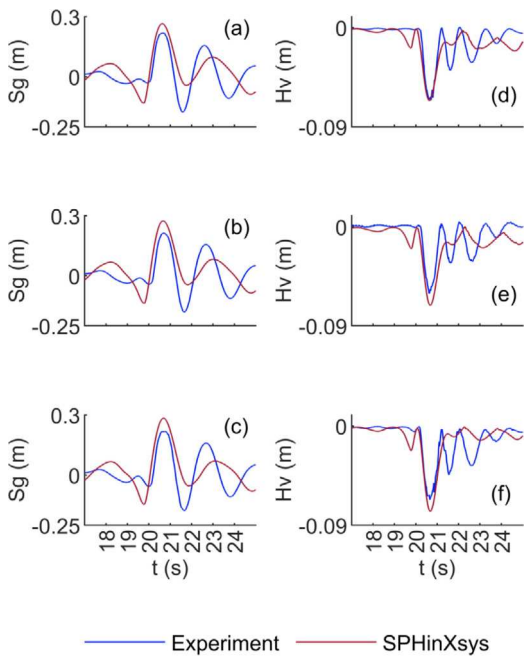

Fig. 13. Wave-induced displacement on the moored floating structure. Panels (a), (b), and (c) surge (Sg) (displacement in y direction); panels (d), (e), and (f) heave (Hv) (displacement in z direction). (a) and (d) WC1, (b) and (e) WC2, (c) and (f) WC3.

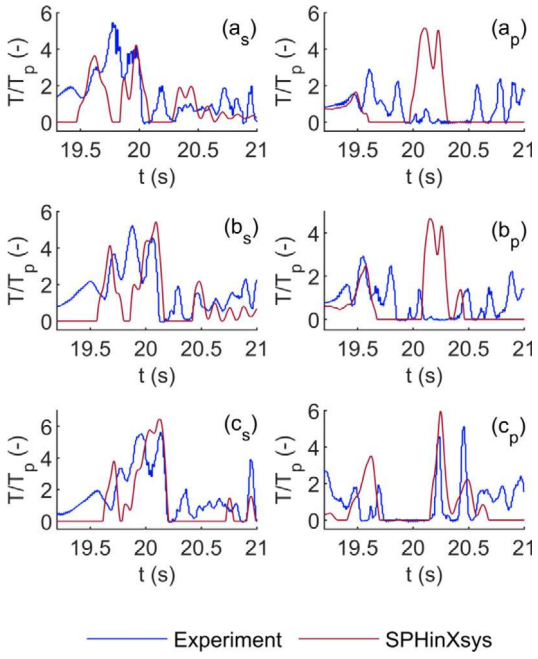

Fig. 14. Wave-induced tension on structure moorings. Tension is normalized with respect to the initial tether pre-tension. In the legend, the letters (a), (b), and (c) refer respectively to WC1, WC2, and WC3 while the letters ($*_s$) and ($*_p$) indicate respectively the sea-side and port-side cable.

considered: one sea-side cable and one port-side cable for each wave condition; minor tension changes may appear between the right and the left cable. Tension is normalized with respect to the initial tension of $T_p = 68.6$ (N). Results of the numerical model are quite close to the experimental ones. The simulated cable tension is smoother than the experimental normalized tension and it approaches zero during the process. Excluding the port-side tension of WC1 and WC2, the maximum stress is, on average, suitably predicted, and the error produced by the numerical model estimating the maximum mooring tension is between 14% and 22%. In Cai et al. (2023), the WC2 impact with this structure is modelled with DualSPHysics at higher spatial resolution, finding cable tension smaller than the experiment due to the smaller surge displacement.

Table 7
Structure displacement error ϵ for surge amplitude $\Delta(Sg) = max(Sg) - min(Sg)$ and heave minimum $min(Hv)$. The subscripts e and s refer respectively to the experimental and simulated signal.

WC	1	2	3
$\Delta(Sg)_e$ (m)	0.395	0.395	0.396
$\Delta(Sg)_s$ (m)	0.353	0.370	0.385
$\epsilon(Sg)$ (%)	10.70	6.44	2.77
$min(Hv)_e$ (m)	−0.066	−0.062	−0.067
$min(Hv)_s$ (m)	−0.065	−0.067	−0.068
$\epsilon(Hv)$ (%)	−1.09	−16.31	−15.92

3.4.3. Impact pressures

The wave-structure interaction phenomenon is a complex combination of several factors: the three-dimensional wave shape, its height, and the impact position influencing the hydrodynamic load. From the symmetry axis of the structure, two air pockets form between the wavefront and the structure vertical wall. The size of the air pockets is bigger when the wave height is higher, e.g., wave tongue impacts onto the top deck. The air pockets are always present and influence the impact pressures: when air is violently slammed between the wavefront and the structure wall, it acts as an elastic buffer. More in-depth, air undergoes subsequent stages of compression and decompression. Therefore, the air cushion reduces the impact pressures. An exhaustive discussion on the wave-shape and air pocket influence on the resulting impact pressures is featured in Luo et al. (2022). At this early stage of the work, we consider only the water phase to test the model capability in simulating wave-structure dynamics. Higher computational effort is required to account for the air phase and its effect on pressure load. This task will be the subject of future research. Therefore, in the following, the pressure time series obtained with single-phase simulations are discussed. Fig. 15 shows the non-dimensional pressures compared with the laboratory experiment in Luo et al. (2020). The first column (a*) refers to WC1. In this case, the wave is highly breaking and impacts on the front structure wall while breaking. The pressure is generally overestimated by the model; for FP1 and BP2, the simulated peak is closer to the experimental one with errors of 1–3 $P/\rho C^2$ (20%–50%). In all probes, even if the pressure is overestimated, the impact duration is captured except BP1. The second column (b*) refers to wave condition 2: the wave is highly breaking and impacts on the vertical structure wall. For most probes, the peak simulated pressure is higher than the experimental one. For the probes FP1, FP2, and FP4, the simulated pressure is relatively close to the experimental one. Similar pressure peaks with errors ranging from 0.1 $P/\rho C^2$ (6%) at FP2 to 4 $P/\rho C^2$ (80%) at FP1 are obtained. Results from Cai et al. (2023), where pressures are modelled with DualSPHysics at a higher spatial resolution, are depicted with a green line. However, peak pressures for FP1, FP2, and FP3 exhibit significant underestimation, with errors ranging from 80% to 98%. Notably, at FP3, the pressure from Cai et al. (2023) is closer to the experimental data than the present results. For BP1, the pressure peak from Cai et al. (2023) is closer to the experimental data; subsequently, the pressure values show significant oscillations, producing large deviations from the experimental measurements and indicating prolonged contact between water and the structure bottom. This discrepancy may potentially be attributed to a less precise wave shape upon impact. In contrast, the present model closely reproduces the duration of the impact pressures. In conclusion, the pressures from Cai et al. (2023) appear less reliable and poorly

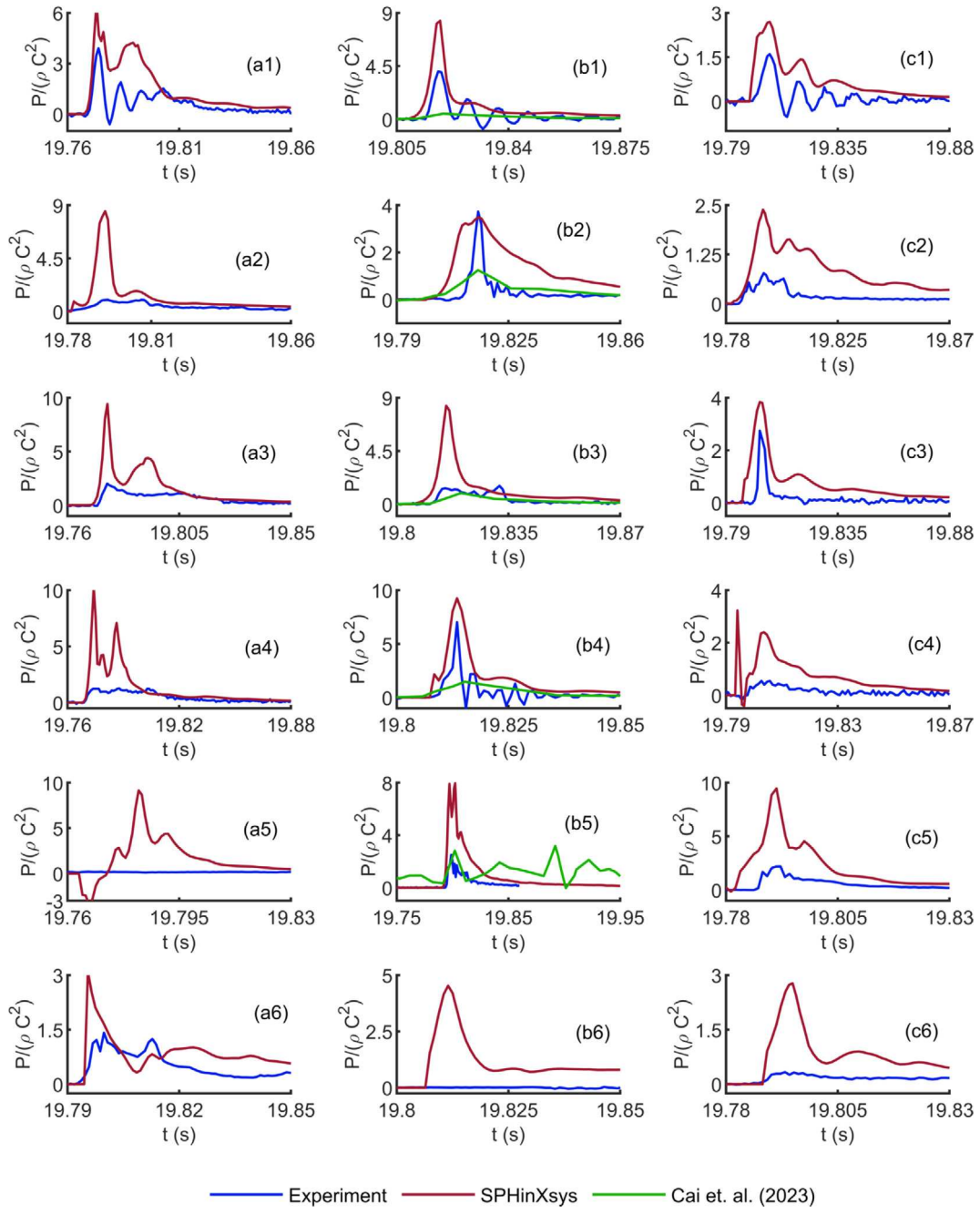

Fig. 15. Wave-induced pressures on structure. The x axis reports the time t (s) while the y axis reports the pressure normalized with respect to the water density and wave celerity squared $P/\rho C^2$ (–). In the plots, the letter (a*) refers to WC1, (b*) refers to WC2 (green line shows results from Cai et al., 2023), and (c*) refers to WC3. Numbers from 1 to 6 refer respectively to FP1, FP2, FP3, FP4, BP1, and BP2.

accurate, replicating the overall trend of impact pressure. The present model for WC2 demonstrates significantly improved results compared to Cai et al. (2023), although further accuracy enhancements are necessary.

The third column (c*) refers to WC3: the wave is non-breaking and impacts on the vertical structure wall. This condition generates lower pressure peaks at the vertical wall probes FP1, FP2, FP3, and FP4, where the calculated pressure overestimates the experimental one with errors between 1 and 2 $P/\rho C^2$ (25%–60%). At FP3, the simulated pressure peak is similar to the experimental one.

Some pressure signals, such as a5, b3, b6, and c6, show experimental pressure values close to zero during impact, whereas the present model exhibits significantly higher pressure values. Given the numerous factors influencing the pressure evolution, exploring the reasons for these discrepancies deserves further investigation, which is beyond the scope of this work. It can be supposed that the absence of the air phase plays a key role, which may slightly affect the three-dimensional shape of the wave after its collapse. As previously discussed, slight modifications in the wave shape can result in significant differences in recorded pressures. For wave conditions 1 and 3 the model weakly reproduces the oscillations found in the experimental signal at FP1. For all three wave conditions, at all structure probes, the air cushion plays a significant role. As a result, the pressure is, on average, overestimated. Despite the single-phase approximation, the present model gives, on average, a suitable estimate of the impact pressures. The single-phase model drawbacks have been highlighted. Modelling the air phase could enhance the pressure time series while significantly increasing the computational effort.

4. Conclusions

This work reports, for the first time, the validation of a 3D Smoothed Particle Hydrodynamics (SPH) model to study the impact and interaction of plunging waves with a moored floating structure. In addition to validating the time series of wave kinematics, hydrodynamic pressure on the structure, and its displacement components, the time representation of stress tension on the tethers has also been compared with experimental data. Results show that the simulated wave dynamics (i.e., height, phase, and wave shape upon impact) closely align with the laboratory experiment. Wave height errors are approximately 5%, which is deemed acceptable for engineering applications; differences between the simulation and the experiment are of the order of the particle dimension.

The simulated structure dynamics is reliable, showing relatively higher surge and slightly higher heave movement. The model predicts the maximum tensions in the anchor cables with a trend similar to the experimental data. The wave-structure impact pressures are largely affected by the air phase, with the air cushion between the wavefront and structure acting as an elastic buffer. Even without considering the air phase, pressures predicted by the single-phase model are quite acceptable at some pressure gauges where the simulated peak is close to the experimental one. Although the model shows relatively higher pressure peaks, the experimental trend is closely reproduced by the model with a duration similar to the experiment.

While air phase modelling is possible, it requires a significantly larger computational effort. The main features of different wave conditions impacting an offshore floating structure are reliably predicted by the single-phase model. Therefore, this model is validated with experimental data. Results featured in this work are compared with Cai et al. (2023), where only WC2 is modelled with DualSPHysics at higher spatial resolution. This comparison shows that the presented model provides, with significantly smaller computational cost, a comprehensive and accurate prediction of the physical processes involved in the three focused waves with structure impact.

CRediT authorship contribution statement

Nicolò Salis: Writing – original draft, Visualization, Validation, Software, Methodology, Conceptualization. **Xiangyu Hu:** Writing – review & editing, Supervision, Software, Methodology, Conceptualization. **Min Luo:** Writing – review & editing, Investigation, Conceptualization. **Alessandro Reali:** Writing – review & editing, Conceptualization. **Sauro Manenti:** Writing – original draft, Supervision, Methodology, Conceptualization.

Declaration of competing interest

The authors declare that they have no known competing financial interests or personal relationships that could have appeared to influence the work reported in this paper.

Data availability

No data was used for the research described in the article.

Acknowledgements

The EOS HPC cluster of the Department of Mathematics “Felice Casorati” at the University of Pavia is gratefully acknowledged.

The authors acknowledge the contribution of the National Recovery and Resilience Plan, Mission 4 Component 2 - Investment 1.4 - NATIONAL CENTER FOR HPC, BIG DATA AND QUANTUM COMPUTING (project code: CN 00000013) - funded by the European Union - NextGenerationEU, as well as the support by the Italian Ministry of University and Research (MUR) through the PRIN project COSMIC (No. 2022A79M75) funded by the European Union - Next Generation EU.

The research has received financial support from ICSC – Italian Research Center on High Performance Computing, Big Data and Quantum Computing, funded by European Union – NextGenerationEU.

References

Adami, S., Hu, X.Y., Adams, N.A., 2012. A generalized wall boundary condition for smoothed particle hydrodynamics. J. Comput. Phys. 231, 7057–7075.

Altomare, C., Gironella, X., Crespo, A.J., 2021. Simulation of random wave overtopping by a wcsph model. Appl. Ocean Res. 116, 102888.

Altomare, C., Tafuni, A., Domínguez, J.M., Crespo, A.J., Gironella, X., Sospedra, J., 2020. Sph simulations of real sea waves impacting a large-scale structure. J. Mar. Sci. Eng. 8, 826.

Antuono, M., Colagrossi, A., Marrone, S., 2012. Numerical diffusive terms in weakly-compressible sph schemes. Comput. Phys. Comm. 183, 2570–2580.

Biésel, F., Suquet, F., 1951. Les appareils générateurs de houle en laboratoire. Houille Blanche.

Bitner-Gregersen, E., Gramstad, O., 2016. Rogue waves-impact on ships and offshore structures. no. 5-2015 in dnv gl position paper. dnv gl strategic research & innovation.

Cai, G., Luo, M., Zhan, Y., Khayyer, A., 2023. Sph simulation of freak wave impact on a floating platform. In: The 33rd International Ocean and Polar Engineering Conference. OnePetro.

Carbonell, J.M., Oñate, E., Suárez, B., 2010. Modeling of ground excavation with the particle finite-element method. J. Eng. Mech. 136, 455–463.

Chan, E., Melville, W., 1988. Deep-water plunging wave pressures on a vertical plane wall. Proc. R. Soc. Lond. Ser. A Math. Phys. Eng. Sci. 417, 95–131.

Chen, L., Zang, J., Hillis, A.J., Morgan, G.C., Plummer, A.R., 2014. Numerical investigation of wave–structure interaction using openfoam. Ocean Eng. 88, 91–109.

Cremonesi, M., Franci, A., Idelsohn, S., Oñate, E., 2020. A state of the art review of the particle finite element method (pfem). Arch. Comput. Methods Eng. 27, 1709–1735.

Deng, Y., Yang, J., Zhao, W., Li, X., Xiao, L., 2016. Freak wave forces on a vertical cylinder. Coast. Eng. 114, 9–18.

Domínguez, J.M., Crespo, A.J., Hall, M., Altomare, C., Wu, M., Stratigaki, V., Troch, P., Cappietti, L., Gómez-Gesteira, M., 2019. Sph simulation of floating structures with moorings. Coast. Eng. 153, 103560.

Domínguez, J.M., Fourtakas, G., Altomare, C., Canelas, R.B., Tafuni, A., García-Feal, O., Martínez-Estévez, I., Mokos, A., Vacondio, R., Crespo, A.J., et al., 2022. Dualsphysics: from fluid dynamics to multiphysics problems. Comput. Part. Mech. 9, 867–895.

Dysthe, K., Krogstad, H.E., Müller, P., 2008. Oceanic rogue waves. Annu. Rev. Fluid Mech. 40, 287–310.

Fochesato, C., Grilli, S., Dias, F., 2007. Numerical modeling of extreme rogue waves generated by directional energy focusing. Wave Motion 44, 395–416.

Gingold, R.A., Monaghan, J.J., 1977. Smoothed particle hydrodynamics: theory and application to non-spherical stars. Mon. Not. R. Astron. Soc. 181, 375–389.

Gómez-Gesteira, M., Cerqueiro, D., Crespo, C., Dalrymple, R., 2005. Green water overtopping analyzed with a sph model. Ocean Eng. 32, 223–238.

Hall, M., 2020. Moordyn v2: New capabilities in mooring system components and load cases. In: International Conference on Offshore Mechanics and Arctic Engineering. Vol. 84416, American Society of Mechanical Engineers, V009T09A078.

Han, L., Hu, X., 2018. Sph modeling of fluid–structure interaction. J. Hydrodyn. 30, 62–69.

Hu, X.Y., Adams, N.A., 2006. A multi-phase sph method for macroscopic and mesoscopic flows. J. Comput. Phys. 213, 844–861.

Karin Magnusson, A., Donelan, M.A., 2013. The andrea wave characteristics of a measured north sea rogue wave. J. Offshore Mech. Arct. Eng. 135.

Kharif, C., Pelinovsky, E., 2003. Physical mechanisms of the rogue wave phenomenon. Eur. J. Mech. B Fluids 22, 603–634.

Khayyer, A., Gotoh, H., Shimizu, Y., Gotoh, K., 2017. On enhancement of energy conservation properties of projection-based particle methods. Eur. J. Mech. B Fluids 66, 20–37.

Khayyer, A., Shimizu, Y., Gotoh, T., Gotoh, H., 2023. Enhanced resolution of the continuity equation in explicit weakly compressible sph simulations of incompressible free-surface fluid flows. Appl. Math. Model. 116, 84–121.

Larese, A., Iaconeta, I., Chandra, B., Singer, V., 2019. Implicit mpm and coupled mpm-fem in geomechanics. Comput. Mech. 175, 226–232.

Lucy, L.B., 1977. A numerical approach to the testing of the fission hypothesis. Astron. J. 82, 1013–1024.

Luo, M., Khayyer, A., Lin, P., 2021. Particle methods in ocean and coastal engineering. Appl. Ocean Res. 114, 102734.

Luo, M., Koh, C.G., Lee, W.X., Lin, P., Reeve, D.E., 2020. Experimental study of freak wave impacts on a tension-leg platform. Mar. Struct. 74, 102821.

Luo, M., Rubinato, M., Wang, X., Zhao, X., 2022. Experimental investigation of freak wave actions on a floating platform and effects of the air gap. Ocean Eng. 253, 111192.

Lyu, H.-G., Sun, P.-N., Liu, P.-Z., Huang, X.-T., Colagrossi, A., 2023. Derivation of an improved smoothed particle hydrodynamics model for establishing a three-dimensional numerical wave tank overcoming excessive numerical dissipation. Phys. Fluids 35.

Manenti, S., Panizzo, A., Ruol, P., Martinelli, L., 2008. Sph simulation of a floating body forced by regular waves. In: Proceedings of 3rd SPHERIC Workshop. pp. 38–41.

Marrone, S., Colagrossi, A., Baudry, V., Le Touzé, D., 2019. Extreme wave impacts on a wave energy converter: load prediction through a sph model. Coast. Eng. J. 61, 63–77.
Monaghan, J.J., 1994. Simulating free surface flows with sph. J. Comput. Phys. 110, 399–406.
Moreno, E.C., Fourtakas, G., Stansby, P., Crespo, A., 2020. Response of the multi-float wec m4 in focussed waves using sph. In: Developments in Renewable Energies Offshore. CRC Press, pp. 199–205.
Oñate, E., Cornejo, A., Zárate, F., Kashiyama, K., Franci, A., 2022. Combination of the finite element method and particle-based methods for predicting the failure of reinforced concrete structures under extreme water forces. Eng. Struct. 251, 113510.
Rapp, R.J., Melville, W.K., 1990. Laboratory measurements of deep-water breaking waves. Philos. Trans. R. Soc. Lond. Ser. A Math. Phys. Sci. 331, 735–800.
Ren, Y., Khayyer, A., Lin, P., Hu, X., 2023a. Numerical modeling of sloshing flow interaction with an elastic baffle using sphinxsys. Ocean Eng. 267, 113110.
Ren, Y., Lin, P., Zhang, C., Hu, X., 2023b. An efficient correction method in riemann sph for the simulation of general free surface flows. Comput. Methods Appl. Mech. Engrg. 417, 116460.
Salis, N., Franci, A., Idelsohn, S., Reali, A., Manenti, S., 2023. Lagrangian particle-based simulation of waves: a comparison of sph and pfem approaches. Eng. Comput..
Salis, N., Luo, M., Reali, A., Manenti, S., 2021. Sph simulation of water waves and impact with a rigid offshore structure in a 2d flume. In: The 31st International Ocean and Polar Engineering Conference. OnePetro.
Salis, N., Luo, M., Reali, A., Manenti, S., 2022. Wave generation and wave–structure impact modelling with wcsph. Ocean Eng. 266, 113228.
Sherman, M.A., Seth, A., Delp, S.L., 2011. Simbody: multibody dynamics for biomedical research. Procedia Iutam 2, 241–261.
Shimizu, Y., Khayyer, A., Gotoh, H., Nagashima, K., 2020. An enhanced multiphase isph-based method for accurate modeling of oil spill. Coast. Eng. J. 62, 625–646.
Soga, K., Alonso, E., Yerro, A., Kumar, K., Bandara, S., 2016. Trends in large-deformation analysis of landslide mass movements with particular emphasis on the material point method. Géotechnique 66, 248–273.
Stansberg, C.T., Baarholm, R., Kristiansen, T., Hansen, E., Rortveit, G., 2005. Extreme wave amplification and impact loads on offshore structures. In: Offshore Technology Conference. OnePetro.
Sun, P.-N., Luo, M., Le Touzé, D., Zhang, A.-M., 2019. The suction effect during freak wave slamming on a fixed platform deck: Smoothed particle hydrodynamics simulation and experimental study. Phys. Fluids 31, 117108.
Sun, P., Pilloton, C., Antuono, M., Colagrossi, A., 2023. Inclusion of an acoustic damper term in weakly-compressible sph models. J. Comput. Phys. 483, 112056.
Tagliafierro, B., Karimirad, M., Altomare, C., Göteman, M., Martínez-Estévez, I., Capasso, S., Domínguez, J.M., Viccione, G., Gómez-Gesteira, M., Crespo, A.J., 2023. Numerical validations and investigation of a semi-submersible floating offshore wind turbine platform interacting with ocean waves using an sph framework. Appl. Ocean Res. 141, 103757.
Tagliafierro, B., Martínez-Estévez, I., Domínguez, J.M., Crespo, A.J., Göteman, M., Engström, J., Gómez-Gesteira, M., 2022. A numerical study of a taut-moored point-absorber wave energy converter with a linear power take-off system under extreme wave conditions. Appl. Energy 311, 118629.
Verbrugghe, T., Domínguez, J.M., Crespo, A.J., Altomare, C., Stratigaki, V., Troch, P., Kortenhaus, A., 2018. Coupling methodology for smoothed particle hydrodynamics modelling of non-linear wave-structure interactions. Coast. Eng. 138, 184–198.
Vila, J.P., 2005. Sph renormalized hybrid methods for conservation laws: applications to free surface flows. In: Meshfree Methods for Partial Differential Equations II. Springer, pp. 207–229.
Wen, H., Ren, B., Yu, X., 2018. An improved sph model for turbulent hydrodynamics of a 2d oscillating water chamber. Ocean Eng. 150, 152–166.
Wendland, H., 1995. Piecewise polynomial, positive definite and compactly supported radial functions of minimal degree. Adv. Comput. Math. 4, 389–396.
Westphalen, J., Greaves, D.M., Raby, A., Hu, Z.Z., Causon, D.M., Mingham, C.G., Omidvar, P., Stansby, P.K., Rogers, B.D., et al., 2014. Investigation of wave-structure interaction using state of the art cfd techniques. Open J. Fluid Dyn. 4, 18.
Wu, D., Zhang, C., Tang, X., Hu, X., 2023. An essentially non-hourglass formulation for total lagrangian smoothed particle hydrodynamics. Comput. Methods Appl. Mech. Engrg. 407, 115915.
Yan, M., Ma, X., Bai, W., Lin, Z., Li, Y., 2020. Numerical simulation of wave interaction with payloads of different postures using openfoam. J. Mar. Sci. Eng. 8, 433.
Yu, Y., Zhu, Y., Zhang, C., Haidn, O.J., Hu, X., 2023. Level-set based pre-processing techniques for particle methods. Comput. Phys. Comm. 289, 108744.
Zago, V., Schulze, L.J., Bilotta, G., Almashan, N., Dalrymple, R., 2021. Overcoming excessive numerical dissipation in sph modeling of water waves. Coast. Eng. 170, 104018.
Zhang, S., Fan, Y., Zhang, C., Adams, N., Xiangyu, H., 2023. A diffusive wetting model for water entry/exit based on the weakly-compressible sph method. arXiv preprint arXiv:2310.11179.
Zhang, C., Hu, X., Adams, N.A., 2017. A weakly compressible sph method based on a low-dissipation riemann solver. J. Comput. Phys. 335, 605–620.
Zhang, C., Rezavand, M., Hu, X., 2020a. Dual-criteria time stepping for weakly compressible smoothed particle hydrodynamics. J. Comput. Phys. 404, 109135.
Zhang, C., Rezavand, M., Hu, X., 2021a. A multi-resolution sph method for fluid–structure interactions. J. Comput. Phys. 429, 110028.
Zhang, C., Rezavand, M., Zhu, Y., Yu, Y., Wu, D., Zhang, W., Wang, J., Hu, X., 2021b. Sphinxsys: An open-source multi-physics and multi-resolution library based on smoothed particle hydrodynamics. Comput. Phys. Comm. 267, 108066.
Zhang, C., Rezavand, M., Zhu, Y., Yu, Y., Wu, D., Zhang, W., Zhang, S., Wang, J., Hu, X., 2020b. Sphinxsys: An open-source meshless, multi-resolution and multi-physics library. Softw. Impacts 6, 100033.
Zhang, C., Wei, Y., Dias, F., Hu, X., 2021c. An efficient fully lagrangian solver for modeling wave interaction with oscillating wave surge converter. Ocean Eng. 236, 109540.

8.3 Final remarks

This work shows that the models produces accurate results with different forcing waves. The model is validated and can be used to reproduce numerically real-scale engineering applications, or to design an experimental campaign.

9

Improvements to the multiphase model

9.1 Introduction

This chapter discusses the final components of the multiphase model, completing the puzzle. As mentioned in the previous chapter, the multiphase model encountered some issues. Figure 9.1 depicts two snapshots of a multiphase plunging wave-structure impact, illustrating the tensile instability between phases. To save computational time, a small number of air particles were considered in this simulation.

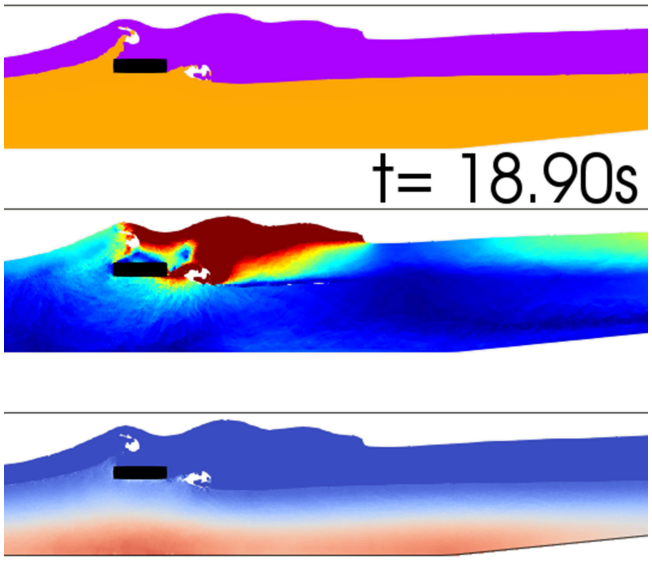

Figure 9.1: Plunging wave-structure impact in a multiphase scenario, showing tensile instability between phases.

Figure 9.2 illustrates the small gap between particles of different phases and the initiation of tensile instability. Additionally, particle clusters inside the air bubble are visible due to the high pressure gradient.

The following sections introduce two schemes aimed at addressing these issues. First, a particle shifting algorithm is presented, along with a novel free surface detection method to reduce tensile instability and particle clusters. Additionally, the interface is treated with a Riemann solver to eliminate the interface gap and prevent tensile instability.

9.2 SPH Formulation

The SPH model presented in the following sections has been developed by introducing relevant modifications independently into the original code SPHERA v.9.0.0 (RSE SpA) [43]. This derived code [62] is redistributed on GitHub under the GNU-GPL license, adhering to the copyright terms of SPHERA. For additional details, the official documentation of the code provides a comprehensive description of the original SPHERA model [43, 63, 46, 47, 64].

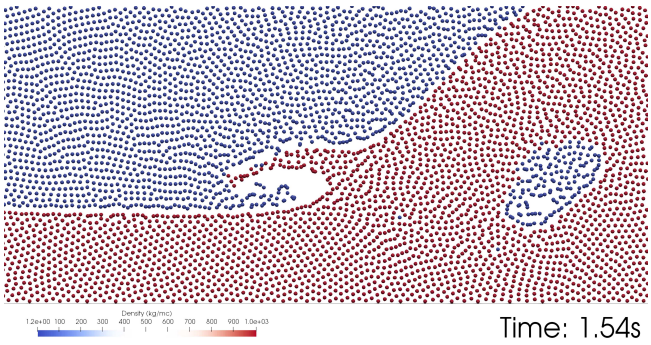

Figure 9.2: Gap between phases in a dam break scenario.

9.2.1 A Reminder on the SPH Approximation of Governing Equations

The mass balance equation is:

$$\begin{aligned}\left\langle \frac{d\rho}{dt} \right\rangle_i &= \sum_j \rho_i(\mathbf{u}_j - \mathbf{u}_i)\cdot\nabla W \frac{m_j}{\rho_j} \\ +2\rho_i \int_{V_h'} [(\mathbf{u}_w - \mathbf{u}_i)\cdot\mathbf{n}]\mathbf{n}\cdot\nabla W dx^3 + C_s \\ +2\delta c_i h \sum_{b=1}^{N} \psi_{ij} \frac{r_{ij}\cdot\nabla W}{||r_{ij}||^2}\frac{m_j}{\rho_j}\end{aligned} \tag{9.1}$$

In the computational framework, the subscript i denotes the computational particle, while subscript j denotes the neighbouring particle. Here, ρ represents particle density, m denotes particle mass, W is the kernel function, and r_{ij} stands for the relative distance between the computational particle and its neighbouring counterpart. The vector $\boldsymbol{n}$ denotes the normal vector to the boundary surface, c_i signifies the artificial sound celerity, and h represents the smoothing length. Additionally, δ denotes the diffusive coefficient, and ψ_{ij} represents the diffusive term formulated as per [60]. The subscripts s and w respectively denote the generic neighbouring surface body particle and the solid contour, as described by [47]. The term C_s characterises the fluid-body interaction contribution to the mass balance equation and is defined as:

$$C_s = 2\rho_i \sum_s [(\mathbf{u}_s - \mathbf{u}_i)\cdot\mathbf{n}_s]\nabla W_s \varpi_s \tag{9.2}$$

In this scheme, ϖ_s represents the volume of the body particle. This approach, initially introduced by [65], can be interpreted as a discretisation of the semi-analytic method. Additionally, it's worth noting that the final term in Equation (9.1) accounts for a diffusive contribution necessary for obtaining a stable pressure field solution [60]. The Smoothed Particle Hydrodynamics (SPH) approximation of the momentum balance equations Eq. (9.3) is expressed as follows:

$$\begin{aligned}\left\langle \frac{d\mathbf{u}}{dt} \right\rangle_i &= -\mathbf{g} + \frac{1}{\rho_i}\sum_j (p_j - p_i)\nabla W \frac{m_j}{\rho_j} \\ &+ \xi \frac{|p_j| + |p_i|}{\rho_i \rho_j} + 2\frac{p_i}{\rho_i}\int_{V_h'} \nabla W dx^3 \\ &- \nu_m \sum_j \frac{m_j}{\rho_j}\frac{1}{r_{ij}^2}(\mathbf{u}_j - \mathbf{u}_i)\cdot(\mathbf{x}_j - \mathbf{x}_i)\nabla W \\ &- 2\frac{\nu_m}{\rho_{0in}}(\mathbf{u}_w - \mathbf{u}_i)\cdot\int_{V_h'} \frac{1}{r_{0_w}^2}(\mathbf{x} - \mathbf{x}_i)\nabla W dx^3 \\ &+ \mathbf{a}_s + 2\nu_i(\mathbf{u}_w - \mathbf{u}_i)\int_{V_h'} \frac{1}{r}\frac{\partial W}{\partial r} dx^3\end{aligned} \tag{9.3}$$

In this context, $\mathbf{g}$ represents the acceleration due to gravity, $\mathbf{x}$ is the position vector of the particle, and ρ_{0in} stands for the initial density of particle 0. The artificial viscosity is defined as $\nu_m = \rho_{0in}\frac{\alpha \cdot h \cdot c}{\rho_i}$, where α is the artificial viscosity coefficient ranging between 0.01 and 0.1 depending on the case study [48]. The second term aims to control the interface sharpness between the two media. In [52], this term is utilised to introduce a small repulsive force between the media to model surface tension. It's important to note that no attempt at correctly modelling surface tension is made. The term $\mathbf{a}_s$ in Equation (9.3) represents the fluid-body interaction contribution to the momentum balance equation and is defined as:

$$\mathbf{a}_s = \sum_s \Big(\frac{p_s + p_i}{\rho_i^2}\Big)\nabla W_s m_s \tag{9.4}$$

The system of equations (Equations (9.1) and (9.3)) is closed by a new formulation of the state equation for slightly compressible fluids, which reads:

$$p = \frac{\rho_{ref\chi} c_{ref\chi}^2}{\gamma_\chi}\Big(\Big(\frac{\rho}{\rho_{ref_\chi}}\Big)^{\gamma_\chi} - 1\Big) + p_i \tag{9.5}$$

Here, the subscript χ refers to the properties of the fluid particle, where $\gamma_\chi = 7$ for water and $\gamma_\chi = 1.4$ for the air phase. In SPH, the artificial sound speed c_{ref} must be assumed to be at least ten times higher than the maximum fluid velocity to ensure a relative density variation of at most 1% [48], and the subscript ref stands for the reference state. Regarding the imposition of boundary conditions, it's noteworthy that no constraints are required to define the free surfaces. Solid walls are treated with the semi-analytic approach [46], where at the boundaries, the kernel support can partially lie outside the fluid domain. The integral terms in Equations (9.1) and (9.3) express these boundary contributions. These terms represent the convolution integral over the portion of the kernel support V_h' that lies outside of the domain and is filled with body particles. A second-order staggered Leapfrog scheme is utilised to integrate the governing equations in time [64]. Equation (9.6) presents the stability criteria for the time integration:

$$dt = \min_i\Big\{0.05\frac{2h^2}{\nu}; CFL\frac{2h}{c + |\mathbf{u}|}\Big\} \tag{9.6}$$

9.2.2 Particle Shifting Technology

Particle shifting algorithms based on Fick's law enable the regularisation of particle concentration within the domain. Particles are relocated from regions of high particle density to those with lower density. In technical literature, particles are shifted using either a spatial shifting vector [66, 67, 68] or a velocity shifting vector [69, 70, 71]. After careful consideration, both approaches are evaluated. This work considers the shifting velocity vector as depicted in Equation (9.7), where the characteristic velocity is defined in Equation (9.8) [71], with the characteristic length being equal to the smoothing length $2h$.

$$\delta\mathbf{u}_i = -0.5\phi\begin{cases} U^{char}\Big(\frac{h}{dx}\Big)^3 h\widehat{\nabla C_i} & \text{if } \Big\|\Big(\frac{h}{dx}\Big)^3 R\widehat{\nabla C_i}\Big\| < 0.5\frac{1}{h}, \\ U^{char}\Big(0.5\frac{h}{dx}\Big)\frac{\widehat{\nabla C_i}}{\|\widehat{\nabla C_i}\|} & \text{otherwise} \end{cases} \tag{9.7}$$

$$U^{char} = \max_{b=1}^{N}\Big(\Big\|(\mathbf{u}_j - \mathbf{u}_i)\cdot\frac{\mathbf{x}_j - \mathbf{x}_i}{\|\mathbf{x}_j - \mathbf{x}_i\|}\Big\|\Big) \tag{9.8}$$

The SPH approximation of the particle concentration gradient is utilised:

$$\widehat{\nabla C_i} = \sum_{b=1}^{N}\Big[\zeta + X_{ij}\Big]\nabla W\frac{m_j}{\rho_j} \tag{9.9}$$

with:

$$X_{ij} = 2\Big(\frac{W_{ij}}{W(dx_0)}\Big)^4 \tag{9.10}$$

Here, X_{ij} denotes an artificial pressure-like function originally introduced in [72] and used as an additive term in the momentum balance equation to prevent tensile instability, where dx_0 is the initial particle dimension. Following

the approach proposed by [67, 68], the magnitude of the velocity vector varies depending on the particle type. Three particle types are identified within the domain: free surface particles ($\mathbb{F}$), buffer particles ($\mathbb{B}$), and inner particles ($\mathbb{I}$). Free surface particles $\mathbb{F}$ are not shifted to avoid non-physical movement of the free surface. Buffer particles $\mathbb{B}$ are treated differently than inner particles, with ζ being added according to the improved particle shifting technique in [67]:

$$\begin{cases} \zeta = 0 & \text{if } pg \in \mathbb{B} \\ \zeta = 1 & \text{if } pg \in \mathbb{I} \end{cases} \tag{9.11}$$

The parameter ϕ controls the intensity of the shifting:

$$\begin{cases} \phi = 0 & \text{if } pg \in \mathbb{F} \\ \phi = \varsigma & \text{if } pg \in \mathbb{B} \\ \phi = 1 & \text{if } pg \in \mathbb{I} \end{cases} \tag{9.12}$$

The function ς changes smoothly from zero to one, and $min(\mathbf{r}_{ij})$ represents the distance from the computational $\mathbb{B}$ particle to the closest free surface particle:

$$\varsigma = \frac{min(\mathbf{r}_{ij}) \cdot \mathbf{n}_i}{2h} \tag{9.13}$$

A particle's normal vector is defined according to [67]:

$$n_i = -\frac{\mathbf{L}\nabla\mathbf{C_i}}{\|\mathbf{L}\nabla C_i\|} \tag{9.14}$$

Here, $-\nabla C_i$ always points in the direction of maximum anisotropy [73], i.e., the region with low particle concentration:

$$\nabla C_i = \sum_{j}^{N} \nabla W \frac{m_j}{\rho_j} \tag{9.15}$$

9.2.3 Free Surface Detection

Particles within the domain must be identified to correctly apply particle shifting. Two similar methods are proposed in the technical literature. In [74], free surface particles are identified using the minimum eigenvalue of the $\mathbf{L}_i$ matrix. After an initial detection with the minimum eigenvalue, the search is extended to an "umbrella-shaped" area. If no particles are detected in this area, the particle is classified as a free surface particle; otherwise, it is not. [68] proposed a similar technique based on the concept of human vision. Both algorithms identify particles near the free surface, i.e., particles with at least one free surface neighbor in their compact support. Here, we propose a new algorithm formulation for particle identification. Initially, free surface particles are identified in a first sweep using a condition on the determinant of the $\mathbf{B}_i$ matrix:

$$\begin{cases} pg_i \in \mathbb{F} & \text{if } \det(\mathbf{B}_i) \leq 0.6, \\ pg_i \notin \mathbb{F} & \text{if } \det(\mathbf{B}_i) > 0.6. \end{cases} \tag{9.16}$$

In a second sweep, particles are distinguished as either belonging to $\mathbb{B}$ or $\mathbb{I}$; where pg_i represents the computational particle and pg_j is the neighbouring particle:

$$\begin{cases} \text{if } \Big[(\mathbf{x}_j - \mathbf{x}_i) \leq 2h \text{ and } pg_j \in \mathbb{F}\Big] \Rightarrow pg_i \in \mathbb{B}, \\ \text{else } pg_i \in \mathbb{I}. \end{cases} \tag{9.17}$$

9.2.4 Two Phase Extension

The two-phase extension is implemented in a single sweep across all particles. The position of the interface remains unaltered due to the newly introduced free surface detection method. Heavier mean particles belonging to the interface are not shifted, while no conditions are imposed on lighter fluid particles near the interface. It is worth noting that with the semi-analytic approach as boundary treatment, particles near the boundary are treated like free surface particles, and thus no shifting is allowed.

9.2.5 Riemann Interface

At the interface, a Riemann solver is applied to achieve the exact solution at the interface, hereafter referred to as the star region and indicated with the apex *. Velocities at the interface are projected along the normalised direction $\mathbf{e}_{ij} = (\mathbf{x}_i - \mathbf{x}_j)/\|\mathbf{r}_{ij}\|$. According to [75], the solution of the Riemann solver at the interface, for fluids with different sound speeds, is given by:

$$\begin{cases} u^*_{ij} = \frac{\rho_j c_j u_j + \rho_i c_i u_i + p_i - p_j}{\rho_j c_j + \rho_i c_i}, \\ p^*_{ij} = \frac{\rho_j c_j p_j + \rho_i c_i p_i + \rho_j c_j \rho_i c_i (u_i - u_j)}{\rho_j c_j + \rho_i c_i}. \end{cases} \tag{9.18}$$

At the interface, the pressure term in Eq. (9.3) and the velocity term in Eq. (9.1) are modified according to [56]:

$$\begin{cases} 2\sum_j \rho_i (\mathbf{u}^* - \mathbf{u}_i) \cdot \nabla W \frac{m_j}{\rho_j}, \\ 2\frac{1}{\rho_i}\sum_j (p^*) \nabla W \frac{m_j}{\rho_j} + \xi \frac{|p_j| + |p_i|}{2\rho_i \rho_j}. \end{cases} \tag{9.19}$$

The velocity at the interface is $\mathbf{u}^* = u^* \mathbf{e}_{ij} + \overline{\mathbf{u}}_{ij} - \overline{u}\mathbf{e}_{ij}$, where $\overline{\mathbf{u}}_{ij} = (\rho_j c_j \mathbf{u}_j + \rho_i c_i \mathbf{u}_i)/(\rho_j c_j + \rho_i c_i)$ and $\overline{u} = (\rho_j c_j u_j + \rho_i c_i u_i)/(\rho_j c_j + \rho_i c_i)$.

9.2.6 SPH solution scheme

The momentum and the mass balance equations are solved as described below. After the first initialisation of the particles in the domain i.e. neighbouring search and computations of: $\mathbf{r_{ij}}$, W, ∇W for the background grid, at each time step:

1. Evaluation of the integrals for the solid neighbouring surface contour
2. Computation of the momentum balance equation and body dynamics Eq. (9.3)
3. Leapfrog integration of the momentum balance equation
4. Particle shifting
5. Update the particle position (Lagrangian trajectory).
6. Neighbouring search and computations of: $\mathbf{r_{ij}}$, W, ∇W
7. Evaluation of the integrals for the solid neighbouring surface contour
8. Computation of the mass balance equation Eq. (9.1)
9. Leapfrog integration of the mass balance equation
10. Pressures computations via the equation of state Eq. (9.5)

9.3 Results and discussion

9.3.1 Taylor-Green Vortices

The Taylor-Green vortex problem is characterised by a set of decaying vortices, for which analytical solutions of the incompressible Navier-Stokes equations can be achieved. These vortices are counter-rotating, resulting in regions of low pressure, i.e., pressure lower than zero, between them. In the Smoothed Particle Hydrodynamics (SPH) framework, tensile instability appears in these regions. This problem serves as a common benchmark to assess the accuracy of SPH schemes, where particles are adjusted from their natural trajectories to achieve a regular distribution in the domain, avoiding non-physical voids. In this work, the Taylor-Green vortex problem is utilised to validate the proposed particle shifting technique. The initial condition for the Taylor-Green vortices is defined by the following velocity field components:

$$\begin{aligned} u_x &= A\cos(ax)\cdot\sin(by)\cdot\sin(cz) \\ u_y &= B\sin(ax)\cdot\cos(by)\cdot\sin(cz) \\ u_z &= C\sin(ax)\cdot\sin(by)\cdot\cos(cz) \end{aligned} \tag{9.20}$$

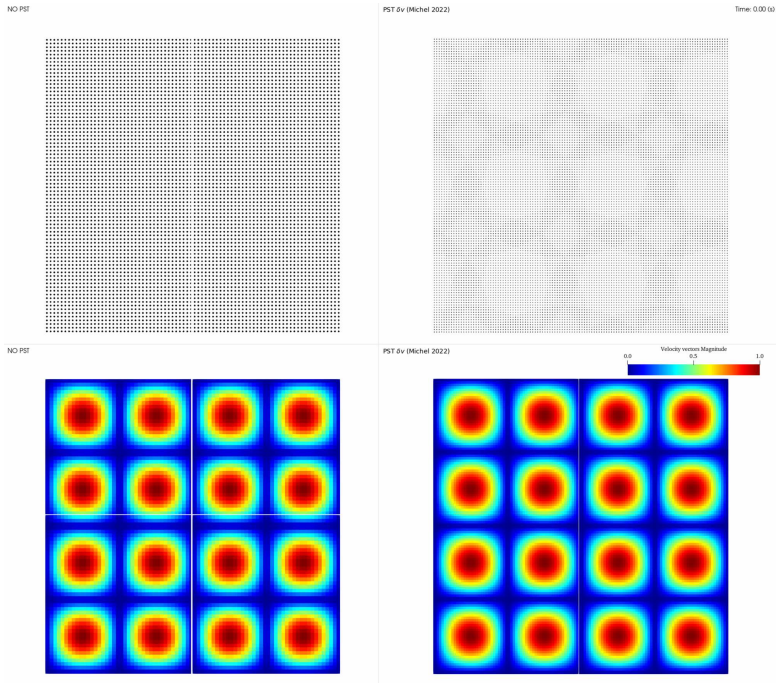

Figure 9.3: Taylor-Green vortices initial condition. Upper panels show particle distribution, lower panels show initial velocity contour.

After imposing the initial conditions, the flow begins. Turbulence is not considered in the SPH model; therefore, the Taylor-Green vortices do not decay over time but rather oscillate indefinitely with constant amplitude. Figure 9.3 illustrates the initial conditions defined in (9.20). The reference density of the fluid is $\rho_w = 1000$ kg m^{-3}, and gravity $g_z = 9.81$ m s^{-2} acts in the $-z$ direction.

Figure 9.4 displays the Taylor-Green vortices after 6 seconds of simulation. It is important to note that with turbulence modelling, the vortices would dissipate, and the velocity field would flatten. In the left-hand panels, the derived model without particle shifting is shown. Tensile instability is evident, and the particle distribution in the domain becomes irregular. In the right-hand panels, the model with particle shifting is depicted. With particle shifting, no voids appear, and the particle distribution is more regular. Small voids form at the domain edges because those particles are considered free surface particles, and thus, particle shifting is not applied to them.

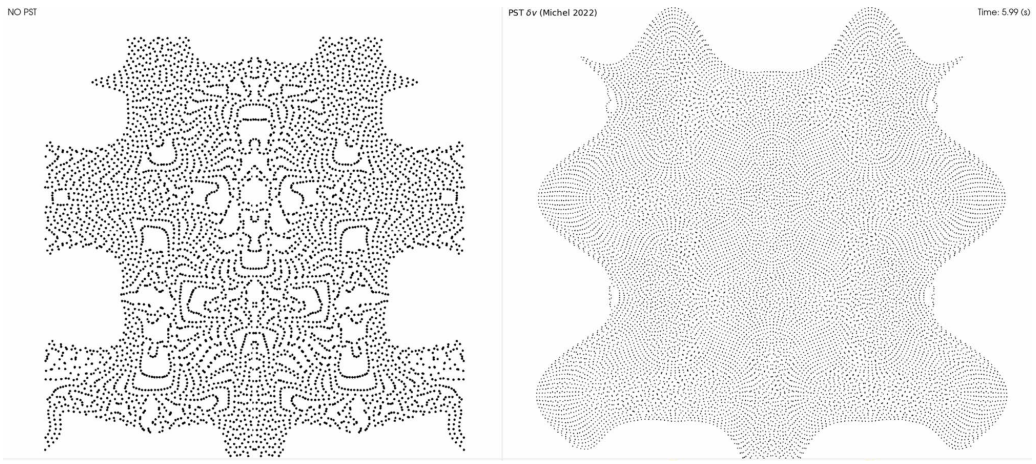

Figure 9.4: Taylor green vortexes at $t = 2.00$ (s) and $t = 5.99$ (s). Upper panels particle distribution, lower panels velocity contour. On the left-hand side there is the derived model without particle shifting, on the right-hand side there is the model with the particle shifting.

9.3.2 Dam Break

The dam break test case is widely adopted to evaluate the response of numerical models due to its relatively simple setup and implementation, low computational cost, and availability of reference results for comparison. Figure 9.5 illustrates the adopted domain.

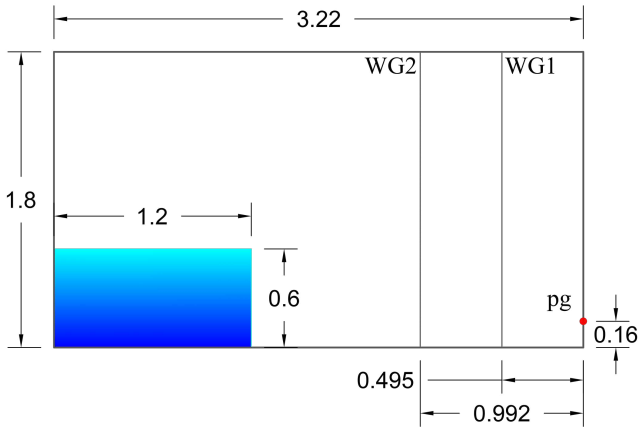

Figure 9.5: Dam-break simulation setup.

The presence of the air phase is crucial as both the pressure measured at pg and the interface are affected. In [76], a multiphase model without interface treatment and particle shifting was presented. The absence of these schemes resulted in particle clusters inside the enclosed air pocket and the formation of non-physical voids in the air phase, especially in the presence of high velocities and pressure gradients. These difficulties are overcome with the present model. Although there is a difference in particle size between the two simulations, this fundamental improvement is evident in Figures 9.6 and 9.7.

Figure 9.8 compares the interface between the single-phase model [76] and the present multiphase model. At WG1, the present model exhibits a more regular interface, while at WG2, the present model interface closely resembles the experimental result. The peak at $t = 1.8s$ observed in the single-phase free surface is attenuated by the presence of the air phase in the present multiphase model.

Figure 9.9 depicts the pressure recorded at the pg gauge. Although there are oscillations due to the coarse particle dimension, the present model closely matches the experimental pressure.

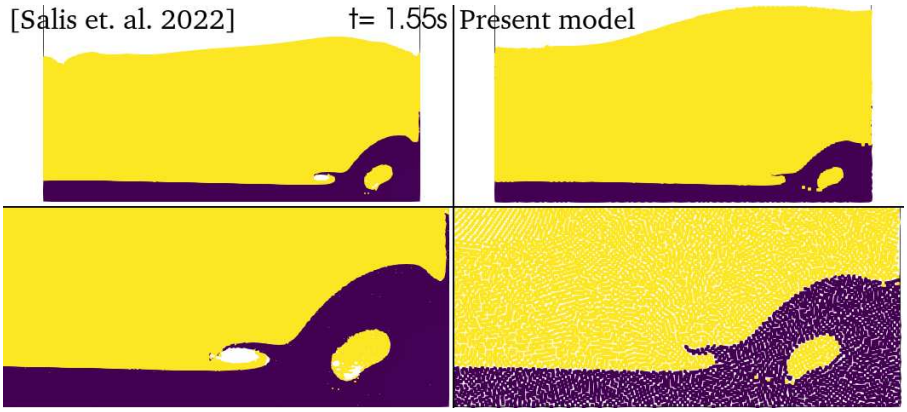

Figure 9.6: Comparison of dam break between the multiphase model [76] and the present model. Focus on the particle clusters in the air pocket and void formation at $t = 1.55s$.

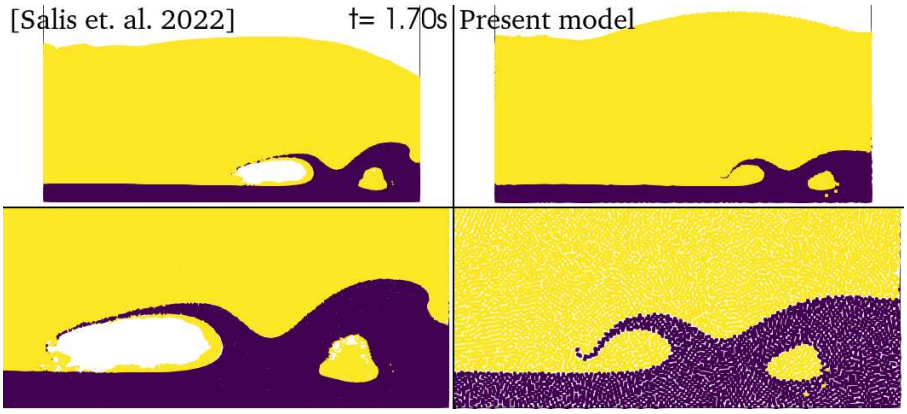

Figure 9.7: Comparison of dam break between the multiphase model [76] and the present model. Focus on the particle clusters in the air pocket and void formation at $t = 1.70s$.

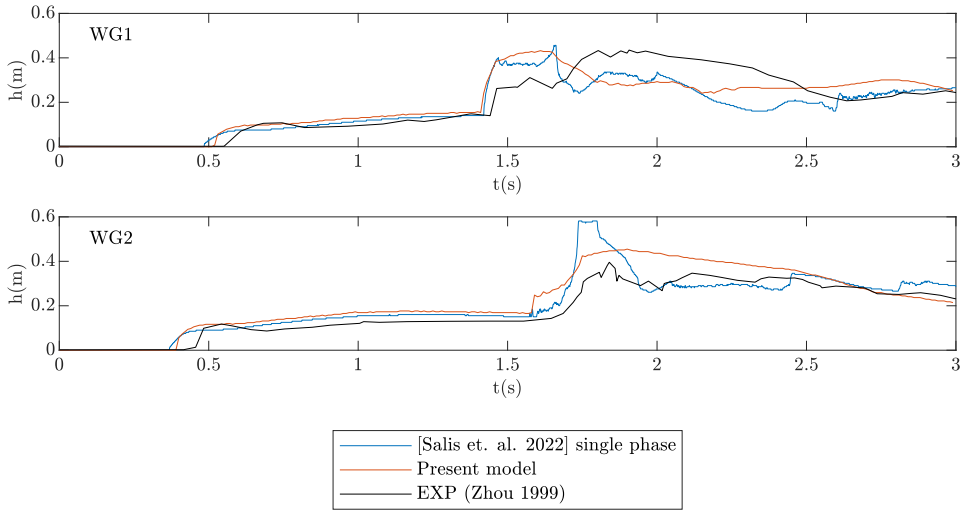

Figure 9.8: Comparison of water-air interface between the single-phase model [76] and the present model.

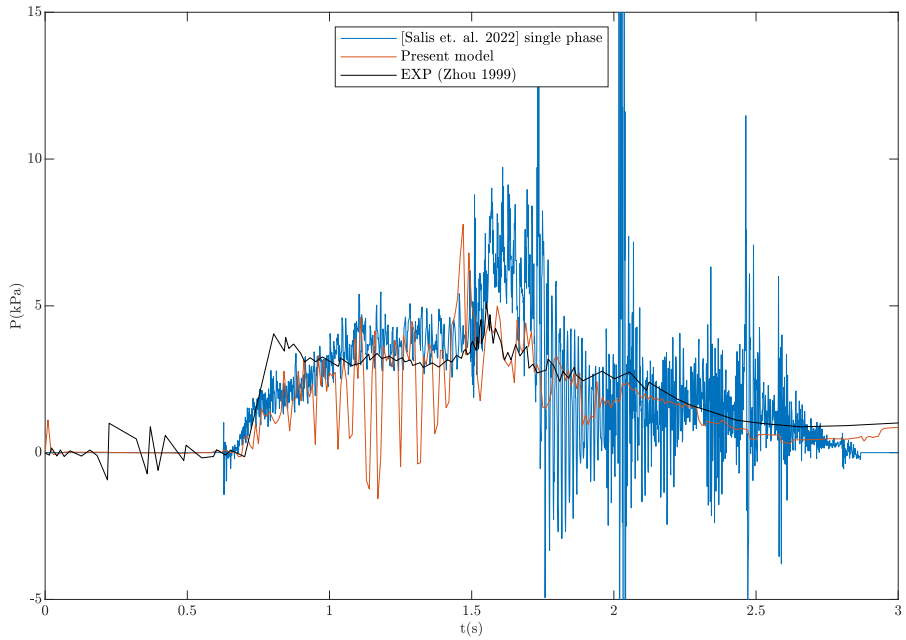

Figure 9.9: Pressure comparison at pg between the single-phase model [76] and the present model.

9.3.3 Falling Droplet

This test case is included to demonstrate the model's capabilities in handling large velocity and pressure gradients. In this scenario, a water droplet is released to fall in air. Figure 9.10 illustrates the domain setup, where $D = 2m$ represents the diameter of the water droplet. For this test case, $\xi = 0.8$ is used to enable the simulation of surface tension.

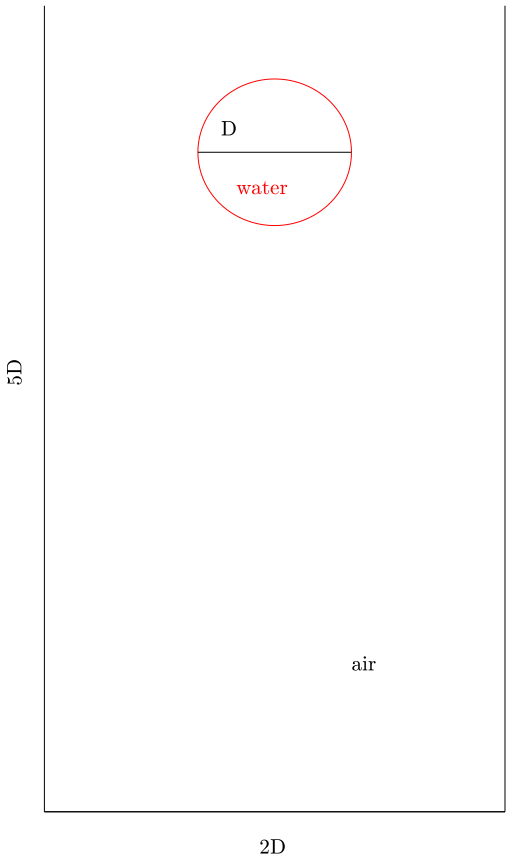

Figure 9.10: Falling droplet domain setup.

Figure 9.11 displays the contours of density, pressure, velocity, and the result of the free surface identification algorithm. In the right-hand panel, black particles represent free surface particles $\mathbb{F}$, orange particles represent buffer particles $\mathbb{B}$, and white particles represent inner particles $\mathbb{I}$. The velocity contour near the falling droplet is smooth and exhibits a very high gradient upon impacting the bottom. Despite these high velocity gradients, void formation is not observed. As the droplet falls, it maintains its circular shape, and the simulation remains stable upon impact, with the water symmetrically diverging toward the side walls.

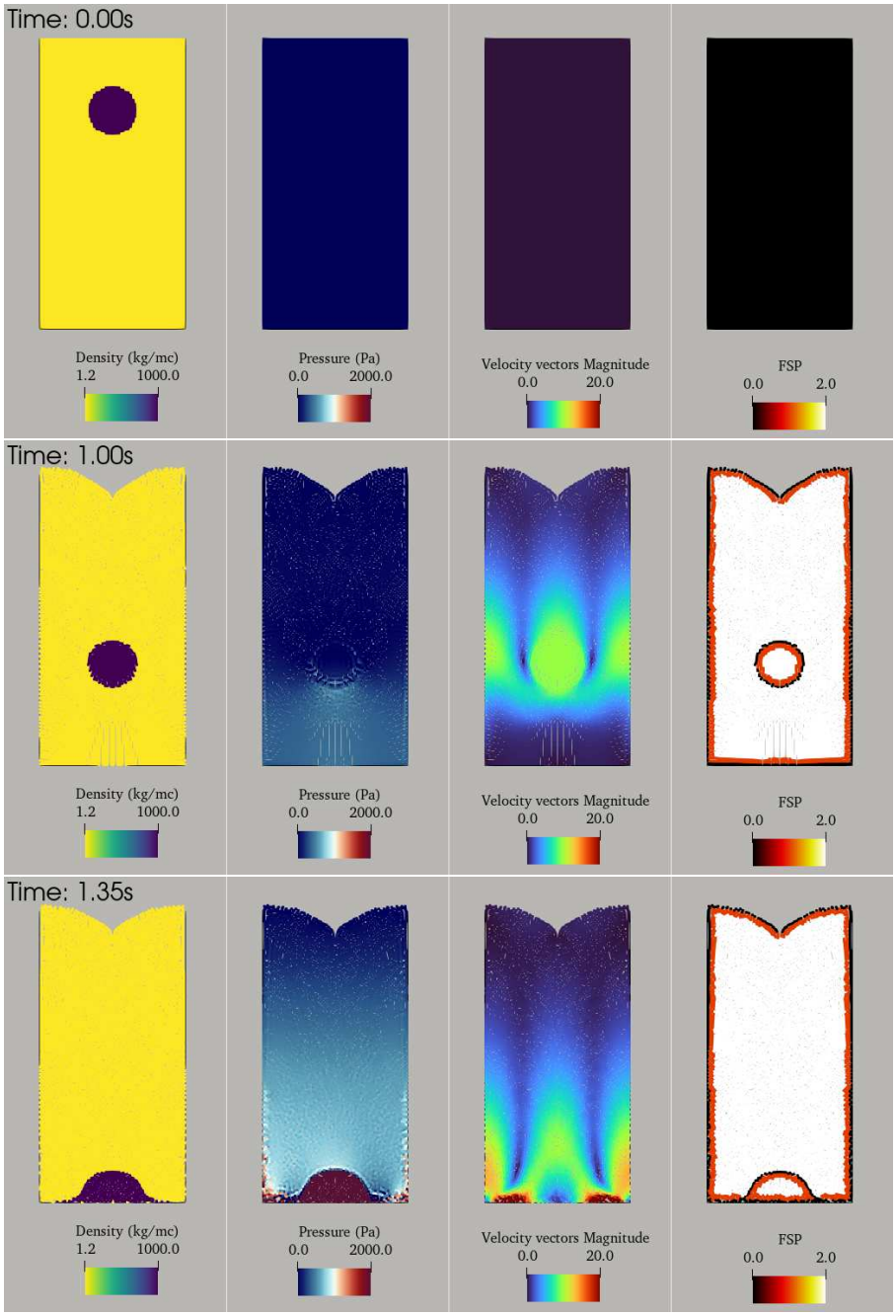

Figure 9.11: Falling droplet and impact with bottom. Left-hand panel: Density between media, middle left.hand panel: pressure, middle right-hand panel: magnitude velocity vectors, right hand panels: free surface particles.

9.3.4 Rising Bubble

This test case is included to demonstrate the model's capabilities in simulating slow dynamics. In this scenario, an air bubble is released to rise in water. Figure 9.12 illustrates the domain setup, where $D = 2m$ represents the diameter of the air bubble. For this test case, $\xi = 0.8$ is used to enable the simulation of surface tension.

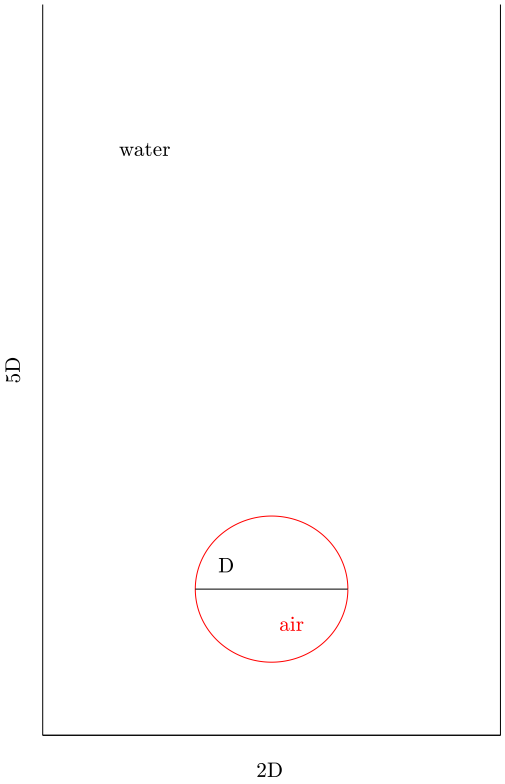

Figure 9.12: Rising bubble domain setup.

Figure 9.13 shows the contours of density, pressure, velocity, and the result of the free surface identification algorithm. The air bubble is initialised with zero pressure, and as the computation starts, the air bubble is suddenly compressed due to the strong pressure gradient with the surrounding water. At $t = 0.8s$, the bubble assumes a lenticular shape as it is pushed upwards. A vertical water jet rises from the bottom in the direction of the bubble axis due to the pressure gradient with respect to the air. The middle right-hand panel shows this water jet with a vertical velocity of approximately $3.5m/s$, increasing to approximately $5m/s$ at $t = 1.15s$. Due to the hydrodynamic thrust of the upward water jet, the bubble moves upwards while its transverse length grows. As the bubble rises, it develops two tails, comparable to the results in [54].

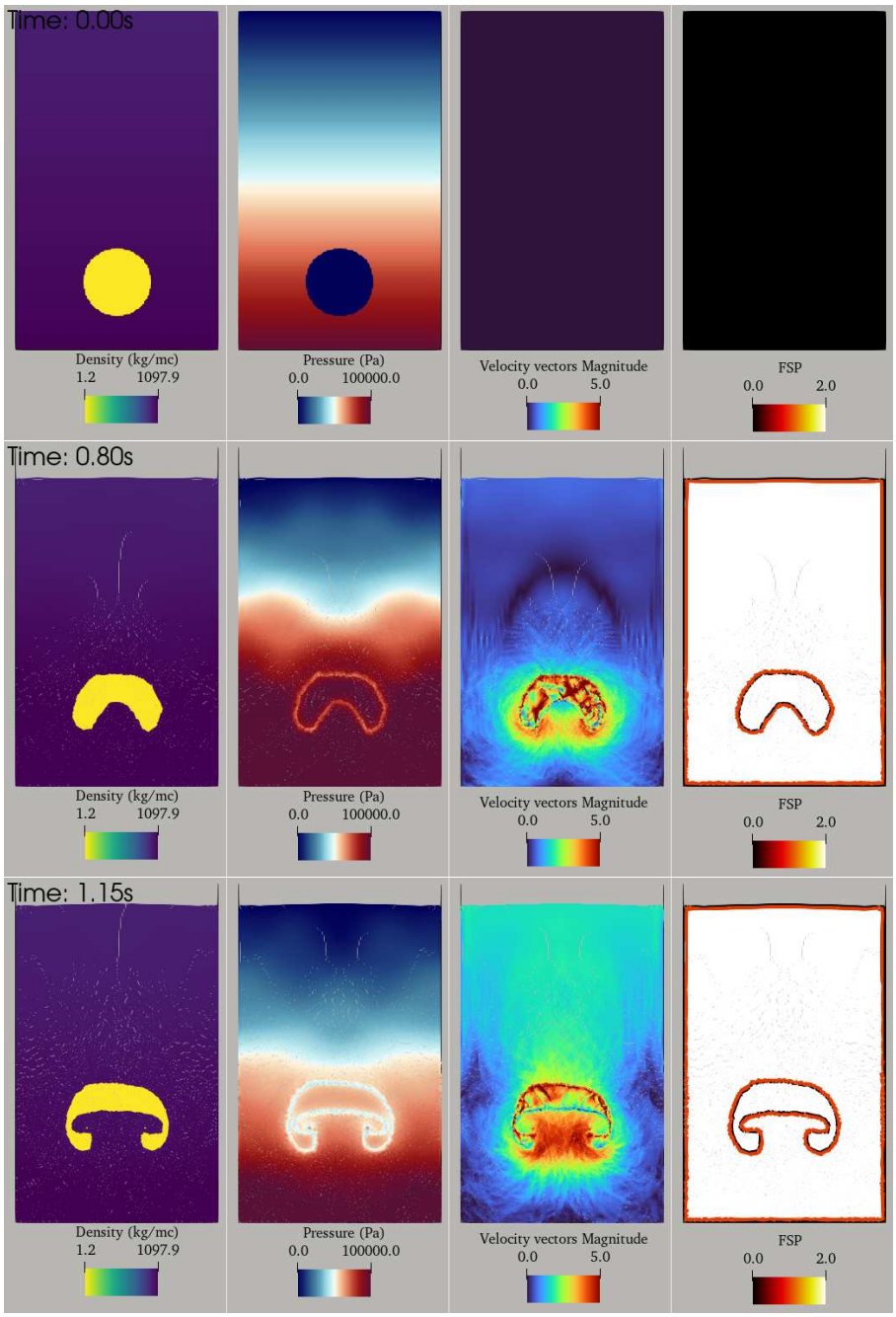

Figure 9.13: Rising bubble. Left panel: Density between media, middle left panel: pressure, middle right panel: magnitude of velocity vectors, right panels: free surface particles.

9.4 Final Remarks

This chapter presents a new strategy to address issues in the multiphase model. A particle shifting technique based on Fick's Law is introduced, along with the use of Riemann solvers to treat the interface. The combination of these methods addresses issues such as tensile instability, particle clusters, and interface gaps. Early applications on three challenging cases are demonstrated. However, the resolution in these early tests is coarse, and smaller particle dimensions are required for a more accurate definition of the fluids. The multiphase dam break is well reproduced, and the pressure results are closer to experimental ones compared to the single-phase model. The rising bubble and falling droplet cases are also successfully modelled, demonstrating high gradients of pressure and velocity without encountering the previously mentioned issues. Therefore, the model is validated. It is important to note that the multiphase model is still in an early development phase, and further testing is needed for validation.

10

Conclusions

This work deals with the modelling of free surface waves using innovative mesh-free particle numerical approaches and discusses the role of numerical models in engineering. It presents the governing equations for a fluid and introduces the SPH and PFEM approaches. The first study focuses on wave hindcasting in the Mediterranean Sea, using the model SWAN to accurately reproduce a storm by hindcasting the significant wave height and spectral period, with validation against field data. SPHERA v9.0.0 model is utilised for modelling regular waves. The introduced improvements to the single-phase model (SPHERA) have enabled accurate modelling of regular waves in a 2D channel and nonlinear waves with structural impact. However, the air cushion interposed between the wave front and structure holds strategic relevance. The current focus lies on developing a multiphase model for high-density ratio between the two media. This new DERIVED model has been validated through accurate modelling of multiphase dam breaks and several single-phase waves; however, it does exhibit some shortcomings that have been addressed subsequently as discussed below. A comparison has been made between this DERIVED model and a PFEM model (Kratos Multiphysics), while new wave cases for both SPH and PFEM are being investigated with results that can accurately reproduce the involved physical phenomena. Another research study explored the interaction of waves with a tension-leg floating structure. The SPHinXsys model is combined with a multibody solver (Simbody) to accurately simulate non-linear wave generation and model structural displacement and impact pressures. The final chapter discusses improvements to the DERIVED model (based on SPHERA v9.0.0) that address the shortcomings identified in previous studies. The last model is tested with simple cases, demonstrating promising results and providing a strong foundation for future investigations. The thesis overall demonstrates the potential of Lagrangian mesh-free particle methods, particularly the smoothed particle hydrodynamics approach, in accurately modelling wave impact on marine structures.

Bibliography

[1] W. Li, S.; Liu, *Meshfree Particle Methods*. Berlin, Germany.: Springer Science & Business Media, 2007.

[2] G.-r. L. Liu, *Smoothed Particle Hydrodynamics: a Meshfree Particle Method*. World Scientific: Singapore, 2003.

[3] S. Manenti, "Continuum mechanics lecture notes," University of Pavia, 2024.

[4] L. B. Lucy, "A numerical approach to the testing of the fission hypothesis," *The astronomical journal*, vol. 82, pp. 1013–1024, 1977.

[5] R. A. Gingold and J. J. Monaghan, "Smoothed particle hydrodynamics: theory and application to non-spherical stars," *Monthly notices of the royal astronomical society*, vol. 181, no. 3, pp. 375–389, 1977.

[6] J. J. Monaghan, "Simulating free surface flows with sph," *Journal of computational physics*, vol. 110, no. 2, pp. 399–406, 1994.

[7] G. R. Johnson, R. A. Stryk, and S. R. Beissel, "Sph for high velocity impact computations," *Computer methods in applied mechanics and engineering*, vol. 139, no. 1-4, pp. 347–373, 1996.

[8] S. Manenti, "Numerical modelling of water waves and wave-structure interactions in an urbanized lagoon," Ph.D. dissertation, University of Rome "La Sapienza", November 2009.

[9] J. Bonet and T.-S. Lok, "Variational and momentum preservation aspects of smooth particle hydrodynamic formulations," *Computer Methods in applied mechanics and engineering*, vol. 180, no. 1-2, pp. 97–115, 1999.

[10] S. Falappi and M. Gallati, "Sph simulations of dam break waves over granular beds," in *1st SPHERIC Workshop*, 2006, p. 22.

[11] S. R. Idelsohn, E. Oñate, and F. D. Pin, "The particle finite element method: a powerful tool to solve incompressible flows with free-surfaces and breaking waves," *International journal for numerical methods in engineering*, vol. 61, no. 7, pp. 964–989, 2004.

[12] E. Oñate, S. Idelsohn, F. Del Pin, and R. Aubry, "The particle finite element method. an overview," *International Journal of Computational Methods*, vol. 2, pp. 267–307, 2004.

[13] A. Franci, "Short course on particle-based method in engineering and applied science (lecture notese)," Eccomas advanced course, Hamburg, 2021.

[14] H. Edelsbrunner and T. Tan, "An upper bound for conforming delaunay triangulations," *Discrete and Computational Geometry*, vol. 10 (2), p. 197:213, 1993.

[15] M. Cremonesi, A. Franci, S. Idelsohn, and E. Oñate, "A state of the art review of the particle finite element method (pfem)," *Archives of Computational Methods in Engineering*, vol. 27, no. 5, pp. 1709–1735, 2020.

[16] E. Oñate, A. Franci, and J. M. Carbonell, "Lagrangian formulation for finite element analysis of quasi-incompressible fluids with reduced mass losses," *International Journal for Numerical Methods in Fluids*, vol. 74, no. 10, pp. 699–731, 2014.

[17] F. Brezzi and M. Fortin, *Mixed And Hybrid Finite Element Methods*. New York: Springer, 1991.

[18] O. C. Zienkiewicz and R. L. Taylor, “The finite element method, volume i,” *Fluid dynamics*, 2000.

[19] E. Oñate, *Structural analysis with the finite element method. Linear statics: volume 2: beams, plates and shells*. Springer Science & Business Media, 2013.

[20] O. C. Zienkiewicz, R. L. Taylor, and J. Z. Zhu, *The finite element method: its basis and fundamentals*. Elsevier, 2005.

[21] N. Booij, L. Holthuijsen, and R. Ris, “The" swan" wave model for shallow water,” in *Coastal Engineering 1996*, 1996, pp. 668–676.

[22] K. Hasselmann, T. P. Barnett, E. Bouws, H. Carlson, D. E. Cartwright, K. Enke, J. Ewing, A. Gienapp, D. Hasselmann, P. Kruseman *et al.*, “Measurements of wind-wave growth and swell decay during the joint north sea wave project (jonswap).” *Ergaenzungsheft zur Deutschen Hydrographischen Zeitschrift, Reihe A*, 1973.

[23] G. B. Whitham, “Linear and nonlinear waves(book),” *New York, Wiley-Interscience, 1974. 651 p*, 1974.

[24] Wiki, “Airy wave theory — Wikipedia, the free encyclopedia,” https://en.wikipedia.org/w/index.php?title=Airy_wave_theory&oldid=927295410, 2019, [Online; accessed 26-November-2019]. [Online]. Available: https://en.wikipedia.org/w/index.php?title=Airy_wave_theory&oldid=927295410

[25] F. Biésel and F. Suquet, “Les appareils générateurs de houle en laboratoire,” *La houille blanche*, no. 2, pp. 147–165, 1951.

[26] P. Frigaard, M. Hgedal, and M. Christensen, “Wave generation theory,” *Hydraulics and Coastal Engineering Laboratory, Dept. of Civil Engineering, Aalborg University, Aalborg (Denmark)*, 1993.

[27] Wikipedia contributors, “John scott russell — Wikipedia, the free encyclopedia,” 2023, [Online; accessed 4-July-2023]. [Online]. Available: https://en.wikipedia.org/w/index.php?title=John_Scott_Russell&oldid=1162288592

[28] K. Dysthe, H. E. Krogstad, and P. Müller, “Oceanic rogue waves,” *Annu. Rev. Fluid Mech.*, vol. 40, pp. 287–310, 2008.

[29] C. Kharif and E. Pelinovsky, “Physical mechanisms of the rogue wave phenomenon,” *European Journal of Mechanics-B/Fluids*, vol. 22, no. 6, pp. 603–634, 2003.

[30] C. Fochesato, S. Grilli, and F. Dias, “Numerical modeling of extreme rogue waves generated by directional energy focusing,” *Wave motion*, vol. 44, no. 5, pp. 395–416, 2007.

[31] A. Karin Magnusson and M. A. Donelan, “The andrea wave characteristics of a measured north sea rogue wave,” *Journal of Offshore Mechanics and Arctic Engineering*, vol. 135, no. 3, 2013.

[32] R. J. Rapp and W. K. Melville, “Laboratory measurements of deep-water breaking waves,” *Philosophical Transactions of the Royal Society of London. Series A, Mathematical and Physical Sciences*, vol. 331, no. 1622, pp. 735–800, 1990.

[33] G. Rodriguez and S. Seatzu, *Introduzione alla Matematica Applicata e Computazionale*. Pitagora Editrice Bologna, 2010.

[34] M. Rahman, D. Riordan, A. Susilo, and S. Mousavizadegan, “The fast fourier transform applied to estimate wave energy spectral density in random sea state,” *WITPRESS LTD.*, 2011.

[35] J. W. Kamphuis, *Introduction to coastal engineering and management*. World Scientific, 2020, vol. 48.

[36] H. U. Sverdrup and W. H. Munk, *Wind, sea and swell: Theory of relations for forecasting*. Hydrographic Office, 1947, no. 601.

[37] C. L. Bretschneider, “Revisions in wave forecasting: deep and shallow water,” *Coastal Engineering Proceedings*, no. 6, pp. 3–3, 1957.

[38] W. S. Richardson, “Forecasting beach erosion along the oceanic coastlines of the northeast and mid-atlantic states,” 1977.

[39] S. A. Hughes *et al.*, “The tma shallow-water spectrum description and applications,” 1984.

[40] L. Cavaleri and P. M. Rizzoli, “Wind wave prediction in shallow water: Theory and applications,” *Journal of Geophysical Research: Oceans*, vol. 86, no. C11, pp. 10 961–10 973, 1981.

[41] G. Komen, S. Hasselmann, and K. Hasselmann, “On the existence of a fully developed wind-sea spectrum,” *Journal of physical oceanography*, vol. 14, no. 8, pp. 1271–1285, 1984.

[42] N. Salis, “Numerical Modelling of Waves in a 2D Flume.” Master’s thesis, University of Pavia., Faculty of Engineering - Department of Civil Engineering and Architecture, 2019.

[43] SPHERA (RSE SpA), https://www.github.com/AndreaAmicarelliRSE/SPHERA, RSE SpA, 2018. [Online]. Available: https://github.com/AndreaAmicarelliRSE/SPHERA

[44] P. Randles and L. D. Libersky, “Smoothed particle hydrodynamics: some recent improvements and applications,” *Computer methods in applied mechanics and engineering*, vol. 139, no. 1-4, pp. 375–408, 1996.

[45] J. Vila, “On particle weighted methods and smooth particle hydrodynamics,” *Mathematical models and methods in applied sciences*, vol. 9, no. 02, pp. 161–209, 1999.

[46] A. Di Monaco, S. Manenti, M. Gallati, S. Sibilla, G. Agate, and R. Guandalini, “Sph modeling of solid boundaries through a semi-analytic approach,” *Engineering Applications of Computational Fluid Mechanics*, vol. 5, no. 1, pp. 1–15, 2011.

[47] A. Amicarelli, R. Albano, D. Mirauda, G. Agate, A. Sole, and R. Guandalini, “A smoothed particle hydrodynamics model for 3d solid body transport in free surface flows,” *Computers & fluids*, vol. 116, pp. 205–228, 2015.

[48] J. J. Monaghan, “Smoothed particle hydrodynamics,” *Reports on progress in physics*, vol. 68, no. 8, p. 1703, 2005.

[49] N. Salis, M. Luo, A. Reali, and S. Manenti, “Sph simulation of water waves and impact with a rigid offshore structure in a 2d flume,” in *The 31st International Ocean and Polar Engineering Conference*. OnePetro, 2021.

[50] M. Gomez-Gesteira, B. D. Rogers, R. A. Dalrymple, and A. J. Crespo, “State-of-the-art of classical sph for free-surface flows,” *Journal of Hydraulic Research*, vol. 48, no. sup1, pp. 6–27, 2010.

[51] M. Antuono, A. Colagrossi, S. Marrone, and D. Molteni, “Free-surface flows solved by means of sph schemes with numerical diffusive terms,” *Computer Physics Communications*, vol. 181, no. 3, pp. 532–549, 2010.

[52] A. Colagrossi, S. Marrone, I. Hammani, G. Oger, and D. Le Touzé, “δ-sph model for multi-phase flow: how to correctly select the sound speeds of the different phases,” in *SPHERIC Harbin 2020*, 2020.

[53] S. Manenti, “Standard wcsph for free-surface multi-phase flows with a large density ratio,” *International Journal of Ocean and Coastal Engineering*, vol. 1, no. 02, p. 1840001, 2018.

[54] A. Colagrossi and M. Landrini, “Numerical simulation of interfacial flows by smoothed particle hydrodynamics,” *Journal of computational physics*, vol. 191, no. 2, pp. 448–475, 2003.

[55] N. Grenier, M. Antuono, A. Colagrossi, D. Le Touzé, and B. Alessandrini, “An hamiltonian interface sph formulation for multi-fluid and free surface flows,” *Journal of Computational Physics*, vol. 228, no. 22, pp. 8380–8393, 2009.

[56] M. Rezavand, C. Zhang, and X. Hu, "A weakly compressible sph method for violent multi-phase flows with high density ratio," *Journal of Computational Physics*, vol. 402, p. 109092, 2020.

[57] G.-R. Liu and M. B. Liu, *Smoothed particle hydrodynamics: a meshfree particle method*. World scientific, 2003.

[58] D. Violeau, *Fluid mechanics and the SPH method: theory and applications*. Oxford University Press, 2012.

[59] D. Molteni and A. Colagrossi, "A simple procedure to improve the pressure evaluation in hydrodynamic context using the sph," *Computer Physics Communications*, vol. 180, no. 6, pp. 861–872, 2009.

[60] M. Antuono, A. Colagrossi, and S. Marrone, "Numerical diffusive terms in weakly-compressible sph schemes," *Computer Physics Communications*, vol. 183, no. 12, pp. 2570–2580, 2012.

[61] M. Antuono, P. Sun, S. Marrone, and A. Colagrossi, "The δ-ale-sph model: An arbitrary lagrangian-eulerian framework for the δ-sph model with particle shifting technique," *Computers & Fluids*, vol. 216, p. 104806, 2021.

[62] "Derived code", https://github.com/ncsalis/SPHERA/tree/SPHERA_v_9_0_0_NS_2P, 2022.

[63] A. Amicarelli, J.-C. Marongiu, F. Leboeuf, J. Leduc, M. Neuhauser, L. Fang, and J. Caro, "Sph truncation error in estimating a 3d derivative," *International journal for numerical methods in engineering*, vol. 87, no. 7, pp. 677–700, 2011.

[64] A. Amicarelli, S. Manenti, R. Albano, G. Agate, M. Paggi, L. Longoni, D. Mirauda, L. Ziane, G. Viccione, S. Todeschini *et al.*, "Sphera v. 9.0. 0: A computational fluid dynamics research code, based on the smoothed particle hydrodynamics mesh-less method," *Computer Physics Communications*, vol. 250, p. 107157, 2020.

[65] S. Adami, X. Y. Hu, and N. A. Adams, "A generalized wall boundary condition for smoothed particle hydrodynamics," *Journal of Computational Physics*, vol. 231, no. 21, pp. 7057–7075, 2012.

[66] S. J. Lind, R. Xu, P. K. Stansby, and B. D. Rogers, "Incompressible smoothed particle hydrodynamics for free-surface flows: A generalised diffusion-based algorithm for stability and validations for impulsive flows and propagating waves," *Journal of Computational Physics*, vol. 231, no. 4, pp. 1499–1523, 2012.

[67] P.-P. Wang, Z.-F. Meng, A.-M. Zhang, F.-R. Ming, and P.-N. Sun, "Improved particle shifting technology and optimized free-surface detection method for free-surface flows in smoothed particle hydrodynamics," *Computer Methods in Applied Mechanics and Engineering*, vol. 357, p. 112580, 2019.

[68] A. Krimi, M. Jandaghian, and A. Shakibaeinia, "A wcsph particle shifting strategy for simulating violent free surface flows," *Water*, vol. 12, no. 11, p. 3189, 2020.

[69] G. Oger, S. Marrone, D. Le Touzé, and M. De Leffe, "Sph accuracy improvement through the combination of a quasi-lagrangian shifting transport velocity and consistent ale formalisms," *Journal of Computational Physics*, vol. 313, pp. 76–98, 2016.

[70] P. Sun, A. Colagrossi, S. Marrone, and A. Zhang, "The δplus-sph model: Simple procedures for a further improvement of the sph scheme," *Computer Methods in Applied Mechanics and Engineering*, vol. 315, pp. 25–49, 2017.

[71] J. Michel, A. Vergnaud, G. Oger, C. Hermange, and D. Le Touzé, "On particle shifting techniques (psts): Analysis of existing laws and proposition of a convergent and multi-invariant law," *Journal of Computational Physics*, vol. 459, p. 110999, 2022.

[72] J. J. Monaghan, "Sph without a tensile instability," *Journal of computational physics*, vol. 159, no. 2, pp. 290–311, 2000.

[73] A. Colagrossi, B. Bouscasse, M. Antuono, and S. Marrone, "Particle packing algorithm for sph schemes," *Computer Physics Communications*, vol. 183, no. 8, pp. 1641–1653, 2012.

[74] S. Marrone, A. Colagrossi, D. Le Touzé, and G. Graziani, "Fast free-surface detection and level-set function definition in sph solvers," *Journal of Computational Physics*, vol. 229, no. 10, pp. 3652–3663, 2010.

[75] A. N. Parshikov and S. A. Medin, "Smoothed particle hydrodynamics using interparticle contact algorithms," *Journal of computational physics*, vol. 180, no. 1, pp. 358–382, 2002.

[76] N. Salis, M. Luo, A. Reali, and S. Manenti, "Wave generation and wave–structure impact modelling with wcsph," *Ocean Engineering*, vol. 266, p. 113228, 2022. [Online]. Available: https://www.sciencedirect.com/science/article/pii/S0029801822025112

[77] ANDREAS, "Adjust legend marker size (), MATLAB Central File Exchange," https://www.mathworks.com/matlabcentral/fileexchange/46105-adjust-legend-marker-size, 2020, [Online; accessed 23-May-2020].

[78] ISCRA, "SCAI - SuperComputing Applications and Innovation," https:/http://www.hpc.cineca.it/services/iscra, 2020, [Online; accessed 23-May-2020].

[79] Wiki, "Galileo (supercomputer) — Wikipedia, the free encyclopedia," https://en.wikipedia.orgwindex.phptitle=Galileo_(supercomputer)&oldid=937753290, 2020, [Online; accessed 23-May-2020].

[80] C. T. Stansberg, "Wave front steepness and influence on horizontal deck impact loads," *Journal of Marine Science and Engineering*, vol. 8, no. 5, p. 314, 2020.

[81] J. W. Kamphuis, *Introduction to coastal engineering and management*. World Scientific, 2010, vol. 30.

[82] D. Reeve, A. Chadwick, and C. Fleming, *Coastal engineering: processes, theory and design practice*. CRC Press, 2012.

[83] S. Manenti, A. Amicarelli, and S. Todeschini, "Wcsph with limiting viscosity for modeling landslide hazard at the slopes of artificial reservoir," *Water*, vol. 10, no. 4, p. 515, 2018.

[84] Y. Wang, J. Liu, K. Yin, L. Yu, H. Zhou, and Z. Huo, "Comparison between the first and second wave crest amplitude generated by landslides," *Ocean Engineering*, vol. 171, pp. 71–77, 2019.

[85] X. Ni, W. Feng, S. Huang, Y. Zhang, and X. Feng, "A sph numerical wave flume with non-reflective open boundary conditions," *Ocean Engineering*, vol. 163, pp. 483–501, 2018.

[86] C. Windt, J. Davidson, P. Schmitt, and J. V. Ringwood, "On the assessment of numerical wave makers in cfd simulations," *Journal of Marine Science and Engineering*, vol. 7, no. 2, p. 47, 2019.

[87] P. Guilcher, G. Ducorzet, B. Alessandrini, and P. Ferrant, "Water wave propagation using sph models," in *Proc. SPHERIC, 2nd Intl. Workshop. Universidad Politecnica de Madrid, Spain, May*, 2007, pp. 23–26.

[88] U. Izquierdo, G. A. Esteban, J. M. Blanco, I. Albaina, and A. Peña, "Experimental validation of a cfd model using a narrow wave flume," *Applied Ocean Research*, vol. 86, pp. 1–12, 2019.

[89] M. Dätig and T. Schlurmann, "Performance and limitations of the hilbert–huang transformation (hht) with an application to irregular water waves," *Ocean Engineering*, vol. 31, no. 14-15, pp. 1783–1834, 2004.

[90] C.-M. Dong and C.-J. Huang, "Generation and propagation of water waves in a two-dimensional numerical viscous wave flume," *Journal of waterway, port, coastal, and ocean engineering*, vol. 130, no. 3, pp. 143–153, 2004.

[91] R. Fatehi and M. T. Manzari, "Error estimation in smoothed particle hydrodynamics and a new scheme for second derivatives," *Computers & Mathematics with Applications*, vol. 61, no. 2, pp. 482–498, 2011.

[92] I. Mirzaii and M. Passandideh-Fard, "Modeling free surface flows in presence of an arbitrary moving object," *International Journal of Multiphase Flow*, vol. 39, pp. 216–226, 2012.

[93] D. De Padova, R. Dalrymple, M. Mossa, and A. Petrillo, "Sph simulations of regular and irregular waves and their comparison with experimental data," *arXiv preprint arXiv:0911.1872*, 2009.

[94] Wiki, “Stokes wave — Wikipedia, the free encyclopedia,” https://en.wikipedia.org/w/index.php?title=Stokes_wave&oldid=952746866, 2020, [Online; accessed 27-April-2020].

[95] ——, “Wave tank — Wikipedia, the free encyclopedia,” https://en.wikipedia.org/w/index.php?title=Wave_tank&oldid=856641715, 2018, [Online; accessed 27-April-2020].

[96] R. Baarholm and C. T. Stansberg, “Extreme vertical wave impact on the deck of a gravity-based structure (gbs) platform,” in *Proc. Conf. on Rogue Waves*, 2004.

[97] W. Wang, A. Kamath, C. Pakozdi, and H. Bihs, “Investigation of focusing wave properties in a numerical wave tank with a fully nonlinear potential flow model,” *Journal of Marine Science and Engineering*, vol. 7, no. 10, p. 375, 2019.

[98] B. Yan, M. Luo, and W. Bai, “An experimental and numerical study of plunging wave impact on a box-shape structure,” *Marine Structures*, vol. 66, pp. 272–287, 2019.

[99] C.-J. Huang, E.-C. Zhang, and J.-F. Lee, “Numerical simulation of nonlinear viscous wavefields generated by piston-type wavemaker,” *Journal of engineering mechanics*, vol. 124, no. 10, pp. 1110–1120, 1998.

[100] F. Ursell, R. G. Dean, and Y. Yu, “Forced small-amplitude water waves: a comparison of theory and experiment,” *Journal of Fluid Mechanics*, vol. 7, no. 1, pp. 33–52, 1960.

[101] M. Anbarsooz, M. Passandideh-Fard, and M. Moghiman, “Fully nonlinear viscous wave generation in numerical wave tanks,” *Ocean Engineering*, vol. 59, pp. 73–85, 2013.

[102] J.-Y. Ahn, J.-K. Choi, and H.-T. Kim, “Investigation of characteristics of waves generated in two-dimensional wave channel,” *Journal of Ocean Engineering and Technology*, vol. 27, no. 4, pp. 68–75, 2013.

[103] S. Manenti, “Fluid mechanics lecture notes,” University of Pavia, 2019.

[104] A. Balzano, “Lezioni di idraulica,” University of Cagliari, 2015.

[105] J. J. Monaghan and A. Kos, “Scott russell’s wave generator,” *Physics of Fluids*, vol. 12, no. 3, pp. 622–630, 2000.

[106] A. Panizzo, P. De Girolamo, and A. Petaccia, “Forecasting impulse waves generated by subaerial landslides,” *Journal of Geophysical Research: Oceans*, vol. 110, no. C12, 2005.

[107] W. Prager, “Introduction to continuum mechanics,” *Ginn, Boston*, 1961.

[108] Wiki, “Newton’s laws of motion — Wikipedia, the free encyclopedia,” https://en.wikipedia.org/wiki/Newton%27s_laws_of_motion, 2019, [Online; accessed 28-July-2019]. [Online]. Available: https://en.wikipedia.org/wiki/Newton%27s_laws_of_motion

[109] R. Courant, K. Friedrichs, and H. Lewy, “Über die partiellen differenzengleichungen der mathematischen physik,” *Mathematische annalen*, vol. 100, no. 1, pp. 32–74, 1928.

[110] S. A. Hughes, “Laboratory wave reflection analysis using co-located gages,” *Coastal Engineering*, vol. 20, no. 3-4, pp. 223–247, 1993.

[111] G. Airy, “Tides and waves, enc,” 1841.

[112] Wiki, “Fourier transform — Wikipedia, the free encyclopedia,” https://en.wikipedia.org/w/index.php?title=Fourier_transform&oldid=934670809, 2020, [Online; accessed 28-January-2020]. [Online]. Available: https://en.wikipedia.org/w/index.php?title=Fourier_transform&oldid=934670809

[113] J. Monaghan and A. Kocharyan, “Sph simulation of multi-phase flow,” *Computer Physics Communications*, vol. 87, no. 1-2, pp. 225–235, 1995.

[114] P.-N. Sun, M. Luo, D. Le Touzé, and A.-M. Zhang, "The suction effect during freak wave slamming on a fixed platform deck: Smoothed particle hydrodynamics simulation and experimental study," *Physics of Fluids*, vol. 31, no. 11, p. 117108, 2019.

[115] M. Gómez-Gesteira, D. Cerqueiro, C. Crespo, and R. Dalrymple, "Green water overtopping analyzed with a sph model," *Ocean Engineering*, vol. 32, no. 2, pp. 223–238, 2005.

[116] Z. Zhou, J. De Kat, and B. Buchner, "A nonlinear 3d approach to simulate green water dynamics on deck," in *Proceedings of the seventh international conference on numerical ship hydrodynamics, Nantes, France*, 1999, pp. 1–15.

[117] K. Gong, S. Shao, H. Liu, B. Wang, and S.-K. Tan, "Two-phase sph simulation of fluid–structure interactions," *Journal of Fluids and Structures*, vol. 65, pp. 155–179, 2016.

[118] I. Hammani, S. Marrone, A. Colagrossi, G. Oger, and D. Le Touzé, "Detailed study on the extension of the δ-sph model to multi-phase flow," *Computer Methods in Applied Mechanics and Engineering*, vol. 368, p. 113189, 2020.

[119] A. C. Kruisbrink, F. Pearce, T. Yue, and H. Morvan, "An sph multi-fluid model based on quasi buoyancy for interface stabilization up to high density ratios and realistic wave speed ratios," *International Journal for Numerical Methods in Fluids*, vol. 87, no. 10, pp. 487–507, 2018.

[120] A. Mokos, B. D. Rogers, and P. K. Stansby, "A multi-phase particle shifting algorithm for sph simulations of violent hydrodynamics with a large number of particles," *Journal of Hydraulic Research*, vol. 55, no. 2, pp. 143–162, 2017.

[121] P. Sun, A. Colagrossi, S. Marrone, M. Antuono, and A.-M. Zhang, "A consistent approach to particle shifting in the δ-plus-sph model," *Computer Methods in Applied Mechanics and Engineering*, vol. 348, pp. 912–934, 2019.

[122] P. Sun, A. Colagrossi, S. Marrone, M. Antuono, and A. Zhang, "Multi-resolution delta-plus-sph with tensile instability control: Towards high reynolds number flows," *Computer Physics Communications*, vol. 224, pp. 63–80, 2018.

[123] C. Altomare, A. Tafuni, J. M. Domínguez, A. J. Crespo, X. Gironella, and J. Sospedra, "Sph simulations of real sea waves impacting a large-scale structure," *Journal of Marine Science and Engineering*, vol. 8, no. 10, p. 826, 2020.

[124] O. S. Areu-Rangel, J. V. Hernández-Fontes, R. Silva, P. T. Esperança, and J. Klapp, "Green water loads using the wet dam-break method and sph," *Ocean Engineering*, vol. 219, p. 108392, 2021.

[125] H. Chanson, "Analytical solutions of laminar and turbulent dam break wave," in *River Flow*, 2006, pp. 465–474.

[126] Z. Chen, Z. Zong, M. Liu, L. Zou, H. Li, and C. Shu, "An sph model for multiphase flows with complex interfaces and large density differences," *Journal of Computational Physics*, vol. 283, pp. 169–188, 2015.

[127] A. Colagrossi, M. Antuono, A. Souto-Iglesias, and D. Le Touzé, "Theoretical analysis and numerical verification of the consistency of viscous smoothed-particle-hydrodynamics formulations in simulating free-surface flows," *Physical Review E*, vol. 84, no. 2, p. 026705, 2011.

[128] R. Guandalini, G. Agate, A. Amicarelli, S. Manenti, M. Gallati, and S. Sibilla, "Sph modelling of a 3d tsunami test case," *Development and Applications of Oceanic Engineering*, vol. 3, pp. 11–21, 2014.

[129] H.-G. Lyu, P.-N. Sun, X.-T. Huang, S.-Y. Zhong, Y.-X. Peng, T. Jiang, and C.-N. Ji, "A review of sph techniques for hydrodynamic simulations of ocean energy devices," *Energies*, vol. 15, no. 2, p. 502, 2022.

[130] G. R. Johnson and S. R. Beissel, "Normalized smoothing functions for sph impact computations," *International Journal for Numerical Methods in Engineering*, vol. 39, no. 16, pp. 2725–2741, 1996.

[131] T. Jiang, Y. Li, P.-N. Sun, J.-L. Ren, Q. Li, and J.-Y. Yuan, "A corrected wcsph scheme with improved interface treatments for the viscous/viscoelastic two-phase flows," *Computational Particle Mechanics*, pp. 1–21, 2021.

[132] S. Lee and J.-W. Hong, "A semi-infinite numerical wave tank using discrete particle simulations," *Journal of Marine Science and Engineering*, vol. 8, no. 3, p. 159, 2020.

[133] M. Luo, A. Khayyer, and P. Lin, "Particle methods in ocean and coastal engineering," *Applied Ocean Research*, vol. 114, p. 102734, 2021.

[134] S. Manenti, "Wcsph for modelling multiphase flows and natural hazards," in *PARTICLES VI: proceedings of the VI International Conference on Particle-Based Methods: fundamentals and applications*. CIMNE, 2019, pp. 702–713.

[135] S. Marrone, A. Colagrossi, D. Le Touzé, and G. Graziani, "A fast algorithm for free-surface particles detection in 2d and 3d sph methods," in *Proc. fourth Int. SPHeric Workshop*, 2009, pp. 27–29.

[136] J. J. Monaghan and R. A. Gingold, "Shock simulation by the particle method sph," *Journal of computational physics*, vol. 52, no. 2, pp. 374–389, 1983.

[137] J. J. Monaghan and A. Rafiee, "A simple sph algorithm for multi-fluid flow with high density ratios," *International Journal for Numerical Methods in Fluids*, vol. 71, no. 5, pp. 537–561, 2013.

[138] C. Pákozdi, A. Östeman, C. T. Stansberg, M. Peric, H. Lu, and R. Baarholm, "Estimation of wave in deck load using cfd validated against model test data," in *The Twenty-fifth International Ocean and Polar Engineering Conference*. OnePetro, 2015.

[139] C. T. Stansberg, R. Baarholm, T. Kristiansen, E. Hansen, and G. Rortveit, "Extreme wave amplification and impact loads on offshore structures," in *Offshore Technology Conference*. OnePetro, 2005.

[140] A. Trimulyono, H. Hashimoto, and A. Matsuda, "Experimental validation of single-and two-phase smoothed particle hydrodynamics on sloshing in a prismatic tank," *Journal of Marine Science and Engineering*, vol. 7, no. 8, p. 247, 2019.

[141] D. Violeau and B. D. Rogers, "Smoothed particle hydrodynamics (sph) for free-surface flows: past, present and future," *Journal of Hydraulic Research*, vol. 54, no. 1, pp. 1–26, 2016.

[142] M. Yan, X. Ma, W. Bai, Z. Lin, and Y. Li, "Numerical simulation of wave interaction with payloads of different postures using openfoam," *Journal of Marine Science and Engineering*, vol. 8, no. 6, p. 433, 2020.

[143] C. Zhang, X. Hu, and N. A. Adams, "A weakly compressible sph method based on a low-dissipation riemann solver," *Journal of Computational Physics*, vol. 335, pp. 605–620, 2017.

[144] S. Koshizuka and Y. Oka, "Moving-particle semi-implicit method for fragmentation of incompressible fluid," *Nuclear science and engineering*, vol. 123, no. 3, pp. 421–434, 1996.

[145] C. Koh, M. Gao, and C. Luo, "A new particle method for simulation of incompressible free surface flow problems," *International journal for numerical methods in engineering*, vol. 89, no. 12, pp. 1582–1604, 2012.

[146] E. Oñate, S. Idelsohn, O. Zienkiewicz, R. Taylor, and C. Sacco, "A stabilized finite point method for analysis of fluid mechanics problems," *Computer methods in applied mechanics and engineering*, vol. 139, no. 1-4, pp. 315–346, 1996.

[147] E. Oñate, S. Idelsohn, O. Zienkiewicz, and R. Taylor, "A finite point method in computational mechanics. applications to convective transport and fluid flow," *International journal for numerical methods in engineering*, vol. 39, no. 22, pp. 3839–3866, 1996.

[148] S. R. Idelsohn, E. Onate, N. Calvo, and F. Del Pin, "The meshless finite element method," *International Journal for Numerical Methods in Engineering*, vol. 58, no. 6, pp. 893–912, 2003.

[149] F. Brezzi and M. Fortin, *Mixed and hybrid finite element methods*. Springer Science & Business Media, 2012, vol. 15.

[150] M. L. Cerquaglia, G. Deliége, R. Boman, V. Terrapon, and J.-P. Ponthot, "Free-slip boundary conditions for simulating free-surface incompressible flows through the particle finite element method," *International Journal for Numerical Methods in Engineering*, vol. 110, no. 10, pp. 921–946, 2017.

[151] A. Larese, "A lagrangian pfem approach for non-newtonian viscoplastic materials," *Revista internacional de métodos numéricos para cálculo y diseño en ingeniería*, vol. 33, no. 3-4, pp. 307–317, 2017.

[152] S. C. Mohapatra, H. Islam, T. S. Hallak, and C. G. Soares, "Solitary wave interaction with a floating pontoon based on boussinesq model and cfd-based simulations," *Journal of Marine Science and Engineering*, vol. 10, no. 9, p. 1251, 2022.

[153] X. Liu, P. Lin, and S. Shao, "Isph wave simulation by using an internal wave maker," *Coastal Engineering*, vol. 95, pp. 160–170, 2015.

[154] M. Luo, D. E. Reeve, S. Shao, H. Karunarathna, P. Lin, and H. Cai, "Consistent particle method simulation of solitary wave impinging on and overtopping a seawall," *Engineering Analysis with Boundary Elements*, vol. 103, pp. 160–171, 2019.

[155] E. Oñate, A. Cornejo, F. Zárate, K. Kashiyama, and A. Franci, "Combination of the finite element method and particle-based methods for predicting the failure of reinforced concrete structures under extreme water forces," *Engineering Structures*, vol. 251, p. 113510, 2022.

[156] A. Franci, M. Masó, I. de Pouplana, A. Cornejo, and E. Oñate, "A lagrangian-eulerian procedure for the coupled solution of the navier-stokes and shallow water equations for landslide-generated waves," *Advanced Modeling and Simulation in Engineering Sciences. (preprint)*, 2022.

[157] R. G. Dean and R. A. Dalrymple, *Water wave mechanics for engineers and scientists*. world scientific publishing company, 1991, vol. 2.

[158] T. Arikawa, "Structural behavior under impulsive tsunami loading," *Journal of Disaster Research*, vol. 4, no. 6, pp. 377–381, 2009.

[159] C. Krautwald, J. Stolle, J. Hitzegrad, P. Niebuhr, N. Goseberg, I. Nistor, and M. Sieder, "Large-scale physical modelling of a broken solitary wave impact on rigid and non-rigid box-like structures," *Coastal Engineering Proceedings*, 2020.

[160] C. Krautwald, H. Von Häfen, P. Niebuhr, K. Vögele, D. Schürenkamp, M. Sieder, and N. Goseberg, "Large-scale physical modeling of broken solitary waves impacting elevated coastal structures," *Coastal Engineering Journal*, vol. 64, no. 1, pp. 169–189, 2022.

[161] C. Krautwald, J. Stolle, I. Robertson, H. Achiari, T. Mikami, R. Nakamura, T. Takabatake, Y. Nishida, T. Shibayama, M. Esteban *et al.*, "Engineering lessons from september 28, 2018 indonesian tsunami: Scouring mechanisms and effects on infrastructure." *Journal of Waterway, Port, Coastal, and Ocean Engineering*, vol. 147, no. 2, p. 04020056, 2021.

[162] M. He, A. Khayyer, X. Gao, W. Xu, and B. Liu, "Theoretical method for generating solitary waves using plunger-type wavemakers and its smoothed particle hydrodynamics validation," *Applied Ocean Research*, vol. 106, p. 102414, 2021.

[163] KratosMultiphysics , https://github.com/KratosMultiphysics/Kratos, 2022.

[164] R. Mulligan, A. Franci, M. Celigueta, and W. Take, "Simulations of landslide wave generation and propagation using the particle finite element method," *Journal of Geophysical Research: Oceans*, vol. 125, p. e2019JC015873, 06 2020.

[165] T. Oliveira, A. Sánchez-Arcilla, and X. Gironella, “Simulation of wave overtopping of maritime structures in a numerical wave flume,” *Journal of Applied Mathematics*, p. 246146, 07 2012.

[166] T. C. A. Oliveira, A. Sanchez-Arcilla, X. Gironella, and O. S. Madsen, “On the generation of regular long waves in numerical wave flumes based on the particle finite element method,” *Journal of Hydraulic Research*, vol. 55, no. 4, pp. 538–556, 2017.

[167] S. R. Idelsohn, J. Marti, P. Becker, and E. Oñate, “Analysis of multifluid flows with large time steps using the particle finite element method,” *International Journal for Numerical Methods in Fluids*, vol. 75, no. 9, pp. 621–644, 2014. [Online]. Available: https://onlinelibrary.wiley.com/doi/abs/10.1002/fld.3908

[168] S. R. Idelsohn, N. Nigro, J. Gimenez, R. Rossi, and J. Marti, “A fast and accurate method to solve the incompressible navier-stokes equations,” *Engineering Computations*, vol. 30, no. 3, 2013.

[169] D. Sulsky, Z. Chen, and H. L. Schreyer, “A particle method for history-dependent materials,” *Computer methods in applied mechanics and engineering*, vol. 118, no. 1-2, pp. 179–196, 1994.

[170] H. Edelsbrunner and E. Mucke, “Three dimensional alpha shapes,” *ACM Transactions on Graphics (TOG)*, vol. 13 (1), pp. 43–72, 1999.

[171] S. Manenti, S. Sibilla, M. Gallati, G. Agate, and R. Guandalini, “Sph simulation of sediment flushing induced by a rapid water flow,” *Journal of Hydraulic Engineering*, vol. 138, no. 3, pp. 272–284, 2012.

[172] S. Meduri, M. Cremonesi, and U. Perego, “An efficient runtime mesh smoothing technique for 3d explicit lagrangian free-surface fluid flow simulations,” *International Journal for Numerical Methods in Engineering*, vol. 117, no. 4, pp. 430–452, 2019.

[173] J. W. Johnson, “Scale effects in hydraulic models involving wave motion,” *Eos, Transactions American Geophysical Union*, vol. 30, no. 4, pp. 517–525, 1949.

[174] S. J. Lind, B. D. Rogers, and P. K. Stansby, “Review of smoothed particle hydrodynamics: towards converged lagrangian flow modelling,” *Proceedings of the Royal Society A*, vol. 476, no. 2241, p. 20190801, 2020.

[175] S. Lee, K. Ko, and J.-W. Hong, “Comparative study on the breaking waves by a piston-type wavemaker in experiments and sph simulations,” *Coastal Engineering Journal*, vol. 62, no. 2, pp. 267–284, 2020.

[176] M. Gallati, G. Braschi, and S. Falappi, “Sph simulations of the waves produced by a falling mass into a reservoir,” *Il nuovo cimento C*, vol. 28, no. 2, pp. 129–140, 2005.

[177] E. Y. Lo and S. Shao, “Simulation of near-shore solitary wave mechanics by an incompressible sph method,” *Applied Ocean Research*, vol. 24, no. 5, pp. 275–286, 2002.

[178] S. Gu, W. Zheng, H. Wu, C. Chen, and S. Shao, “Dualsphysics simulations of spillway hydraulics: a comparison between single-and two-phase modelling approaches,” *Journal of Hydraulic Research*, vol. 60, no. 5, pp. 835–852, 2022.

[179] M. Luo, C. Koh, W. Bai, and M. Gao, “A particle method for two-phase flows with compressible air pocket,” *International Journal for Numerical Methods in Engineering*, vol. 108, no. 7, pp. 695–721, 2016.

[180] E. Chan and W. Melville, “Deep-water plunging wave pressures on a vertical plane wall,” *Proceedings of the Royal Society of London. A. Mathematical and Physical Sciences*, vol. 417, no. 1852, pp. 95–131, 1988.

[181] E. Bitner-Gregersen and O. Gramstad, “Rogue waves-impact on ships and offshore structures. no. 5-2015 in dnv gl position paper. dnv gl strategic research & innovation,” 2016.

[182] M. Luo, C. G. Koh, W. X. Lee, P. Lin, and D. E. Reeve, “Experimental study of freak wave impacts on a tension-leg platform,” *Marine Structures*, vol. 74, p. 102821, 2020.

[183] M. Luo, M. Rubinato, X. Wang, and X. Zhao, “Experimental investigation of freak wave actions on a floating platform and effects of the air gap,” *Ocean Engineering*, vol. 253, p. 111192, 2022.

[184] N. Salis, M. Luo, A. Reali, and S. Manenti, “Wave generation and wave–structure impact modelling with wcsph,” *Ocean Engineering*, vol. 266, p. 113228, 2022.

[185] L. Chen, J. Zang, A. J. Hillis, G. C. Morgan, and A. R. Plummer, “Numerical investigation of wave–structure interaction using openfoam,” *Ocean Engineering*, vol. 88, pp. 91–109, 2014.

[186] J. Westphalen, D. M. Greaves, A. Raby, Z. Z. Hu, D. M. Causon, C. G. Mingham, P. Omidvar, P. K. Stansby, B. D. Rogers *et al.*, “Investigation of wave-structure interaction using state of the art cfd techniques,” *Open Journal of Fluid Dynamics*, vol. 4, no. 01, p. 18, 2014.

[187] Y. Deng, J. Yang, W. Zhao, X. Li, and L. Xiao, “Freak wave forces on a vertical cylinder,” *Coastal Engineering*, vol. 114, pp. 9–18, 2016.

[188] T. Verbrugghe, J. M. Domínguez, A. J. Crespo, C. Altomare, V. Stratigaki, P. Troch, and A. Kortenhaus, “Coupling methodology for smoothed particle hydrodynamics modelling of non-linear wave-structure interactions,” *Coastal Engineering*, vol. 138, pp. 184–198, 2018.

[189] S. Manenti, A. Panizzo, P. Ruol, and L. Martinelli, “Sph simulation of a floating body forced by regular waves,” in *Proceedings of 3rd SPHERIC Workshop*, 2008, pp. 38–41.

[190] B. Tagliafierro, M. Karimirad, I. Martínez-Estévez, J. M. Domínguez, G. Viccione, and A. J. Crespo, “Numerical assessment of a tension-leg platform wind turbine in intermediate water using the smoothed particle hydrodynamics method,” *Energies*, vol. 15, no. 11, p. 3993, 2022.

[191] N. Salis, A. Franci, S. Idelsohn, A. Reali, and S. Manenti, “Lagrangian particle-based simulation of waves: a comparison of sph and pfem approaches,” *Engineering with Computers*, 2023. [Online]. Available: https://doi.org/10.1007/s00366-023-01831-w

[192] M. A. Sherman, A. Seth, and S. L. Delp, “Simbody: multibody dynamics for biomedical research,” *Procedia Iutam*, vol. 2, pp. 241–261, 2011.

[193] D. Wu, C. Zhang, X. Tang, and X. Hu, “An essentially non-hourglass formulation for total lagrangian smoothed particle hydrodynamics,” *Computer Methods in Applied Mechanics and Engineering*, vol. 407, p. 115915, 2023.

[194] Y. Ren, A. Khayyer, P. Lin, and X. Hu, “Numerical modeling of sloshing flow interaction with an elastic baffle using sphinxsys,” *Ocean Engineering*, vol. 267, p. 113110, 2023.

[195] C. Zhang, M. Rezavand, Y. Zhu, Y. Yu, D. Wu, W. Zhang, J. Wang, and X. Hu, “Sphinxsys: An open-source multi-physics and multi-resolution library based on smoothed particle hydrodynamics,” *Computer Physics Communications*, vol. 267, p. 108066, 2021.

[196] C. Zhang, Y.-j. Zhu, D. Wu, N. A. Adams, and X. Hu, “Smoothed particle hydrodynamics: Methodology development and recent achievement,” *Journal of Hydrodynamics*, vol. 34, no. 5, pp. 767–805, 2022.

[197] L. Han and X. Hu, “Sph modeling of fluid-structure interaction,” *Journal of Hydrodynamics*, vol. 30, pp. 62–69, 2018.

[198] C. Zhang, M. Rezavand, and X. Hu, “Dual-criteria time stepping for weakly compressible smoothed particle hydrodynamics,” *Journal of Computational Physics*, vol. 404, p. 109135, 2020.

[199] C. Zhang, M. Rezavand, Y. Zhu, Y. Yu, D. Wu, W. Zhang, S. Zhang, J. Wang, and X. Hu, “Sphinxsys: An open-source meshless, multi-resolution and multi-physics library,” *Software Impacts*, vol. 6, p. 100033, 2020.

[200] C. Zhang, M. Rezavand, and X. Hu, “A multi-resolution sph method for fluid-structure interactions,” *Journal of Computational Physics*, vol. 429, p. 110028, 2021.

[201] C. Zhang, J. Wang, M. Rezavand, D. Wu, and X. Hu, “An integrative smoothed particle hydrodynamics method for modeling cardiac function,” *Computer Methods in Applied Mechanics and Engineering*, vol. 381, p. 113847, 2021.

[202] Y. Zhu, C. Zhang, Y. Yu, and X. Hu, “A cad-compatible body-fitted particle generator for arbitrarily complex geometry and its application to wave-structure interaction,” *Journal of Hydrodynamics*, vol. 33, no. 2, pp. 195–206, 2021.

[203] C. Zhang, Y. Zhu, X. Lyu, and X. Hu, “An efficient and generalized solid boundary condition for sph: Applications to multi-phase flow and fluid–structure interaction,” *European Journal of Mechanics-B/Fluids*, vol. 94, pp. 276–292, 2022.

[204] Y. Zhu, C. Zhang, and X. Hu, “A dynamic relaxation method with operator splitting and random-choice strategy for sph,” *Journal of Computational Physics*, vol. 458, p. 111105, 2022.

[205] C. Zhang, H. Gao, and X. Hu, “A multi-order smoothed particle hydrodynamics method for cardiac electromechanics with the purkinje network,” *Computer Methods in Applied Mechanics and Engineering*, vol. 407, p. 115885, 2023.

[206] Y. Yu, Y. Zhu, C. Zhang, O. J. Haidn, and X. Hu, “Level-set based pre-processing techniques for particle methods,” *Computer Physics Communications*, vol. 289, p. 108744, 2023.

[207] X. Y. Hu and N. A. Adams, “A multi-phase sph method for macroscopic and mesoscopic flows,” *Journal of Computational Physics*, vol. 213, no. 2, pp. 844–861, 2006.

[208] C. Zhang, Y. Wei, F. Dias, and X. Hu, “An efficient fully lagrangian solver for modeling wave interaction with oscillating wave surge converter,” *Ocean Engineering*, vol. 236, p. 109540, 2021.

[209] J. M. Domínguez, A. J. Crespo, M. Hall, C. Altomare, M. Wu, V. Stratigaki, P. Troch, L. Cappietti, and M. Gómez-Gesteira, “Sph simulation of floating structures with moorings,” *Coastal Engineering*, vol. 153, p. 103560, 2019.

[210] Y. Ren, P. Lin, C. Zhang, and X. Hu, “An efficient and generalized consistency correction method for weakly-compressible sph,” *arXiv preprint arXiv:2304.14865*, 2023.

[211] G. Cai, M. Luo, Y. Zhan, and A. Khayyer, “Sph simulation of freak wave impact on a floating platform,” in *The 33rd International Ocean and Polar Engineering Conference*. OnePetro, 2023.

[212] N. Akinci, G. Akinci, and M. Teschner, “Versatile surface tension and adhesion for sph fluids,” *ACM Transactions on Graphics (TOG)*, vol. 32, no. 6, pp. 1–8, 2013.